

MIMO Application for the Quadrifilar Helix Antenna

Mohd Fais Bin Mansor

Submitted for the Degree of
Doctor of Philosophy
from the
University of Surrey



Centre for Communication Systems Research
Faculty of Engineering and Physical Sciences
University of Surrey
Guildford, Surrey GU2 7XH, U.K.

April 2012

© Mohd Fais Bin Mansor 2012

Abstract

Capacity increase of the current land mobile satellite (LMS) communication systems is highly desirable to cater for more data-centric applications such as broadcasting. Since the Multiple-input Multiple-output (MIMO) offers high spectral efficiency without additional bandwidth and transmit power, its implementation in the LMS system has been widely investigated in terms of channel characterisation, channel modelling and coding algorithms. However, the aspect of receive antenna design and its performance evaluation has not yet been considered even though it has enormous impacts on the system performance.

This thesis presents a study on designing a novel dual circularly polarised receive antenna system for the LMS MIMO system that utilises the printed quadrifilar helix antenna (PQHA) and also the required performance evaluation methods. The PQHA was miniaturised using two new methods, which are the element folding and combination of element folding and meandering where more than 50% size reduction can be achieved. These miniaturised PQHAs were combined to create a variety of dual circularly polarised arrays such as the dual circularly polarised single folded PQHA (SFPQHA) horizontal array and folded meandered PQHA (FMPQHA) vertical array.

For evaluating the branch power ratio of these arrays, a newly derived formulation of the mean effective gain (MEG) in a Ricean fading channel that incorporates the polarisation of the line-of-sight (LoS) component and the corresponding antenna gain has been proposed. Further evaluation of these arrays as the receive antenna in this system was carried out using measurement campaigns. Results show that both arrays provide substantial capacity increase when compared to a single link system in both LoS and NLoS channels. A more comprehensive study on the effect of antenna properties was conducted using a newly developed channel model that integrates the array characteristics with the propagation channel. This modelling approach allows for a performance comparison between the designed SFPQHA array and other antennas to be easily implemented, which is very useful in the process of designing MIMO antennas.

Key words: Land mobile satellite system, MIMO, Quadrifilar helix antenna, MIMO antenna evaluation, LMS MIMO channel model

Email: m.mansor@surrey.ac.uk

WWW: <http://www.feps.surrey.ac.uk/>

Acknowledgements

This thesis would not have been possible without the supervision of Dr. Tim Brown throughout these four years. I would like to express my sincere gratitude for his expert guidance and continual support in completing this research work successfully. Many thanks also go to Prof. Barry Evans for his advices at the start of this work. My thanks also to Mr. Unwana Ekpe and Mr. Tengku Faiz for their help in conducting outdoor measurement trials and fruitful discussions on the research matters. I also would like to thank the National University of Malaysia and Malaysia Ministry of Higher Education for sponsoring my Ph.D. study.

My deepest love and thanks go to my family for their love, encouragement and support in pursuing my dream, especially that of my father Mr. Mansor Ariffin. To my sisters Mursyidah, Suhaila and Nor Faizah, my brother Ainuddin and my brother-in-law Azhar, I owe them my sincere gratitude for their unequivocal support and patience. I would also like to dedicate this thesis to my late mother, Mrs. Satun Mat Salleh who passed away in the early months of this study. The memory of her love and care have helped me to push through the difficult stages in this study.

My life in Guildford has been greatly enriched with the friendships of many wonderful people. Firstly, I would like to express my deepest thanks to my beloved fiancée Ms. Hazrina Mansor who has always been there for me, providing advices, motivation and support. My sincere gratitude also extends to my good friends Mohd Khairul, Yazmin and family, Mustafasanie and family, Lukman Hanif, Dilla and husband, Anas and family, Azhar and family, Iskandar, Ashrani and the 'Cabellian' group. Their friendship has make my life here so full of laughter and good memories.

Lastly, all praises are due to Allah the Almighty with his compassion and mercifulness which allows me to complete this Ph.D. study.

Contents

List of Figures	v
List of Tables	xii
Nomenclature	xiv
Acronyms	xviii
1 Introduction	1
1.1 Motivation	1
1.2 Structure of thesis	2
1.3 Contributions	4
1.4 Publications	5
2 Literature Review	6
2.1 Introduction	6
2.2 Land mobile satellite MIMO system	7
2.2.1 Circular polarisation based MIMO	7
2.2.2 Effect of propagation channel	10
2.2.3 Single satellite MIMO system	15
2.2.4 Main challenges in terms of satellite channel	17
2.2.5 Satellite MIMO measurements	18
2.2.6 Dual polarised satellite MIMO channel modeling approaches	21
2.2.7 Antenna design impacts on LMS MIMO system	26
2.2.8 Candidate antennas for satellite MIMO receiver	27
2.3 Quadrifilar helix antenna	30

2.3.1	Applications to satellite communication and navigation systems .	30
2.3.2	Physical structure and feed arrangement	31
2.3.3	Radiation and impedance properties	32
2.3.4	Bandwidth and multi-band operation	35
2.3.5	Miniaturisation techniques	37
2.4	Evaluating antennas in MIMO system	39
2.4.1	Figures of Merit	40
2.4.2	Evaluation methods	44
2.4.3	Antenna impacts on MIMO system	48
2.5	Summary	51
3	Miniaturisation of printed quadrifilar helix antenna by element folding methods	53
3.1	Introduction	53
3.2	Miniaturisation of 0.5λ PQHA using element folding method	54
3.2.1	Single folded configuration	55
3.2.2	Double folded configuration	61
3.2.3	Prototype fabrication	68
3.2.4	Scattering parameters measurement	71
3.2.5	Radiation pattern measurement	74
3.3	Miniaturisation of 0.75λ PQHA	74
3.3.1	Element folding and meandering method	76
3.3.2	Simulation results	78
3.3.3	Prototype fabrication	81
3.3.4	Scattering parameters measurement	83
3.3.5	Radiation pattern measurement	83
3.4	Summary	85
4	Dual circular polarisation design using printed quadrifilar helix antenna	86
4.1	Introduction	86
4.2	Inside-out configuration of dual polarised CPQHA	87
4.2.1	Design configuration	87

4.2.2	Simulation results	89
4.2.3	Fabrication and measurement	91
4.3	Dual polarised FMPQHA vertical array	94
4.3.1	Design configuration	94
4.3.2	Feed network	95
4.3.3	Simulation results	97
4.3.4	Fabrication and measurement	98
4.4	Dual polarised SFPQHA horizontal array	102
4.4.1	Design configuration	102
4.4.2	Simulation results	103
4.4.3	Fabrication and measurement	106
4.5	Summary	107
5	Branch power and correlation analyses of a dual circularly polarised SFPQHA array	110
5.1	Introduction	110
5.2	Branch power analysis	111
5.2.1	Limitation of current MEG formulations	112
5.2.2	MEG formulation in Ricean fading channel with antenna and LoS component phases	112
5.2.3	MEG analysis of a dual circularly polarised SFPQHA array	120
5.3	Correlation analysis	128
5.3.1	Complex correlation in Rayleigh and Ricean channels	128
5.3.2	Effect of the channel properties	129
5.3.3	Effect of antenna spacing	131
5.3.4	Effect of antenna polarisation	134
5.4	Summary	140
6	Evaluation of receive MIMO antennas in LMS MIMO system via measurement campaigns	142
6.1	Introduction	142
6.2	Measurement equipments and procedures	143
6.2.1	Elektrobit Propsound MIMO wideband channel sounder	143

6.2.2	Transmit antennas	148
6.2.3	Receive antennas	149
6.2.4	Procedures	150
6.3	Measurement campaigns	153
6.3.1	Newlands Corner measurement	153
6.3.2	Bishops Court measurement	156
6.4	Results from Newlands Corner measurement	160
6.4.1	Narrowband channel characteristics	160
6.4.2	Received power	163
6.4.3	Correlation	164
6.4.4	Capacity	165
6.4.5	Eigenvalue distribution	167
6.5	Results from Bishops Court measurement	169
6.5.1	Narrowband channel characteristics	169
6.5.2	Received power	171
6.5.3	Correlation	172
6.5.4	Capacity	172
6.5.5	Eigenvalue distribution	174
6.6	Summary	174
7	LMS MIMO channel simulation for receive antennas evaluation	176
7.1	Introduction	176
7.2	Basic channel description	177
7.3	Large scale fade modelling	178
7.3.1	Markov state modelling	178
7.3.2	Shadowing	179
7.4	Small scale fade modelling	180
7.4.1	3-D geometric scattering model	181
7.4.2	Coherent component	186
7.4.3	Incoherent component	187
7.4.4	Inclusion of receive antenna properties	187
7.5	Narrowband simulation and results comparison with measurement	191

7.5.1	Measurement used in result comparison	191
7.5.2	Simulation procedure and parameters	191
7.5.3	Results comparison	193
7.6	Effects of receive antenna orientation	200
7.6.1	Antennas parameters and orientations	200
7.6.2	Simulation parameters and procedure	201
7.6.3	Results	203
7.7	Effects of receive antenna spacing	205
7.7.1	Antennas parameters	205
7.7.2	Simulation parameters and procedure	205
7.7.3	Results	206
7.8	Effects of receive antenna polarisation	208
7.8.1	Antennas parameters	208
7.8.2	Simulation parameters and procedure	208
7.8.3	Results	209
7.9	Performance comparison of several receive antennas	213
7.9.1	Objectives	213
7.9.2	Receive antennas	214
7.9.3	Simulation parameters and procedure	216
7.9.4	Correlation results	217
7.9.5	Capacity and eigenvalues results	219
7.10	Summary	225
8	Conclusions and Further Work	229
8.1	Conclusions	229
8.2	Further Work	232
A	Derivation of turns of straight segment N_{ss} of the FMPQHA	235
B	Equation of the transmitted wave plane	237
	Bibliography	239

List of Figures

2.1	Basic MIMO system model	9
2.2	Single satellite dual circularly polarised MIMO system	16
2.3	Quadrifilar helix antenna (QHA) in wrapped and unwrapped configurations.	32
2.4	Simulated 3D radiation pattern of a typical $\frac{3}{4}\lambda$ QHA.	33
2.5	Reverberation chamber configuration for multiple antennas evaluation [1].	47
2.6	Basic configuration of a spatial fading emulator	48
3.1	Single folded PQHA (SFPQHA) in wrapped and unwrapped configurations.	55
3.2	Configuration of the arc radial with respect to the antenna circumference (top view).	56
3.3	Reflection coefficient of conventional PQHA (Control) and SFPQHAs with different turns and arc radial angles.	58
3.4	Elevation gain pattern (dBic) with $\phi = 0^\circ$ at 2.45 GHz frequency of conventional PQHA (Control) and SFPQHAs with different turns and arc radial angles.	59
3.5	Current distribution of helical element 1 of the 0.375 turn SFPQHA with 30° arc radial angle.	60
3.6	Radiation pattern properties of conventional PQHA (Control) and SFPQHAs with different turns and arc radial angles.	62
3.7	Double folded PQHA (DFPQHA) in wrapped and unwrapped configurations.	63
3.8	Reflection coefficient of conventional PQHA (Control) and DFPQHAs with different turns and arc radial angles.	65
3.9	Elevation gain pattern (dBic) with $\phi = 0^\circ$ at 2.45 GHz frequency of conventional PQHA (Control) and DFPQHAs with different turns and arc radial angles.	65

3.10	Current distribution of helical element 1 of the 0.25 turns DFPQHA with 30° arc radial angle.	66
3.11	Radiation pattern properties of conventional PQHA (Control) and DFPQHAs with different turns and arc radial angles.	67
3.12	The fabricated SFPQHA and DFPQHA.	70
3.13	Configuration of the designed feed network for PQHA, SFPQHA and DFPQHA with 5 mm radius (dimension in mm).	72
3.14	Simulated reflection and transmission coefficients of input port and feed ports of the designed feed network.	73
3.15	Measured reflection coefficient of each element on the fabricated SFPQHA and DFPQHA.	73
3.16	Simulated and measured elevation gain patterns (dBic) of the fabricated SFPQHA.	75
3.17	Simulated and measured elevation gain patterns (dBic) of the fabricated DFPQHA.	75
3.18	Folded meandered PQHA in wrapped and unwrapped configurations	77
3.19	Reflection coefficient of the conventional PQHA and FMPQHAs.	79
3.20	Elevation gain patterns (dBic) with $\phi = 0^\circ$ at 2.4 GHz frequency of the conventional PQHA and FMPQHAs.	80
3.21	Current distribution of helical element 1 of the FMPQHA 0.5.	80
3.22	The fabricated FMPQHA.	82
3.23	Simulated reflection and transmission coefficients of input port and feed ports of the designed feed network.	83
3.24	Measured reflection coefficient of each element on the fabricated FMPQHA.	84
3.25	Simulated and measured elevation gain patterns (dBic) of the fabricated FMPQHA.	84
4.1	Configuration of a CPQHA and its helical elements numbering.	88
4.2	Reflection coefficients of element 1 on the inner PQHA and element 5 on the outer PQHA with varying δ	89
4.3	Isolation between the element 1 on the inner PQHA and the element 5 on the outer PQHA with varying δ	90
4.4	Elevation gain patterns (dBic) with $\phi = 0^\circ$ at 2 GHz frequency of the inner and outer PQHAs with varying δ	91
4.5	The fabricated CPQHA.	92
4.6	Simulated and measured reflection coefficient and isolation of the element 1 (E1) and the element 5 (E5) on the fabricated CPQHA.	93

4.7	Simulated and measured elevation gain patterns (dBic) with $\phi = 0^\circ$ at 2 GHz frequency of the fabricated CPQHA.	93
4.8	Configuration of dual polarised FMPQHA vertical array.	94
4.9	Configuration of bottom and top feed circuits for FMPQHA vertical array (dimension in mm).	96
4.10	Simulated reflection coefficients of the feed network of the lower and upper FMPQHAs.	97
4.11	Simulated transmission coefficient of the feed network of the lower and upper FMPQHAs.	98
4.12	Reflection coefficients of element 1 and element 5 on the lower and upper FMPQHAs respectively with varying vertical spacing δ_v	99
4.13	Isolation between element 1 and 5 on lower and upper FMPQHAs respectively with varying vertical spacing δ_v	99
4.14	Elevation gain patterns (dBic) with $\phi = 0^\circ$ at 2.4 GHz frequency of the dual polarised FMPQHA vertical array with varying vertical spacing δ_v	100
4.15	The fabricated dual polarised FMPQHA vertical array.	101
4.16	Reflection coefficient and isolation of the fabricated dual polarised FMPQHA vertical array together with the feeding network.	102
4.17	Simulated and measured elevation gain pattern (dBic) with $\phi = 0^\circ$ at 2.4 GHz frequency of the fabricated dual polarised FMPQHA vertical array.	103
4.18	Configuration of a dual polarised SFPQHA horizontal array.	103
4.19	Feed network configuration of the SFPQHA horizontal array.	104
4.20	Reflection coefficient of element 1 and 5 on RHCP and LHCP SFPQHAs respectively with varying horizontal spacing δ_h	105
4.21	Isolation between element 1 and 5 on RHCP and LHCP SFPQHAs respectively with varying horizontal spacing δ_v	105
4.22	Elevation pattern ($\phi = 0^\circ$) of the RHCP and LHCP SFPQHAs with varying horizontal spacing δ_v	106
4.23	The fabricated dual polarised SFPQHA horizontal array.	107
4.24	Reflection coefficient and isolation of the fabricated dual polarised SFPQHA horizontal array together with the feeding network.	108
4.25	Simulated and measured elevation pattern ($\phi = 0^\circ$) of the fabricated dual polarised SFPQHA horizontal array.	108
5.1	3-D co and cross polarised gain patterns of the SFPQHA array.	121
5.2	MEG of the RHCP and LHCP SFPQHAs at Ricean K factor of $-\infty$ dB with varying XPD.	123

5.3	MEG of the RHCP and LHCP SFPQHAs at Ricean K factor of -20 , -10 and -5 dB with varying XPD and ψ_{ch}	124
5.4	MEG of the RHCP and LHCP SFPQHAs at Ricean K factor of 0 dB with varying XPD and ψ_{ch}	125
5.5	MEG of the RHCP and LHCP SFPQHAs at Ricean K factor of 5 , 10 and 20 dB with varying XPD and ψ_{ch}	127
5.6	MEG of the RHCP and LHCP SFPQHAs at Ricean K factor of ∞ dB with varying XPD and ψ_{ch}	128
5.7	MEG of the RHCP and LHCP SFPQHAs with fixed XPD = 0 dB and varying Ricean K factor and ψ_{ch}	129
5.8	Magnitude of complex correlation of SFPQHA array with 20 mm antenna spacing with various values of channel XPD, $m_{\theta \phi}$ and $\sigma_{\theta \phi}$ of the AoA distribution.	132
5.9	Magnitude of complex correlation of SFPQHA array with 80 mm antenna spacing with various values of channel XPD, $m_{\theta \phi}$ and $\sigma_{\theta \phi}$ of the AoA distribution.	133
5.10	Magnitude of complex correlation of SFPQHA array with various antenna spacing in channels characterised by XPD, $m_{\theta \phi}$ and $\sigma_{\theta \phi}$ of the AoA distribution.	135
5.11	The polarisation ellipse showing the amplitudes A_z and A_y and angle α	136
5.12	Magnitude of complex correlation of polarised array where antenna 1 is LHCP and antenna 2 polarisation is varied based on α_2 and ψ_2 in a channel characterised by various values of XPD and $\sigma_{\theta \phi}$ of the AoA.	139
6.1	Elektrobit Propsounder wideband channel sounder.	144
6.2	Channel sounder's transmitter architecture.	145
6.3	Channel sounder's receiver architecture.	146
6.4	Timing diagram of the channel sounder.	147
6.5	Photographs of the transmit antennas and reference antenna used in the measurements.	149
6.6	RHCP and LHCP transmit antennas elevation patterns (dBic).	150
6.7	Elevation pattern ($\phi = 90^\circ$) of RHCP and LHCP reference antennas.	151
6.8	Top view of Newlands Corner measurement route.	154
6.9	Photograph of the transmit antennas used in Newlands Corner measurement.	154
6.10	Setup of the receive antennas in Newlands Corner measurement.	155
6.11	Top view of Bishops Court measurement route.	157

6.12	Photograph of the transmit antennas used in Bishops Court measurement.	158
6.13	Photograph of the receive antennas used in Bishops Court measurement.	158
6.14	Measurement setup for Bishops Court.	160
6.15	Doppler spectrum in LoS and NLoS areas.	162
6.16	Received power CDFs of the reference antenna in LoS and NLoS areas.	164
6.17	Received power CDFs of the FMPQHA array in LoS and NLoS areas. .	165
6.18	Capacity CDFs of all receive antennas configurations in the LoS and NLoS areas (R-reference antennnas, S-Straight FMPQHA array, T-75° tilted FMPQHA array).	167
6.19	Eigenvalues CDFs of all receive antennas configurations in the LoS and NLoS areas (R-reference antennnas, S-Straight FMPQHA array, T-75° tilted FMPQHA array).	168
6.20	Doppler spectrum in LoS and NLoS areas.	170
6.21	Received power CDFs of the SFPQHA array in LoS and NLoS areas. . .	172
6.22	Capacity CDFs at SNR of 10 dB of the straight and 50° tilted SFPQHA arrays in the LoS and NLoS areas.	174
6.23	Eigenvalues CDFs at SNR of 10 dB of the straight and 50° tilted SF-PQHA arrays in the LoS and NLoS areas.	175
7.1	3-D hemisphere scattering model for LMS channel.	182
7.2	PDF of the Angle-of-Arrival of the 3-D hemisphere geometrical scattering model.	183
7.3	PDF of the ToA in ϕ and θ angles.	186
7.4	Antenna azimuth pointing and inclination angles definition.	189
7.5	Transformation of antenna local axes based on its orientation.	190
7.6	Flowchart of the new LMS MIMO channel model.	192
7.7	Received power CDFs of the straight and 50° tilted SFPQHA arrays in the LoS channel.	196
7.8	Received power CDFs of the straight and 50° tilted SFPQHA arrays in the NLoS channel.	196
7.9	Capacity CDFs at SNR of 10 dB of the straight and 50° tilted SFPQHA arrays in measured and simulated channels.	199
7.10	Eigenvalues CDFs at SNR of 10 dB of the straight and 50° tilted SF-PQHA arrays in measured and simulated channels.	199
7.11	Orientation configuration of the receive array.	201

7.12	10% outage capacity at SNR of 10 dB for various azimuth and inclination orientation of the SFPQHA array in the LoS channel with its direct component at 30° in elevation.	204
7.13	10% outage capacity at SNR of 10 dB for various azimuth and inclination orientation of the SFPQHA array in the NLoS channel.	205
7.14	Capacity CDFs at SNR of 10 dB of the SFPQHA array with varying antenna spacing in both LoS and NLoS channels.	206
7.15	Eigenvalues CDFs at SNR of 10 dB of the SFPQHA array with varying antenna spacing in both LoS and NLoS channels.	207
7.16	Correlation coefficients for various values of transmit and receive antennas' XPR in the LoS channel.	211
7.17	10% outage capacity at SNR of 10 dB for various values of transmit and receive antennas' XPR in the LoS channel.	212
7.18	Correlation coefficients for various values of transmit and receive antennas' XPR in the NLoS channel.	213
7.19	10% outage capacity at SNR of 10 dB for various values of transmit and receive antennas' XPR in the NLoS channel.	214
7.20	3-D co and cross polarised gain patterns of the patch array.	215
7.21	3-D absolute gain patterns of the dipole array and cross dipoles.	216
7.22	Capacity CDFs at SNR of 10 dB of the SFPQHA array (S), patch array (P), cross dipoles (XD) and dipole array (D) with $(\phi_{ant} = 0^\circ, \theta_{ant} = 0^\circ)$ orientation in both LoS and NLoS channels.	221
7.23	Eigenvalues CDFs at SNR of 10 dB of the SFPQHA array (S), patch array (P), cross dipoles (XD) and dipole array (D) with $(\phi_{ant} = 0^\circ, \theta_{ant} = 0^\circ)$ orientation in both LoS and NLoS channels.	222
7.24	Capacity CDFs at SNR of 10 dB of the SFPQHA array (S), patch array (P), cross dipoles (XD) and dipole array (D) with $(\phi_{ant} = 0^\circ, \theta_{ant} = 60^\circ)$ orientation in both LoS and NLoS channels.	223
7.25	Eigenvalues CDFs at SNR of 10 dB of the SFPQHA array (S), patch array (P), cross dipoles (XD) and dipole array (D) with $(\phi_{ant} = 0^\circ, \theta_{ant} = 60^\circ)$ orientation in both LoS and NLoS channels.	224
7.26	Capacity CDFs at SNR of 10 dB of the SFPQHA array (S), patch array (P), cross dipoles (XD) and dipole array (D) with $(\phi_{ant} = 90^\circ, \theta_{ant} = 0^\circ)$ orientation in both LoS and NLoS channels.	225
7.27	Eigenvalues CDFs at SNR of 10 dB of the SFPQHA array (S), patch array (P), cross dipoles (XD) and dipole array (D) with $(\phi_{ant} = 90^\circ, \theta_{ant} = 0^\circ)$ orientation in both LoS and NLoS channels.	226
7.28	Capacity CDFs at SNR of 10 dB of the SFPQHA array (S), patch array (P), cross dipoles (XD) and dipole array (D) with $(\phi_{ant} = 90^\circ, \theta_{ant} = 60^\circ)$ orientation in both LoS and NLoS channels.	227

7.29 Eigenvalues CDFs at SNR of 10 dB of the SFPQHA array (S), patch array (P), cross dipoles (XD) and dipole array (D) with ($\phi_{ant} = 90^\circ, \theta_{ant} = 60^\circ$) orientation in both LoS and NLoS channels.	228
B.1 2-D view of the transmitted wave and hemisphere planes.	237

List of Tables

2.1	Relationship of winding and phasing directions with multifilar antenna radiation.	34
2.2	Comparison of radiation properties between $\lambda/4$, $\lambda/2$, $3\lambda/4$ and 1λ QHAs with numbers of turns of 0.25, 0.5, 0.75 and 1.	35
2.3	Techniques for multi-band operation of QHA.	37
3.1	Axial length (in mm) of SFPQHAs and its reduction percentage for different turns and arc radial angles.	57
3.2	Reflection coefficient bandwidth $S_{11} < -10$ dB (in MHz) of single folded PQHA for different turns and arc radial angles.	62
3.3	Axial length (in mm) of DFPQHAs and its size reduction percentage for different turns and arc radial angles.	64
3.4	Reflection coefficient bandwidth $S_{11} < -10$ dB (in MHz) of double folded PQHAs for different turns and arc radial angles.	68
3.5	Specifications of the flexible printed circuit board for antenna fabrication.	70
3.6	Structural dimensions of a conventional PQHA and FMPQHAs with their size reduction percentage.	79
3.7	Radiation pattern properties of the three designed FMPQHAs and one conventional PQHA.	81
4.1	Physical parameters of simulated CPQHAs.	88
6.1	Channel sounder parameters configuration in Newlands Corner measurement.	156
6.2	Channel sounder parameters configuration.	159
6.3	Small scale distribution of co-polarised signals in LoS and NLoS areas.	161
6.4	XPD and CPR of the dual polarised channel in LoS and NLoS areas.	163
6.5	Complex correlation of receive antennas in LoS and NLoS areas (R - Reference antennas, S - Straight FMPQHA array, T - 75° Tilted FMPQHA array).	166

6.6	Small scale distribution of co-polarised signals in LoS and NLoS areas.	169
6.7	XPD and CPR of the dual polarized channel in LoS and NLoS environments.	171
6.8	Complex correlation of receive antennas in LoS and NLoS areas.	173
7.1	Simulation parameters	194
7.2	Comparison of envelope distribution of the co-polarised subchannels.	195
7.3	Comparison of the measured and simulated cross polarisation discriminations.	195
7.4	Comparison of measured and simulated receive, co-polar subchannels and cross-polar subchannels correlations in the LoS channel.	197
7.5	Comparison of measured and simulated receive, co-polar subchannels and cross-polar subchannels correlations in the NLoS channel.	198
7.6	Simulation parameters	202
7.7	Simulation parameters	209
7.8	Simulation parameters	217
7.9	Receive, co-polar subchannels and cross-polar subchannels correlations for arrays with various orientations in the LoS channel.	218
7.10	Receive, co-polar subchannels and cross-polar subchannels correlations for arrays with various orientations in the NLoS channel.	219

Nomenclature

\mathbf{a}	Complex amplitude
\mathbf{C}	Correlation matrix
\mathbf{H}	MIMO channel matrix
$\mathbf{H}_{s,corr}$	Correlated shadowing channel matrix
\mathbf{H}_s	Shadowing channel matrix
\mathbf{e}_ϕ	Unit vector in ϕ direction
\mathbf{e}_θ	Unit vector in θ direction
δ	Spacing between inner and outer CQHA
δ_h	Spacing between SFQHAs
δ_v	Spacing between lower and upper FMQHAs
η_{rad}	Antenna radiation efficiency
η_{ref}	Antenna reflection efficiency
Γ	Reflection coefficient
λ	Wavelength
ω	Arc radial angle
\otimes	Kronecker operation
ϕ	Azimuth angle
ϕ_{ant}	Antenna azimuth pointing angle
$\psi_{ant,\phi}$	Phase of ϕ component of antenna field
$\psi_{ant,\theta}$	Phase of θ component of antenna field
ψ_{ant}	Phase difference between ϕ and θ components of antenna field
$\psi_{c,\phi}$	Phase of ϕ component of LoS incident field

$\psi_{c,\theta}$	Phase of θ component of LoS incident field
ψ_c	Phase difference between ϕ and θ components of LoS incident field
ρ_{cp}	Co-polar subchannels correlation
ρ_r	Receive correlation
ρ_t	Transmit correlation
ρ_{xp}	Cross-polar subchannels correlation
σ_a	Mean of azimuth angle of the AoA distribution of the incident waves
σ_e	Mean of co-elevation angle of the AoA distribution of the incident waves
σ_L	Location variability
$\text{vec}(\cdot)$	Vectorisation operator
θ	Co-elevation angle
θ_{ant}	Antenna inclination angle
$\tilde{\mathbf{C}}$	Shadowing correlation matrix
$\tilde{\mathbf{C}}$	Small scale fading correlation matrix
$\tilde{\mathbf{H}}$	Small scale fading channel matrix
$\tilde{\mathbf{H}}_{corr}$	Correlated small scale fading channel matrix
φ_p	Pitch angle of a QHA
A_ϕ	Antenna ϕ electric field pattern
A_θ	Antenna θ electric field pattern
B_{rf}	Bandwidth of the transmitted signal
C	Capacity
C_{out}	Outage capacity
$E\{\cdot\}$	Expectation operator
E_ϕ	ϕ component of the incoming waves
E_θ	θ component of the incoming waves
f_{samp}	Sampling frequency
G_ϕ	Antenna ϕ gain pattern
G_θ	Antenna θ gain pattern
G_{cp}	Antenna co-polarised gain pattern

G_{xp}	Antenna cross-polarised gain pattern
h	Element of channel matrix
K	Ricean K factor
L_{ω}	Length of arc radial
L_{arm}	Length of segmented arm
L_{ax}	Axial length of a QHA
L_{corr}	Shadowing correlation distance
L_{ele}	Element length of a QHA
L_{fd}	Length of feed radial
L_{nfd}	Length of non feed radial
m_{ϕ}	Mean of azimuth angle of the AoA distribution of the incident waves
m_{θ}	Mean of co-elevation angle of the AoA distribution of the incident waves
m_{corr}	Mean of shadowing power
N	Number of turn of a QHA
N_{arm}	Number of segmented arm
N_{norm}	Normalisation factor
N_{Rx}	Number of receive antennas
N_{sc}	Number of scatterer
N_{ss}	Number of turn of the straight segment
N_{Tx}	Number of transmit antennas
P_T	Transmit power
$p_{\phi}(\Omega)$	Angle-of-Arrival density functions of ϕ component
$p_{\theta}(\Omega)$	Angle-of-Arrival density functions of θ component
P_{rec}	Received power
R_c	Chip rate
V_{oc}	Open circuit voltage
w	Angular frequency
λ	Eigenvalue

Acronyms

ADC	Analog-to-digital converter.
AoA	Angle-of-Arrival.
AoD	Angle-of-Departure.
AR	Axial ratio.
ASU	Antenna switching unit.
BPR	Branch power ratio.
BPSK	Binary phase-shifted keying.
CDF	Cumulative density function.
CP	Circular polarisation.
CPR	Co-polarised power ratio.
CQHA	Contrawound quadrifilar helix antenna.
DFPQHA	Double folded printed quadrifilar helix antenna.
FB	Front-to-back.
FMPQHA	Folded meandered printed quadrifilar helix antenna.
GEO	Geosynchronous earth orbit.
IEEE	Institute of Electrical and Electronics Engineers.
LAN	Local area network.
LEO	Low earth orbit.
LHCP	Left hand circular polarisation.
LMS	Land mobile satellite.
LoS	Line-of-sight.
LP	Linear polarisation.

LTE	Long term evolution.
MEG	Mean effective gain.
MEO	Medium earth orbit.
MIMO	Multiple-input multiple-output.
NLoS	Non line-of-sight.
OTA	Over-the-air.
PDF	Probability density function.
PN	Pseudo noise.
PQHA	Printed quadrifilar helix antenna.
RF	Radio frequency.
RHCP	Right hand circular polarisation.
SFE	Spatial fading emulator.
SFPQHA	Single-folded printed quadrifilar helix antenna.
SISO	Single-input single-output.
SNR	Signal-to-noise ratio.
VSWR	Voltage standing wave ratio.
XPD	Cross polarisation discrimination.
XPR	Cross polarisation ratio.

Chapter 1

Introduction

1.1 Motivation

Multiple-input multiple output (MIMO) has become one of the key enabling technologies of the next generation wireless communications systems such as LTE-Advanced and IEEE 802.11n wireless LAN due to its increased spectral efficiency without additional bandwidth and transmit power in rich scattering environment. The MIMO system exploits the rich multipath environment to provide independent channels which can be used for simultaneous data transmission and therefore increases the capacity of the system. Although MIMO has been widely researched and developed for implementation in future terrestrial communication systems, its adaptation into the land mobile satellite (LMS) communications is still quite new. Due to the different propagation channel characteristics between the terrestrial and satellite systems such as scattering environment and free-space path loss, integration of MIMO techniques into a LMS communication system is very challenging. Many open questions on how the system can benefit from this technique remain unanswered, which provides opportunities for researchers.

Although signal processing and coding are the main components of the MIMO communication, any successful implementation of a MIMO system ultimately depends on the multiple antenna properties and propagation channel characteristics. Considerable research has been conducted to investigate the impact of multiple antenna properties and

configurations on the performance of a MIMO system. However, integration of multiple antennas and its RF circuit in the user terminal remains one of the biggest challenges in practical implementation of a MIMO system. This problem is compounded by the consumer appetite for smaller handheld terminals and the importance of aesthetic value of the devices. Apart from the antenna design, accurate method in evaluating MIMO devices over the air, affected by the properties of the antenna is also fast becoming one of the key research areas. The classical techniques in evaluating single antenna are inadequate to accurately evaluate the influence of multiple antennas on the performance of a MIMO system.

The main objective of the project is to develop a novel MIMO antenna for an LMS MIMO system receiver terminal that utilises the printed quadrifilar helix antenna as the main component and also an accurate and comprehensive evaluation technique for the antenna performance. The printed quadrifilar helix antenna (PQHA) is one of the most popular receiver terminal antennas for LMS communication system and it is only natural to extend the antenna capability to cater for the requirement of the LMS MIMO system. As the LMS MIMO system utilises circular polarisation multiplexing in a line-of-sight (LoS) case for its capacity increase, the proposed antenna system needs to have dual orthogonal polarisation capability, low correlation and excellent received power behaviour. It is also crucial for the antenna to be as compact and lightweight as possible in order for the antenna to be fitted on handheld terminal.

1.2 Structure of thesis

Chapter 2 of this thesis provides a comprehensive review of three main areas that relates to this work, which are the LMS MIMO system, quadrifilar helix antenna and performance evaluation of the MIMO antennas. To begin with, the basic theory of the LMS MIMO system and the effect of propagation channel on the system performance are described. This is followed by a compilation of measurements and modelling approaches of the LMS MIMO channel. The next section focuses on the physical and radiation properties of the QHA as well as the recent advancements on the antenna's miniaturisation and wideband or multiband operation. Finally, the chapter presents

the figures of merit and methods of evaluating MIMO antennas and ends with a review of the multiple antennas impact on the system performance.

Chapter 3 describes two new methods of miniaturising PQHAs with 0.5λ and 0.75λ element lengths, which are the element folding and combination of element folding and meandering methods. Then, the effects of the miniaturisation on the antenna's radiation and impedance properties are also presented. Meanwhile, chapter 4 shows several designs of dual circularly polarised array that utilises the miniaturised PQHAs that were investigated using extensive simulations. Selected optimum array designs then fabricated and its radiation pattern and scattering parameters are measured and compared with simulation results.

In order to evaluate the received power of circularly polarised antennas, chapter 5 provides a new formulation of the mean effective gain (MEG) equation in a Ricean fading channel that takes into account the polarisation of the LoS component of the incident wave and the corresponding antenna gain. This formulation was then utilised to study the branch power ratio of the newly designed dual circularly polarised array in a Ricean channel with varying channel cross polarisation discrimination XPD and LoS component polarisation. Chapter 5 concludes with the correlation analyses of the dual polarised array and the impact of antenna polarisation on the correlation of the received signals.

Chapter 6 presents the measurement campaigns that have been conducted with the designed dual polarised arrays were used as the receive antenna so that its performance in terms of MIMO figures of merit can be evaluated. Preliminary analysis of the effect of antenna orientation on the capacity of the LMS MIMO system was also conducted using the measured data. Further investigations on the effect of the receive array properties such as orientation, spacing and polarisation on the performance of the LMS MIMO system are provided in chapter 7 using a newly developed channel model that incorporates the characteristics of the receive antennas. Finally, the analysis finishes off with a performance comparison between the designed single folded QHA (SFQHA) array and several other arrays in terms of the MIMO figures of merit using the LMS MIMO channel simulations.

The thesis concludes with chapter 8 where it contains conclusions of this research work and also several ideas for further work.

1.3 Contributions

The following original contributions to knowledge are included in this work:

- Introduction of two new methods of miniaturising 0.5λ and 0.75λ printed quadri-filar helix antennas which are the element folding and combination of element folding and meandering methods. These methods are able to reduce the axial length of the QHA without significant impact on its radiation pattern and impedance.
- Several designs of dual circularly polarised array including co-located antenna elements are proposed based on extensive simulations where their main elements are the newly developed miniaturised PQHAs, which are the inside-out Contra-wound PQHA (CPQHA), folded meandered PQHA (FMPQHA) vertical array and single folded PQHA (SFPQHA) horizontal array.
- Derivation a new mean effective gain (MEG) formulation in Ricean fading channel that takes into account the polarisation of the LoS component and the corresponding antenna gain.
- Evaluation of the branch power ratio of the proposed dual circularly polarised SFPQHA array using the newly proposed MEG formulation.
- Investigation of the impact of antenna polarisation on the correlation between two circularly polarised antennas.
- Performance evaluation of the two proposed dual circularly polarised receive arrays which are the FMPQHA and SFPQHA arrays with proposed deployment in LMS MIMO devices using measurement campaign.
- Development and validation of a new LMS MIMO channel model that incorporates the properties of the receive antennas such as its polarimetric radiation

pattern, spacing and orientation. By utilising this channel model, the impacts of array properties such as orientation, spacing and polarisation on the system performance were investigated. This model can be used to evaluate the performance of various receive arrays in the LMS MIMO system.

1.4 Publications

Parts of this research work have been published in peer-reviewed journal and presented in international conferences. List of the publications is as follows:

1. M. F. B. Mansor, T. W. C. Brown and B. G. Evans, "Satellite MIMO Measurement with Colocated Quadrifilar Helix Antennas at the Receiver Terminal", *IEEE Antennas and Wireless Propagation Letters*, vol. 9, 2010, pp. 712-715.
2. M. F. B. Mansor, T. W. C. Brown and B. G. Evans, "Mutual coupling analysis of a dual circularly polarised contra wound quadrifilar helix antenna (CQHA) in land mobile satellite (LMS) MIMO systems", *27th IET and AIAA International Communications Satellite Systems Conference (ICSSC 2009)*, 1-4 June 2009, IET Conf. Pub. 2009, 321 (2009), DOI:10.1049/cp.2009.1181.
3. M. F. B. Mansor, T. W. C. Brown and B. G. Evans, "A dual circularly polarised Contrawound Quadrifilar Helix Antenna for land mobile satellite MIMO terminal", *3rd European Conference on Antennas and Propagation, 2009*, 23-27 March 2009, pp. 1072-1075.

Chapter 2

Literature Review

2.1 Introduction

This chapter gives an overview of the state of the art of the three main areas that are related to this research work namely land mobile satellite (LMS) multiple-input multiple-output (MIMO) system, quadrifilar helix antenna and performance evaluation of a MIMO antenna. In the first section, an extensive review of the LMS MIMO system is given where the basic theory of circular polarisation based MIMO and the effects of propagation channel are explained. Afterward, a compilation of several measurement campaigns that were conducted for LMS MIMO channel characterisation is provided together with the channel modelling approaches. The next part of the section deals with the LMS MIMO antenna design and also how its effects were investigated in the measurement and included in the channel simulation. The section concludes by comparing several antenna candidates that can be used in LMS MIMO receiver terminal.

The second part of the chapter focuses on the quadrifilar helix antenna in terms of its physical and radiation properties as well as its applications in mobile satellite systems. Starting with the antenna's physical structures and their effects to the impedance and radiation characteristics, the section later describes the recent advancements of the antenna in the area of multiband operation and more importantly the techniques used for the antenna's miniaturisation. The chapter ended with a section on the evaluation of multiple antennas in terms of its MIMO capabilities. First, the figures of merit

that are pertinent in determining the performance of MIMO antenna are described in detail. Then, various methods that have been proposed in evaluating multiple antennas in terrestrial MIMO system are also given where the advantages and disadvantages of each method are discussed. Finally, the impact of multiple antennas properties such as radiation pattern and mutual coupling on the performance of a MIMO system is included in this section although most of the reviewed works are based on terrestrial communication systems.

2.2 Land mobile satellite MIMO system

Since MIMO technique has been widely adapted in the next generation terrestrial communication systems, its integration into land mobile satellite system is seen as a natural progression of this technology. The scope of this work is limited to the implementation of MIMO in a single satellite system, where a satellite is communicating to a single receiver terminal on the ground. In order to apply MIMO technique in this system, circular polarisation based MIMO where dual circularly polarised antennas are used at both transmitter and receiver is considered to be one of the most attractive options.

2.2.1 Circular polarisation based MIMO

Multiple-input multiple-output is defined as a transmission system that utilises multiple antennas and appropriate signal processing at the transmitter and receiver. The main concept is to use multipath propagation, which before was categorised as detrimental to a wireless system, to create independent subchannels which increases the data rate or decrease the error rate (i.e. diversity) compared to a system using only a single antenna.

The idea behind the usage of multiple antennas at the transmitter and receiver has been around since 1950s when antenna diversity and combining techniques were first investigated in analog wireless communication [2]. One of the first studies of MIMO cellular was carried out by Winters [3] where they investigated the maximum data

rate for any given outage probability of multiple antennas transmitter and receiver in Rayleigh fading environment using various optimal combining techniques. Seminal works by Foschini [4] introduces the first coding algorithm for spatial multiplexing using multiple antennas at the transmitter and receiver called Bell Labs Layered Space-Time Architecture (BLAST) and Telatar [5] which provides the information-theoretic framework for the study of MIMO capacity in Rayleigh fading environment.

Although much research have been carried out in integrating MIMO into the next generation wireless communication systems, its practical implementation especially in small handheld devices remains a major challenge that needs to be solved. One of the major issues in the MIMO application is the required antenna spacing at the transmitter and receiver for low signal correlation. For example, the antenna spacing at the mobile terminal has to be at least half a wavelength in a multipath environment while a much further antenna spacing in the range of tens of wavelength is required at the base station due to a smaller angular spread. One way of solving this problem is by utilising cross-polarised antennas at both transmitter and receiver, instead of spatially separated antennas [6]. Due to the orthogonality of the antenna polarisation, these antennas can be co-located while maintaining a sufficiently low correlation. The use of cross-polarised antennas at the base station and mobile receiver is not new since the problem of large antenna spacing was also encountered in the antenna diversity system. Several notable studies on polarisation diversity show the benefits of using cross-polarised antennas especially at the base station [7], [8], [9].

System model and capacity

The basic model of a 2×2 circularly polarised MIMO system can be represented in Fig. 2.1. In the signal processing domain, the discrete input symbols are first encoded using space-time encoder and fed into pulse shaping filter to generate continuous-time baseband signals, $x'(w)$ where w is the angular frequency. The signals are up-converted in the RF subsystem and sent to dual circularly polarised antennas for transmission. At the receiver, the received signals $y(w)$ are down-converted and fed to the signal processing subsystem. Using matched filtering and space-time decoder, discrete output

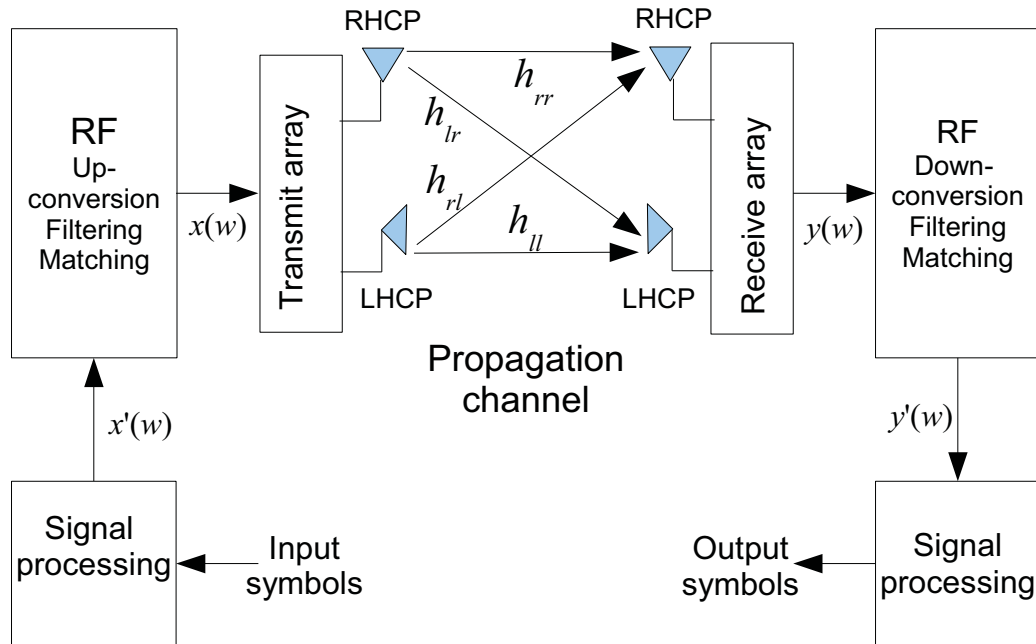


Figure 2.1: Basic MIMO system model

symbols are generated. The single user input-output relation of a general 2×2 dual polarised MIMO system in flat-frequency channel can be written as:

$$\mathbf{y} = \mathbf{H}\mathbf{x} + \mathbf{n} \quad (2.1)$$

where \mathbf{y} is a received signal column vector ($\mathbf{y} \in \mathbb{C}^{2 \times 1}$), \mathbf{H} is the channel matrix ($\mathbf{H} \in \mathbb{C}^{2 \times 2}$), \mathbf{x} is a transmitted signal column vector ($\mathbf{x} \in \mathbb{C}^{2 \times 1}$) and \mathbf{n} denotes the additive white Gaussian noise vector. The polarised channel matrix \mathbf{H} is defined as:

$$\mathbf{H} = \begin{pmatrix} h_{rr} & h_{rl} \\ h_{lr} & h_{ll} \end{pmatrix} \quad (2.2)$$

where the subscripts r and l indicate the two orthogonal circular polarisations of the transmit and receive antennas respectively namely right hand circular polarisation (RHCP) and left hand circular polarisation (LHCP). The h_{rr} , h_{rl} , h_{lr} and h_{ll} are the channel response from the RHCP antenna to the RHCP antenna, the LHCP antenna to the RHCP antenna, the RHCP antenna to the LHCP antenna and the LHCP antenna to the LHCP antenna respectively.

Capacity is defined as the maximum of the average mutual information between transmitted and received signals of a communication system. Increase in capacity without additional bandwidth and power is the main benefit of implementing MIMO in a wireless system. The single link instantaneous capacity with no channel state information at the transmitter can be written as [10]:

$$C_{\text{noCSIT}} = \log_2 \det \left(\mathbf{I}_{N_{Rx}} + \frac{P_{Tx}}{N_{Tx}\sigma^2} \mathbf{H}\mathbf{H}^* \right) \quad (2.3)$$

where N_{Rx} and N_{Tx} are the number of receive and transmit antennas respectively, $\mathbf{I}_{N_{Rx}}$ is a $N_{Rx} \times N_{Rx}$ identity matrix, P_{Tx} is the total transmit power, σ^2 denotes the noise variance and $(\cdot)^*$ is conjugate transpose operation.

It is also common that instead of transmit power, receive signal-to-noise ratio (SNR) is used in the capacity formulation which removes the effect of path loss and channel attenuation. In this case, the capacity can be defined as:

$$C_{\text{noCSIT}} = \log_2 \det \left(\mathbf{I}_{N_{Rx}} + \frac{\text{SNR}}{N_{Tx}} \bar{\mathbf{H}}\bar{\mathbf{H}}^* \right) \quad (2.4)$$

where $\bar{\mathbf{H}}$ is the normalised channel matrix to the unity SNR of SISO channel. Mathematically, the normalisation process is written as:

$$\bar{\mathbf{H}} = \frac{\mathbf{H}}{N} \quad (2.5)$$

with N_{norm} is the normalisation factor and it is defined as:

$$N_{norm} = \left[\frac{1}{N_{Tx}N_{Rx}} \sum_{i=1}^{N_{Rx}} \sum_{j=1}^{N_{Tx}} E\{|h_{ij}|^2\} \right]^{1/2}. \quad (2.6)$$

2.2.2 Effect of propagation channel

Aside from signal processing and coding, the propagation channel is the fundamental factor in determining the performance of a MIMO system. Three major characteristics of the channel that can significantly affect the system performance in terms of MIMO capabilities are channel correlation, line-of-sight component of the channel and channel polarisation properties. These characteristics are determined by the small scale fading behaviour of the channel. Therefore, an introduction to the channel small scale fading is provided for completeness.

Small scale fading

Description of a wireless propagation channel can be divided into three components which are path loss, shadowing and small scale fading. This categorisation is based on the received signal variation in different time or distance scale where path loss refers to mean power level that varies very slowly in time or distance while small scale fading characterises the received signals in very fast time or distance variation. Since the main focus is on the channel small scale fading, its properties in terms of first order statistics are presented in both line-of-sight (LoS) and non-line-of-sight (NLoS) channels.

In the NLoS channel, the received signal consists of the sum of multiple random waves due to various propagation mechanisms such as specular and rough surface reflections, diffraction and scattering between the transmitter and the receiver. As a result, each of these waves exhibits different amplitude and phase. The received signal can be written as:

$$a = x + jy \quad (2.7)$$

where a denotes the received complex signal, x is the real component of the signal, j is the imaginary unit and y is the imaginary component of the received signal. Both real and imaginary components of the received signal are normally distributed since they are composed of the sum of large number of random waves [11]. Based on the distribution of the real and imaginary components of the received signal, the distribution of the signal amplitude r is shown to be Rayleigh, where its probability density function (PDF) is given as:

$$p_r(r) = \left(\frac{r}{\sigma^2}\right) e^{-r^2/2\sigma^2} \quad (2.8)$$

where σ^2 is the variance of the multipath components.

Meanwhile, the received signal in a LoS channel is consisting of the sum of a coherent LoS component and the random multipath components that was modelled earlier using Rayleigh distribution. The magnitude of the received signal in a LoS channel can be modelled using Rice distribution where its PDF is written as:

$$p_r(r) = \left(\frac{r}{\sigma^2}\right) e^{-(r^2+s^2)/2\sigma^2} I_0\left(\frac{rs}{\sigma^2}\right) \quad (2.9)$$

where s is the magnitude of the LoS component, σ^2 has the same meaning as in Rayleigh distribution and I_0 denotes the modified Bessel function of the first kind and zeroth order [11]. Another way of expressing this distribution is by introducing Ricean K factor that is defined as the power ratio between the LoS component and the multipath components. Mathematically, it can be given as:

$$K = \frac{s^2}{2\sigma^2}. \quad (2.10)$$

Then, by including the K factor into Equation (2.9), the Rice PDF can be written as:

$$p_r(r) = \left(\frac{r}{\sigma^2}\right) e^{-r^2/(2\sigma^2)} e^{-K} I_0\left(\frac{r\sqrt{2K}}{\sigma}\right) \quad (2.11)$$

Channel correlation

For a 2×2 MIMO system, the full correlation matrix of the channel is defined as:

$$\mathbf{R} = \begin{bmatrix} 1 & \rho_{t1} & \rho_{r1} & \rho_{cp} \\ \rho_{t1}^* & 1 & \rho_{xp} & \rho_{r2} \\ \rho_{r1}^* & \rho_{xp}^* & 1 & \rho_{t2} \\ \rho_{cp}^* & \rho_{r2}^* & \rho_{t2}^* & 1 \end{bmatrix} \quad (2.12)$$

where $(\cdot)^*$ is the conjugate transpose operation and

- ρ_{t1} and ρ_{t2} are the transmit correlations as observed by the receive antennas 1 and 2 respectively.
- ρ_{r1} and ρ_{r2} are the receive correlations as observed by the transmit antennas 1 and 2 respectively.
- ρ_{cp} and ρ_{xp} are the co-polar and cross-polar subchannels correlation respectively.

It is well established that transmit or receive correlations have a negative effect on the capacity potential of a MIMO system as indicated in [12]. The study shows the effect of receive correlation on the MIMO capacity using geometric scattering channel model where as the correlation becomes more severe, the capacity decreases from the optimum value of independent and identically distributed (i.i.d.) Rayleigh fading channel. Capacity increase of a MIMO system is mainly due to simultaneous signal transmission over uncorrelated parallel subchannels where the number of the subchannels depends

on the rank of the channel matrix. Each of the subchannels transmission quality is then determined by the channel singular values. For an uncorrelated channel, its transfer matrix has full rank and the singular values of the channel matrix are almost equally high, which provide the maximum capacity increase. However, if the channel is highly correlated, then difference of strength between singular values will be large. This reduces the capacity as some of the parallel subchannels can not be utilised due to very low signal strength.

In a NLoS channel, the transmit and receive correlations are mainly determined by the angular spectrum of the incoming waves and the multiple antennas characteristics [13]. More specifically, instead of the type of angular distribution, the angular spread has more dominant effect on the channel correlation magnitude as investigated in [14]. They have compared three Angle-of-Arrival (AoA) distributions such as uniform, truncated Gaussian and Laplacian with several angular spreads, which showed that different distributions with similar angular spread have almost similar spatial correlation while varying the angular spread leads to different spatial correlation characteristics for each distribution. Several aspects of multiple antennas configuration such as antenna spacing, element radiation pattern and polarisation and array configuration also affect the channel correlation in a more complicated manner. Detailed explanation on the effect of antenna in MIMO system parameters such as received power, correlation and capacity are given in section 2.4.3.

In contrast to the transmit and receive correlations, it also has been shown that the diagonal correlations (i.e. co and cross-polarised subchannel correlations) of the channel have beneficial impact on the capacity of a MIMO system [15]. In [16], its effects were further investigated by comparing the ergodic and outage capacities of the diagonally correlated channel with the uncorrelated Rayleigh channel. Interestingly, the study concluded that the diagonally correlated channel provides slightly better ergodic capacity but lower outage capacity at low outage probability level than the i.i.d. Rayleigh fading channel.

Line-of-sight component

Another important aspect of channel characteristic that has an impact on the MIMO system capacity is the availability of LoS component or the Ricean K factor. In order to accurately quantify its effect on MIMO capacity, the evaluation must specify the normalisation process of the received signal whether it is based on equal receive mean SNR or fixed transmit power, which implies varied receive SNR. In [17], the effect of LoS component on MIMO capacity was investigated in equal receive mean SNR which indicates that for a closely spaced antennas, the capacity decreases as the Ricean K factor increases. However, when fixed transmit power is considered, then the existence of a LoS component will increase the receive SNR which can lead to higher capacity even in highly correlated channel [18]. In [19], the relationship between signal strength, which implies the availability of LoS component and multipath richness was investigated using indoor measurement where they showed how unnormalised capacity rises as the LoS component becomes more dominant due to the increase of SNR even with the loss of multipath.

Channel depolarisation

For a polarised based MIMO system, two other aspects of channel properties that can influence its performance are the channel cross polarisation discrimination XPD and the co-polarised power ratio CPR. The XPD can be defined as the power ratio of the co-polarised channel to the cross-polarised channel that has the same transmit polarisation as the co-polarised channel. The formulations of XPDs of a dual circularly polarised system are given as:

$$\text{XPD}_r = \frac{E\{|h_{rr}|^2\}}{E\{|h_{lr}|^2\}} \quad (2.13)$$

$$\text{XPD}_l = \frac{E\{|h_{ll}|^2\}}{E\{|h_{rl}|^2\}} \quad (2.14)$$

where $E\{\cdot\}$ is the expectation operator. Meanwhile, the power ratio of the two co-polarised subchannels indicates the power imbalance of a channel and it can be computed by the following equation:

$$\text{CPR} = \frac{E\{|h_{rr}|^2\}}{E\{|h_{ll}|^2\}}. \quad (2.15)$$

Measured values of XPD and CPR in the terrestrial wireless system which uses linear polarisation have been reported in literature. Generally, the value of XPD in both indoor and outdoor channels depends on the availability of LoS component where the the stronger the LoS component is, the higher the value of XPD will be [20], [21]. This is expected as the polarisation of the transmitted waves are better preserved in a LoS scenario when compared to a NLoS channel. Apart from that, it is also indicated in [21] that the XPDs of the vertical and horizontal polarisations have similar value in an outdoor LoS environment while in a NLoS area, the XPD of the vertical polarisation is higher compared to the horizontal polarisation. Extensive measurements in various outdoor environments found that vertically and horizontally polarised incident waves have equal power on average which gives the mean value of CPR to be nearly 0 dB [22]. The effects of the XPD on the performance of a MIMO system depends on the used transmission schemes whether it is polarisation diversity or polarisation multiplexing. A high value of XPD which indicates increased orthogonality between polarised sub-channels reduces the ability to exploit polarisation diversity but on the other hand, provides a better performance in terms of multiplexing gain.

2.2.3 Single satellite MIMO system

A single satellite MIMO system has been proposed as a practical implementation of the MIMO technique in land mobile satellite system operating in S band frequency [23]. It is characterised by one satellite transmitting dual-orthogonal circularly polarised signals to a ground receiver equipped with dual-circularly polarised antennas in order to create dual-polarised 2×2 MIMO system as illustrated in Fig. 2.2. Instead of using spatial based MIMO where antennas at both transmitter and receiver are spatially separated, polarisation based MIMO is considered to be a better solution for integrating MIMO into a land mobile satellite system.

Its main advantages are it is easier to be implemented and less costly compared to multi-satellite MIMO. Advancement in satellite payload especially in the area of antenna and RF technology has made it possible even for multibeam satellites to transmit dual circular polarised signals simultaneously [24]. Apart from that, due to colocation of

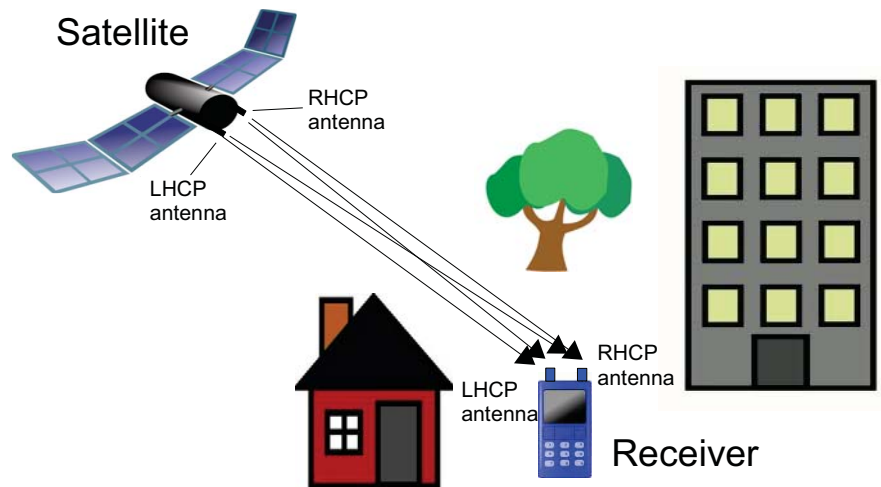


Figure 2.2: Single satellite dual circularly polarised MIMO system

transmit antennas at the satellite, the signal synchronisation can be done more easily as the difference between propagation delay of transmitted signals is extremely small. However its main drawback is limited capacity increase as only two independent parallel channels can be created based on polarisation orthogonality especially at the receiver.

For land mobile satellite systems that operate in S band frequency, local scattering environment at the mobile receiver is of great importance to the channel as opposed to the effects from troposphere and ionosphere. The tropospheric effects such as rain attenuation, gaseous absorption and scintillation have negligible impact on the S band frequency signal as they are more relevant to higher frequency bands. As for the ionospheric effects, one main phenomenon that can alter the polarisation of the transmitted signal is the Faraday rotation which is due to the combined effects of free electrons and the earth's magnetic field [11]. However, the use of circular polarisation in the mobile satellite system mitigates the effect of Faraday rotation on the transmitted signal in the ionosphere. Therefore, most of the works on measuring and modelling the satellite channel in the S band frequency mainly concentrated on the effects of the scattering environment of the ground terminal [25].

2.2.4 Main challenges in terms of satellite channel

Huge distance between satellite and ground terminal

One of the challenges in implementing MIMO in mobile satellite system is the huge distance separating satellite and ground terminal. For a Geosynchronous Earth Orbit (GEO) satellite, the transmitted signal needs to travel for approximately 35800 km before reaching its receiver. As for Low Earth Orbit (LEO) and Medium Earth Orbit (MEO), the distance varies depending on the height of the satellite where for LEO satellites are at a height of 500 to 2000 km of altitude while MEO satellites at a height of 8000 to 12000 km [26]. As the result, satellite system suffers from huge path loss and thus necessitates LoS propagation condition for transmission. Therefore, conventional MIMO schemes which rely on multipath environment for capacity increase is not suitable for a satellite network.

Statistical variation in received signal

In a mobile satellite system, the received signal experiences very slow variation of large scale fading in an environment due to the effect of blockage by buildings and groups of trees. This variation of large scale fading indicates the changes in receiver surrounding when it moves from one channel condition to another. This very slow variation is usually modelled using state-oriented approach such as Markov and Semi-Markov, which permit power level variation between defined states such as LoS, moderate shadowing and NLoS [27]. The rate of state change and its duration depends on the type of environment and the satellite elevation angle, where a more densely populated environment such as urban area will experience higher rate of total blockage and loss of LoS channel when compared with rural and suburban areas.

In each state, the received signal also exhibits different small scale statistics where in the LoS condition, its small scale amplitude variation is Ricean distributed with high K factor while in shadowed and NLoS states, it is most likely to be Rayleigh distributed. Therefore, it can be assumed that channel correlation in LoS state is significantly high and in shadowed and NLoS states, low channel correlation can be expected. These

variations of signal statistics in large scale and small scale fading present important challenges for integrating MIMO in mobile satellite system as it requires adaptability in the MIMO technique so that it can be implemented in such diverse channel conditions.

Asymmetric scatterers distribution

The distribution asymmetry arises as only the mobile terminal is surrounded by scatterers while the satellite is completely void of any scatterer in its own surrounding [28]. We may consider the channel as a single-bounce scattering process where the transmitted signal from satellite travels huge distance before being scattered at the mobile terminal surrounding. Due to this channel characteristic, the angular spread of approaching waves at the satellite is almost non-existent while the angular spread at the mobile terminal may vary depending on the operating environment. For spatial based MIMO applications in such systems, the antennas at the satellite need to be spaced far from each other in order to realise uncorrelated channel. This requirement for large antenna spacing makes it unrealistic to implement spatial based MIMO with a single satellite due to its size constraint.

2.2.5 Satellite MIMO measurements

The main objective of any measurement campaign is to characterise the channel properties so that the obtained information can be used for channel modelling and system simulation. For a polarised satellite MIMO system, apart from the characterisation of the channel first and second order statistics, it is also extremely important to measure the channel correlation and the channel cross polarisation discrimination. Although several measurements have been conducted for these purposes, there are still much to be done since each measurement has its own limitation in terms of satellite elevation angle, measurement environment and transmit and receive antennas properties.

University of Surrey measurement

The first measurement campaign of satellite MIMO system was conducted in Guildford, UK to characterise dual-circularly polarised satellite MIMO channel and investigate

the performance of circular polarisation based MIMO technique on system capacity [29]. Two closely spaced satellites were emulated by a transmit platform fitted with 4 orthogonal circularly polarised directional antennas (2 RHCP and 2 LHCP) was placed on top of a hill with elevation angle of 15° communicating with mobile van equipped with 4 omnidirectional receive patch antennas where two antennas are RHCP and the other two are LHCP. Three environments were considered in this measurement which are urban, suburban and rural tree-lined road areas. Due to the low elevation angle of the emulated satellite, this measurement only represents a limited case of mobile satellite system which usually utilises higher satellite elevation angle to reduce the probability of blockage and shadowing.

Extensive analysis on the measurement data has been carried out where its large scale and small scale statistics were estimated in wideband and narrowband domain. One of the most important results are the dual circularly polarised channel correlation in large and small scale fading in all three environments which are extremely fundamental in predicting the performance of satellite MIMO system. The results indicates that channels in all three environments are highly correlated in large scale fading as all receive antennas experienced the same blockage and shadowing. However, very low correlation in the channel small scale fading provides opportunity for MIMO technique to be implemented.

The measurement also estimated the spectral efficiency of using dual circularly polarised MIMO technique in single mobile satellite system where significant increase of 10% outage capacity from 0.02, 0.09 and 0.03 bit/s/Hz in SISO channel to 0.14, 0.37 and 0.26 bit/s/Hz for MIMO channel in tree-lined road, suburban and urban environments respectively [23].

MiLaDY measurement

The MiLady (Mobile satellite channel with angle diversity) project was carried out by several European institutions with the objectives of developing new channel models for multiple satellites with angle diversity and also to study the potential benefits of angle and time diversity to mobile satellite system operating in L and S band frequency [30].

One of the measurements was conducted in east coast of United State where power level from two GEO satellites of XM Satellite Radio and three HEO satellites of Sirius Satellite Radio were measured in five different environments. The satellite elevation angle of the two GEO satellites is in the range of 25° to 55° while for the three HEO satellite are from 50° to 85° .

Evaluation of angle diversity was performed by comparing the cumulative distribution function (CDF) of carrier-to-noise ratio (C/N) between single satellite signal and maximum-ratio-combining (MRC) of two satellite signals in all measured environments [31]. Significant increase of signal availability can be achieved by utilising satellite angular diversity especially for HEO satellite system where up to 10dB diversity gain are possible in urban environment. The results also show that the technique provides better diversity gain to HEO satellite system compared to GEO system which probably due to more varied azimuth and elevation angle separation in HEO satellite system.

MIMOSA measurement

Extension of MiLady project is the MIMOSA project by European Space Agency (ESA) with the objective of developing propagation channel model that considers satellite and polarisation diversity for L to C band frequency [32]. In the first measurement of the project, the main aims are to characterise the dual circularly polarised channel between one satellite with mobile receiver on the ground and also to evaluate the performance of several antenna configurations at the receiver [33]. The W2A satellite was used as the transmitter with dual circularly polarised antennas while the receiver was equipped with five different antennas which include separated right hand and left hand circular polarised antennas and colocated dual circularly polarised antennas. Some preliminary results has been presented in [33] where the correlation of large scale fading for colocated antennas is higher when compared with separated antennas and the channel cross polarisation discrimination (XPD) characteristics in suburban environment.

2.2.6 Dual polarised satellite MIMO channel modeling approaches

In general, two approaches were utilised for modelling the dual polarised mobile satellite MIMO channel. The first approach is the extension of the physical statistical model that was first developed for single polarised land mobile satellite channel. The second category of these approaches is the statistical model that borrows its concept heavily from terrestrial MIMO statistical modelling methods.

Physical statistical model

The main concept of the physical statistical approach is the combination of statistical model in terms of environment properties with ray-tracing method, which normally are used in deterministic modelling [34]. This method significantly reduces the complexity of full deterministic model where instead of detailed description of an environment, the evaluated environment is formed using basic geometric shapes and its properties are statistically generated based on several probability density functions. Using the ray-tracing technique on the generated canonical environment, accurate distribution of channel characteristics can be obtained. This approach has been successfully implemented in modelling wireless terrestrial and land mobile satellite channels [35], [36].

One of the first channel models for multiple satellites or high altitude platforms (HAP) MIMO system was developed using a physical statistical model [37] although it excluded the depolarisation effect of the channel. The synthetic environment was generated by randomly positioned clusters of scatterer, where each cluster represents buildings or trees above a plane. For better physical realisation, the building height in the model followed log-normal distribution and the density of the clusters and its type (building or tree) in the environment was specified by the type of environment such as urban, suburban and rural.

Extension of the model in order to include polarisation in the channel description has been presented in [38] where it considered a dual circularly polarised channel from a single satellite fitted with RHC and LHP polarised antennas communicating with mobile receiver also equipped with RHC and LHC polarised antennas. One important

assumption is that the LoS component of the co and cross polar channels are fully correlated while the channels are fully decorrelated for the multipath components. The high resolution time series signals, $\alpha_{M,N}$ between satellite antenna M and mobile receiver N are defined in [38] as follows:

$$\alpha_{M,N} = \begin{cases} P_{M,N}e^{jkd_{M,N}} + b \sum_{i=1}^n T_i \Gamma_i P_{M,N,i} e^{jkd_{M,N,i}} & \text{clear co-polar} \\ b \sum_{i=1}^n T_i \Gamma_i P_{M,N,i} e^{jkd_{M,N,i}} & \text{clear cross-polar} \\ D_{M,N} P_{M,N} e^{jkd_{M,N}} + b \sum_{i=1}^n T_i \Gamma_i P_{M,N,i} e^{jkd_{M,N,i}} & \text{block co-polar} \\ S_b D_{M,N} P_{M,N} e^{jkd_{M,N}} + b \sum_{i=1}^n T_i \Gamma_i P_{M,N,i} e^{jkd_{M,N,i}} & \text{block cross-polar} \\ T_{M,N} P_{M,N} e^{jkd_{M,N}} + b \sum_{i=1}^n T_i \Gamma_i P_{M,N,i} e^{jkd_{M,N,i}} & \text{tree co-polar} \\ S_t T_{M,N} P_{M,N} e^{jkd_{M,N}} + b \sum_{i=1}^n T_i \Gamma_i P_{M,N,i} e^{jkd_{M,N,i}} & \text{tree cross-polar} \end{cases} \quad (2.16)$$

where $P_{M,N}$ is the LoS path loss between satellite M and mobile receiver N , k is the wavenumber, $d_{M,N}$ is the distance between satellite and receiver, b is the clutter factor parameter, n is the valid scatterer number and T_i defines the tree attenuation applied to reflected wave from scatterer i . $P_{M,N,i}$ is the path loss from satellite and receiver via scatterer i , $d_{M,N,i}$ denotes the total distance from satellite to scatterer i to receiver, $D_{M,N}$ denotes the LoS diffraction loss, Γ_i is the complex reflection coefficient at the scatterer i , $T_{M,N}$ is the LoS tree loss, S_b and S_t defines the attenuation of cross polar channel for blocked and tree-shadowed environments respectively.

A specialised physical statistical model for dual polarised LMS MIMO channel in a tree-lined road environment was proposed in [39]. The complex structure and properties of a single tree were modelled as a cylinder consisting of randomly distributed thin lossy dielectric discs as leaves and finite lossy dielectric cylinder as branches. The mean and variance values of coherent and incoherent scattering fields due to the generated synthetic trees were calculated using Multiple Scattering Theory (MST) [40].

Two different methods were used to account for the shadowing and small scale correlation between subchannels in the model. Polarisation shadowing correlation was estimated by Finite-Difference Time-Domain (FDTD) computation of a single tree while small scale fading characteristic was then considered as independent and fully decorrelated. Finally, a statistical simulator was built where generated zero mean Gaussian random processes are weighted with the mean and variance values of coherent and in-

coherent components (based on the result of MST computation) and correlated based on shadowing and small scale correlation matrices.

Statistical model

Any statistical method for channel modelling requires parameterisation from measurement or full electromagnetic simulation since the method only provides an analytical framework for channel description. Accuracy of this method in modelling channel largely depends on the details of parameterisation. Several statistical models have been proposed for dual polarised mobile satellite MIMO channel [41], [29], [42], [43].

In [41], the channel model was developed by categorising the incident waves into three components, which are LoS signal \mathbf{L} , specular coherent reflected signal \mathbf{S} and diffuse signal \mathbf{D} . The magnitude of LoS and specular reflected signals were characterised by its Ricean K factor K_l and K_s respectively. Mathematically, the channel can be written as:

$$\mathbf{H} = \underbrace{\begin{bmatrix} l_{11} & l_{21} \\ l_{12} & l_{22} \end{bmatrix}}_{\mathbf{L}} \begin{bmatrix} \sqrt{\frac{K_{1l}}{K_{1l}+K_{1s}+1}} & 0 \\ 0 & \sqrt{\frac{K_{2l}}{K_{2l}+K_{2s}+1}} \end{bmatrix} + \underbrace{\begin{bmatrix} s_{11} & s_{21} \\ s_{12} & s_{22} \end{bmatrix}}_{\mathbf{S}} \begin{bmatrix} \sqrt{\frac{K_{1s}}{K_{1l}+K_{1s}+1}} & 0 \\ 0 & \sqrt{\frac{K_{2s}}{K_{2l}+K_{2s}+1}} \end{bmatrix} + \underbrace{\begin{bmatrix} d_{11} & d_{21} \\ d_{12} & d_{22} \end{bmatrix}}_{\mathbf{D}} \begin{bmatrix} \sqrt{\frac{1}{K_{1l}+K_{1s}+1}} & 0 \\ 0 & \sqrt{\frac{1}{K_{2l}+K_{2s}+1}} \end{bmatrix} \quad (2.17)$$

where K_{1l} , K_{1s} and K_{2l} , K_{2s} are the K factors for LoS and specular components in polarisation 1 and 2. Meanwhile, the elements in \mathbf{L} , \mathbf{S} and \mathbf{D} are related to the XPD of LoS, specular reflected and diffuse components respectively. Signal correlation was only considered in the diffuse component where for orthogonal polarised subchannels, it is assumed to be fully decorrelated while for co-polarised signals, the correlation value of 0.3 to 0.7 was used based on terrestrial measurements.

A more comprehensive 2×2 circularly polarised statistical model was provided in [44]

where the model parameterisation was based on an extensive measurement campaign at low satellite elevation angle. Three main channel components which are large scale, shadowing and small scale fading were modelled independently and later combined to generate the complete land mobile satellite MIMO channel. The large scale effect was modelled using a 2 state Markov chain approach where the state probability matrix and state transition probability matrix were evaluated from the measurement.

As for the shadowing, it was modelled as an auto and cross correlated random process with lognormal distribution for each channel. In order to create the correct temporal behaviour, the processes were filtered using first order recursive linear time invariant filter and later scaled based on its mean and standard deviation. Cross correlation was introduced to the shadowing channels by multiplying the channel with shadowing correlation matrix derived from the measurement as follows:

$$\text{vec}(\mathbf{H}_{s,corr}) = \mathbf{C}_s^{1/2} \cdot \text{vec}(\mathbf{H}_s) \quad (2.18)$$

where $\text{vec}(\cdot)$ defines the matrix vectorisation, \mathbf{H}_s and $\mathbf{H}_{s,corr}$ denote the uncorrelated and cross-correlated 2×2 shadowing channels and \mathbf{C}_s is the 4×4 polarisation shadowing correlation matrix. The small scale fading was modelled as Ricean distributed random process with the K factor taken from measurement data. Using the same method as in shadowing modelling, the small scale fading was cross correlated using its correlation matrix.

Although the statistical model given by [44] is adequate in modelling the LMS MIMO channel, its strict dependency on measurement data renders it unusable for other environments or satellite elevation angles. With this problem in mind, a consolidation approach of measurement validated LMS SISO model with established polarised terrestrial MIMO parameters to extrapolate the characteristics of LMS MIMO channel was presented in [42]. Its main advantage lies on the fact that by carefully combining the LMS SISO model with terrestrial MIMO model, generation of LMS MIMO channel can be made at various satellite elevation angles and environment types.

In the model, the effect of shadowing and small scale fading were modelled using Loo distribution [45] which is characterised by three parameters: α and ψ are the mean and standard deviation of the lognormally distributed shadowing component and MP is the

average power of the multipath component. Extensive compilation of Loo parameters (α, ψ, MP) can be obtained in [46]. One similarity of this model with the model before is its generation of auto and cross correlated large scale components where the same process was applied as in [44]. However, for the small scale fading component, this model used the Kronecker method in forming its correlation matrix. The process of generating correlated small scale components can be written as:

$$\text{vec}(\tilde{\mathbf{H}}_{corr}) = \tilde{\mathbf{C}}^{1/2} \cdot \text{vec}(\tilde{\mathbf{H}}) \quad (2.19)$$

where

$$\tilde{\mathbf{C}} = \tilde{\mathbf{R}}_{tx} \otimes \tilde{\mathbf{R}}_{rx}. \quad (2.20)$$

$\tilde{\mathbf{H}}_{corr}$ and $\tilde{\mathbf{H}}$ are the correlated and uncorrelated small scale components of the channel, $\tilde{\mathbf{C}}$ denotes the polarisation small scale correlation matrix which is derived with Kronecker product (\otimes) of transmit antennas correlation, $\tilde{\mathbf{R}}_{tx}$ and receive antennas correlation, $\tilde{\mathbf{R}}_{rx}$.

A more precise method of modelling the small scale fading of the dual circularly polarised satellite MIMO channel was presented in [43] where two different ways were used to model the correlated small scale fading signals in LoS and NLoS channels. In a NLoS channel, the small scale fading signals are correlated using the Kronecker model where the correlation matrix was constructed by combining the transmit and receive correlations as shown in Equation (2.20). The use of Kronecker method for modelling of a LoS channel however is not accurate since the assumption that co-polar and cross-polar correlations are the Kronecker product of transmit and receive correlations may not hold in this channel. Therefore, it is proposed for a LoS channel, the process of correlating the LoS signals is implemented by introducing two 2×2 correlation matrix, one for co-polarised signals and the other one for cross-polarised signals which are:

$$\mathbf{R}_{cp} = \begin{pmatrix} 1 & \rho_{cp}^* \\ \rho_{cp} & 1 \end{pmatrix} \quad (2.21)$$

$$\mathbf{R}_{xp} = \begin{pmatrix} 1 & \rho_{xp}^* \\ \rho_{xp} & 1 \end{pmatrix} \quad (2.22)$$

where ρ_{cp} is the complex correlation of h_{rr} and h_{ll} and ρ_{xp} is the average of the correlation of h_{rl} and h_{ll} and correlation of h_{lr} and h_{rr} . The LoS co-polarised signal vector \mathbf{h}_{cp} which consists of channel elements h_{rr} and h_{ll} is correlated using the first correlation matrix (Equation (2.21)). Meanwhile, the LoS cross-polarised signal vector \mathbf{h}_{xp} which contains channel elements h_{lr} and h_{rl} is correlated using the second correlation matrix (Equation (2.22)).

2.2.7 Antenna design impacts on LMS MIMO system

Although antennas are integral to the LMS MIMO system at both satellite and ground receiver, its impacts to the overall system performance have not been extensively investigated. In the most extensive measurement that was conducted to characterise the LMS MIMO channel [44], more attention was given to ensure the validity of the measured polarised channel data with regards to the receive antenna cross polarisation discrimination. The effects of other antenna characteristics such as array orientation and gain pattern to the measured channel data however were not studied. As for most of the dual polarised LMS MIMO channel models, only the antenna cross polarisation ratio (XPR) is included where it is represented as a constant, regardless of the direction of the incident waves. This is of course a crude approximation since for a realistic antenna, its cross-polarised gain has different value for each azimuth and elevation angle hence different value of antenna cross polarisation ratio (XPR). This is especially true for closely spaced multiple antennas due to the effect of mutual coupling.

The antenna system for LMS MIMO small terminal needs to be designed to meet the combined requirements of three technical areas, which are land mobile satellite communication, polarisation based MIMO technique and small terminal antenna design. An ideal antenna system which can fulfill all requirements may not be feasible since in practice, some compromises need to be made especially for the antenna to be fitted in a small terminal. In a mobile satellite system, the shape of antenna radiation pattern does have significant impact on the system performance. It is highly recommended that such antennas radiate in hemispherical or cardioid pattern in order to cover wide variation of satellite angle [47]. In addition, the wide beam pattern of the antenna

must also exhibit a good axial ratio (i.e. good polarisation purity with cross-polarised pattern 10 to 15 dB less than the co-polar pattern).

The main requirement of an antenna system for a dual-circular polarised MIMO technique is the ability to simultaneously transmit or receive in dual circular polarisation. Although numerous designs of dual circularly polarised antenna have been published, most of them were not compact enough to be fitted in a small terminal or require complicated switching mechanism to operate [48], [49]. Secondly, the antennas also need to exhibit low mutual coupling since high mutual coupling may result in higher correlation and power ratio imbalance between antenna branches as well as compromising the antennas efficiency.

Lastly, for the antennas to be fitted in a small terminal, they must be compact while maintaining the radiation characteristics for a mobile satellite MIMO system. The need for compactness will certainly require some compromises on the radiation pattern properties since it is well known that miniaturisation of antenna can lead to reduction in polarisation purity and beamwidth. It is then important to produce antenna solutions with the most optimum compromises between the required radiation pattern and antenna size.

2.2.8 Candidate antennas for satellite MIMO receiver

Microstrip antennas

Microstrip antennas can be configured to radiate in circular polarisation by using two methods, which are feed network arrangement and alteration of the antenna geometry. Circular polarisation is achieved by exciting two orthogonal modes of the antenna generating two signals of equal magnitude with 90° phase difference. This can be implemented by the use of two feeds for a single antenna where each feed excites different orthogonal mode of the antenna and they are connected to a 90° hybrid [50]. A single feed can also be utilised for circular polarisation where the feed is placed at a specific point on the diagonal line of a nearly square rectangular patch antenna [51]. The second technique for microstrip antennas to radiate in circular polarisation is by

altering the antenna dimension and shape which includes introducing slot in the patch interior, truncating corners of the patch and using elliptical patch shape [52].

In order to obtain dual circular polarisation capability for a single structure of microstrip antenna, two techniques can be utilised namely switching mechanism to alter the antenna properties and multiple feed arrangement. An example of switching mechanism is presented in [53] where two pin diodes were used to switch on or off two orthogonal slots in the interior of a patch antenna. Using the same method, switches were also used to turn on or off slots in the ground plane of a square patch antenna so that both right hand and left hand circular polarisation can be excited [54]. It is however important to note that the switching method to obtain dual polarisation is not practical for a MIMO system since the MIMO system requires simultaneous transmission or reception of dual polarised signals while the switching method only provides the ability to choose either one of the polarisations. The other method of radiating dual circular polarisation is by using multiple feeds to excite two orthogonal circular modes of a circularly polarised patch antenna. In [55], a novel patch antenna design consists of a coupling aperture between a radiating patch and a microstrip feed network enable the antenna to radiate both circular polarisation simultaneously. Its main problem is the relatively small bandwidth range of low mutual coupling between the two radiation modes.

Although microstrip antennas can be used in circular polarisation operation, their usage in land mobile satellite handheld receiver is very limited due to several important reasons. The first main reason is its narrow beamwidth of circularly polarised radiation beam of a microstrip antenna which limits its coverage of satellite elevation angle. Apart from that, although the antennas are low profile, the need for sufficiently large ground plane for good impedance match and radiation pattern make it difficult for a microstrip antenna to be placed inside a small device with the antenna boresight pointing to the satellite elevation angle. Also their polarisation purity is affected when dielectric materials, such as water or conductors are on top of them as what usually happened for vehicular antennas.

Monopoles

A monopole is inherently a linearly polarised antenna. Its main advantage over other types of antenna is that it can be easily miniaturised using various methods such as meandering and folding without significant loss of performance. Therefore, it is not surprising that monopole and its variants such as inverted-L and inverted-F antennas are very attractive for small handheld devices due to its compactness. For circular polarisation operation, various combinations of multiple monopole or its variants with some specific geometric configuration and feed requirement have been proposed. In [56], a circular array of bent monopoles was utilised to radiate circular polarised beam for L-band mobile satellite communication although the array and its feed network are far too large for small handheld terminal. A more compact design can be achieved using inverted-L and inverted-F antennas as proposed in [57] and [58] where multiples of these antennas were positioned as a circular array and fed with equal amplitude and 90° phase difference.

Even though the antenna can be miniaturised so that the resulting circularly polarised array is sufficiently small, incorporating dual circular polarisation capability will certainly increase the complexity of the overall array design and also its size since another set of orthogonally polarised antenna is required. Furthermore, this type of antenna is not very directional which makes it less suitable to operate in a LoS channel.

Helical antennas

The use of helical antennas has been primarily for circular polarisation operation since it was first introduced [59]. Since then, various types of helical antennas have been proposed where their properties in terms of radiation pattern and impedance are depended on the physical structure of the helices. One of the first helical antenna variations is a helical antenna with multiple turns where it radiates a circularly polarised beam in the direction of the antenna boresight when the antenna circumference is nearly one wavelength [60]. This type of single element helical antenna has relatively large size due to the long element length. Apart from that, the antenna has significantly narrow

beamwidth which may not be suitable as a handheld terminal antenna for land mobile satellite system.

One variant of helical antenna that has an important role in mobile satellite communication and global positioning systems is the multifilar helix antenna. The antenna consists of multiple helical elements with element length less than one wavelength that were fed with a specific phase difference in order to radiate in circular polarisation. Its main advantages are significantly broad circularly polarised beamwidth with good axial ratio and it is also relatively small compared to single element helical antenna. It is more difficult to incorporate dual circular polarisation for this type of antenna since each single polarised antenna requires its own feed network. However, due to the fact that it has many more favourable characteristics when compared to microstrip and monopole/dipole antennas, thus make it a stronger candidate for the LMS MIMO system.

2.3 Quadrifilar helix antenna

2.3.1 Applications to satellite communication and navigation systems

Since its first development by Kilgus [61], the quadrifilar helix antenna (QHA) has found various applications especially in the area of space and satellite communications. Some of its earliest applications are in variety of spacecraft programs such as navigation satellite, satellite telemetry and tracking and interplanetary spacecraft [62]. It is also one of the best antenna candidates for land mobile satellite communications and satellite radio systems. A QHA design for Inmarsat's ICO (for Intermediate Circular Orbit) handheld terminal antenna was demonstrated in [63] where they compared different physical parameters of QHA and its effect on the radiation pattern of the QHA.

More recently, the applications of QHA have been extended to antenna diversity and the MIMO system. Significant diversity gain up to 13 dB has been achieved when the QHA is used as a four branch diversity system with equal gain combining (EGC) method in a rich multipath environment [64]. Further investigation on the high diversity gain of QHA was conducted in [65]. It was concluded that the diversity gain is achieved due

to the angular decorrelation and increase of received power. Initial theoretical studies on the use of meandered QHA in MIMO system can be found in [66]. Although the capacity of MIMO using QHA is lower than 4×4 monopoles, the advantage in terms of small size makes the QHA a very practical MIMO antenna. Narrowband indoor non-line-of-sight measurements were conducted to validate the theoretical MIMO capacity increase of the QHA. Even though the capacity is slightly lower than monopoles, the size reduction is very significant, which gives the QHA an advantage compared to other antennas [67].

2.3.2 Physical structure and feed arrangement

A resonant quadrifilar helix antenna (QHA) is a combination of four helical element with length less than one wavelength of the resonant frequency. The elements are spaced at $\frac{\pi}{2}$ angular distance from each other to form a cylindrical structure. A typical configuration of printed bottom-fed printed QHA is shown in Fig. 2.3. There are six important physical parameters of the QHA namely the number of turns N , radius of the cylinder r , axial length of the antenna L_{ax} , element length L_{ele} , pitch angle φ_p and direction of winding. Each of these parameters affects the radiation pattern and impedance properties of the antenna. The relationship between axial length, element length, number of turn and radius can be written as [68]:

$$L_{ax} = N \sqrt{\frac{1}{N^2} (L_{ele} - Ar)^2 - (2\pi r)^2} \quad (2.23)$$

where

$$A = \begin{cases} 1 & \text{if } L_{ele} = \frac{n\pi}{4} \text{ with } n \text{ is odd integer} \\ 2 & \text{if } L_{ele} = \frac{n\pi}{4} \text{ with } n \text{ is even integer.} \end{cases}$$

For the length of the helical element, its value is taken as a multiplication of quarter wavelength of the antenna frequency. One design rule that needs to be followed once the element length has been decided is for even multiplication, the antenna non-fed radials need to be shortened whereas for odd multiplicative length, the non-fed radials remain open.

In order for any multifilar helix antenna with W elements to radiate in circular polarisation and axial mode, each element is fed with equal amplitude and $\frac{2\pi}{W}$ phase difference

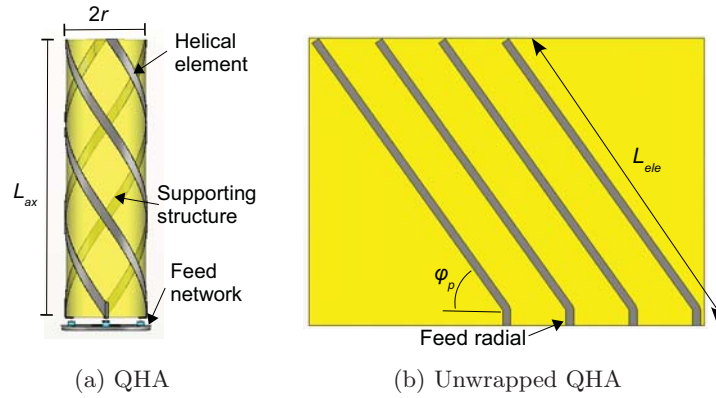


Figure 2.3: Quadrifilar helix antenna (QHA) in wrapped and unwrapped configurations.

in angular direction between the elements. For the QHA, the phase difference between each elements is $\pi/2$. In this work, direction of phase difference is defined as angular direction either clockwise (CW) or counterclockwise (CCW) of increase of phase delay between one element and the other when looking into the antenna from outside.

2.3.3 Radiation and impedance properties

Radiation pattern

The general shape of the radiation pattern of a conventional QHA is hemispherical or cardioid with azimuthal omnidirectionality as shown in Fig. 2.4. The circular polarisation sense of the main radiated beam is determined by the direction of the element winding. The antenna will radiate right hand polarised beam when the element winding is CW directed while the orthogonal polarisation is radiated for CCW direction of winding. As for the direction of the main beam, similar directions between winding and phase difference produces backfire radiation and opposite direction of the two parameters will cause the antenna to radiate in endfire direction. Table 2.1 summarises the relationship of element winding and feed phasing directions with the antenna's sense of circular polarisation and its beam direction. Again, it is important to note that the clockwise and counterclockwise direction are defined when looking into the antenna from outside.

Extensive experimental study of the effect of QHA's parameters such as element length,

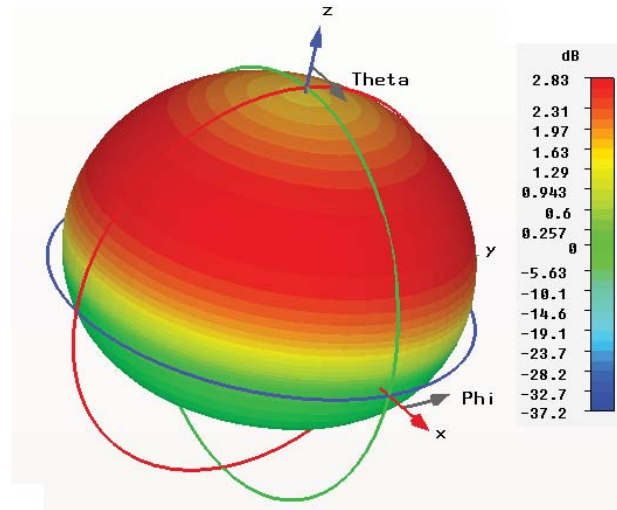


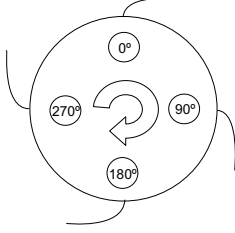
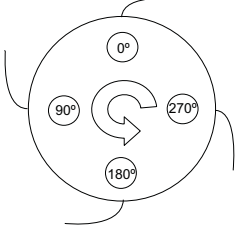
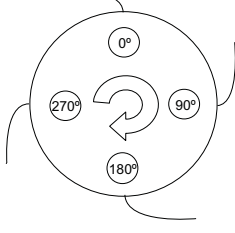
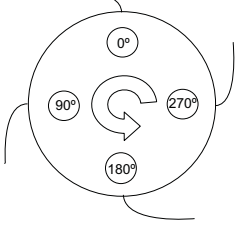
Figure 2.4: Simulated 3D radiation pattern of a typical $\frac{3}{4}\lambda$ QHA.

number of turns and axial length on its radiation pattern has been carried out in [68]. Four types of QHA were investigated which are $\lambda/4$, $\lambda/2$, $3\lambda/4$ and 1λ element length. For each element length, the number of turns were varied in the value of 0.25, 0.5, 0.75 and 1 while the antenna radius remained fixed. Measured 3 dB beamwidth, axial ratio over the beamwidth and front-back ratio were compared for each number of turns and element length. A summary of the presented results are listed in Table 2.2.

It is clear from Table 2.2 that number of turns of the helical elements significantly affects the properties of QHA's radiation pattern although the study only investigated four number of turn which are 0.25, 0.5, 0.75 and 1. A more detailed study of the effect of helical element number of turn on the radiation properties of half wavelength ($\lambda/2$) QHA was presented in [69]. By increasing the number of turn of the antenna from 0.25 to 0.653 and fixing the value of antenna radius, changes to radiation characteristics such as 3dB beamwidth, boresight gain, front-back ratio and axial ratio of a $\lambda/2$ QHA were investigated and are listed as below:

- 3 dB beamwidth reduces from 118° to 98° .
- Maximum gain on boresight increases from 2.8 dB to 6.5 dB.
- Front-back ratio decreases from 24 dB (120° to 180°) to 15 dB beyond 218° .
- Maximum axial ratio within 3 dB beamwidth decreases from 11 dB to 1 dB for

Table 2.1: Relationship of winding and phasing directions with multifilar antenna radiation.

Winding direction	Phasing direction	
	Clockwise	Counterclockwise
Clockwise	 <p>RHCP-backfire</p>	 <p>RHCP-endfire</p>
Counterclockwise	 <p>LHCP-endfire</p>	 <p>LHCP-backfire</p>

the highest number of turns.

- Increase of cross polarisation isolation with the increase of number of turns.

Input impedance

Impedance characteristics of a QHA have not been extensively studied if compared with its radiation pattern. Limited studies on its impedance and bandwidth properties indicates complicated interplay of number of turns and element length that affect the antenna's input impedance. In [61] which only investigated $\lambda/2$ QHA at a resonant frequency of 400 MHz, increasing the number of turns from 0.25 to 1 will reduce the input impedance from 75Ω to 15Ω . Using the same element length (in wavelength) but at different resonant frequency of 1220 MHz, similar effects were also reported in [69] where the input resistance reduces from 50Ω to nearly zero when the number of turns of $\lambda/2$ QHA is increased from 0.25 to 0.653. The effect of element length on the

Table 2.2: Comparison of radiation properties between $\lambda/4$, $\lambda/2$, $3\lambda/4$ and 1λ QHAs with numbers of turns of 0.25, 0.5, 0.75 and 1.

Element length	3 dB beamwidth	Front-back ratio	Peak axial ratio in 3 dB beamwidth
$\lambda/4$	90° to 120° with 0.5 turn has the biggest value	0.25 and 1 turns with value less than 10 dB and 0.5 and 0.75 turns with value above 10 dB	Comparable for all turns with value less than 10 dB
$\lambda/2$	$0.25 > 0.5 > 0.75 > 1$ with max. value of 220° for 0.25 turn	$0.5 > 0.75 > 1 > 0.25$ with max. value of 20 dB for 0.5 turn	All turns give value below 6 dB
$3\lambda/4$	$0.5 > 0.75 > 1$ turns with max. value of 180° for 0.5 turn	$1 > 0.75 > 0.5$ turns with value above 10 dB for 1 and 0.75 turns and value less than 5 dB for 0.5 turn	Comparable for all turns with value less than 6 dB
1λ	Comparable from 100° to 200° for all turns	$1 > 0.75 > 0.5$ turns with value above 10 dB for 1 and 0.75 turns and value less than 5 dB for 0.5 turn	Comparable for all turns with value less than 8 dB

impedance is even less investigated when only once mentioned in [62] where it stated that with element length of half a wavelength, input impedance is in the range of 10Ω to 20Ω and for one wavelength of element length, the impedance is nearly 50Ω .

2.3.4 Bandwidth and multi-band operation

The typical bandwidth of a QHA is several percent of the operating frequency since such antennas with element length less than one wavelength is strongly resonant [62]. However, the number of turn of the helices can significantly alters the antenna bandwidth as indicated in [69] where increase of number of turns reduces the bandwidth of voltage standing wave ratio (VSWR) below 2 dB from 5% to approximately 0.27%. Contrary to many previous studies where the helix number of turns was varied and its effects were studied, the bandwidth of a QHA with a fixed number of turns of 0.5 was

studied in [70] and its dependency on other parameters such as axial length and diameter was characterised. Its main finding shows that bandwidth is directly proportional to the diameter to height (axial length) ratio of the element length of a QHA.

Bandwidth improvement

Techniques on improving or widening the bandwidth of a QHA are mostly concentrated on adjusting the helical element width or adding an extra conducting strip to each helical element. With regards to the former method, it has been showed in [71] that by varying the element width along a printed QHA (tapering), significant improvements of bandwidth can be achieved. More specifically, the width at the start of the element has to be several times bigger than at the end with gradual decrease between two ends. By using this method, increase in bandwidth from 7% to 14% in L band and 5% to 16% in S band were recorded in [71] with start to end element width ratio of 8.

A more promising method of widening the bandwidth is by introducing parasitic helical strip to the each helical elements. Two different approaches of connecting the parasitic strip to the main helical element were introduced in order to increase the QHA's bandwidth. In [72], impedance bandwidth ($VSWR < 2$ dB) of 39% and bandwidth with respect to axial ratio $AR < 3$ dB of 160 MHz can be gained by placing grounded parasitic helical strips near to each radiating element. A slightly different technique of using a parasitic helix is proposed in [73] where the parasitic helix is connected to the top end of the radiating element and grounded at the other end to create a folded helical element. Increase of impedance bandwidth of the antenna to 30% by utilising this method is due to the increase of effective width caused by the folded configuration and susceptance reduction by the reactive component of the added element.

Multi-band operation

It is common for land mobile satellite communication systems and global positioning systems to use several frequency bands for their operations. As QHA is inherently a narrowband antenna, multi-band capability can be a necessity in order for the QHA to operate in these systems. Several design techniques have been proposed for multi-band

Table 2.3: Techniques for multi-band operation of QHA.

Technique	Implementation
Adjustment to effective element length	<ul style="list-style-type: none"> · RF switches - PIN diode on the elements to switch on and off part of the elements [74]. · Passive circuit - placement of parallel LC circuit which has infinite impedance at resonant frequency as a switch at certain length of the helical element [75].
Combination of two QHAs	<ul style="list-style-type: none"> · Incorporating two QHAs with a small difference in resonant frequency into one structure [76] [77].
Geometric adjustment to helical element	<ul style="list-style-type: none"> · Introduction of multiple arms at the top end of the helical elements for multi-band operation [78]. · Folding of the helical elements [79]. · Incorporating microstrip spur-line band stop filter at the helical elements [80]. · Introducing gap at the centre of the helical element and mechanically varying the gap between the separated elements [81].

operation of the QHA and they can be categorised into three general techniques, which are adjustment to the effective element length, combination of two QHAs and geometric adjustment to the helical elements. Table 2.3 provides an overview of method for QHA to operate with multi-band capability.

2.3.5 Miniaturisation techniques

One of the most challenging aspects of handheld terminal antenna design is that the antenna must be as compact and lightweight as possible without compromising on its performance. With its conventional size, a QHA can be considered as too large and bulky to be fitted in current handheld terminal. Therefore, reduction of its size remains one of the most active research activities concerning the antenna. Three major categories of miniaturisation methods for QHA are meander line and element folding, dielectric loading and coupling technique. All three categories are detailed out in the subsequent subsections.

Meander line and element folding

The meander line technique has been utilised for size reduction of a wire antenna with only a slight decrease in efficiency [82]. One of the first implementations of meander line to reduce the size of QHA is proposed in [83] where axial length reduction of 53% and significant improvement in the impedance bandwidth were achieved. A comprehensive study on various type of meander line shape with size reduction from 9.8% to 35% and its effect of impedance bandwidth and radiation pattern were carried out in [84]. Contrary to a previous study [83], this investigation shows that by reducing the size of the antenna by meandering, the bandwidth is also decreased by several per cent.

A slightly different type of meandering was introduced in [85], where instead of rectangular shape of meander segment, a sinusoidal function shape was applied to the radiating element. By combining various sinusoidal functions, axial length of a quarter wavelength QHA can be reduced by 48% to 62.5% and its impedance match was also improved.

Although the meander line technique has been shown to provide considerable reduction in size, several works have been conducted to investigate combination of the meander line technique with element folding or variable pitch angle methods. By incorporating those two methods with meander line technique, axial length reduction from 43% to 54.5% are achievable as shown in [79], [86].

Dielectric loading

The first study on the effect of dielectric rod to the resonant frequency of a QHA provides an important foundation in using dielectric material for miniaturisation [87]. In the study, two parameters of the dielectric rod which is placed in the centre of the QHA were investigated namely the relative permittivity of the material and the rod radius. It showed that by increasing the relative permittivity of the material, a bigger shift of the resonant frequency to the lower frequency can be expected. This result indicates that by having dielectric rod inside a QHA, a targeted resonant frequency can be obtained with shorter element length compared to a QHA without dielectric rod. Thus, in effect the dielectric rod reduces the size of the QHA.

Apart from the permittivity of the material, the radius of the dielectric rod also affects the amount of frequency shift experienced by the QHA's resonant frequency where the maximum shift is when the dielectric rod's radius is the same as the QHA's radius. One limitation of this investigation is the low value of the relative permittivity used for the dielectric rods which are 2.15 and 3.38. These values permit only a small shift in resonant frequency hence small reduction in size.

Higher value of relative permittivity of dielectric material has been utilised in several studies for size reduction of a QHA [88] [89]. Extremely small QHAs can be realised by using material with high relative permittivity in the range of 30 to 40 where its size is about 2% to 3% of conventional size. However, one significant problem of this method is the very low input resistance which then reduces its impedance bandwidth and radiation efficiency.

Coupling technique

The last category of miniaturisation techniques used for QHA is the coupling method where helical element is separated into two or more disconnected segments by inserting gap. In [90], the two disconnected segments were placed parallel to each other for coupling and thus reduces its axial length. A different method of structuring the disconnected segments where instead of placing them in parallel, parts of the segments were folded around the cylindrical surface [91]. It also studied the effect of axial length reduction to the radiation parameters of the half wavelength QHA.

2.4 Evaluating antennas in MIMO system

Evaluation of MIMO antennas require joint contribution between the multiple antennas properties and the propagation channel characteristics. Single antenna evaluation methods which are usually conducted in isolated environment are no longer adequate for a MIMO antenna. Figures of merit used as performance parameters in evaluating MIMO antenna will be presented first followed by compilation of various methods

of performance evaluation. Finally, the impact of antenna parameters on the MIMO system performance is discussed based on previous published works.

2.4.1 Figures of Merit

Capacity

Capacity has been widely used as the ultimate performance parameter in evaluating multiple antennas in a MIMO system [92], [93], [94]. As defined by Equation (2.3) in Section 2.2.1, the capacity of a MIMO system depends on the total transmit power and the channel matrix which incorporates the propagation channel as well as the transmit and receive antennas effects. Therefore, comparison of multiple antennas performance can be evaluated provided that the propagation channel remains nearly the same so that the changes in capacity can be directed to the antenna effect. Quite commonly, the capacity of a MIMO system is also calculated based on the SNR at the receive antenna as shown in Equation (2.4) in Section 2.2.1 especially when comparing the performance of various signal processing techniques for a multiple antennas system with the same SNR value. When comparing the capacity values of multiple antennas configurations with the same SNR, it is extremely important to normalise the channel data with one common normalisation factor in order to preserve the difference between each configuration's received power.

One main drawback of using capacity as a performance parameter is that it does not provide information on the reason and clue on why one antenna configuration is better than the others. It is therefore difficult to use capacity as an optimisation parameter in designing multiple antennas. The reason behind this drawback is that even when the propagation channel is the same, the capacity are determined by a complicated interplay between various antenna properties such as mutual coupling, radiation pattern and antenna-induced correlation. Therefore, it is very difficult to pinpoint the exact cause of any capacity change with regards to specific antenna characteristics.

Correlation

It is established that multiple antennas configurations can significantly affect the correlation of received signals. Therefore, if two different antennas configurations that operate in the same channel are considered, then the one with the lowest correlation can be regarded as better than the other. In general, correlation at the transmit and receive antennas can be calculated based on the measured or simulated channel matrix. However this method requires significant effort to be made for each evaluation and is not suitable for early design evaluation.

In [95], a numerical formulation to calculate the complex correlation between the received voltage of two antennas has been proposed where it combines the antennas electric field patterns with the angular density function of the incoming wave. This formulation which can be solved numerically provides an efficient and consistent method in evaluating the correlation of various antennas configurations. However, the formulation does require an embedded 3 dimension (3-D) pattern of the each antenna electric fields in order to include the effect of mutual coupling. The complex correlation can be written as:

$$\rho_{12} = \frac{\oint (\text{XPD} \cdot A_{\theta 1}(\Omega) A_{\theta 2}^*(\Omega) p_{\theta}(\Omega) + A_{\phi 1}(\Omega) A_{\phi 2}^*(\Omega) p_{\phi}(\Omega)) \cdot e^{-j\beta x} d\Omega}{\sqrt{\oint (\text{XPD} \cdot A_{\theta 1}(\Omega) A_{\theta 1}^*(\Omega) p_{\theta}(\Omega) + A_{\phi 1}(\Omega) A_{\phi 1}^*(\Omega) p_{\phi}(\Omega)) d\Omega} \times \sqrt{\oint (\text{XPD} \cdot A_{\theta 2}(\Omega) A_{\theta 2}^*(\Omega) p_{\theta}(\Omega) + A_{\phi 2}(\Omega) A_{\phi 2}^*(\Omega) p_{\phi}(\Omega)) d\Omega}} \quad (2.24)$$

where Ω represents the coordinate point (θ, ϕ) in spherical coordinate system and

$$\oint d\Omega = \int_0^{\pi} \int_0^{2\pi} \sin \theta d\phi d\theta. \quad (2.25)$$

Meanwhile, the XPD denotes the cross polarisation discrimination of the channel, $A_{\theta n}$ and $A_{\phi n}$ are the θ and ϕ electric field patterns of antenna n respectively, x defines the phase difference between the antennas and $p_{\theta}(\Omega)$ and $p_{\phi}(\Omega)$ are the AoA density functions of the θ and ϕ components and must satisfy the following equation:

$$\oint p_{\theta}(\Omega) = \oint p_{\phi}(\Omega) = 1. \quad (2.26)$$

Earlier investigations on spatial correlation between antennas demonstrated that for the correlation to be negligible, spacing between antennas is required to be 0.5λ or more in an isotropic environment [96]. However, these studies excluded the effect of mutual coupling on the antenna radiation patterns. When the effect of mutual coupling is incorporated in the analysis, it has been found that as the antennas are placed closer to each other, correlation between the antennas decreases as the mutual coupling distorts the radiation patterns and introduces angular decorrelation [97].

Received power and branch power ratio

In a MIMO system, the difference in received power at each antenna branches plays a significant role in determining the achievable capacity increase. It is shown in [98] that reduction of signal power at selected antenna branches reduces the magnitude of several eigenvalues, which then decreases the MIMO capacity. Signal power at multiple antennas depends on the interaction between antennas gain patterns with the incident waves. For multiple antennas, mutual coupling can distort the radiation pattern of the antennas, which leads to received power imbalance between closely radiating antennas.

To evaluate the received power of a single antenna element in an array, a mean effective gain parameter can be used. Mean effective gain (MEG) of an antenna is defined as average received power by an antenna over a random environment to that received by an isotropic antenna [99]. In terms of multiple antennas evaluation, MEG value is utilised to determine the average branch power ratio between antenna elements. The analytical expression of MEG in Rayleigh environment is first derived in [99] and can be written as the following:

$$\text{MEG} = \oint \left(\frac{\text{XPD}}{1 + \text{XPD}} G_{\theta}(\Omega) p_{\theta}(\Omega) + \frac{1}{1 + \text{XPD}} G_{\phi}(\Omega) p_{\phi}(\Omega) \right) d\Omega \quad (2.27)$$

where XPD, $p_{\theta}(\theta, \phi)$ and $p_{\phi}(\theta, \phi)$ are already defined for Equation (2.24). Meanwhile, the $G_{\theta}(\theta, \phi)$ and $G_{\phi}(\theta, \phi)$ denote the θ and ϕ components of the antenna embedded gain pattern.

Branch power ratio indicates the difference in received power between antenna elements in the same array. Aside from using measured or simulated received power for the

branch power ratio calculation, MEG value can also be taken as an approximation of the average received power by a single antenna. This provides us with a simple method of evaluating the branch power ratio of multiple antennas without having to conduct a measurement campaign or complicated simulation. The branch power ratio BPR between two adjacent antennas can then be calculated as:

$$\max \text{BPR} = \left(\frac{\text{MEG}_{\text{ant1}}}{\text{MEG}_{\text{ant2}}}, \frac{\text{MEG}_{\text{ant2}}}{\text{MEG}_{\text{ant1}}} \right) \quad (2.28)$$

where MEG_{ant1} and MEG_{ant2} are the mean effective gain of the first and second antennas. To obtain the maximum capacity increase from a MIMO system, the received power of all antenna elements must be nearly equal which causes the value of the branch power ratio between two antennas to be almost one.

Efficiency

Radiation efficiency of an antenna is defined as “the ratio of the total power radiated by an antenna to the net power accepted by the antenna from the connected transmitter” [100]. This definition however does not take into account the effect of impedance mismatch of the antenna with the transmitter. The overall antenna efficiency that includes the impedance effect can be written as [101]:

$$\eta_{\text{total}} = \eta_{\text{ref}} \cdot \eta_{\text{rad}} \quad (2.29)$$

where η_{ref} is the reflection efficiency which can be calculated as $\eta_{\text{ref}} = (1 - |\Gamma|^2)$ with Γ is the reflection coefficient and η_{rad} denotes the radiation efficiency. In contrast to a single antenna where its efficiency mainly depends on the design and user proximity, the efficiency of multiple antennas can also be affected by the mutual coupling between adjacent antennas. Therefore, it is very much important to investigate the impact of multiple antennas design which includes the array spacing and configuration on the efficiency of each radiating elements.

Multiplexing efficiency

Although capacity does provide the means to compare the performance of antennas in a MIMO system, it is less intuitive and quite cumbersome to be used in designing and

optimising antennas. A new performance metric called multiplexing efficiency η_{mux} was introduced in [102] which compared the received power of real array with ideal array in spatial multiplexing mode. Mathematically, multiplexing efficiency is defined as:

$$\eta_{mux} = \frac{\text{SNR}_0}{\text{SNR}_T} \quad (2.30)$$

where SNR_0 denotes the required SNR to achieve a specified capacity using an ideal array while SNR_T is the required SNR to achieve the same specified capacity using a real array.

In order to simplify its use, closed form expressions of multiplexing efficiency have been provided in [102]. In a high SNR condition, the multiplexing efficiency can be written in a simple formulation as:

$$\tilde{\eta}_{mux} = \det(\mathbf{R})^{1/N} \quad (2.31)$$

where \mathbf{R} denotes the receive correlation matrix that fully describes the effect of antenna in the channel and N is the number of antennas used. For a more generalised case, the closed form expression can be written as:

$$\eta_{mux} = \frac{(\det(\mathbf{I}_N + \text{SNR}_T \mathbf{R})^{1/N}) - 1}{\text{SNR}_T}. \quad (2.32)$$

2.4.2 Evaluation methods

Single antenna evaluation is usually carried out by measuring the radiation pattern and S-parameters in an isolated environment, e.g. anechoic chamber. As for multiple antennas, its performance evaluation requires the interaction between the antennas and also its operating environment, which make the isolated measurement inadequate. Several methods of evaluating MIMO antennas are given in subsections below.

Computational analysis and simulation

Evaluation of a MIMO antenna can be conducted by incorporating measured or simulated antenna radiation properties into the analytical formulation for MEG (Equation (2.27)) and correlation (Equation (2.24)) and for capacity, into MIMO channel simulation to generate channel matrix. Calculation of MEG and correlation is quite

straightforward as long as the correct AoA distribution and XPD are chosen for the intended environment. Integration of antenna properties into MIMO channel simulation is the most commonly used in evaluating the impact of antenna to the capacity of MIMO systems. Therefore, accuracy of the evaluation depends on the channel model used in the simulation, which can varied from the basic i.i.d Rayleigh channel to sophisticated 3-D ray tracing algorithm.

Direct measurement

Direct measurement using to-be-evaluated multiple antennas at the transmitter and/or receiver of a channel sounder system can be considered as the most accurate evaluation as well as the most costly and time consuming. Due to these reasons, direct measurement is normally used to validate another newly proposed method for antenna evaluation [103] and also to investigate the impact of novel antenna design on the MIMO system [104]. There is also one important factor, apart from cost and time, which make direct measurements less practical in evaluating MIMO antenna that it is impossible to repeat the measurement with the exact channel characteristics as before. This lack of repeatability causes difficulty in optimising MIMO antenna design as the variation of performance parameter can also be directed to channel variation.

Combination of antenna properties and measured channel

This computational method basically combines measured or simulated complex 3-D antenna radiation patterns with measured radio propagation channel data. One of such methods, called Experimental Plane Wave Based Method (EPWBM), is demonstrated in [103]. Based on joint contribution of antenna properties and propagation data, the channel matrix for each data sample is generated and used for MEG and capacity calculation. The main advantage of the EPWBM is it can be repeated with the same channel characteristics for different antenna configuration. This repeatability aspect of EPWBM is very useful in the optimisation of MIMO antenna parameter as any variation of performance parameter is only due to the antenna effect, not the channel.

One drawback of this method is its requirement for double directional radio channel data of various indoor and outdoor environments.

Using a similar approach, a composite channel model was proposed in [105] which also combines a double directional measurement with measured complex radiation pattern of antennas with user influence. In this technique, the multiantenna complex far-field patterns are represented by spherical vector harmonics or modes instead of field representation in angular domain. By doing so, it avoids the use of complex interpolation when used in combination with AoA and AoD which can be of any arbitrary direction.

MIMO Over-the-Air (OTA) testing

Over-the-air (OTA) testing for a single antenna terminal has been standardised [106] and used to evaluate the performance of a mobile terminal in transmit and receive mode. Extension of this testing technique to evaluate multiple antennas terminal has been a major research activity recently since the next generation wireless systems which utilise MIMO techniques are now in the early stage of mass deployment. Two main techniques that have been proposed for OTA testing of multiple antennas terminal which are reverberation chamber and spatial fading emulator.

Reverberation chambers consists of metal cavity with an adequate size to support many resonant modes, which are generated by perturbation of transmitted waves using mechanical stirrers, in order to generate multipath fading in the cavity. It can be excited by one or several transmit antennas depending on the required fading environment. An illustration of a reverberation chamber with multiple transmit and receive antennas is given in Fig. 2.5. Its application in multiple antennas evaluation has been demonstrated in [1] where diversity gain and capacity of six monopoles circular antenna array is analysed using reverberation chamber. In recent years, several important advancements have been achieved in further developing reverberation chamber for multiple antennas evaluation platform. One of such improvements is its emulation of Ricean fading environment with variable value of K factor by changing the chamber and/or transmit antennas configurations [107].

Apart from the reverberation chamber, a new technique called a spatial fading emulator

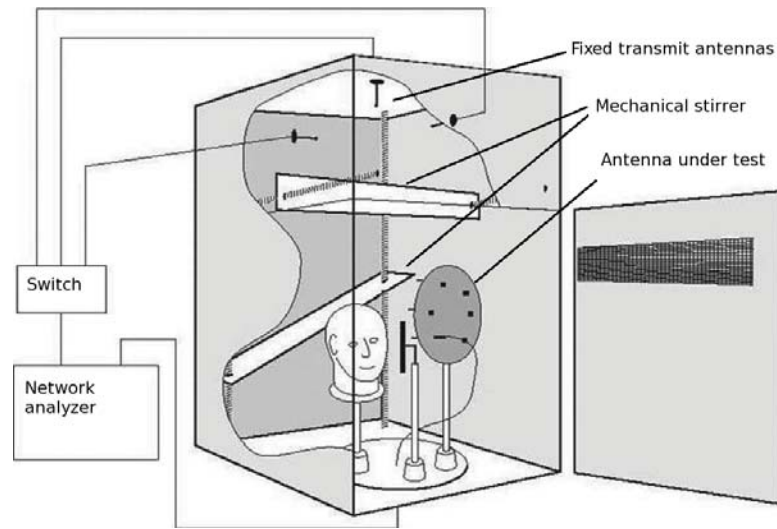


Figure 2.5: Reverberation chamber configuration for multiple antennas evaluation [1].

(SFE) is also proposed for multiple antennas OTA testing [108]. In order to create artificial multipath environment around the device-under-test (DUT), the technique utilises array of transmit antennas which are connected to a multichannel fading emulator as shown in Fig. 2.6. Geometric positions of the transmit antenna array depends on the AoA characteristic of the emulated channel. For emulation of a channel with only 2-D azimuth AoA distribution, circular configurations of transmit array to surround the DUT where the transmit antennas are spaced with a specific angle is sufficient for the evaluation.

There are however various open research questions regarding the use and configuration of OTA testing in evaluating multiple antennas terminal. Among the most significant are the extent of channel characteristics that are required for antennas evaluation where the balance between accuracy of channel used and the high complexity of emulating such channel must be investigated. Apart from that, validation of this technique by comparing its result with results obtained from field measurement is also important to ensure its accuracy.

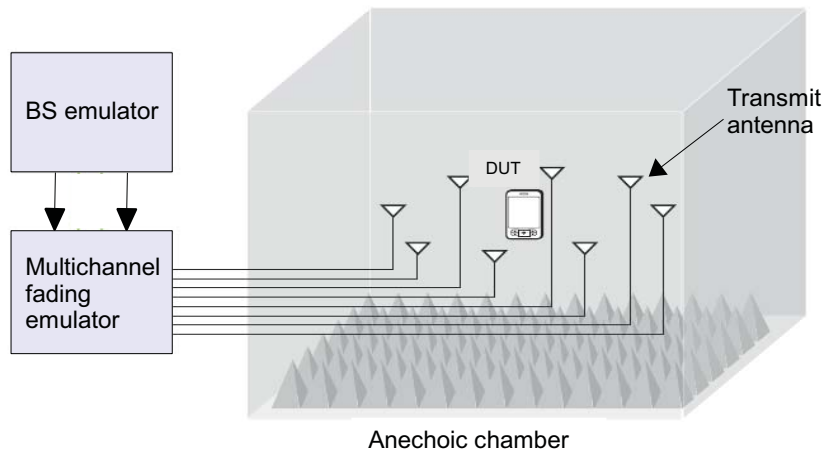


Figure 2.6: Basic configuration of a spatial fading emulator

2.4.3 Antenna impacts on MIMO system

Radiation pattern and polarisation

The effect of the antenna on the performance of a MIMO system can be first investigated with regards to its radiation pattern and polarisation. Its impact to signal correlation and received power can be easily studied using analytical equations, Equation (2.24) and Equation (2.27) respectively. If an isotropic multipath environment is considered, then increase of pattern directionality may result in lower value of correlation as the antennas will scan different sets of multipath. However, the use of directional antennas is also expected to exhibit power imbalance between antennas which can reduce the achievable capacity. An interesting study has been conducted on the effect of antenna directionality in a MIMO system [109] where the comparison between directional and omnidirectional antennas in terms of capacity with varying SNR and spacing. It shows that in low angular spread channel, the increase in directionality improves the capacity while the opposite for bigger angular spread. One limitation of this study is it assumed the beam of directional antennas can be steered to the estimated mean of AoA direction.

The direction of the antenna main beam can also affect the capacity of a MIMO system. In [110], capacity comparisons between dipole antennas with higher gain spiral antennas whose main beams are directed at 45° and 135° were carried out using indoor

measurements and simulation. The study indicated that the dipole antennas provide better capacity than the spiral antennas since the dipole's main beam is in the horizontal plane where the concentration of multipath components is the highest.

The benefits of using polarisation to create artificial independent subchannels in a MIMO system have been well documented in [111], [112]. Regardless of the environment, at least two independent channels can be generated by a polarised MIMO system, which depends entirely on the antenna polarisation orthogonality. Therefore, the antenna XPR, which defines the antenna's ability to reject opposite polarisation plays a major role in determining the capacity performance.

Mutual coupling

Mutual coupling has significant impact on the performance of a MIMO system because of its effects on the antennas' pattern and efficiency. More specifically, for closely spaced antennas, its radiation patterns can be distorted and its efficiency reduces. It is well known that the severity of the mutual coupling effect depends on the distance separating the antennas where the closer the antennas are, the stronger the effects will be. In terms of MIMO capabilities, the effect of mutual coupling on capacity is not straightforward as it simultaneously decreases the correlation due to pattern diversity while at the same time reduces the antenna efficiency which affects the receive SNR of the antennas.

Because of these two factors, contradictory results on the effect of mutual coupling to the capacity can be found in open literature where both increase and decrease of capacity are reported. In [113], mutual coupling is shown to reduce the correlation and thus increases the MIMO capacity where comparison between antenna spacing of 0.1λ and 0.5λ were considered. However, another study indicates that as the numbers of antennas increases in a fixed length which means that the spacing is reduced, then capacity decreases as the spacing goes below 0.5λ [114]. This capacity decrease is mainly because of the drop in receive SNR. Such difference in capacity performance due to mutual coupling is also apparent in measurements where in [115], the same capacity can be achieved even with decrease of spacing from 0.5λ to 0.2λ . A MIMO measure-

ment with an actual MIMO radio in [116] however reported that small antenna spacing reduces the ability of a MIMO system to transmit or receive multiple subchannels when it compared the eigenvalues distribution for various antenna spacing.

A more comprehensive analysis on the impact of antenna coupling to MIMO figures of merit was presented in [117] which are channel correlation, the Frobenius norm that represents channel power and mean capacity without channel state information at the transmitter. The study compared all performance metrics in omnidirectional and directional scattering scenarios and its results are listed as follows:

- In omnidirectional scattering, inclusion of antenna coupling causes the channel correlation to be lower.
- Decrease of correlation in directional scattering condition due to mutual coupling where the main beams of the antennas are not similarly oriented to the mean AoA.
- In general, mutual coupling has detrimental effect to the channel Frobenius norm except in the case of directional scattering with the array oriented orthogonally to the main direction of the AoA.
- Impact of antenna coupling on the capacity depends on the SNR at the receiver.
- In low SNR, negative effect of the coupling causes the capacity to be lower when compared with ideal case of no antenna coupling.
- The opposite case may occur where the stronger mutual coupling (i.e. closer antenna spacing) causes capacity increase in high SNR condition.

Array configuration

Aside from antenna spacing which determines the severity of the mutual coupling effect, the geometrical shape of the array also plays a role in influencing the received signal correlation and ultimately the system capacity. However, it is difficult to provide a definite conclusion on the best geometric configuration as it is highly dependent on the channel properties such as angular spread in azimuth and elevation and availability of LoS component. The most widely used configuration of array in simulation and measurement of MIMO system is the uniform linear array (ULA). In [118], azimuthal

orientation of a ULA in multipath channel with small and large angular spreads was investigated in terms of its effect on correlation and capacity. A more pronounced impact of the ULA orientation on the correlation and capacity is evident for channel with smaller angular spread. In general, the best orientation of ULA for capacity maximisation regardless of angular spread is broadside to the mean AoD and AoA.

Other geometric configurations apart from ULA were also considered for a MIMO system for example nonuniformly-spaced linear array (NULA), uniform circular array (UCA) and 3D uniform cubic array (UCuA) [119], [120]. Overall, the ULA is shown to be the best geometric configuration of MIMO array but with some exceptions depending on the channel conditions. One of such exceptions is implied in [119] where better capacity performance was recorded using ‘Star’ configuration instead of ULA or other configurations for channel with high correlation.

2.5 Summary

The application of dual circularly polarised antennas as a practical implementation of MIMO in land mobile satellite system has been validated as the method provides significant capacity increase over single polarised system in measurement campaigns. Although various aspects of the LMS MIMO system have been investigated, one main area that received little attention is the impact of antenna characteristics to overall system performance. In several measurement campaigns that have been conducted, none has investigated this matter thoroughly as most are intended to characterise the MIMO channel. As for the channel models that have been proposed for this system, little considerations have been made on ways to include antenna characteristics in the channel description. The lack of any study on the effect of antennas on the LMS MIMO system performance provides new research opportunities such as measurement campaign can be dedicated solely to investigate this matter and extending the current channel models or introduce a new modelling approach in order to include more realistic antenna properties.

The quadrifilar helix antenna has been identified as a very promising antenna candidate to be further developed for the use at the receiver terminal of a LMS MIMO system.

Two areas of to advance for the antenna that need to be considered are dual circular polarisation capability and size reduction so that it can be fitted inside small terminal. The question on how to evaluate the performance of a new antenna design for the LMS MIMO system also needs to be answered. Although the proposed antenna can be evaluated using field measurements, comprehensive campaign that can cover various system parameters such as satellite elevation angle and type of environment is very costly and difficult to be conducted. Therefore, a new technique in evaluating MIMO antennas in a LMS MIMO system is also considered to be a major task in this research work.

Chapter 3

Miniaturisation of printed quadrifilar helix antenna by element folding methods

3.1 Introduction

Integration of printed quadrifilar helix antenna (PQHA) into a mobile terminal or onto a vehicle for the land mobile satellite (LMS) MIMO system would necessitate the antenna to be as compact as possible while maintaining its desirable circularly polarised pattern and impedance characteristic. Miniaturisation of 0.5λ and 0.75λ PQHAs were investigated where the axial length of each PQHA type is reduced using two different proposed methods namely element folding and combination of element folding and meander line methods. Effects of these methods on the antenna characteristics were studied by comparing the antenna's scattering parameters (S-parameters) and radiation properties with a conventional PQHA without any miniaturisation. Based on the optimum design configuration obtained from the simulations, a prototype of the selected antenna design from each type of PQHA was fabricated and its impedance and radiation characteristics were measured and compared with simulation results.

The two element lengths of 0.5λ and 0.75λ are chosen as both lengths provide the

desirable radiation and impedance properties that are required for a land mobile satellite system even with their small sizes. As mentioned in Section 2.3, the quadrifilar helix antenna is one of the best antenna candidate for mobile satellite communication and satellite positioning systems where the two element lengths are considered to be the optimum value for obtaining the required radiation characteristics and also have relatively compact dimensions. The 0.5λ element length PQHA is designed for mobile receiver devices of the LMS system while the 0.75λ is utilised for vehicular applications of such system where the antenna is placed on top of a vehicle rooftop.

3.2 Miniaturisation of 0.5λ PQHA using element folding method

Miniaturisation of a 0.5λ element length PQHA can be achieved by implementing an element folding method where helical elements of the PQHA are folded once or several times to form segmented arms with equal length. For each helical element, the segmented arms are spaced from one another and linked by an arc radial. Although the element folding method has been used to reduce the axial length of a PQHA [121] and [122], our proposed method extends this approach by folding more than half of the helical element length. The utilisation of element folding method to reduce PQHA's axial length and its impact to the antenna radiation pattern and bandwidth are investigated using electromagnetic simulation software CST Microwave Studio[®].

In this study, the basic physical parameters for the 0.5λ element length PQHA are as follows:

- Targeted resonant frequency of 2.45 GHz.
- Antenna radius of 5 mm.
- Initial element length L_{ele} of 61.5 mm which corresponds to 0.5λ at 2.45 GHz frequency. In each simulation, the element length is optimised to obtain the lowest possible reflection coefficient at the resonant frequency.
- Helical element width of 0.5 mm.
- Antenna is right hand circularly polarised (RHCP) which means that the direction

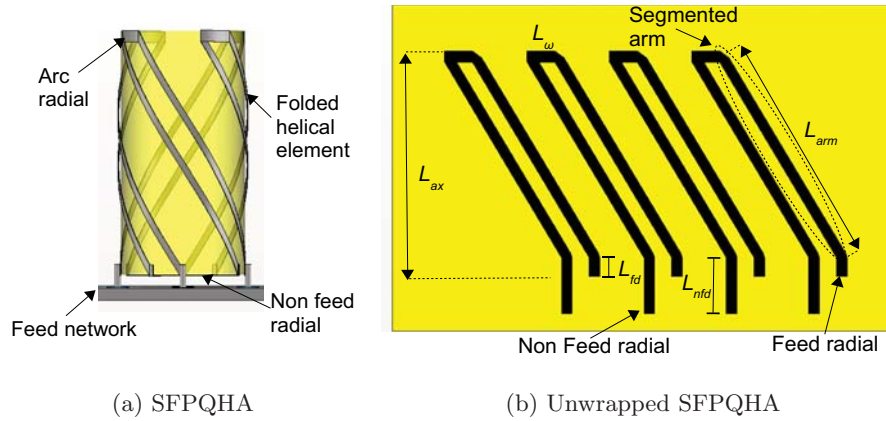


Figure 3.1: Single folded PQHA (SFPQHA) in wrapped and unwrapped configurations.

of winding is clockwise when looking from the top of the antenna.

The resonant frequency of 2.45 GHz is chosen as it is within the S band frequency which is used for mobile satellite communication systems and Digital Video Broadcasting - Satellite Services for Handheld (DVB-SH). Although it is not exactly the same frequencies as allocated for these systems, this frequency make it easier for field measurement with the designed antennas to be conducted since the carrier frequency of the available channel sounder is within this frequency range. Meanwhile, the value of 5 mm has been selected for the antenna radius so that the designed antenna can be fitted in a small receiver terminal of the mobile satellite communication system.

3.2.1 Single folded configuration

Single folding of the helical elements of a quadrifilar helix antenna can be considered as the most basic application of element folding method. The helical elements are single folded where two equal length segmented arms were constructed as a result. These segmented arms are connected with an arc radial at the top of the antenna structure. As the antenna is a half wavelength PQHA, then the non feed radials must be shortened where in the case of single folded PQHA (SFPQHA), they are shortened at the bottom of the structure [123]. Configuration of a single folded PQHA and its unwrapped elements are shown in Fig. 3.1.

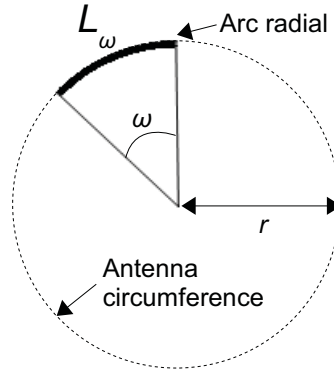


Figure 3.2: Configuration of the arc radial with respect to the antenna circumference (top view).

Axial length reduction

In this configuration, two main parameters of the SFPQHA were investigated for their effects on the antenna's radiation pattern and bandwidth namely the number of turns on the antenna and the length of arc radial given as L_ω . Three values of number of turns were used in the simulation which are 0.375, 0.5 and 0.625. Higher value of turns is not advisable to be used for a conventional 0.5λ PQHA as it reduces the input resistance and impedance bandwidth of the antenna significantly as presented in [69]. As for the length of the arc radial, it is calculated based on the arc radial angle ω which is indicated in Fig. 3.2 and it is given as:

$$L_\omega = \left(\frac{\omega}{360}\right) 2\pi r \quad (3.1)$$

where ω is given in degree and r denotes the antenna radius. In order to provide a more comprehensive view of the arc radial, the arc radial angle was used as the defining parameter since it does not rely on the antenna circumference value. Four values of arc radial angle were utilised in this simulation which are 15° , 30° , 45° and 60° .

In order to obtain the length of one segmented arm L_{arm} , the length of the feed radial, non feed radial and arc radials is subtracted from the total length of the helical arm and the resultant length is later divided by the number of segmented arm. With reference to Fig. 3.1b which shows the configuration of the unwrapped SFPQHA, the length of

Table 3.1: Axial length (in mm) of SFPQHAs and its reduction percentage for different turns and arc radial angles.

Arc radial angle ω	Number of turns		
	0.375	0.5	0.625
Conventional	56	55	53
15°	24.6 (56.1%)	22.8 (58.5%)	20.4 (61.5%)
30°	23.5 (58.0%)	22.2 (60.0%)	19.5 (63.2%)
45°	22.6 (60.0%)	20.5 (62.7%)	18.5 (65.1%)
60°	21.6 (61.4%)	19.5 (64.5%)	16.0 (69.8%)

segmented arm is given as:

$$L_{arm} = \frac{L_{ele} - (L_{fd} + L_{nfd} + L_{\omega})}{N_{arm}} \quad (3.2)$$

where L_{ele} denotes the total element length, L_{fd} , L_{nfd} and L_{ω} are the length of feed radial, non feed radial and arc radial respectively and N_{arm} is the number of segmented arm which in the case of SFPQHA is two. The axial length of the antenna can then be calculated using Equation (2.23) where the segmented arm length is used instead of the total element length. Table 3.1 provides the values of axial length for SFPQHAs with different turns and lengths of arc radial and also their size reduction percentage when compared to a conventional PQHA design with the same number of turns.

By using a simple single folding method, a substantial reduction in the axial length of a PQHA can be obtained. All design variations stated in Table 3.1 reduces the PQHA's axial length by more than half of its conventional form. The lowest percentage of miniaturisation of 56.1% is for a single folded PQHA with 0.375 turns and $\omega = 15^\circ$ while the highest percentage of 69.8% can be achieved by having 0.625 as the number of turns and 60° as the value of ω . Although the highest possible miniaturisation factor is always desirable, it is important to balance the size reduction with its effects on the antenna radiation and impedance properties.

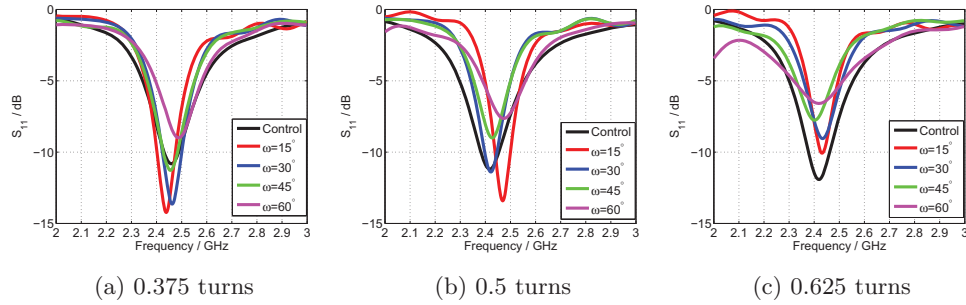


Figure 3.3: Reflection coefficient of conventional PQHA (Control) and SFPQHAs with different turns and arc radial angles.

Simulation results

Simulation results of the SFPQHAs are presented in the form of reflection coefficient and co and cross-polarised elevation gain patterns at azimuth angle $\phi = 0^\circ$. Comparison with conventional PQHA without any miniaturisation is also provided for each case of number of turns. As a single PQHA consists of four helical elements, each element has its own reflection coefficient value. However, due to the fact that each element has the same shape and configuration, they have exactly the same impedance characteristic and hence reflection coefficient value. This is especially true in computer simulations where there is a perfect repeatability of the element construction of a PQHA. This characteristic is summarised as $S_{22} = S_{33} = S_{44} = S_{11}$ where the subscript represents the numbering of the helical element. Therefore, in this work, only reflection coefficient of the first helical element S_{11} of the SFPQHAs is compared for various turns and arc radial angles as a representative of the whole antenna characteristic. The simulated reflection coefficients of the helical element of SFPQHAs and conventional PQHAs are presented in Fig. 3.3. In general, an increase of number of turns for the SFPQHA in our case from 0.375 to 0.625 has worsened the reflection coefficient of the helical element regardless of the length of the arc radial. If a SFPQHA with $\omega = 30^\circ$ is taken as an example, then the reflection coefficient of the helical element with number of turns of 0.375, 0.5 and 0.625 at 2.45 GHz frequency are -13.1 dB, -9.5 dB and -8.6 dB respectively.

The co and cross-polarised elevation gain patterns ($\phi = 0^\circ$) of the SFPQHAs are also

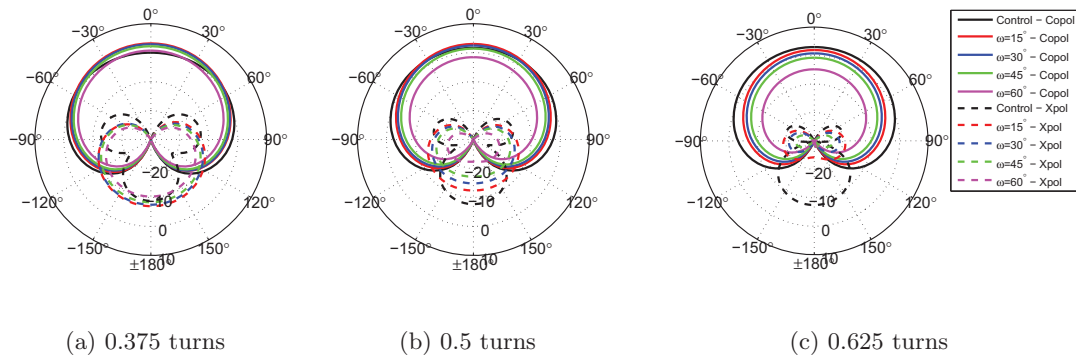


Figure 3.4: Elevation gain pattern (dBic) with $\phi = 0^\circ$ at 2.45 GHz frequency of conventional PQHA (Control) and SFPQHAs with different turns and arc radial angles.

shown in Fig. 3.4. The type of gain used in this comparison is realised gain in order to include the effects of impedance mismatch and radiation efficiency. One important aspect of the simulated pattern of SFPQHAs is its pattern is omnidirectional in the azimuth domain where the pattern does not change with the azimuth angle. The results also indicate that for each number of turns, increase in the length of arc radial causes the antenna to have a lower co-polarised gain pattern in the upper hemisphere. As for the effect of number of turns, reduction of the co-polarised gain pattern of the SFPQHA is evident by increasing its turns from 0.375 to 0.625. The main effect of the turn variation is on the cross-polarised gain pattern where there is a significant reduction of the cross-polarised gain pattern in the lower hemisphere as the number of turns increases.

Fig. 3.5 presents the current distribution of element 1 of the 0.375 turns SFPQHA with 30° arc radial angle. In the figure, the arrows with different colour and size indicate the magnitude and direction of the surface current of the helical element. Although the element is folded, the direction of the current is the same at both element regions. Originally, an unfolded element has opposite direction at the upper and lower regions. Therefore, when the element is equally folded, the current of the whole element is directed in one direction. Due to this effect, it is expected that a SFPQHA's gain pattern to be more directional when compared to a conventional PQHA.

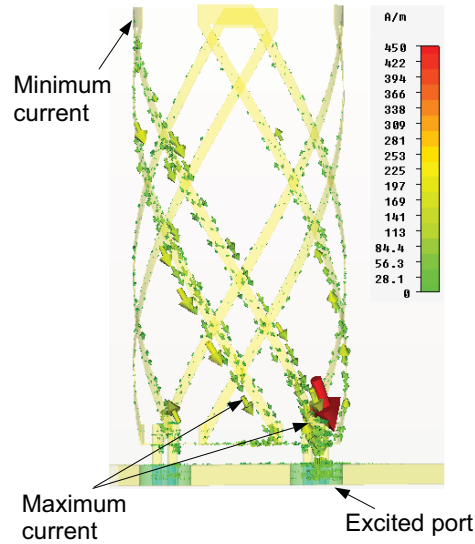


Figure 3.5: Current distribution of helical element 1 of the 0.375 turn SFPQHA with 30° arc radial angle.

Impact on radiation pattern

Effects of single folding method on the antenna's radiation pattern are studied by comparing four pattern parameters which are maximum realised gain in the upper hemisphere, 3 dB gain beamwidth, front-to-back (FB) ratio and 3 dB axial ratio (AR) beamwidth. Results for each of the pattern parameter are presented in Fig. 3.6. For turns of 0.375 and 0.5, the single folded method has positive impact on the antenna's realised gain except for arc radial angle of 60° . However, an opposite reaction occurred for the 0.625 turns where the realised gain decreases substantially with the application of the single folding method. As for the 3 dB gain beamwidth, a SFPQHA with 0.375 turns has the widest beamwidth around 120° for all arc radial angles when compared with 0.5 and 0.625 turns. However, when compared to a conventional PQHA with the same turns, it clearly shows that the single folding method reduces the pattern beamwidth significantly especially for antenna with 0.375 turns.

Fig. 3.6c and 3.6d show the effect of single folding method on the FB ratio and 3 dB AR beamwidth of the SFPQHAs' gain pattern. An increase of FB ratio is observed when the antenna is single folded although its value depends on the number of turns.

For 0.375 turns, no substantial increase of the FB ratio is evident while the opposite case occurred for the two other turns. There is a significant difference of 11 to 17 dB when comparing the FB ratio of 0.625 turns with 0.375 turns. Hence, by using higher value of turns, the backlobe of the SFPQHA pattern can be reduced substantially. For the 3 dB AR beamwidth, the single folding method has a different impact depending on the number of turns where the 0.625 turns suffers a reduction in its AR beamwidth while the 0.375 turns has the opposite reaction with an increase of its beamwidth. Even so, the 0.625 turns provides the widest AR beamwidth among the turns for all arc radial angles where the maximum value of 178° is achievable for arc radial angle of 60° . Meanwhile, the 3 dB AR beamwidth of 0.375 turns is in the range of 140° to 150° .

Impact on impedance bandwidth

The effect on the antenna impedance bandwidth due to the single folding method was investigated and comparison with impedance bandwidth of conventional PQHA is also provided for each number of turns. Table 3.2 lists the impedance bandwidth of SFPQHA for variations of number of turns and arc radial angle as well as conventional PQHA. The dash symbol (-) in the table indicates that for the corresponding number of turns and arc radial angle, the lowest value of reflection coefficient does not exceed -10 dB which implies poor impedance match between the antenna and the feed. The maximum impedance bandwidth with the value of 75 MHz is achieved by applying 0.375 turns and arc radial angle of 30° . As for the 0.625 turns, single folding method substantially increases the impedance mismatch between the antenna and the feed hence reduces the impedance bandwidth of the SFPQHA.

3.2.2 Double folded configuration

The helical elements of a PQHA can also be further folded and thus further miniaturised to construct a double folded PQHA (DFPQHA). Each helical element is divided into three equal length segmented arms which are connected via two arc radials at the top and bottom of the antenna. Instead at the bottom of the antenna, the non feed radials

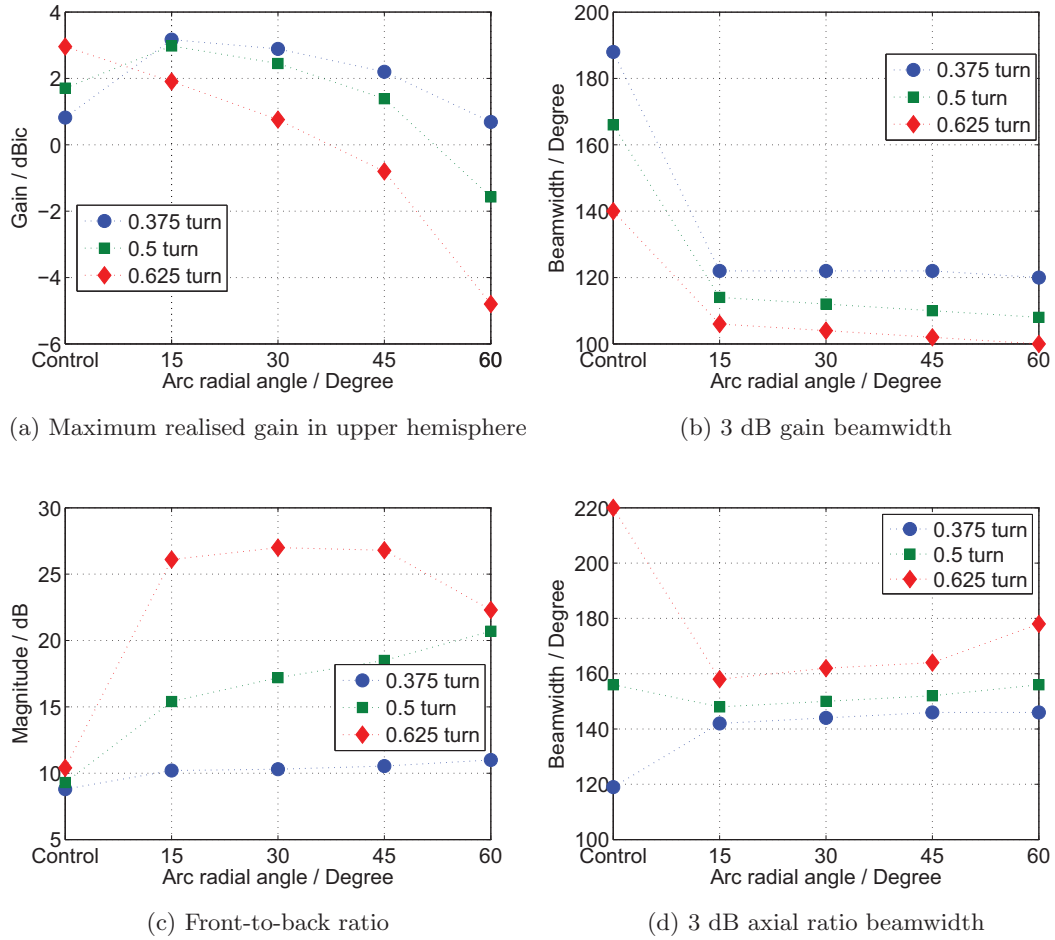


Figure 3.6: Radiation pattern properties of conventional PQHA (Control) and SF-PQHAs with different turns and arc radial angles.

Table 3.2: Reflection coefficient bandwidth $S_{11} < -10$ dB (in MHz) of single folded PQHA for different turns and arc radial angles.

Arc radial angle ω	Number of turns		
	0.375	0.5	0.625
Conventional	60	69	81
15°	72	60	12
30°	75	50	-
45°	51	-	-
60°	-	-	-

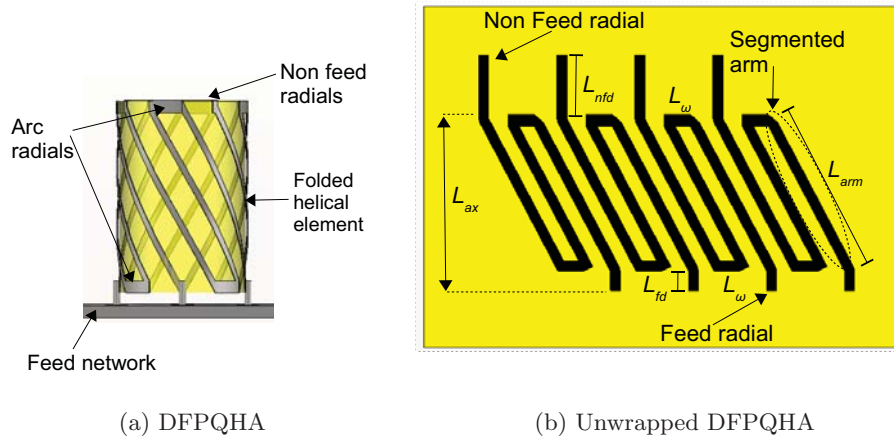


Figure 3.7: Double folded PQHA (DFPQHA) in wrapped and unwrapped configurations.

are positioned at the top of the antenna and shortened with one another as in SFPQHA. It is important to reiterate the fact that the radius of the antenna does not change with the increase of the number of folding where it remains fixed at 5 mm. Fig. 3.7 shows the configuration of double folded PQHA and its unwrapped structure.

Axial length reduction

Similar to the SFPQHA, variations of number of turns and the length of arc radial were investigated for their impacts on the DFPQHA's radiation pattern and impedance. Three numbers of turns with the values of 0.25, 0.375 and 0.5 and two values of arc radial angle which are 15° and 30° were considered in the double folded configuration. The number of turns is limited to 0.5 as higher turns are not realistic for the design of a double folded PQHA. Meanwhile, the arc radial angle is also confined to 30° as it is the maximum angle for an equal spacing between segmented arms and between helical elements.

By using the method as described in designing SFPQHA, the length of the segmented arm of a DFPQHA is calculated by deducting the length of feed radial L_{fd} , non feed radial L_{nfd} and arc radials L_{ω} from the total length of the helical element. The result from this calculation is then divided by the number of the segmented arms in a single

helical element. By studying the configuration of the unwrapped DFPQHA as provided in Fig. 3.7b, the length of the segmented arm can be written as:

$$L_{arm} = \frac{L_{ele} - (L_{fd} + L_{nfd} + 2L_{\omega})}{N_{arm}} \quad (3.3)$$

where in the case of DFPQHA, the number of segmented arm N_{arm} is three. The axial length of the DFPQHA was then calculated using the same equation (Equation (2.23)) as in SFPQHA where the length of a single segmented arm is used. The calculated axial length of DFPQHAs and their percentage of size reduction are provided in Table 3.3. As expected, utilisation of the double folding method in reducing the size of a PQHA has better miniaturisation percentage where the maximum axial length reduction of 80.9% can be achieved with 0.5 turns and arc radial angle of 30° .

Table 3.3: Axial length (in mm) of DFPQHAs and its size reduction percentage for different turns and arc radial angles.

Arc radial angle ω	Number of turns		
	0.25	0.375	0.5
Conventional	58	56	55
15°	22.8 (60.7%)	20.0 (64.3%)	16.8 (69.5%)
30°	18.0 (69.0%)	15.4 (72.5%)	10.5 (80.9%)

Simulation results

Simulated reflection coefficient of the first helical element of DFPQHAs for various numbers of turns and arc radial angles and also conventional PQHAs are shown in Fig. 3.8. Generally, the double folding method improves the impedance match of the helical elements with 50Ω feed as indicated by the values of reflection coefficient of the first helical elements for all values of turns. In contrast to the SFPQHA, an increase of the number of turns for a DFPQHA is not detrimental to its impedance match with the feeds as the reflection coefficient of a DFPQHA with 0.25 turns has nearly the same characteristics as a DFPQHA with 0.5 turns.

Comparisons of the realised elevation gain pattern of the DFPQHAs with two values of arc radial angles and conventional PQHAs for numbers of turns of 0.25, 0.375 and 0.5

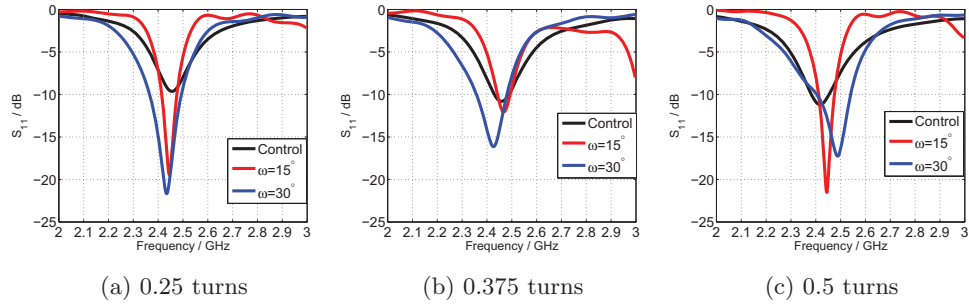


Figure 3.8: Reflection coefficient of conventional PQHA (Control) and DFPQHAs with different turns and arc radial angles.

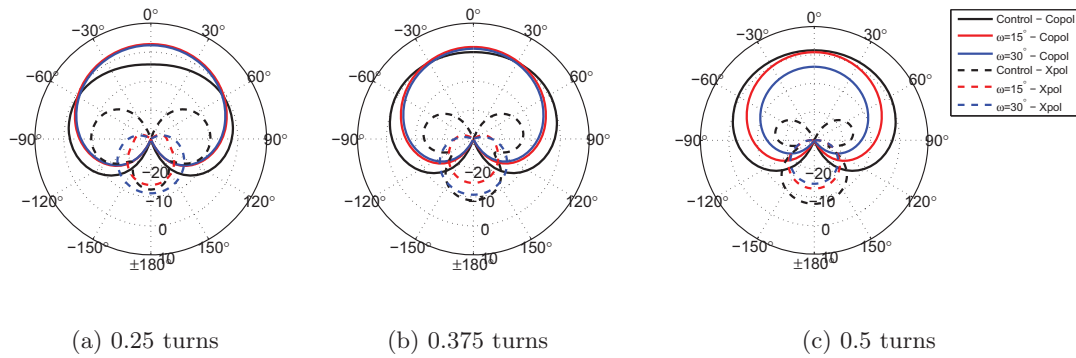


Figure 3.9: Elevation gain pattern (dBic) with $\phi = 0^\circ$ at 2.45 GHz frequency of conventional PQHA (Control) and DFPQHAs with different turns and arc radial angles.

are given in Fig. 3.9. For numbers of turns of 0.25 and 0.375, the gain patterns of the DFPQHAs are more directional when compared to the conventional PQHAs. Apart from that, the arc radial angles also have no visible effect to the gain pattern of both DFPQHAs where almost similar gain patterns are obtained for arc radial angles of 15° and 30° . Contrary to the 0.25 and 0.375 turns, significant loss of gain is evident for DFPQHA with number of turns of 0.5 as indicated in Fig. 3.9c. An increase of arc radial angle from 15° to 30° has also caused a further reduction of the gain pattern of the DFPQHA with 0.5 number of turns.

The current distribution of element 1 of the 0.25 turns DFPQHA with 30° arc radial angle is shown in Fig. 3.10 where the arrows in the figure provide the magnitude and direction of the current. For a double folded element, two folded regions have the same

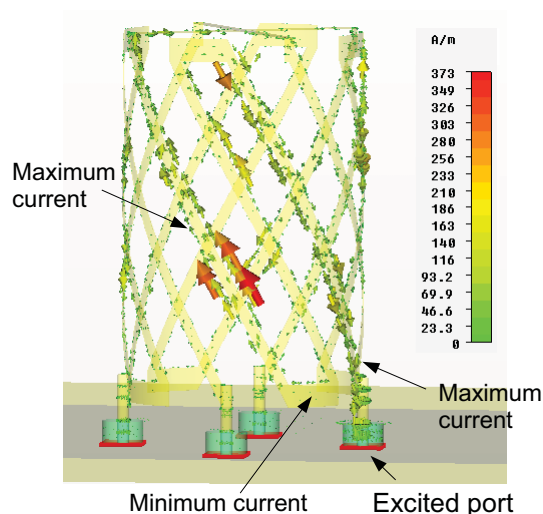


Figure 3.10: Current distribution of helical element 1 of the 0.25 turns DFPQHA with 30° arc radial angle.

current direction while the current in the first folded region has the opposite direction. Therefore, PQHAs with double folded configuration would still be able to exhibit good gain at the upper hemisphere as indicated by Fig. 3.9.

Impact on radiation pattern

Similar to the previous SFPQHA analysis, four pattern parameters which are maximum realised gain, 3 dB gain beamwidth, FB ratio and 3 dB axial ratio beamwidth are compared in Fig. 3.11 to study the effect of double folding on the antenna radiation pattern. As shown by the DFPQHAs with 0.25 and 0.375 turns, the double folding method increases the maximum realised gain of the antenna for both values of arc radial angle. However, the same can not be said about 0.5 turns PQHA where by applying the double folding method, a marked decrease of gain was obtained especially in the case of arc radial angle of 30° . One of the most pronounced effects on the antenna radiation pattern is the 3 dB gain beamwidth where it is shown in Fig. 3.11b that the gain beamwidth has reduced substantially for all cases of turns from above 160° to just below 110° .

Improvement to the FB ratio and 3 dB axial ratio beamwidth is obtained by utilising

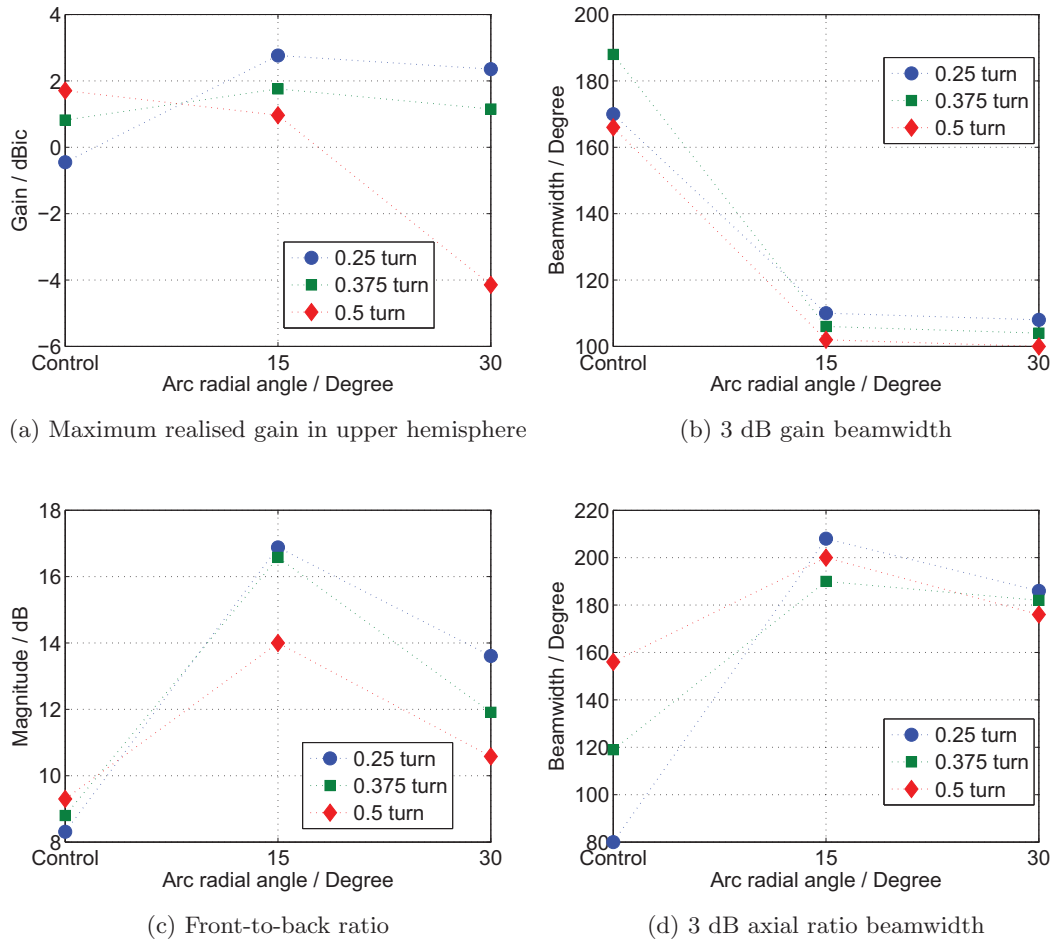


Figure 3.11: Radiation pattern properties of conventional PQHA (Control) and DF-PQHAs with different turns and arc radial angles.

double folding method. Conventional PQHAs with 0.25, 0.375 and 0.5 turns have FB ratio values below 10 dB while DFPQHAs with the same turns provide better FB ratio regardless of the arc radial angles. This is especially in the case of 0.25 turns where the FB ratio value doubles from 8.3 dB for conventional PQHA to 16.9 dB from DFPQHA with arc radial angle of 15° . As for the 3 dB AR beamwidth, it is shown in Fig. 3.11d that the double folding method increases the purity of the radiated beam as indicated by the increase of AR beamwidth for DFPQHAs of the three numbers of turns. The highest increase is for 0.25 turns DFPQHA with the value of 208° whereas for the conventional PQHA, its AR beamwidth is 80° .

Table 3.4: Reflection coefficient bandwidth $S_{11} < -10$ dB (in MHz) of double folded PQHAs for different turns and arc radial angles.

Arc radial angle ω	Number of turns		
	0.25	0.375	0.5
Conventional	-	60	69
15°	70	48	63
30°	126	120	132

Impact on impedance bandwidth

The impact of the double folding method on the antenna impedance bandwidth is given in Table 3.4 where the method has a positive effect on the impedance matching between the helical element and its 50Ω reference feed. A marked increase of bandwidth can be seen when the arc radial angle is 30° for all three values of turns. For a conventional PQHA with 0.25 turns, its bandwidth is represented by the dash (-) symbol due to its poor impedance match with the reference impedance of 50Ω . The widest impedance bandwidth with the value of 132 MHz is obtained when the DFPQHA has 0.5 turns and arc radial angle of 30° . It is however important to note that although the impedance bandwidth of such configurations is wider compared to the others, it has much lower gain pattern as shown in Fig. 3.9c which indicates reduction in its radiation efficiency.

3.2.3 Prototype fabrication

Selection of optimal design parameters

For both single and double folded design configurations, various values of turns and arc radial angles were investigated via simulations to identify their impact on the antenna's S-parameters and radiation pattern. Based on these extensive simulation runs, optimal value of both parameters for each design configuration can be obtained which offer substantial reduction in size while at the same time maximising the impedance bandwidth and gain pattern suitability.

For the single folded configuration, 0.375 turns and arc radial angle of 30° were chosen

as the optimal parameter for a SFPQHA due to its good impedance matching and gain pattern. Although the selected parameters only provide 58.0% miniaturisation from the original size, the SFPQHA has the widest impedance bandwidth at 75 MHz frequency when compared to other SFPQHAs. Higher percentages of miniaturisation that are achieved by other values of these two parameters have been shown to reduce the matching between the antenna and reference impedance of 50Ω as indicated by Table 3.2. In terms of radiation characteristics, 0.375 turns obtain the highest maximum realised gain as well as the gain beamwidth for all values of arc radial angle. However, its main disadvantages are relatively low FB ratio and slightly lower axial ratio beamwidth when compared to other set of parameters.

Based on the simulation results, the optimal number of turns and arc radial angle for the double folded configuration are taken to be 0.25 and 30° respectively. By using these two values in the design configuration, the DFPQHA exhibits excellent impedance bandwidth with the value of 126 MHz frequency as stated in Table 3.4 as well as impressive size reduction of 69.0%. Furthermore, the DFPQHA with 0.25 turns has better radiation characteristics than other values of turns which is evident in Fig. 3.11. As for the arc radial angle of 30° , it is mainly chosen due to its effect on impedance bandwidth even though it has a slightly negative impact on the radiation properties of the DFPQHA.

Antenna fabrication

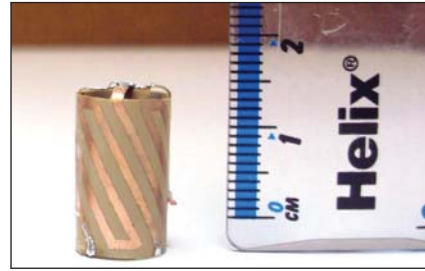
Two antenna prototypes were fabricated with one for each type of folding configuration where their designs and dimensions are based on the simulation. For the SFPQHA, the prototype was built with 0.375 turns and arc radial angle of 30° . Meanwhile, the fabricated DFPQHA has number of turns of 0.25 and 30° for the arc radial angle. Fabrication of a printed QHA or its variant can be implemented by using a standard printed circuit board method. The unwrapped designs of both SFPQHA and DFPQHA were first converted to Gerber format for fabrication process. These unwrapped antennas were then printed on a flexible circuit board supplied by Rogers Corporation. Specifications of the flexible printed circuit board are provided in Table 3.5. In order

Table 3.5: Specifications of the flexible printed circuit board for antenna fabrication.

Layer	Material	Thickness (μm)	Dielectric constant (1 GHz)	Loss tangent (1 GHz)	Conductivity (S m^{-1})
Insulating	Polyimide - Kapton	50	3.0	0.01	-
Conducting	Copper	17.5	-	-	5.8×10^7



(a) SFPQHA



(b) DFPQHA

Figure 3.12: The fabricated SFPQHA and DFPQHA.

to create the cylindrical structure of the antenna, the printed board was wrapped from one end to the other where the resultant structure will have a radius of 5 cm and the targeted axial length. Apart from that, the non feed radials were also connected to each other where for SFPQHA and DFPQHA, they are connected at the bottom and top of the structure respectively. The fabricated SFPQHA and DFPQHA are shown in Fig. 3.12a and Fig. 3.12b respectively.

Feed circuit design and fabrication

As stated in Section 2.3.2, each helical element of a SFPQHA or DFPQHA needs to be fed with an equal amplitude and 90° phase difference. For a RHCP PQHA, the direction of the phase difference is counterclockwise when looking from the top of the antenna. Apart from that, since the designed antennas have been optimised with reference impedance of 50Ω in the simulations, the feed network will also be designed with 50Ω as the output impedance. Therefore, the feed circuit must be designed to fulfill these requirements while at the same time it needs to be as compact as possible.

A cascaded Wilkinson power divider network that consists of three equal power dividers

was used to feed all four helical elements with equal amplitude. The feed network was configured by connecting two power dividers to each output of the first single power divider thus creating four equal amplitude feeds for the antenna. Meanwhile, the required quadrature phase difference for each helical element was achieved by simply varying the track length of each feed after the power divider network. Without any miniaturisation, the resultant feed network is too large for the purpose of this work. Therefore, in order to reduce the size of the feed network, two steps were taken which are the use of high relative permittivity substrate and folding of the Wilkinson power divider. The high permittivity material used as the board substrate is ceramic loaded laminate CER-10 from Taconic Corporation with relative permittivity of 10 which significantly reduces the track dimension of the feeds. Then, the size of each Wilkinson power divider was further reduced by folding its quarter wavelength arms. This requires simulations to be conducted to get the most optimum design of a folded compact Wilkinson power divider.

Configuration of the optimised feed network was presented in Fig. 3.13. Evaluation of the designed feed network was done by looking at the reflection and transmission coefficient of the feed circuit input port and its four feed ports. Ideally, the reflection coefficients of the all input and feed ports must be as low as possible at the targeted frequency and the transmission coefficient of each output port needs to be at -6 dB for equal power transfer. The simulated reflection coefficients of the input port and feed ports are given in Fig. 3.14a which shows good impedance match between the ports with reference impedance of 50Ω . As for the transmission coefficient, Fig. 3.14b indicates that each feed port has nearly the same value at the targeted frequency. This shows that the designed feed network is able provide equal power to all four helical elements of a PQHA.

3.2.4 Scattering parameters measurement

Measurement of the scattering parameters (S-parameters) of each helical element of the fabricated SFPQHA and DFPQHA was carried out using a vector network analyser and a specially designed measurement circuit. In this S-parameters measurement, the re-

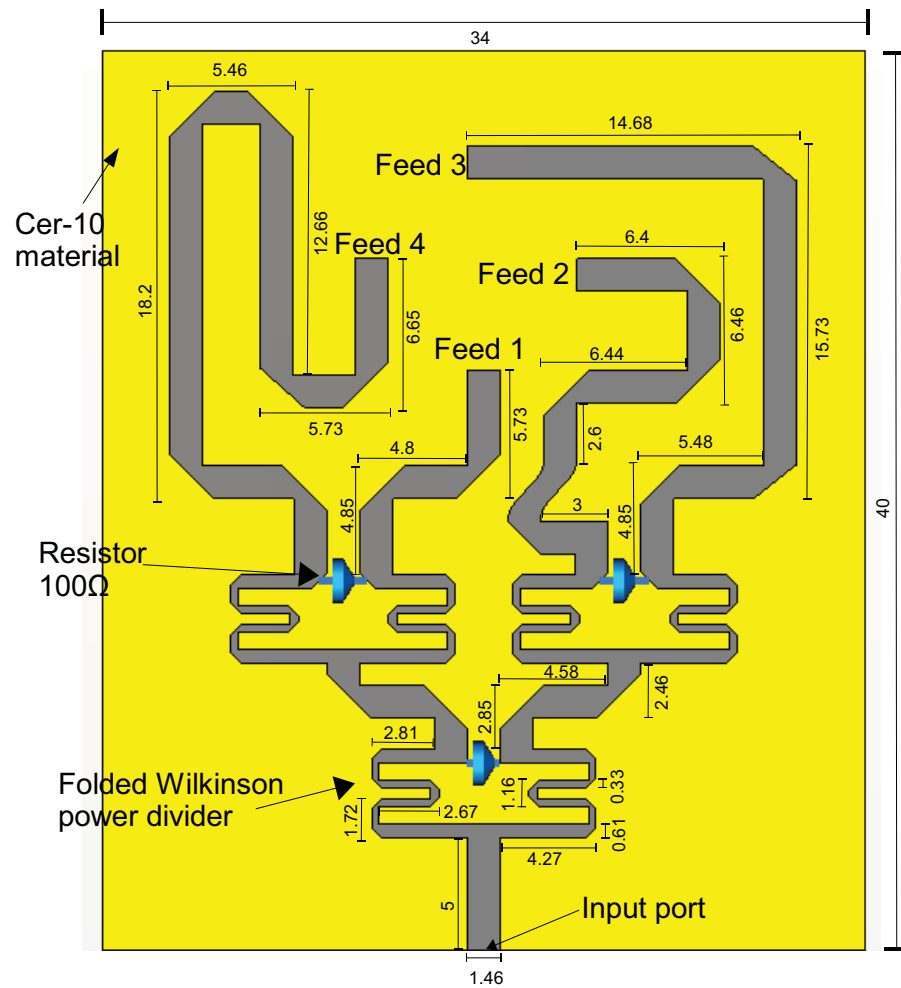


Figure 3.13: Configuration of the designed feed network for PQHA, SFPQHA and DFPQHA with 5 mm radius (dimension in mm).

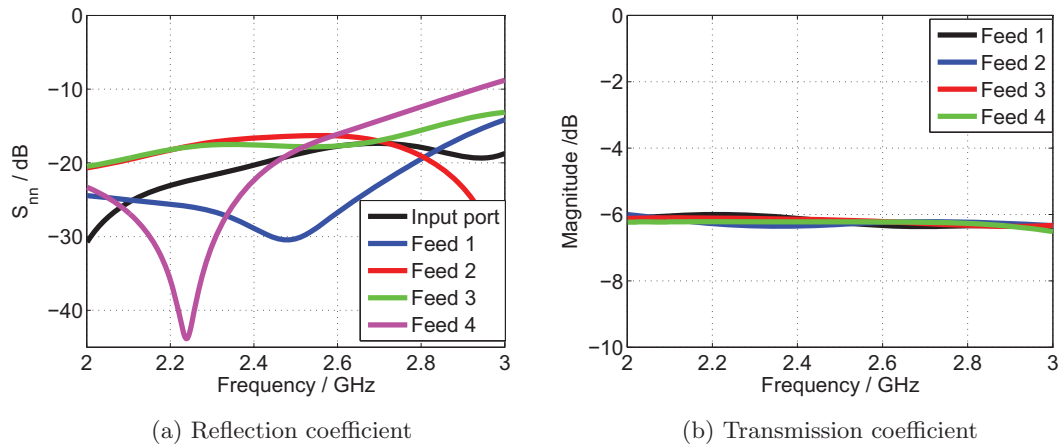


Figure 3.14: Simulated reflection and transmission coefficients of input port and feed ports of the designed feed network.

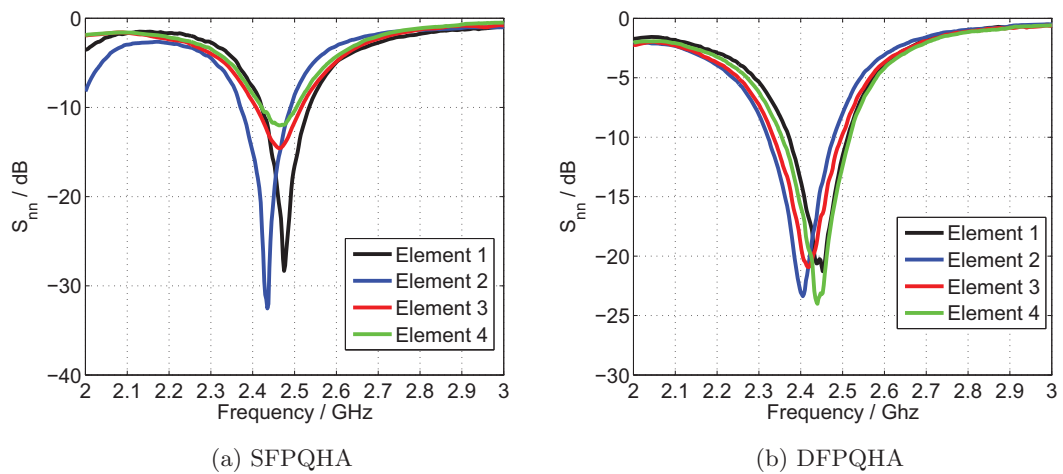


Figure 3.15: Measured reflection coefficient of each element on the fabricated SFPQHA and DFPQHA.

flection coefficient of the helical elements of both antennas which signifies the matching of the radiating element with its reference impedance is considered as the most important characteristic to be evaluated. Fig. 3.15a shows the reflection coefficient of each element of the fabricated SFPQHA which is designed to operate in 2.45 GHz frequency. Although there is a difference in the reflection coefficient value of the elements in the presented frequency range, each element exhibits good impedance matching with the value of reflection coefficient lower than -10 dB at the targeted frequency. As for the DFPQHA, it is indicated in Fig. 3.15b that each element has almost identical reflection coefficient characteristic that demonstrates excellent impedance match with reference impedance of 50Ω .

3.2.5 Radiation pattern measurement

Co and cross-polarised elevation gain patterns at azimuth angles ϕ of 0° and 90° of both fabricated SFPQHA and DFPQHA were measured and their results were compared with the simulated patterns. In Fig. 3.16, the measured co-polarised elevation gain pattern at both azimuth angles follows closely with the simulated patterns apart from the existence of co-polarised pattern backlobe which is not indicated by the simulation. As for the cross-polarised pattern, the simulation seems to overestimate its value in the lower hemisphere where the measurement provides a much lower cross-polarised gain. The measurement also indicated that the cross-polarised pattern in the upper hemisphere is higher when compared to the simulated result. Meanwhile, Fig. 3.17 shows almost the same behaviour of the DFPQHA's measured patterns where the measurement shows a significant co-polarised backlobe at the lower hemisphere and an increase of cross-polarised gain in the upper hemisphere.

3.3 Miniaturisation of 0.75λ PQHA

Aside from the 0.5λ PQHA, miniaturisation of a 0.75λ PQHA using a slightly different method from the one introduced in the previous subsection was also investigated in this research work. Due to the odd multiplication of quarter wavelength of the helical

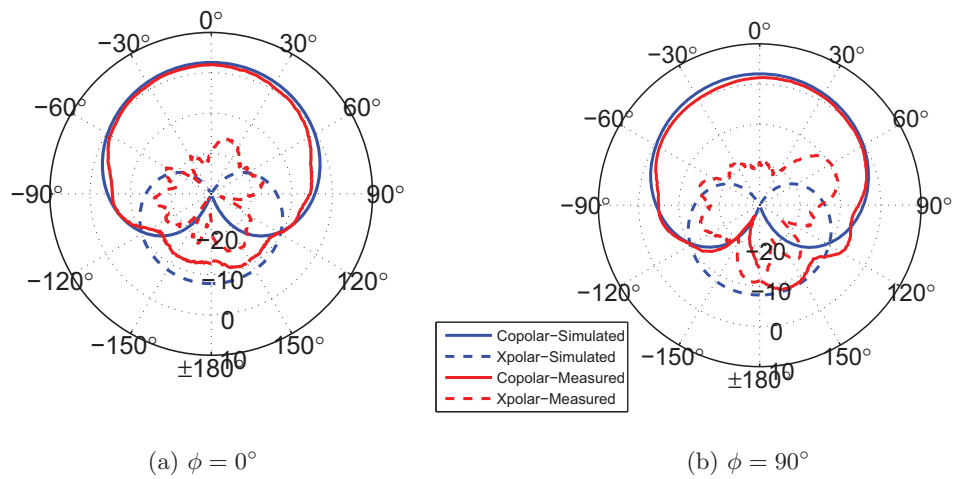


Figure 3.16: Simulated and measured elevation gain patterns (dBic) of the fabricated SFPQHA.

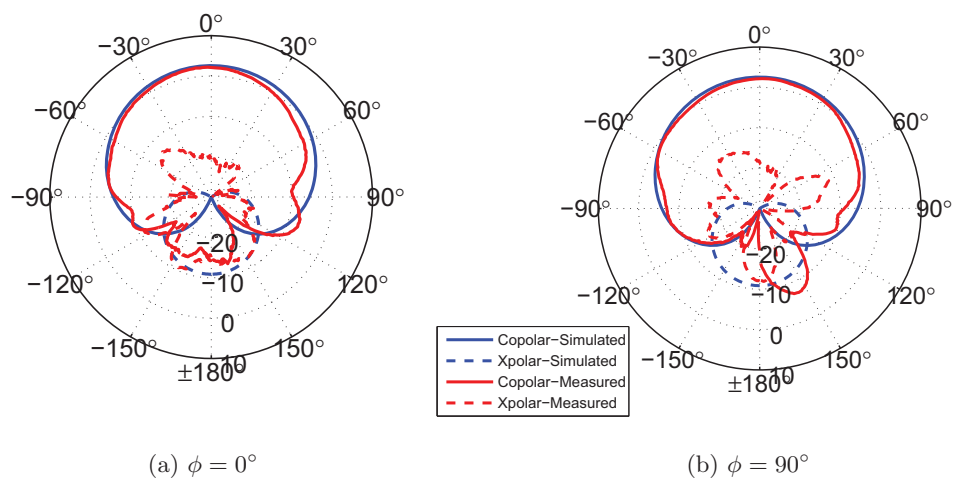


Figure 3.17: Simulated and measured elevation gain patterns (dBic) of the fabricated DFPQHA.

element length, the structure of 0.75λ PQHA requires no connection of the non feed radials. The basic parameters of the 0.75λ PQHA are as follows:

- Targeted resonant frequency of 2.4 GHz.
- Antenna radius of 10 mm.
- Initial element length L_{ele} of 93.75 mm which corresponds to 0.75λ at 2.4 GHz frequency. In each simulation, the element length is optimised to obtain the lowest possible reflection coefficient at the resonant frequency.
- Helical element width of 1 mm.
- Antenna is RHCP which means that the direction of winding is clockwise when looking from the top of the antenna.

The selection of 2.4 GHz as the resonant frequency is due to the same reason as explained in the previous section of the 0.5λ PQHA miniaturisation. However, the antenna radius in this section is twice the value of the one used for the 0.5λ PQHA as the antenna is designed for vehicular application which provide a much bigger space than a handheld device. Futhermore, a bigger radius is also needed in order to further reduce the antenna's axial length since the helical element length has increased to 0.75λ of 93.75 mm.

3.3.1 Element folding and meandering method

This method combines two miniaturisation techniques namely element folding that was used earlier for 0.5λ PQHA miniaturisation and meandering of the helical elements. The helical elements of a PQHA are folded to create two segments, which are straight segment (SS) and meandered segment (MS). An example of a folded meandered PQHA (FMPQHA) and its unwrapped structure is given in Fig. 3.18.

Dimension of folded meandered PQHA structure

In order to ease the design process of a FMPQHA, the length of the helical elements is divided into five components, which are a , b , c , d and e . The length of the straight segment is represented by a while the length of the meandered segment is a summation

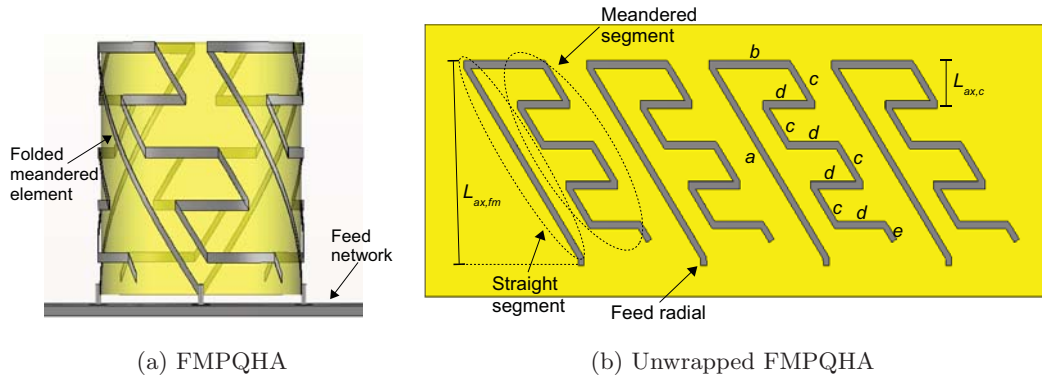


Figure 3.18: Folded meandered PQHA in wrapped and unwrapped configurations

of b , c , d and e . Contrary to the previous element folding method where the same number of turns was used after the helical elements were folded, the turn of the helical elements in this method was modified so that the pitch angle of the helical elements remains the same as the conventional PQHA. Therefore, the calculation of the axial length of a FMPQHA which is based on the value of a can be done by using the following steps:

1. The turn of straight segment N_{ss} is calculated based on the conventional PQHA's pitch angle φ_p using the following equation (see Appendix A)

$$N_{ss} = \frac{a}{2\pi r \sqrt{\tan^2 \varphi_p + 1}}. \quad (3.4)$$

2. Using the calculated N_{ss} , the axial length of a FMPQHA $L_{ax,fm}$ is then computed by the following equation which is identical to Equation (2.23) except that the length of straight segment is used instead of the total element length

$$L_{ax,fm} = N_{ss} \sqrt{\frac{1}{N_{ss}^2} (a)^2 - (2\pi r)^2}. \quad (3.5)$$

As for the meandered segment where its length consists of a combination of b , c , d and e , the values of b and d depend on the design of the meandering component of the antenna. In this case, their values were taken to be $1/6$ and $1/9$ (60° and 40° in angular form) of the antenna circumference respectively. Therefore, the meandered segment length L_{ms} can be written as:

$$L_{ms} = b + N_c c + N_d d \quad (3.6)$$

where N_d denotes the number of horizontal component d and N_c is the number of vertical component c . After a simple rearrangement of Equation (3.6), the length of vertical component c is given as:

$$c = \frac{L_{ms} - (b + N_d d)}{N_c} \quad (3.7)$$

Then, the axial length of the meandered segment's vertical component $L_{ax,c}$ is computed based on the same technique as shown in calculating the axial length of a FMPQHA. Finally, the e component is provided as an optimisation parameter in simulations to get the antenna to resonant at the targeted frequency.

Axial length reduction

Reduction of the axial length of a PQHA that can be achieved by using this method is mainly determined by the ratio of the length of the straight segment and the length of the meandered segment. Therefore, three length ratio with the values of 2, 1 and 0.5 were investigated where in the case of ratio of 2, the length of the straight segment is twice of the meandered segment. As for the ratio value of 1, the length of both segments is the same while the length of the straight segment is half of the meandered segment for the case of ratio 0.5. Therefore, FMPQHAs with the ratio of 2, 1 and 0.5 are labelled as FMPQHA 2, FMPQHA 1 and FMPQHA 0.5 respectively. Apart from that, the designed FMPQHAs are also compared with a conventional PQHA without any miniaturisation in terms of their size reduction and effects on the antennas radiation and impedance properties. Table 3.6 provides various structural properties of the three designed FMPQHAs and their size reductions when compared with a conventional PQHA. For the conventional PQHA, the length of its meandered segment (MS) and its size reduction are represented by a dash (-) symbol which indicate that both values are non existant since it consisting of straight segment entirely.

3.3.2 Simulation results

Simulation results of the three FMPQHAs and one conventional PQHA in the form of reflection coefficient of the helical element of the antennas and elevation gain pattern

Table 3.6: Structural dimensions of a conventional PQHA and FMPQHAs with their size reduction percentage.

Antenna	Length of SS (mm)	Length of MS (mm)	Pitch angle φ_p	Turns	Axial length (mm)	Size reduction
Conventional	85.2	-	59.1°	0.75	68.7	-
FMPQHA 2	62.7	30.7	59.1°	0.49	53.8	21.7%
FMPQHA 1	45.7	44.1	59.1°	0.37	38.5	44.0%
FMPQHA 0.5	30.6	62.6	59.1°	0.24	25.2	63.3%

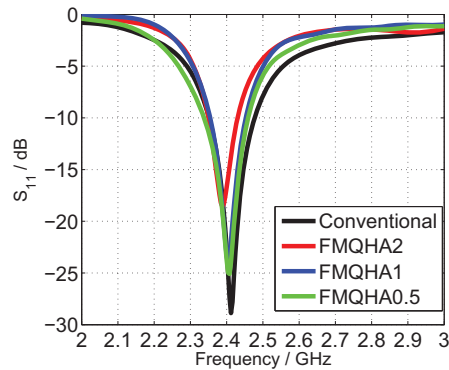


Figure 3.19: Reflection coefficient of the conventional PQHA and FMPQHAs.

are given in Fig. 3.19 and Fig. 3.20 respectively. It clearly shows that the miniaturisation method has no significant impact on the antenna's impedance matching with reference impedance of 50Ω as indicated by the reflection coefficient result. The antenna impedance bandwidth which is defined as the bandwidth for reflection coefficient below -10 dB, of the conventional PQHA, FMPQHA 2, FMPQHA 1 and FMPQHA 0.5 are given as 124 MHz, 80 MHz, 96 MHz and 120 MHz respectively. As for the current distribution of the FMPQHA, an example for the FMPQHA 0.5 is given in Fig. 3.21. The vertical segments of the FMPQHA 0.5 has the same direction for their current which explains the increase of gain at the boresight of the FMPQHA 0.5.

Comparison of the radiation properties of the three FMPQHAs and one conventional PQHA is provided in Table 3.7 where four parameters are highlighted which are maximum gain in upper hemisphere, front-to-back ratio, 3 dB gain beamwidth and 3 dB

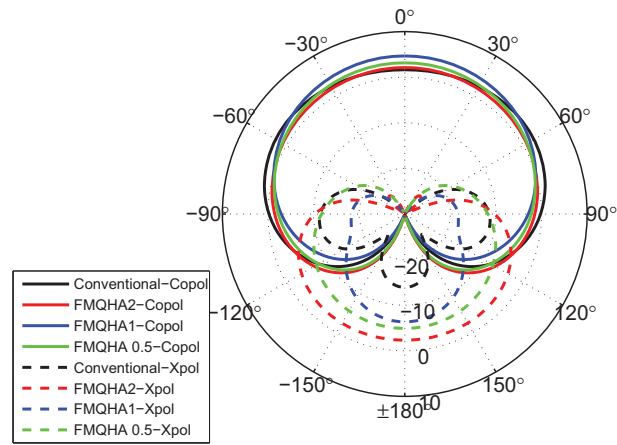


Figure 3.20: Elevation gain patterns (dBic) with $\phi = 0^\circ$ at 2.4 GHz frequency of the conventional PQHA and FMPQHAs.

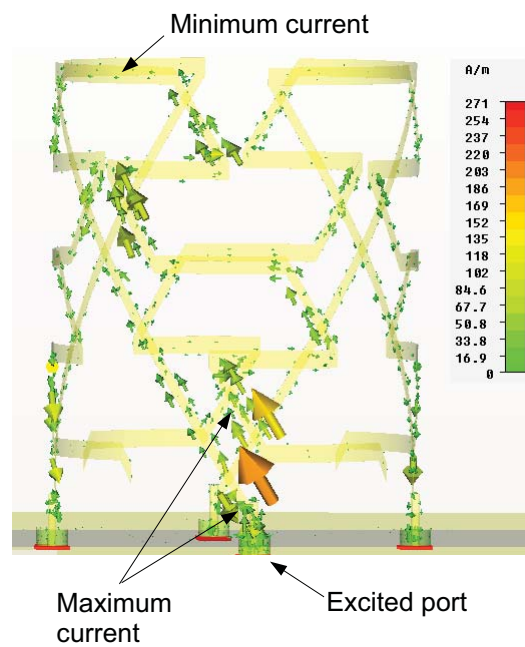


Figure 3.21: Current distribution of helical element 1 of the FMPQHA 0.5.

Table 3.7: Radiation pattern properties of the three designed FMPQHAs and one conventional PQHA.

Antenna	Max. gain (dBic) and its elevation angle	Front-to-back ratio (dB)	3 dB gain beamwidth	3 dB Axial ratio beamwidth
Conventional	2.83 / 50°	15.6	184°	154°
FMPQHA 2	2.10 / 0°	4.0	180°	158°
FMPQHA 1	4.65 / 0°	11.0	122°	182°
FMPQHA 0.5	3.14 / 0°	8.0	142°	144°

axial ratio beamwidth. For the maximum gain, the FMPQHA 1 gives the highest gain of 4.65 dBic at the antenna boresight while the conventional antenna has its maximum gain of 2.83 dBic at 50° co-elevation angle from the zenith. The miniaturisation also has a negative effect to the 3 dB gain beamwidth of the radiation pattern where there is a sharp decrease from 184° for conventional PQHA to 142° for FMPQHA 0.5. These results clearly show that the element folding and meandering technique causes the radiation pattern of the antenna to be more directional at the boresight. The miniaturisation also increases the cross polarised gain at the lower hemisphere as indicated by Fig. 3.20 and the decrease of FB ratio from 15.6 dB for conventional PQHA to 8.0 dB for FMPQHA 0.5.

3.3.3 Prototype fabrication

Design parameters of the FMPQHA 0.5 was selected for fabrication based on its trade-offs between percentage of miniaturisation and effect on the impedance and radiation characteristics. For the FMPQHA 0.5, a good miniaturisation percentage of 63.3% from conventional PQHA can be achieved without substantial degradation on its radiation pattern and impedance. It has been shown in Fig. 3.19 that the miniaturisation method has no visible impact on the simulated reflection coefficient of each FMPQHA. Therefore, this selection of FMPQHA 0.5 was undertaken mainly due to its excellent miniaturisation percentage while at the same time exhibits comparable radiation characteristics as indicated in Table 3.7.

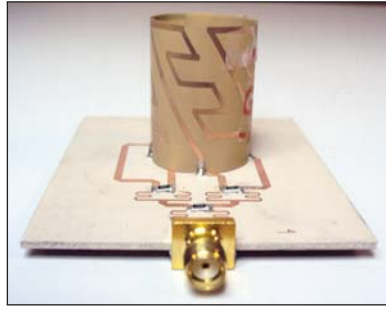


Figure 3.22: The fabricated FMPQHA.

Antenna fabrication

The miniaturised antenna was fabricated using the same method and material as described in the fabrication process of the SFPQHA and DFPQHA in Section 3.2.3. Since the antenna is based on 0.75λ element length, the non feed radials of the helical elements are not required to be connected with each other. The fabricated FMPQHA 0.5 with its unwrapped structure is shown in Fig. 3.22.

Feed circuit design and fabrication

The basic design parameters of the FMPQHA's feed network are the same as the SFPQHA as in Section 3.2.3 but with one important difference which is the antenna radius is 10 mm instead of 5 mm. Therefore, the output feed tracks of the cascaded Wilkinson power dividers need to be redesigned so that they can be connected to an antenna with radius of 10 mm. Although each port exhibits different characteristic of reflection coefficient as shown in Fig. 3.23a, all feed ports provide sufficient impedance match to the antenna with reflection coefficient values below -10 dB at the targeted frequency. Meanwhile, Fig. 3.23b shows the transmission coefficient of each feed that indicates the quality of power transfer between the input port and the feed ports. There is a slight reduction of 0.9 dB for the transmission coefficient of Feed 4 at 2.4 GHz frequency when compared to the ideal value of -6 dB for equal power between four feeds.

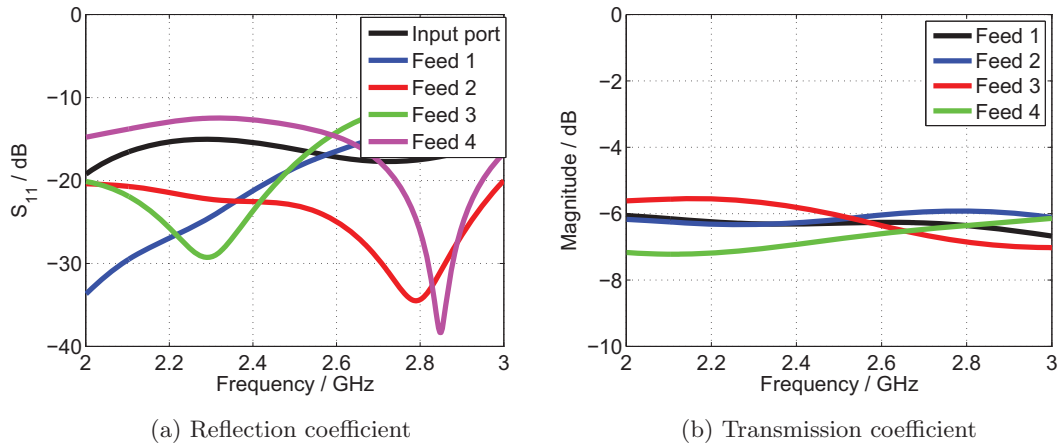


Figure 3.23: Simulated reflection and transmission coefficients of input port and feed ports of the designed feed network.

3.3.4 Scattering parameters measurement

Similar to the miniaturisation of the 0.5 wavelength antenna, the reflection coefficient of each helical element of the fabricated FMPQHA was measured and plotted in Fig. 3.24. At the targeted frequency of 2.4 GHz, each element has good and almost identical impedance matching as implied by the value of each element's reflection coefficient.

3.3.5 Radiation pattern measurement

Fig. 3.25 presents the simulated and measured elevation gain patterns at azimuth angles ϕ of 0° and 90° of the fabricated FMPQHA. Based on this comparison, there is a very slight discrepancy between the simulated and measured co-polarised patterns in the range of 30° to 110° . Furthermore, it is also observed in the measurement that the co-polarised pattern has pronounced sidelobe in the lower hemisphere which was not indicated by the simulation. In the lower hemisphere, the measured cross-polarised gain pattern at both azimuth angles is significantly lower when compared to the simulated patterns. However, there is a slight increase of cross-polarised gain in the upper hemisphere especially at the direction of the antenna boresight.

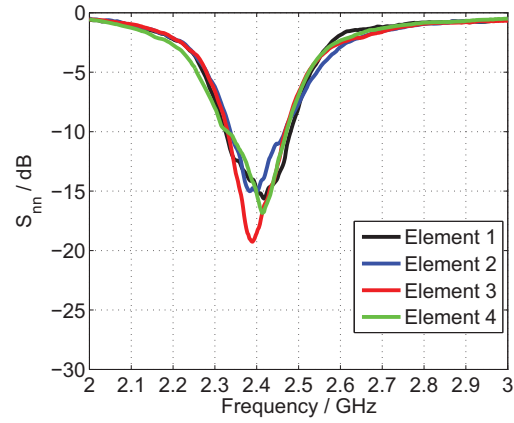


Figure 3.24: Measured reflection coefficient of each element on the fabricated FM-PQHA.

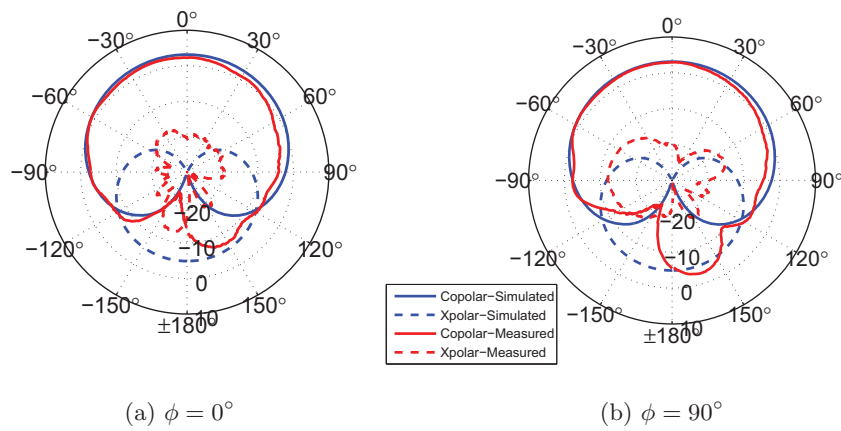


Figure 3.25: Simulated and measured elevation gain patterns (dBic) of the fabricated FMPQHA.

3.4 Summary

Two miniaturisation methods which are element folding and combination of element folding and meandering have been proposed for 0.5λ and 0.75λ quadrifilar helix antennas respectively. Evaluation of these methods was conducted using simulations by studying the size reduction effect on the antenna's radiation pattern and scattering parameters and later validated by measurement of selected fabricated antennas. For a 0.5λ PQHA, although a much higher miniaturisation percentage than the one selected for fabrication can be obtained, attention must be given on its negative impact on the antenna's radiation and impedance properties to avoid having an extremely compact antenna but with undesirable gain pattern and bandwidth. Meanwhile, the element folding and meandering method has been shown to be able to reduce the axial length of a 0.75λ PQHA substantially. However, successful implementation of this method requires optimisation of various physical dimensions especially at the meandered segment which necessitates extensive simulations and measurements.

One prototype for each proposed design of the 0.5λ and 0.75λ miniaturised PQHAs has been fabricated and its radiation pattern and S-parameters were measured and compared with the simulation results. One common disadvantage of these miniaturisation approaches is the resultant radiation pattern of the compact PQHAs becomes more directional as implied by the 3 dB gain beamwidth reduction. For the 0.5λ antenna, the element folding method is able to widen the impedance bandwidth of the helical elements which has been demonstrated by the double folding configuration (Table 3.4).

The next step in enhancing the PQHA's suitability as the preferred antenna for LMS MIMO receiver is for the antenna to develop a dual circular polarisation capability. The newly designed miniaturised PQHAs can then be used as the basic component to produce an antenna system that capable in transmitting and receiving both circular polarisations.

Chapter 4

Dual circular polarisation design using printed quadrifilar helix antenna

4.1 Introduction

The main requirement of an antenna system in order to be utilised in a land mobile satellite (LMS) MIMO system is the ability to transmit and receive in two orthogonal circular polarisations, which are right hand circular polarisation (RHCP) and left hand circular polarisation (LHCP). Therefore, in this chapter, several dual polarised configurations for three different printed quadrifilar helix antennas (PQHA) are proposed and their characteristics were examined by conducting extensive simulation runs. Based on the simulation results, selected designs for each configuration were fabricated and their scattering parameters (S-parameters) and radiation pattern were measured for comparison.

The first dual polarised configuration, called “inside-out” is for a conventional PQHAs where one PQHA is placed at the centre of another PQHA with larger radius. In this configuration, the major concern is to balance the need in reducing the mutual coupling between the two antennas while at the same time, striving for the most compact

size. The next configuration is the vertical array of two folded meandered PQHAs (FMPQHA) with orthogonal polarisations where one FMPQHA together with its feed network is stacked on top of another FMPQHA. As for the last configuration, a horizontal array of single folded PQHAs (SFPQHA) also with opposing polarisations was designed and its properties in terms of S-parameters and radiation pattern were investigated.

4.2 Inside-out configuration of dual polarised CPQHA

4.2.1 Design configuration

The proposed design of a dual polarised contrawound printed quadrifilar helix antenna (CPQHA) is based on the combination of two PQHAs with opposite helical winding direction as presented in Fig. 4.1. In order to reduce the size of such combination, one antenna structure is positioned inside of the other antenna. A major disadvantage of the configuration is the strong mutual coupling between the antenna elements due to their close proximity, which reduces the efficiency of the antennas and distorts their radiation patterns. It is known that mutual coupling is inversely proportional to the distance between elements and its effect can be reduced by increasing the distance between antenna elements. Mutual coupling reduction for this configuration is achieved by increasing the radius of the outer PQHA while keeping the radius of the inner PQHA fixed. As the radius of the outer PQHA increases, its axial length reduces as indicated by Equation (2.23). This technique, however, is limited by the maximum radius achievable by the element length of the PQHA.

A parametric study to find the optimum distance between inner and outer PQHAs operating at 2 GHz frequency was carried out by conducting electromagnetic simulation using CST Microwave Studio[®]. The radius of the inner PQHA is fixed at 7 mm while the radius of the outer PQHA is varied from 17 mm to 22 mm. This variation of outer PQHA radius corresponds to separation distance between 0.067λ and 0.1λ at 2 GHz frequency. The radius of inner PQHA is chosen at 7 mm because it is the optimum radius for PQHA to radiate upper hemispherical circular polarised pattern. Without

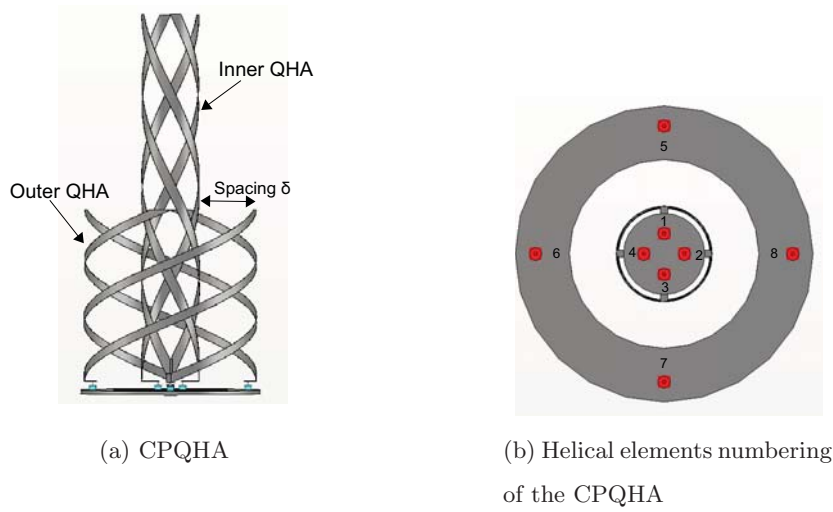


Figure 4.1: Configuration of a CPQHA and its helical elements numbering.

Table 4.1: Physical parameters of simulated CPQHAs.

Antenna	Radius (mm)	Turn	Element length (mm)	Axial length (mm)	Separation distance δ (mm)
Inner PQHA	7	1	104.6	90	-
Outer PQHA	17	0.75	109.6	70	10
	18	0.75	109.4	64	11
	19	0.75	109.9	58	12
	20	0.75	109.9	50	13
	21	0.75	110.7	42	14
	22	0.75	111.1	30	15

any loss of generality, the inner PQHA was configured to radiate in right hand circular polarisation while the outer PQHA radiate the opposite polarisation which is left hand circular. Table 4.1 summarises the physical parameters of simulated inner PQHA with a varying radius of the outer PQHA.

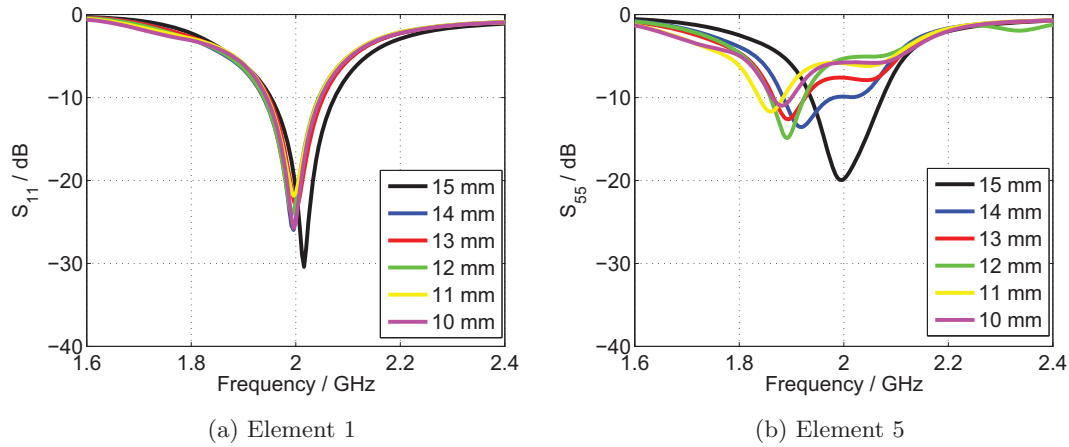


Figure 4.2: Reflection coefficients of element 1 on the inner PQHA and element 5 on the outer PQHA with varying δ .

4.2.2 Simulation results

Reflection coefficient and mutual coupling

Evaluation of the reflection coefficient of the CPQHA with varying radius of the outer PQHA from 17 mm to 22 mm (separation spacing from 10 mm to 15 mm) was carried out by comparing the simulated reflection coefficient of element 1 on the inner PQHA and element 5 on the outer PQHA as shown in Fig. 4.2. It can be assumed that element 1 on the inner PQHA and element 5 on the outer PQHA are the representation of all elements in each PQHA since there is a perfect repeatability of the helical element construction in simulation. Quite clearly it can be seen that reflection coefficient of the inner PQHA elements are very much unaffected by the mutual coupling while for the outer PQHA, reflection coefficient better than -10 dB can be achieved at the separation spacing of 15 mm. Therefore, for the outer PQHA to have good impedance match, a separation distance of 15 mm is needed between inner and outer PQHAs.

The mutual coupling effect of the two PQHAs are represented by the isolation between the helical elements on the inner PQHA and the helical elements on the outer PQHA. In our case, the isolation between element 1 on the inner PQHA and element 5 on the outer PQHA have been chosen as a representation of the mutual coupling effect due to

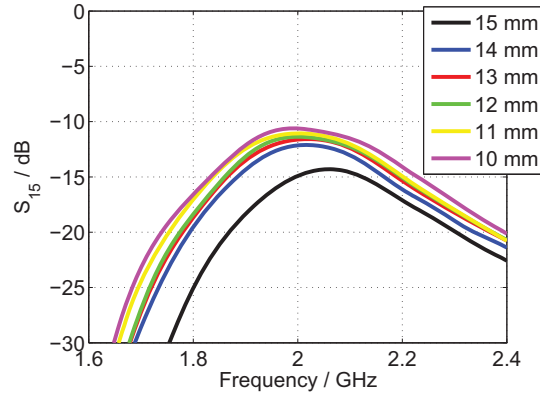


Figure 4.3: Isolation between the element 1 on the inner PQHA and the element 5 on the outer PQHA with varying δ .

the fact that it gives the highest value among all element combinations. The effect of varying the radius of the outer PQHA from 17 mm to 22 mm, which corresponds to separation distance of 10 mm to 15 mm on the transmission coefficient was investigated and its result is presented in Fig. 4.3.

Radiation pattern

The simulated co and cross-polarised elevation gain patterns at azimuth angle $\phi = 0^\circ$ of the inner and outer PQHAs for separation spacing of 10 mm and 15 mm are given in Fig. 4.4. These two values of spacing are chosen to better illustrate the effect of spacing on the co and cross-polarised patterns of the PQHA. One main characteristic of the CPQHA radiation patterns is the high cross-polarised radiation for both PQHAs at the lower hemisphere even at separation spacing of 15 mm. Although the cross-polarised patterns are high, its effect on the CPQHA applicability is small due to the opposite direction of the cross-polarised beam. The co-polarised radiation patterns for inner and outer PQHAs are clearly improved by increasing the separation spacing between the two structures. An increase in the co-polar gain patterns is evident for both PQHAs when the spacing is increased from 10 mm to 15 mm. However, due to the increased radius of the outer PQHA, its co-polar pattern becomes more directional as its 3 dB gain beamwidth decreases from 186° to 101° .

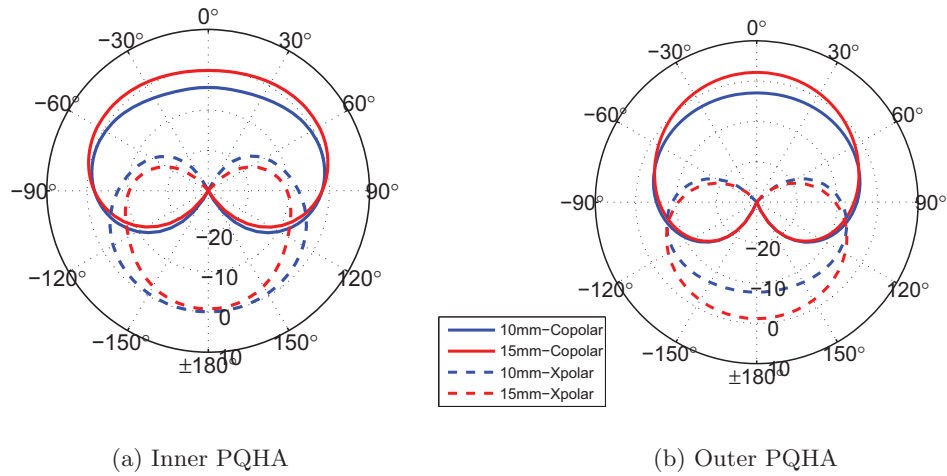


Figure 4.4: Elevation gain patterns (dBic) with $\phi = 0^\circ$ at 2 GHz frequency of the inner and outer PQHAs with varying δ .

4.2.3 Fabrication and measurement

The dual circularly polarised CPQHA with separation distance of 15 mm was chosen for prototype fabrication due to its good simulated reflection coefficient of the helical elements and low mutual coupling between inner and outer PQHAs. Each PQHA in the CPQHA was fabricated using the same method as described in Section 3.2.3. The CPQHA was fed using thin semi rigid coaxial cable to a combination of hybrid couplers to create the required phase difference between the helical elements.

The S-parameters of the fabricated CPQHA elements were measured using vector network analyser and compared with the simulated results. As before, element 1 and element 5 were selected as the reference for the inner and outer PQHA elements, respectively. The simulated and measured reflection coefficients of the element 1 and 5 of the CPQHA with separation distance of 15mm are shown in Fig. 4.6a. The discrepancy between simulated and measured reflection coefficients of element 5 of the outer PQHA up to 10 dB are most likely due to imperfection in fabricating the outer PQHA, which caused the element impedance to deviate slightly. Mutual coupling effects of elements 1 and 5 were also investigated by comparing the simulated and measured results. They show good agreement between simulated and measured values of the coupling between



Figure 4.5: The fabricated CPQHA.

inner and outer PQHA, which is indicated by the isolation between element 1 with element 5 as presented in Fig. 4.6b.

Measurement of the radiation pattern of the fabricated CPQHA was conducted in an anechoic chamber and its results were compared with the simulation as shown in Fig. 4.7. For the inner PQHA, the measured elevation pattern has a slightly directional co-polarised beam and much lower cross-polarised beam at the lower hemisphere when compared with simulated pattern. Meanwhile, the measured co-polarised elevation pattern of the outer PQHA has a pronounced backlobe which is not present in the simulation. The cross-polarised beam of the outer PQHA also has a lower value in the lower hemisphere when compared with the simulation. The main discrepancy between the simulated and measured pattern is the cross-polarised beam of both PQHAs where the measured cross-polarised pattern has lower value when compared to the simulated pattern. This difference may be due to the effect of placing a combination of hybrid couplers at the back of the CPQHA, which is necessary for the feeding requirement of the PQHAs.

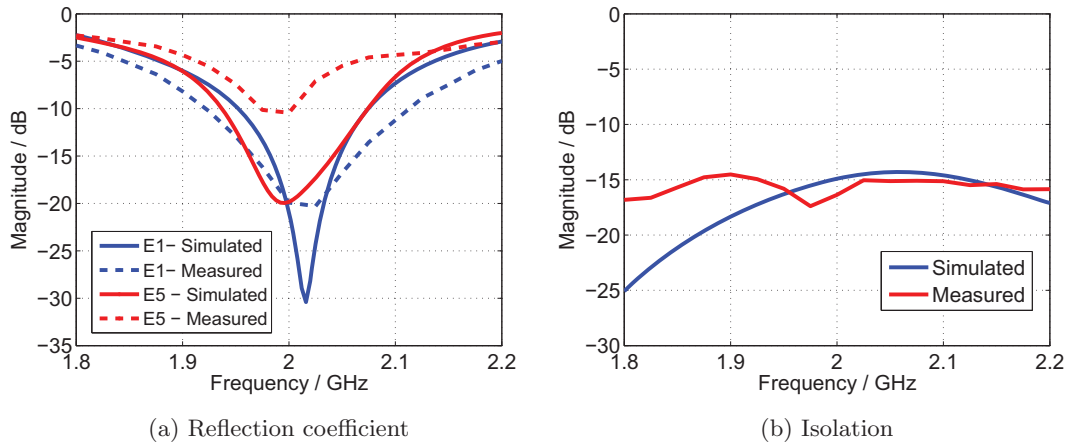


Figure 4.6: Simulated and measured reflection coefficient and isolation of the element 1 (E1) and the element 5 (E5) on the fabricated CPQHA.

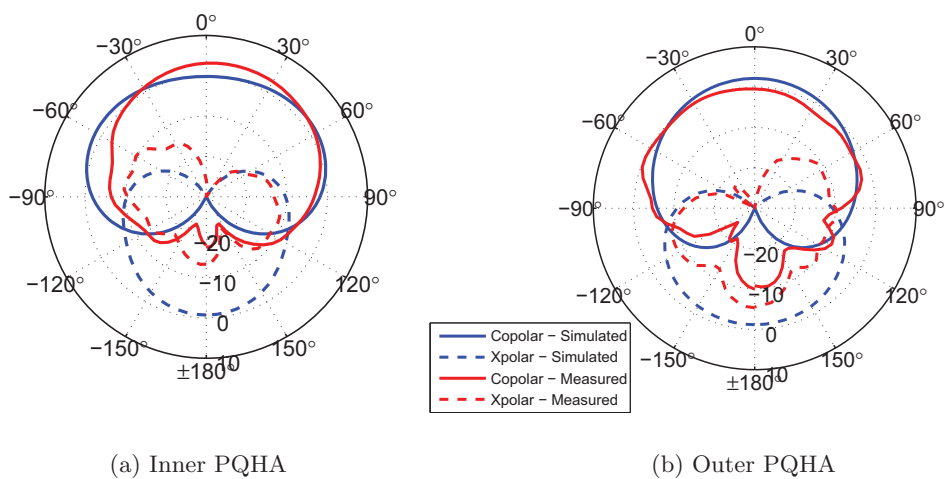


Figure 4.7: Simulated and measured elevation gain patterns (dBic) with $\phi = 0^\circ$ at 2 GHz frequency of the fabricated CPQHA.

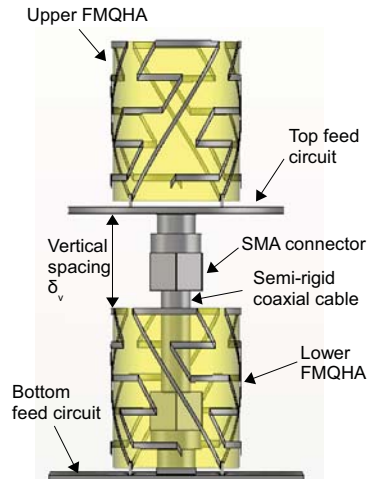


Figure 4.8: Configuration of dual polarised FMPQHA vertical array.

4.3 Dual polarised FMPQHA vertical array

4.3.1 Design configuration

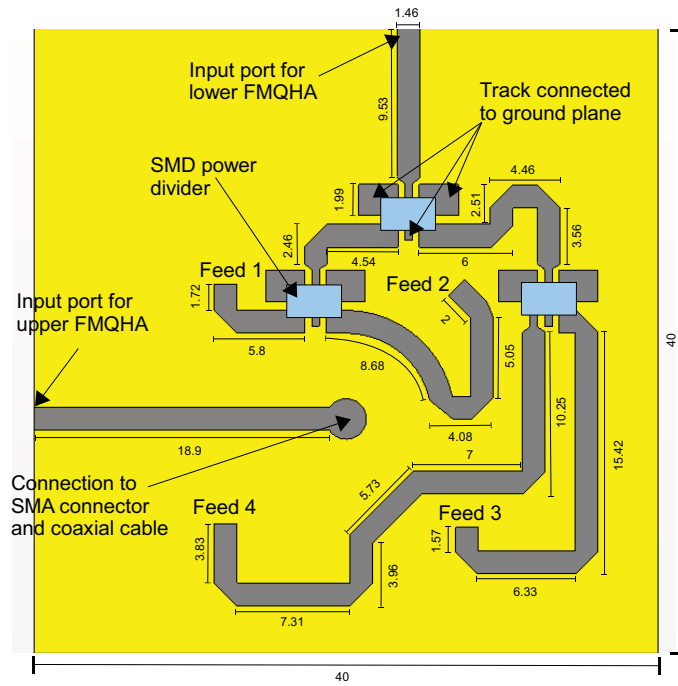
The main idea of this configuration is to construct a dual circularly polarised antenna array operating at 2.4 GHz frequency by vertically stacking two compact PQHAs where each antenna radiates an orthogonal polarisation. In this work, the compact PQHA that was used is the folded meandered PQHA (FMPQHA) 0.5 where its design parameters have been presented in Section 3.3. This antenna has been selected mainly due to its large radius which allows for a connection between feed circuits of the two antennas and also good radiation and impedance properties. Fig. 4.8 shows the configuration of a dual circularly polarised FMPQHA vertical array with its feed network. The vertical spacing δ_v between the two antennas is an important parameter in determining the performance of the array because of its influence on the mutual coupling effect between the two antennas and also blockage effect by the top feed circuit. Therefore, the vertical spacing can be optimised to provide adequate separation between the two antennas which does not severely degrade the performance of both antennas.

4.3.2 Feed network

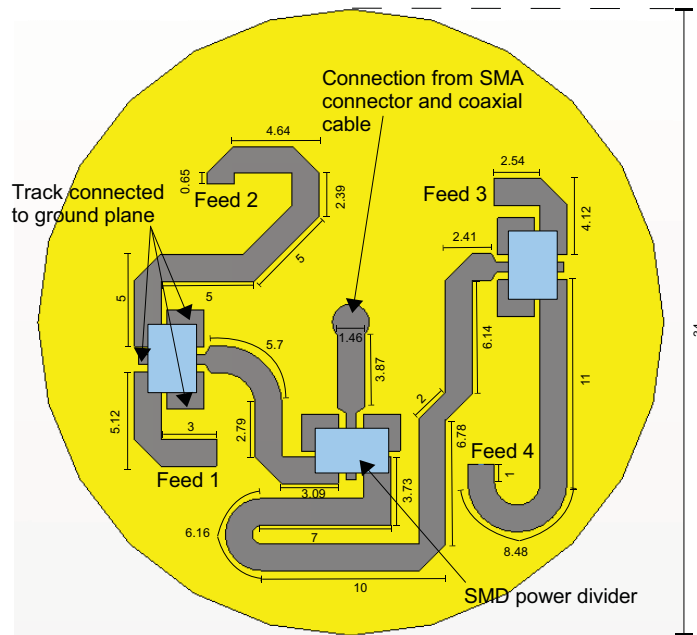
The feed network of the dual polarised FMPQHA vertical array is constructed by combining two circuits, where the lower circuit is for the lower antenna and the upper circuit is designed for the upper antenna with connection between the two circuits as illustrated in Fig. 4.8. It is important especially for the upper PQHA's feed circuit to be as compact as possible since it is positioned on top of the lower PQHA. Therefore, in order to achieve substantial compactness of the feed circuits, surface mount power dividers were used to provide equal power to each of the helical elements. Furthermore, the same high dielectric constant substrate which are Cer-10 material that was used in fabricating the feed circuit for a single compact PQHA is also utilised in constructing this feed network.

The design of the bottom feed circuit is shown in Fig 4.9a where it contains two input ports, one port for each circuit. The input port for the upper PQHA is connected to the top circuit using thin semi rigid coaxial cable and SMA (SubMiniature version A) connectors. In order for a connection to be made between lower and upper circuits, the bottom feed circuit track will be on the bottom side of the substrate while the ground plane is on the top side of the material. For the design of the top feed circuit, its size is considered to be the main constraint where it must be as small as possible to ensure minimum distortion of the lower FMPQHA's pattern. Configuration of the circuit is described in Fig. 4.9b where the circular form of the circuit was chosen mainly for symmetrical reason.

Based on the simulation of the bottom and top feed circuits, the reflection coefficients of the input port and feed ports and also the transmission coefficients between the input port and feed ports of both circuits are presented in Fig. 4.10 and Fig. 4.11 respectively. Although all ports on both circuit have a reflection coefficient near to or better than -10 dB at 2.4 GHz frequency as indicated in Fig. 4.10, it is however evident that the miniaturisation process has a negative impact to the impedance matching of several ports in both circuits. Apart from that, the power transfer property of the circuits is also affected by the miniaturisation, which can be quantified by the transmission coefficients between input port and feed ports. In both circuits, the difference of the



(a) Bottom feed circuit



(b) Top feed circuit

Figure 4.9: Configuration of bottom and top feed circuits for FMPQHA vertical array (dimension in mm).

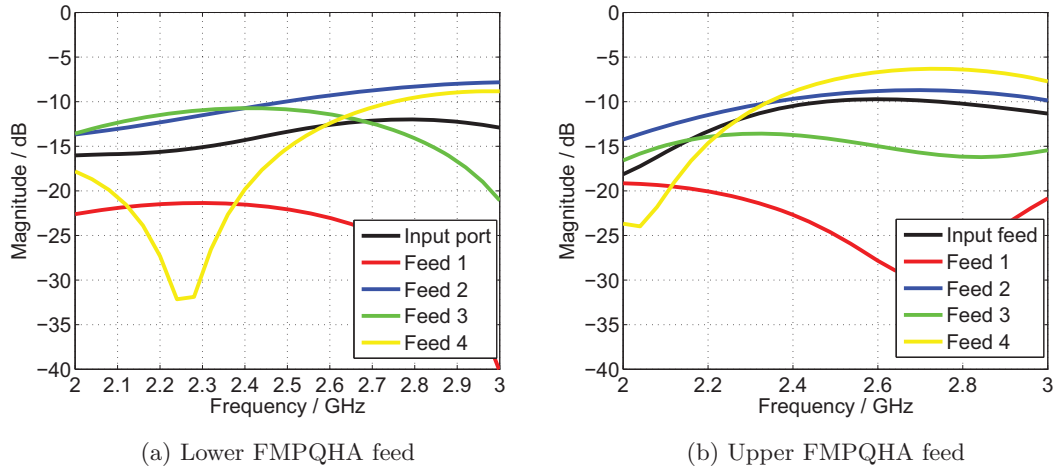


Figure 4.10: Simulated reflection coefficients of the feed network of the lower and upper FMPQHAs.

transmission coefficient of the feed ports is within 1 dB at 2.4 GHz frequency.

4.3.3 Simulation results

The effects of vertical spacing δ_v on the FMPQHA's properties was analysed by comparing the simulated results of vertical arrays with three different vertical spacing values of 10 mm, 15 mm and 20 mm. Furthermore, it is also important to study the impact of blockage by the upper FMPQHA and its feed circuit on the radiation performance of the lower FMPQHA.

Reflection coefficient and mutual coupling

Fig. 4.12 shows the impact of vertical spacing on the reflection coefficient of element 1 and element 5 of the lower and upper FMPQHAs respectively. These two elements are taken as the representative of the helical elements of each antenna. It is expected that element 1 exhibits a slightly different impedance properties due to its proximity with SMA connectors, coaxial cable and top feed circuit. Meanwhile, almost no change in the value of reflection coefficient for element 5 is evident when the vertical spacing is varied from 10 mm to 20 mm. In general, Fig. 4.13 indicates that vertically stacked

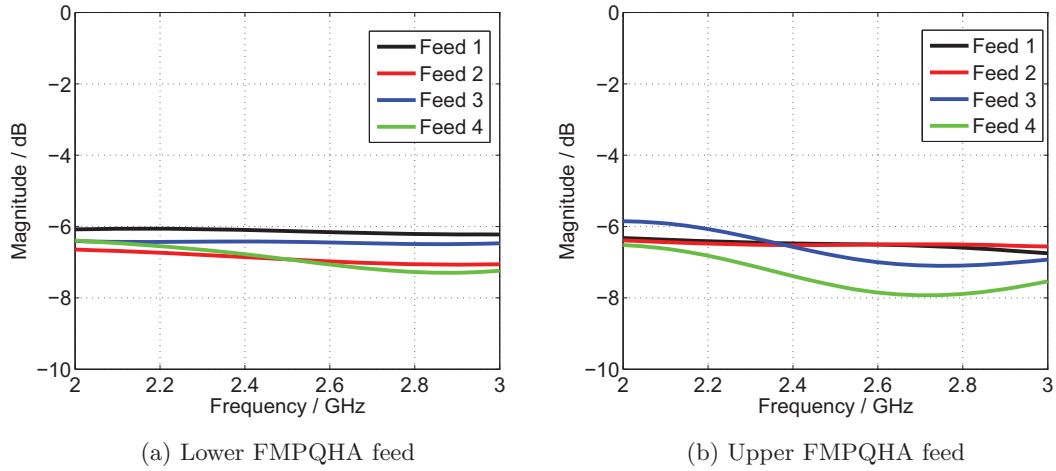


Figure 4.11: Simulated transmission coefficient of the feed network of the lower and upper FMPQHAs.

FMPQHAs have low mutual coupling between their helical elements as it can be inferred from the simulated transmission coefficient between element 1 and element 5. Variation of the vertical spacing also has almost negligible impact to the transmission coefficient that may be due to the effect of having top feed circuit between the two FMPQHAs.

Radiation pattern

One main disadvantage of this vertical array configuration is the distortion of the radiation pattern of the lower FMPQHA. As shown in Fig. 4.14a, there is a huge increase of the cross-polarised gain pattern of the lower FMPQHA at the opposite direction of the main polarised beam mainly due to the blockage effect of the top feed circuit. Meanwhile, the co-polarised pattern of the upper FMPQHA is largely unaffected by this spacing variation which is widely expected of the antenna because of its uninterrupted surrounding.

4.3.4 Fabrication and measurement

A prototype of a dual polarised FMPQHA vertical array with vertical spacing of 20 mm has been fabricated based on the simulated design provided earlier in this chapter.

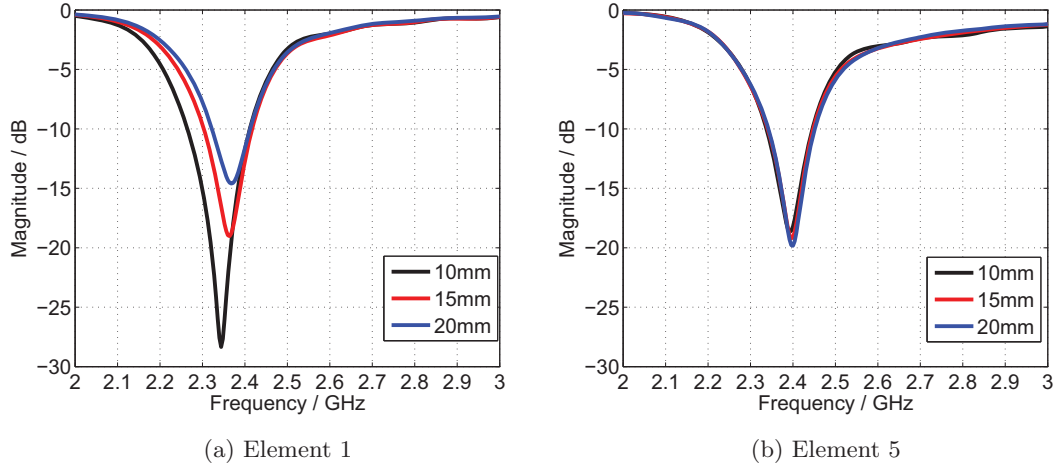


Figure 4.12: Reflection coefficients of element 1 and element 5 on the lower and upper FMPQHAs respectively with varying vertical spacing δ_v .

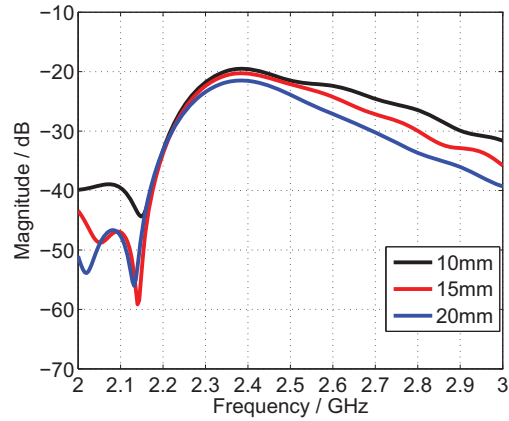


Figure 4.13: Isolation between element 1 and 5 on lower and upper FMPQHAs respectively with varying vertical spacing δ_v .

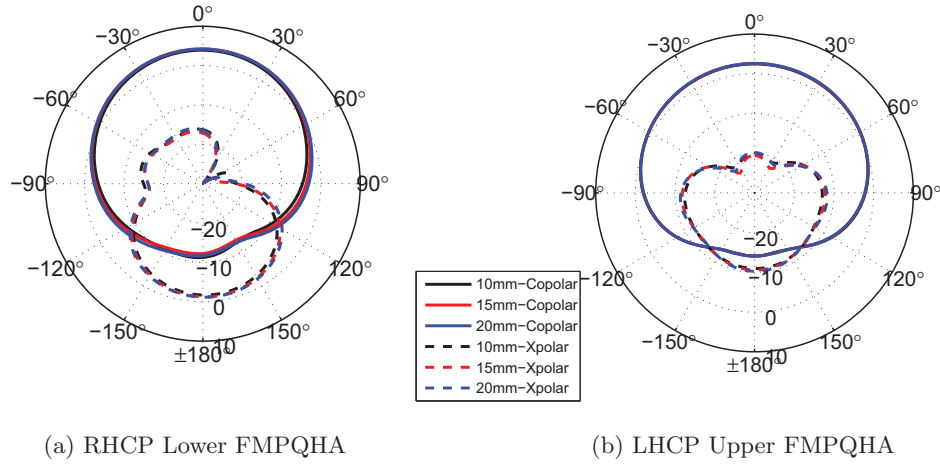


Figure 4.14: Elevation gain patterns (dBi) with $\phi = 0^\circ$ at 2.4 GHz frequency of the dual polarised FMPQHA vertical array with varying vertical spacing δ_v .

Although simulations show comparable performance for the three values of vertical spacing, the value of 20 mm between the top of the lower FMPQHA with the top feed circuit was chosen mainly to facilitate the construction of the array. The fabricated array prototype is shown in Fig. 4.15.

Evaluation of the antenna's impedance characteristic was carried out by measuring the S-parameter of the two input ports of the fabricated antenna, which includes the effect of their feed networks. Contrary to the simulation result where the reflection coefficient of one helical element on each FMPQHA was investigated, this measurement provides the reflection coefficient of the complete system of FMPQHAs and their respective feed circuits. Therefore, no comparison was made between the measurement and simulation results for this parameter. Based on the measurement data, both FMPQHAs have good impedance match at the targeted frequency of 2.4 GHz even though there is a significant difference in their characteristics when looking within the range of 2 GHz to 3 GHz as shown in Fig. 4.16a.

Meanwhile, the measured transmission coefficient between the two input ports of the FMPQHA vertical array indicates the overall coupling effect between the lower and upper FMPQHAs together with their feed networks. Although the simulated transmission coefficient of the FMPQHA array was taken based on the coupling between one helical

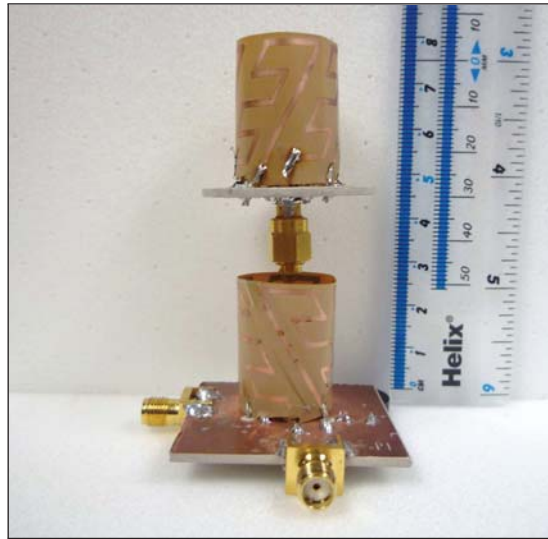


Figure 4.15: The fabricated dual polarised FMPQHA vertical array.

element on each FHQMA, comparison can still be made between the measured and simulated transmission coefficient since it also depends on the distance between the antennas. Fig. 4.16b shows the simulated and measured transmission coefficients of the FHQMA array, where although substantial difference is evident in the frequency range, their values around the targeted frequency of 2.4 GHz are almost similar. Therefore, it can be safely assumed that the simulated transmission coefficient of the helical elements on the lower and upper FHQMAs can be utilised to provide an approximation of the coupling between the lower and upper FHQMAs.

Comparison between the simulated and measured elevation pattern with an azimuth angle of 0° of the lower and upper FMPQHAs are provided in Fig. 4.17a and Fig. 4.17b respectively. For the lower FMPQHA, the main difference between the measured and simulated patterns is the co-polarised gain pattern where the measured pattern has lower gain of about 3 to 4 dB in the upper hemisphere when compared with simulated pattern. Meanwhile, the opposite condition occurred for the cross-polarised pattern where the higher gain was recorded in the measurement. The discrepancy between simulated and measured co-polarised patterns of the lower FMPQHA may be attributed to the effect of upper FMPQHA and feed circuit blockage on the radiation pattern of the lower FMPQHA, which is not fully captured in the simulation. This shows that in practice, the impact of the blockage on the lower FHQMA's radiation pattern is much

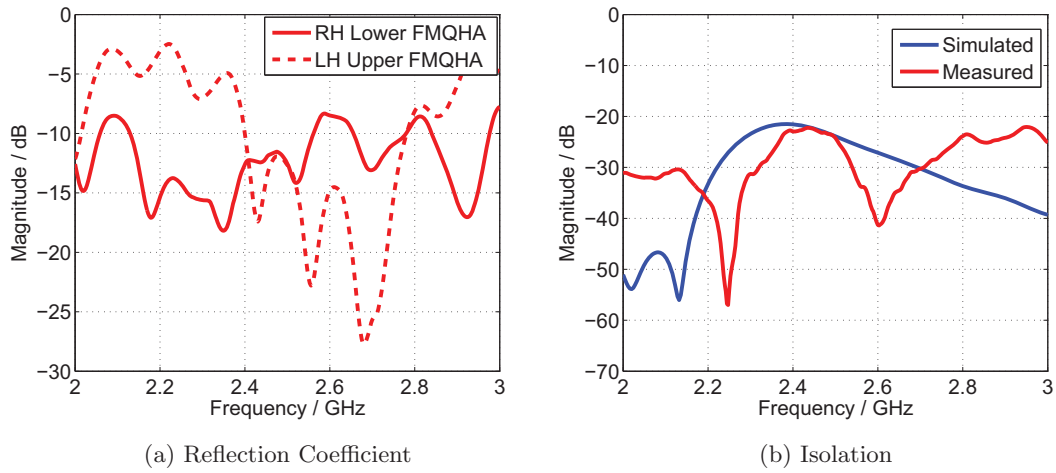


Figure 4.16: Reflection coefficient and isolation of the fabricated dual polarised FM-PQHA vertical array together with the feeding network.

worse than predicted by the simulation. As for the upper FMPQHA, the measured co-polarised pattern is largely comparable with the simulated result. However the simulation seems to overestimate the cross-polarised gain of the upper FMPQHA when equated with the measurement result.

4.4 Dual polarised SFPQHA horizontal array

4.4.1 Design configuration

A dual polarised horizontal array consisting of two single folded PQHAs (SFPQHA) with orthogonal polarisation is a typical configuration where the antennas are spaced horizontally with a certain distance as shown in Fig. 4.18. The SFPQHA with 0.375 turns and angular radial length of 30° is chosen as the basic element of this array due to its good radiation performance despite its small size. Horizontal spacing between the two SFPQHAs was then investigated for its impact on the both antennas' characteristics. As for its feeding arrangement, the array utilises a combination of feeding circuits with opposing phase direction that was originally used in a single miniaturised PQHA system as presented in Section 3.2.3. Fig. 4.19 shows the complete feeding

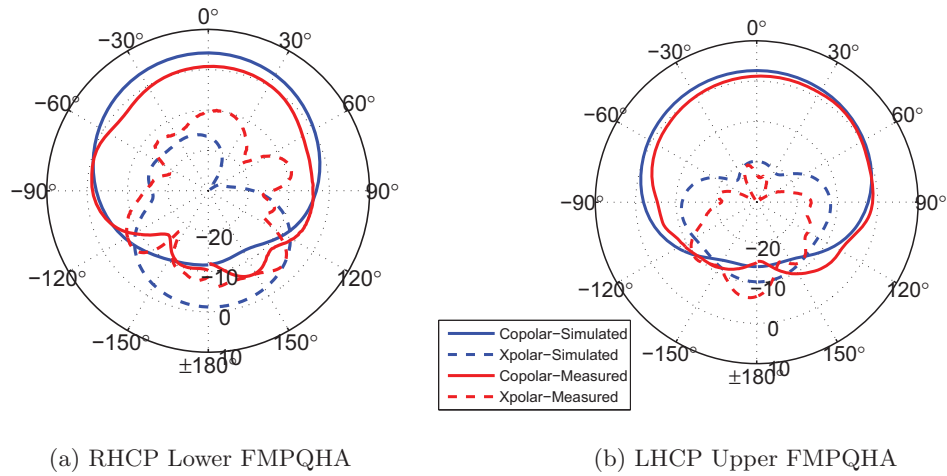


Figure 4.17: Simulated and measured elevation gain pattern (dBic) with $\phi = 0^\circ$ at 2.4 GHz frequency of the fabricated dual polarised FMPQHA vertical array.

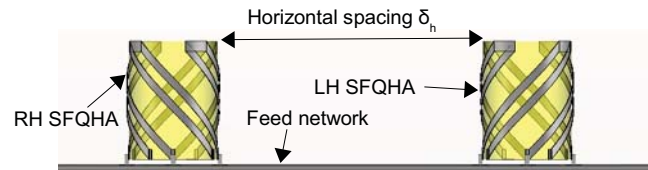


Figure 4.18: Configuration of a dual polarised SFPQHA horizontal array.

network of the horizontal array. Since the feeding network is merely a combination of two previously designed feed circuits, its ports reflection and transmission coefficients are identical to the single SFPQHA feed network. It is well known that the impact of mutual coupling between two antennas depends on the their separation distance where the closer the two antennas are, the stronger the impact will be and vice versa. Therefore, the effects of the horizontal spacing between the two SFPQHAs on each antenna's impedance and radiation pattern were also studied using simulation.

4.4.2 Simulation results

The effects of horizontal spacing δ_h between the two SFPQHAs on each antenna's radiation pattern and impedance were studied by comparing the simulated S-parameters and radiation pattern of the two antennas with varying horizontal spacing. Six values

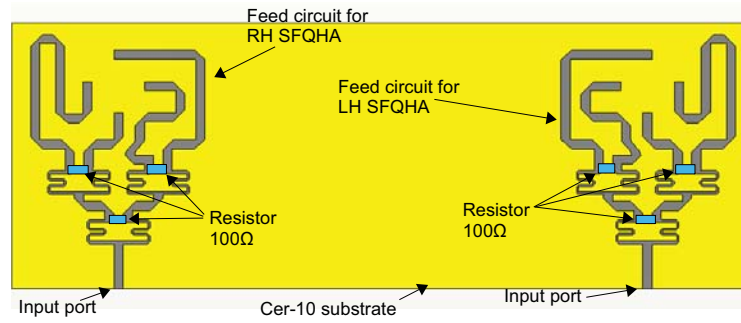


Figure 4.19: Feed network configuration of the SFPQHA horizontal array.

of spacing were investigated, which are 20 mm, 40 mm, 60 mm, 80 mm, 100 mm and 120 mm that correspond to 0.16λ , 0.33λ , 0.49λ , 0.65λ , 0.82λ and 0.98λ at 2.45 GHz frequency.

Reflection coefficient and mutual coupling

Simulated reflection coefficients of element 1 and element 5 on the RHCP and LHCP SFPQHAs respectively for various values of horizontal spacing are taken as an indicator for the influence of separation spacing on the antenna's reflection coefficient. As shown in Fig. 4.20, the reflection coefficient of the helical elements is not strongly affected by the separation spacing between the two antennas and both elements seem to exhibit similar reflection coefficient characteristic. Meanwhile, the isolation between the two elements which quantify their coupling indicates that low coupling is achievable even for a spacing of 20 mm which is 0.16 wavelengths at 2.45 GHz frequency. Fig. 4.21 presents the overall effect of the separation spacing on the value of isolation between the two SFPQHAs.

Radiation pattern

Elevation gain patterns of the RHCP and LHCP SFPQHAs with varying horizontal spacing from 20 mm to 120 mm were provided in Fig. 4.22 for comparison of its influence on the antennas radiation pattern. The co-polarised elevation patterns of both antennas indicate that the spacing between the two antennas has no substantial impact on their

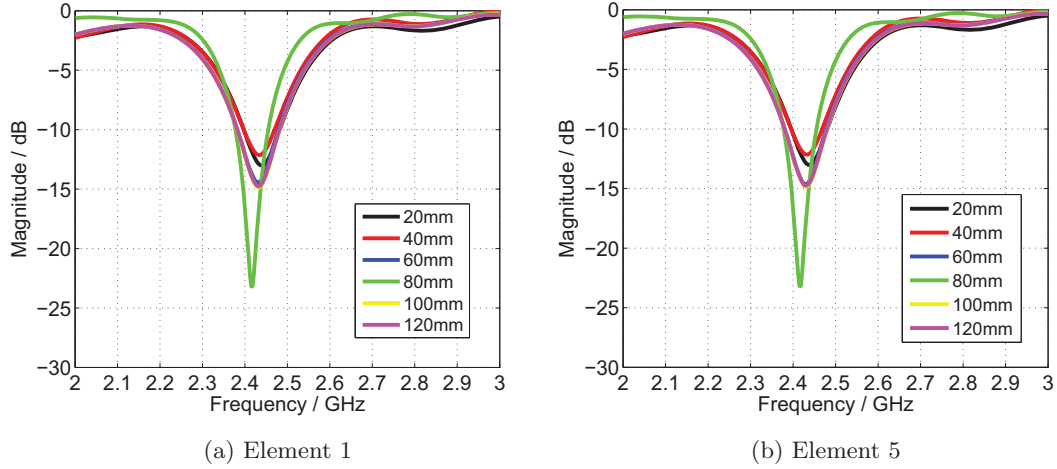


Figure 4.20: Reflection coefficient of element 1 and 5 on RHCP and LHCP SFPQHAs respectively with varying horizontal spacing δ_h .

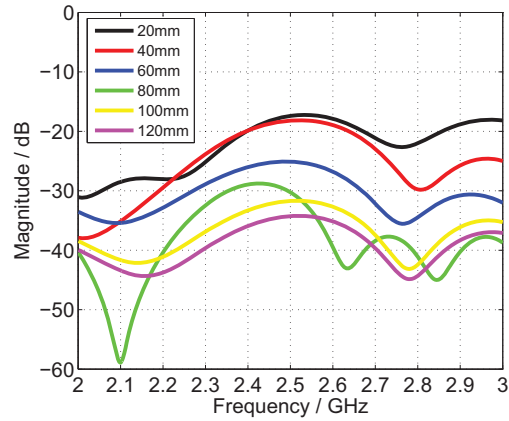


Figure 4.21: Isolation between element 1 and 5 on RHCP and LHCP SFPQHAs respectively with varying horizontal spacing δ_v .

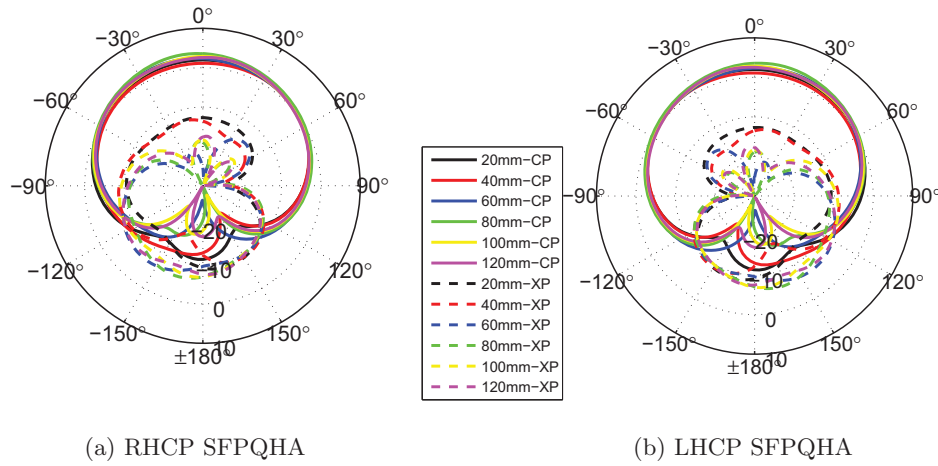


Figure 4.22: Elevation pattern ($\phi = 0^\circ$) of the RHCP and LHCP SFPQHAs with varying horizontal spacing δ_v .

co-polarised patterns even at the separation of 20 mm. One possible explanation of this non-effect is the opposing sense of polarisation between the two antennas which reduces the mutual coupling effect, hence less distortion of the radiation pattern. On the contrary, the cross-polarised patterns of both antennas are affected by the separation spacing where an increase of the cross-polarised gain is evident when the antennas were separated with a distance of 20 mm and 40 mm.

4.4.3 Fabrication and measurement

Fabrication of a dual polarised SFPQHA horizontal array with 80 mm separation spacing and its feed network was implemented in order to validate the proposed array design. Its separation spacing of 80 mm or 0.65λ was mainly chosen as it is slightly wider than 0.5λ at 2.45 GHz frequency which provides good signal decorrelation in both line-of-sight (LoS) and non-line-of-sight (NLoS) environments. Apart from that, the value of 80 mm is considered to be the maximum spacing available on a typical large handheld device. The fabrication process is practically the same as presented for a single SFPQHA in Section 3.2.3. Fig. 4.23 shows the fabricated SFPQHA array completes with its feed network and input ports.

In order to evaluate the overall antenna system's impedance matching with reference



Figure 4.23: The fabricated dual polarised SFPQHA horizontal array.

impedance of 50Ω , the reflection coefficient of both SFPQHAs was measured and presented in Fig. 4.24a. Since the measurement includes the effect of feed network on the overall reflection coefficient, therefore it would be impractical to compare its value with simulation results, which provide the reflection coefficient of only one helical element in each SFPQHA. Evaluation of the mutual coupling between the two antennas was conducted by measuring the transmission coefficient between their input ports. Using the same reasoning as described in Section 4.3.4, comparison between the simulated and measured isolation is presented in Fig. 4.24b.

Finally, the evaluation of the fabricated SFPQHA array is completed by measuring the co and cross-polarised elevation patterns of both antennas and comparing them with the simulated results. In both Fig. 4.25a and Fig. 4.25b, the measured co-polarised patterns follow the simulated patterns much closely than earlier design of FMPQHA vertical array. The same characteristic can also be observed for the cross-polarised pattern of both antennas where the measured patterns are comparable with the simulated patterns.

4.5 Summary

Three different configurations of a dual circularly polarised antenna system utilising the PQHA and its compact variants have been proposed and their characteristics investi-

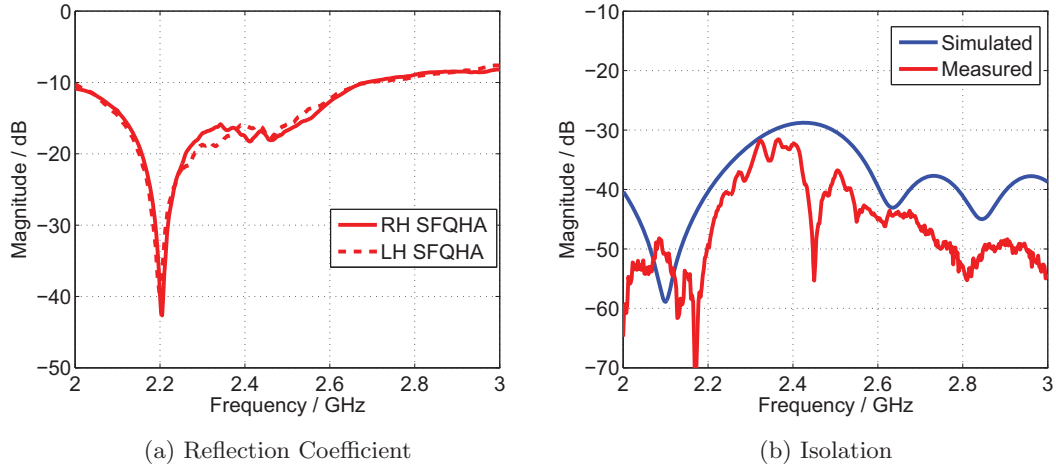


Figure 4.24: Reflection coefficient and isolation of the fabricated dual polarised SF-PQHA horizontal array together with the feeding network.

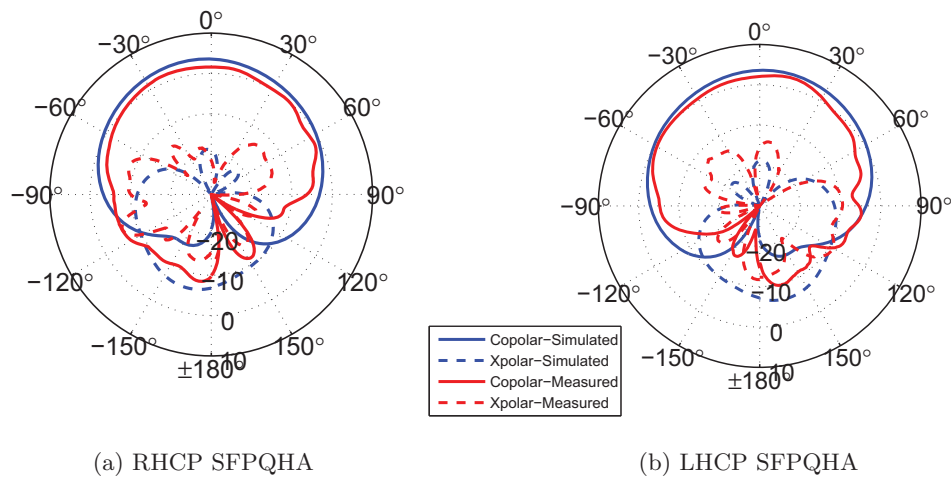


Figure 4.25: Simulated and measured elevation pattern ($\phi = 0^\circ$) of the fabricated dual polarised SFPQHA horizontal array.

gated in terms of S-parameters and radiation patterns. An inside-out dual polarised configuration that uses two conventional PQHAs was first studied to provide a proof-of concept design of a colocated dual circularly polarised array with PQHA as the basic element. Due to its large size and also bulky feeding arrangement, it is not suitable for application in handheld or vehicular terminals. However, it serves as a useful preliminary work in studying the impact of PQHA collocation on each antenna's characteristics.

The next configuration is the vertical array of FMPQHAs with opposing senses of polarisation that equipped with its specially designed feed network. Its main challenge is to design and fabricate a sufficiently small feed circuit for the upper FMPQHA in order to minimise the effect of blockage on the lower FMPQHA. Based on the measurement results, it is clear that further miniaturisation of the top feed circuit is very much desirable as the measured co-polarised pattern of the lower FMPQHA degrades moderately and there is a significant increase of cross polarisation. Therefore, power imbalance on the received signals may be materialised in this configuration due to difference in co and cross-polarised patterns of both FMPQHAs. Although the size of the FMPQHA vertical array is too big for handheld receiver, it is however suitable for vehicular applications where it can be fitted on top of a vehicle rooftop together with dielectric radome.

Lastly is the dual polarised horizontal array of two SFPQHAs with opposite sense of polarisation and their feed networks. This array was designed primarily to be utilised as an antenna system for handheld devices of the LMS MIMO system. Simulation results reveal that separation spacing between the two antennas has no substantial impact on their impedance and radiation properties. The radiation characteristics of the SFPQHAs are slightly distorted due to the effect of mutual coupling as indicated by the simulation and measurement results.

Chapter 5

Branch power and correlation analyses of a dual circularly polarised SFPQHA array

5.1 Introduction

In determining the performance of dual polarised antennas in a land mobile satellite (LMS) MIMO system, the branch power ratio and correlation between antennas are among the most important parameters that need to be evaluated. This is mainly due to the fact that the capacity increase of a MIMO system is highly dependent on both parameters albeit in a complicated matter. Calculation of these parameters in this system requires the evaluation method to consider that the antenna will be operating in a Ricean fading channel where there is a dominant line-of-sight (LoS) component. Apart from that, since we are using circularly polarised antennas at both ends, the polarisation of the incident waves (especially the LoS component) and also the polarisation purity of the antenna radiation pattern need to be included in the evaluation since it will have a major impact to both figures of merit.

In this chapter, the evaluation of the circularly polarised antennas in terms of its branch power ratio was conducted by utilising a new formulation of the mean effective gain

(MEG) that considers the impact of Ricean fading and also polarisation mismatch between the LoS component and the corresponding antenna field pattern. This formulation allows for a more precise MEG evaluation of the receive antennas which then will be used in calculating the branch power ratio between these antennas. As for the correlation between receive antennas, complex correlation of several selected SFPQHA arrays was evaluated to study the impact of the antenna properties as well as the channel characteristics. Finally, the impact of antenna polarisation on the signal correlation was explicitly investigated with the use of modified correlation formulation.

5.2 Branch power analysis

Evaluation of multiple antennas performance in a MIMO system requires investigation and comparison of the received power of these antennas in a specified environment where ideally, each antenna must exhibit equal received power. Although various parameters are available to represent an antenna performance in terms of received power, mean effective gain MEG is the most frequently used as it provides a simple mathematically tractable method of combining the effect of channel into the antenna gain formulation. A more comprehensive view on the antenna performance can be obtained since the antenna is evaluated with respect to its operating environment. The branch power ratio BPR between two neighbouring antennas (antenna 1 and 2) can be given as:

$$\max \text{BPR} = \left(\frac{\text{MEG}_{\text{ant1}}}{\text{MEG}_{\text{ant2}}}, \frac{\text{MEG}_{\text{ant2}}}{\text{MEG}_{\text{ant1}}} \right) \quad (5.1)$$

or if it is decibel scale, then $\text{BPR (dB)} = |\text{MEG}_{\text{ant1}}(\text{dB}) - \text{MEG}_{\text{ant2}}(\text{dB})|$ if $\text{MEG}_{\text{ant1}} > \text{MEG}_{\text{ant2}}$. The best case scenario for a non-line-of-sight (NLoS) channel is when both antennas have equal average received power, where the relationship between MEG of the two antennas is written as:

$$\text{MEG}_{\text{ant1}} \approx \text{MEG}_{\text{ant2}}. \quad (5.2)$$

Meanwhile, high value of BPR is preferable for antennas in a LoS channel especially for a polarised MIMO system since this implies that the antennas are orthogonally polarised.

5.2.1 Limitation of current MEG formulations

The first MEG formulation was developed by Taga [99] in order to evaluate an antenna performance in Rayleigh channel by combining the propagation channel with the antenna gain pattern. In this formulation as described in Equation (2.27), the Rayleigh channel is specified by the channel cross polarisation discrimination (XPD) and the Angle-of-Arrival (AoA) distribution of the incident waves. For almost 10 years, this formulation has been utilised by numerous researchers without any modification especially in terms of generalisation of its channel properties. An important improvement of the MEG parameter was presented in [124] where the formulation was extended to Ricean fading channel by including the impact of LoS component on the antenna gain performance. However, one major deficiency of the proposed formulation is that it does not consider the phases of the LoS component and the corresponding antenna field pattern. This limitation make the formulation suitable solely for vertically or horizontally polarised LoS component, which by itself is not the general condition of an electromagnetic wave. Furthermore, by disregarding the antenna field phase, the formulation is not capable of evaluating the interaction between antennas with elliptical or circular polarisation and LoS incident wave. Therefore, a new formulation is needed in order to include these phases so that a more general term of polarisation of both antenna and LoS component can be taken into account.

5.2.2 MEG formulation in Ricean fading channel with antenna and LoS component phases

The formulation of MEG that includes antenna and LoS component phases relies heavily on the previous works on deriving MEG in a Ricean channel especially from [124] and [125]. The mean effective gain is defined as the ratio of the average received power P_{rec} at the mobile antenna and the sum of the average power of the θ and ϕ polarised waves received by isotropic antenna given as $P_{tot,\theta}$ and $P_{tot,\phi}$ respectively [99]. Mathematically, it is written as:

$$\text{MEG} = \frac{P_{rec}}{P_{tot,\theta} + P_{tot,\phi}}. \quad (5.3)$$

The first step in determining the average received power of the mobile antenna is by defining the open circuit voltage $V_{oc}(t)$ at the antenna port. This voltage can be calculated based on the interaction between incident waves and the antenna field pattern [95] as:

$$V_{oc}(t) = \oint \mathbf{E}^*(\Omega) \mathbf{A}(\Omega) e^{-j(\frac{2\pi}{\lambda}) \mathbf{u} \cdot \mathbf{r}(\Omega) t} d\Omega \quad (5.4)$$

where $\mathbf{E}(\Omega)$ denotes the incident field, $\mathbf{A}(\Omega)$ is the antenna field pattern, (Ω) denotes (θ, ϕ) direction in the spherical coordinate system, \mathbf{u} is the mobile velocity, $\mathbf{r}(\Omega)$ is the unit vector of the radiating direction. We further define the incident field which is a combination of LoS and scattering components as:

$$\mathbf{E}(\Omega) = E_{\theta}(\Omega) \mathbf{e}_{\theta} + E_{\phi}(\Omega) \mathbf{e}_{\phi} \quad (5.5)$$

where $E_{\theta}(\Omega)$ and $E_{\phi}(\Omega)$ are the θ and ϕ components of the complex incident waves respectively. Meanwhile, \mathbf{e}_{θ} and \mathbf{e}_{ϕ} denote the unit vector in θ and ϕ directions. The antenna field pattern can also be separated into two orthogonal components, which are A_{θ} and A_{ϕ} as the following:

$$\mathbf{A}(\Omega) = A_{\theta}(\Omega) \mathbf{e}_{\theta} + A_{\phi}(\Omega) \mathbf{e}_{\phi}. \quad (5.6)$$

As stated earlier, incident waves in Ricean channel consisting of one or more deterministic field component and random or scattering field components. Several assumptions of the properties of this incident field are made in order to provide a compact representation of the incident field in terms of its correlation formulation [124]. First, it is assumed that the phases of the co-polarised fields are independent in different Angle-of-Arrival (AoA) given as Ω and Ω' . Secondly, the phases of the cross-polarised waves are also independent in different AoA but correlated in a fixed LoS Angle-of-Arrival Ω_l . Based on these statements, the correlation characteristic of the incident field in Ricean channel is provided as [125]:

$$\langle E_a(\Omega) E_b^*(\Omega') \rangle = E_{la}(\Omega) E_{lb}^*(\Omega) \delta(\Omega - \Omega_l) \delta(\Omega' - \Omega_l) + \langle |E_a(\Omega)|^2 \rangle \delta(\Omega - \Omega') \delta_{ab} \quad (5.7)$$

where $E_a(\Omega)$ and $E_b(\Omega)$ are two orthogonally polarised (a and b polarisations) components of the incident field, E_{la} and E_{lb} are the direct components of each polarisation, $\langle \cdot \rangle$ is the process of averaging over an ensemble, $\delta(\cdot)$ denotes the Dirac delta function and δ_{ab} is the Kronecker delta function.

It is important to note that $V_{oc}(t)$ which has been defined earlier is a random complex signal. Therefore, the autocorrelation function of the open circuit voltage must first be derived and it is given as:

$$\begin{aligned}
R_{V_{oc}}(\Delta t) &= \frac{1}{2} \langle V_{oc}(t) V_{oc}^*(t + \Delta t) \rangle \\
&= \frac{1}{2} \left\langle \int \mathbf{E}^*(\Omega) \mathbf{A}(\Omega) e^{-j\frac{2\pi}{\lambda} \mathbf{u} \cdot \mathbf{r}(\Omega) t} d\Omega \cdot \left(\int \mathbf{E}^*(\Omega') \mathbf{A}(\Omega') e^{-j\frac{2\pi}{\lambda} \mathbf{u} \cdot \mathbf{r}(\Omega') (t + \Delta t)} d\Omega' \right)^* \right\rangle \\
&= \frac{1}{2} \iint \langle \mathbf{E}^*(\Omega) \mathbf{A}(\Omega) \cdot \mathbf{E}(\Omega') \mathbf{A}^*(\Omega') \rangle e^{-j\frac{2\pi}{\lambda} \mathbf{u} \cdot (\mathbf{r}(\Omega) - \mathbf{r}(\Omega')) t + j\frac{2\pi}{\lambda} \mathbf{u} \cdot \mathbf{r}(\Omega') \Delta t} d\Omega d\Omega'
\end{aligned} \tag{5.8}$$

By inserting Equation (5.5) and (5.6) into Equation (5.8), the autocorrelation function is then defined using the θ and ϕ components of both incident field and antenna pattern field as:

$$\begin{aligned}
R_{V_{oc}}(\Delta t) &= \frac{1}{2} \iint \langle (E_{\theta}^*(\Omega) \mathbf{e}_{\theta} + E_{\phi}^*(\Omega) \mathbf{e}_{\phi}) (A_{\theta}(\Omega) \mathbf{e}_{\theta} + A_{\phi}(\Omega) \mathbf{e}_{\phi}) \\
&\quad (E_{\theta}(\Omega') \mathbf{e}_{\theta} + E_{\phi}(\Omega') \mathbf{e}_{\phi}) (A_{\theta}^*(\Omega') \mathbf{e}_{\theta} + A_{\phi}^*(\Omega') \mathbf{e}_{\phi}) \rangle \\
&\quad e^{-j\frac{2\pi}{\lambda} \mathbf{u} \cdot (\mathbf{r}(\Omega) - \mathbf{r}(\Omega')) t + j\frac{2\pi}{\lambda} \mathbf{u} \cdot \mathbf{r}(\Omega') \Delta t} d\Omega d\Omega' \\
&= \frac{1}{2} \iint \langle E_{\theta}^*(\Omega) E_{\theta}(\Omega') A_{\theta}(\Omega) A_{\theta}^*(\Omega') + E_{\phi}^*(\Omega) E_{\phi}(\Omega') A_{\phi}(\Omega) A_{\phi}^*(\Omega') \\
&\quad + E_{\theta}^*(\Omega) E_{\phi}(\Omega') A_{\theta}(\Omega) A_{\phi}^*(\Omega') + E_{\theta}(\Omega') E_{\phi}^*(\Omega) A_{\theta}^*(\Omega') A_{\phi}(\Omega) \rangle \\
&\quad e^{-j\frac{2\pi}{\lambda} \mathbf{u} \cdot (\mathbf{r}(\Omega) - \mathbf{r}(\Omega')) t + j\frac{2\pi}{\lambda} \mathbf{u} \cdot \mathbf{r}(\Omega') \Delta t} d\Omega d\Omega'
\end{aligned} \tag{5.9}$$

Then, Equation (5.9) is further simplified by utilising the correlation characteristic of the incident field as provided in Equation (5.7). The autocorrelation function is then written as:

$$\begin{aligned}
R_{V_{oc}}(\Delta t) &= \frac{1}{2} \oint [\langle |E_{\theta}(\Omega)|^2 \rangle |A_{\theta}(\Omega)|^2 + \langle |E_{\phi}(\Omega)|^2 \rangle |A_{\phi}(\Omega)|^2] e^{j\frac{2\pi}{\lambda} \mathbf{u} \cdot \mathbf{r}(\Omega) \Delta t} d\Omega \\
&\quad + \underbrace{\left[|E_{l\theta}(\Omega_l)|^2 |A_{l\theta}(\Omega_l)|^2 + |E_{l\phi}(\Omega_l)|^2 |A_{l\phi}(\Omega_l)|^2 \right]}_{\text{LoS part without phase}} \\
&\quad + \underbrace{\left[E_{l\theta}^*(\Omega_l) E_{l\phi}(\Omega_l) A_{l\theta}(\Omega_l) A_{l\phi}^*(\Omega_l) + E_{l\phi}^*(\Omega_l) E_{l\theta}(\Omega_l) A_{l\phi}(\Omega_l) A_{l\theta}^*(\Omega_l) \right]}_{\text{LoS part with phase}} e^{j\frac{2\pi}{\lambda} \mathbf{u} \cdot \mathbf{r}(\Omega_l) \Delta t}.
\end{aligned} \tag{5.10}$$

where $E_{l\theta}(\Omega_l)$ and $E_{l\phi}(\Omega_l)$ are the θ and ϕ components of the LoS incident field. The corresponding antenna field that interacts with the LoS incident field is denoted as

$A_{l\theta}(\Omega_l)$ and $A_{l\phi}(\Omega_l)$ for both components. The (Ω) and (Ω_l) symbols are dropped from this formulation onwards for brevity with the understanding that all incident field and antenna pattern are function of angular direction.

The phases of the LoS component of the incident field and the corresponding antenna field phase in the direction of the LoS component's AoA are introduced in the 'LoS part with phase' of Equation (5.10) as follows:

$$\begin{aligned} E_{l\theta}^* E_{l\phi} A_{l\theta} A_{l\phi}^* + E_{l\phi}^* E_{l\theta} A_{l\phi} A_{l\theta}^* &= |E_{l\theta}| e^{-j\psi_{c,\theta}} |E_{l\phi}| e^{j\psi_{c,\phi}} |A_{l\theta}| e^{j\psi_{a,\theta}} |A_{l\phi}| e^{-j\psi_{a,\phi}} \\ &\quad + |E_{l\theta}| e^{j\psi_{c,\theta}} |E_{l\phi}| e^{-j\psi_{c,\phi}} |A_{l\theta}| e^{-j\psi_{a,\theta}} |A_{l\phi}| e^{j\psi_{a,\phi}} \end{aligned} \quad (5.11)$$

where $|\cdot|$ denotes the magnitude of a complex variable, $\psi_{c,\theta}$ and $\psi_{c,\phi}$ are the phases of θ and ϕ components of LoS incident field respectively and $\psi_{a,\theta}$ and $\psi_{a,\phi}$ denote the phases of corresponding antenna θ and ϕ field components in the direction of LoS incident field. Further simplification of Equation (5.11) can be made by considering the phase difference of the ϕ and θ components of the LoS incident field and antenna field, which is given as $\psi_{ch} = \psi_{c,\phi} - \psi_{c,\theta}$ and $\psi_{ant} = \psi_{a,\phi} - \psi_{a,\theta}$. Therefore the LoS part with phase is written as:

$$\begin{aligned} E_{l\theta}^* E_{l\phi} A_{l\theta} A_{l\phi}^* + E_{l\phi}^* E_{l\theta} A_{l\phi} A_{l\theta}^* &= |E_{l\theta}| |E_{l\phi}| e^{j(-\psi_{c,\theta} + \psi_{c,\phi})} |A_{l\theta}| |A_{l\phi}| e^{j(\psi_{a,\theta} - \psi_{a,\phi})} \\ &\quad + |E_{l\theta}| |E_{l\phi}| e^{j(\psi_{c,\theta} - \psi_{c,\phi})} |A_{l\theta}| |A_{l\phi}| e^{j(-\psi_{a,\theta} + \psi_{a,\phi})} \\ &= |E_{l\theta}| |E_{l\phi}| e^{j\psi_{ch}} |A_{l\theta}| |A_{l\phi}| e^{-j\psi_{ant}} \\ &\quad + |E_{l\theta}| |E_{l\phi}| e^{-j\psi_{ch}} |A_{l\theta}| |A_{l\phi}| e^{j\psi_{ant}} \\ &= |E_{l\theta}| |E_{l\phi}| |A_{l\theta}| |A_{l\phi}| \left(e^{j(\psi_{ch} - \psi_{ant})} + e^{-j(\psi_{ch} - \psi_{ant})} \right) \\ &= 2 |E_{l\theta}| |E_{l\phi}| |A_{l\theta}| |A_{l\phi}| \cos(\psi_{ch} - \psi_{ant}). \end{aligned} \quad (5.12)$$

For both LoS incident wave and corresponding antenna field, their polarisation can be described by the magnitude ratio and phase difference between the θ and ϕ components. Using the LoS component as an example, several special polarisation cases are listed below together with its corresponding characteristics of the θ and ϕ components:

- $E_{l\theta}$ is not zero, $E_{l\phi} = 0$ and ψ_{ch} for any value \rightarrow vertical linear polarisation.
- $E_{l\theta} = 0$, $E_{l\phi}$ is not zero and ψ_{ch} for any value \rightarrow horizontal linear polarisation.

- $E_{l\theta} = E_{l\phi}$ and $\psi_{ch} = 0$ rad $\rightarrow 45^\circ$ slanted linear polarisation.
- $E_{l\theta} = E_{l\phi}$ and $\psi_{ch} = \pm\pi$ rad $\rightarrow -45^\circ$ slanted linear polarisation
- $E_{l\theta} = E_{l\phi}$ and $\psi_{ch} = -0.5\pi$ rad \rightarrow RH circular polarisation
- $E_{l\theta} = E_{l\phi}$ and $\psi_{ch} = 0.5\pi$ rad \rightarrow LH circular polarisation

By replacing ‘LoS part with phase’ in Equation (5.10) with Equation (5.12), the auto-correlation function can then be written as:

$$\begin{aligned}
R_{V_{oc}}(\Delta t) = & \frac{1}{2} \oint [\langle |E_\theta|^2 \rangle |A_\theta|^2 + \langle |E_\phi|^2 \rangle |A_\phi|^2] e^{j\frac{2\pi}{\lambda} \mathbf{u} \cdot \mathbf{r}(\Omega) \Delta t} d\Omega \\
& + \underbrace{\left[|E_{l\theta}|^2 |A_{l\theta}|^2 + |E_{l\phi}|^2 |A_{l\phi}|^2 \right]}_{\text{LoS part without phase}} \\
& + 2 \underbrace{\left[|E_{l\theta}| |E_{l\phi}| |A_{l\theta}| |A_{l\phi}| \cos(\psi_{ch} - \psi_{ant}) \right]}_{\text{LoS part with phase}} e^{j\frac{2\pi}{\lambda} \mathbf{u} \cdot \mathbf{r}(\Omega) \Delta t}. \quad (5.13)
\end{aligned}$$

It is well known that the average received power of the random complex voltage can be defined as:

$$P_{rec} = \frac{1}{2} \langle V_{oc}(t) V_{oc}^*(t) \rangle. \quad (5.14)$$

We can see that the right side of this equation is equivalent to the autocorrelation function of the complex voltage with the value of Δt is set to zero. Therefore, the formulation of the average received power in terms of autocorrelation function can be written as:

$$\begin{aligned}
P_{rec} = & R_{V_{oc}}(0) \\
= & \frac{1}{2} \oint [\langle |E_\theta|^2 \rangle |A_\theta|^2 + \langle |E_\phi|^2 \rangle |A_\phi|^2] d\Omega \\
& + [|E_{l\theta}|^2 |A_{l\theta}|^2 + |E_{l\phi}|^2 |A_{l\phi}|^2 + 2 |E_{l\theta}| |E_{l\phi}| |A_{l\theta}| |A_{l\phi}| \cos(\psi_{ch} - \psi_{ant})]. \quad (5.15)
\end{aligned}$$

Although the average received power can be defined using Equation (5.15), the equation contains polarimetric incident field parameters that are difficult to be characterised. In order to obtain a more tractable formulation, several characteristics of the incident and antenna pattern fields are utilised [125], which are:

- $\langle |E_\theta|^2 \rangle = 2P_\theta p_\theta$
- $\langle |E_\phi|^2 \rangle = 2P_\phi p_\phi$

- $|E_{l\theta}|^2 = 2P_{l\theta}$
- $|E_{l\phi}|^2 = 2P_{l\phi}$
- $|A_{\theta|\phi}|^2 = G_{\theta|\phi}$

where $P_{\theta|\phi}$ is the available power in the θ and ϕ polarisations of the incident field's scattering component and $p_{\theta|\phi}$ denotes the Angle-of-Arrival (AoA) density functions of the θ and ϕ components and $P_{l\theta|\phi}$ is the power of the LoS component of the incident field. For the first two incident field characteristics to be used, both AoA density functions p_θ and p_ϕ must satisfy the following condition [99]:

$$\oint p_\theta(\Omega)d\Omega = \oint p_\phi(\Omega)d\Omega = 1. \quad (5.16)$$

The antenna gain pattern also must satisfy a condition where its gain is normalised as:

$$\oint \{G_\theta(\Omega) + G_\phi(\Omega)\}d\Omega = \eta 4\pi \quad (5.17)$$

where η is the antenna efficiency. Then, by using the listed characteristics, a new formulation of the average received power is defined as:

$$\begin{aligned} P_{rec} &= \frac{1}{2} \oint [2P_\theta p_\theta |A_\theta|^2 + 2P_\phi p_\phi |A_\phi|^2] d\Omega \\ &\quad + 2P_{l\theta} |A_{l\theta}|^2 + 2P_{l\phi} |A_{l\phi}|^2 + 2\sqrt{2P_{l\theta}(2P_{l\theta})} A_{l\theta} A_{l\phi} \cos(\psi_{ch} - \psi_{ant}) \\ &= \underbrace{\oint [P_\theta p_\theta G_\theta + P_\phi p_\phi G_\phi] d\Omega}_{\text{Scattering part}} + \underbrace{\oint [P_{l\theta} G_{l\theta} + P_{l\phi} G_{l\phi} + 2\sqrt{P_{l\theta} P_{l\phi} G_{l\theta} G_{l\phi}} \cos(\psi_{ch} - \psi_{ant})]}_{\text{LoS part}} \end{aligned} \quad (5.18)$$

In order to further simplify this formulation, two propagation channel properties which are Ricean K factor and the cross polarisation discrimination (XPD) are utilised where both are related to the powers of the LoS and scattering components. In our case, the Ricean K factor for the θ and ϕ components of the incident waves K_θ and K_ϕ can be defined as the ratio between the power of LoS component and the power of the scattering component of the incident field. Therefore, they are written as:

$$K_\theta = \frac{P_{l\theta}}{P_\theta} \quad K_\phi = \frac{P_{l\phi}}{P_\phi} \quad (5.19)$$

As for the channel XPD, its definition is separated into two categories where first one is the cross polarisation discrimination of the scattering component XPD_{sc} and the second

is the total incident field XPD. Mathematically, both XPD parameters are defined in this thesis as:

$$\text{XPD}_{sc} = \frac{P_\theta}{P_\phi} \quad (5.20)$$

$$\text{XPD} = \frac{P_{l\theta} + P_\theta}{P_{l\phi} + P_\phi} \quad (5.21)$$

The XPD can be written in terms of XPD_{sc} as:

$$\begin{aligned} \text{XPD} &= \frac{P_\theta}{P_\phi} \left(\frac{1 + K_\theta}{1 + K_\phi} \right) \\ &= \text{XPD}_{sc} \left(\frac{1 + K_\theta}{1 + K_\phi} \right) \end{aligned} \quad (5.22)$$

Using Equation (5.19), it is possible to replace $P_{l\theta}$ and $P_{l\phi}$ in the LoS part of Equation (5.18) so that the average received power can be written as:

$$\begin{aligned} P_{rec} &= \oint [P_\theta p_\theta G_\theta + P_\phi p_\phi G_\phi] d\Omega \\ &\quad + K_\theta P_\theta G_{l\theta} + K_\phi P_\phi G_{l\phi} + 2\sqrt{K_\theta P_\theta K_\phi P_\phi G_{l\theta} G_{l\phi}} \cos(\psi_{ch} - \psi_{ant}) \end{aligned} \quad (5.23)$$

Going back to the MEG formulation as provided in Equation (5.3), the total power available in both polarisations is also need be formulated as this will be the reference power level for the average received power by an antenna. By considering the LoS and scattering components, the total available power in both polarisations is defined as:

$$\begin{aligned} P_{tot} &= P_{tot,\theta} + P_{tot,\phi} \\ &= P_{l\theta} + P_\theta + P_{l\phi} + P_\phi \end{aligned} \quad (5.24)$$

Combination of Equations (5.23) and (5.24) produces a crude formulation of MEG of an antenna in Ricean channel that includes the antenna and LoS component phases, which is given by:

$$\begin{aligned} \text{MEG} &= \frac{P_{rec}}{P_{tot}} \\ &= \frac{\oint \left[\underbrace{P_\theta p_\theta G_\theta}_{\text{i}} + \underbrace{P_\phi p_\phi G_\phi}_{\text{ii}} \right] d\Omega + \underbrace{K_\theta P_\theta G_{l\theta}}_{\text{iii}} + \underbrace{K_\phi P_\phi G_{l\phi}}_{\text{iv}}}{P_{l\theta} + P_\theta + P_{l\phi} + P_\phi} \\ &\quad + \frac{2\sqrt{K_\theta P_\theta K_\phi P_\phi G_{l\theta} G_{l\phi}} \cos(\psi_{ch} - \psi_{ant})}{\underbrace{\phantom{2\sqrt{K_\theta P_\theta K_\phi P_\phi G_{l\theta} G_{l\phi}} \cos(\psi_{ch} - \psi_{ant})}}_{\text{v}}} \end{aligned} \quad (5.25)$$

Although Equation (5.25) provides the complete formulation of MEG, the use of power parameters which are P_θ , $P_{l\theta}$, P_ϕ and $P_{l\phi}$ in the formulation is not suitable as these values are very rarely utilised in characterising any propagation channel. This creates a problem where the formulation can not be used for various types of environment since the required channel parameters are not easily available in the literature. Therefore, it is important to consider the availability of the channel parameters when constructing such formulation in order for it to be more robust and able to take advantage from numerous channel measurements or simulations that have been conducted. With this in mind, the underbraced items of Equation (5.25) with the common denominator are further simplified with the use of Ricean K factor and XPD definitions as described in Equations (5.19), (5.21) and (5.22). Below are the list of underbraced items which have been simplified:

$$\begin{aligned}
\text{i. } & \frac{P_\theta p_\theta G_\theta}{P_{l\theta} + P_\theta + P_{l\phi} + P_\phi} = \left(\frac{\text{XPD}}{1 + \text{XPD}} \right) \frac{p_\theta G_\theta}{(1 + K_\theta)} \\
\text{ii. } & \frac{P_\phi p_\phi G_\phi}{P_{l\theta} + P_\theta + P_{l\phi} + P_\phi} = \left(\frac{1}{1 + \text{XPD}} \right) \frac{p_\phi G_\phi}{(1 + K_\phi)} \\
\text{iii. } & \frac{K_\theta P_\theta G_{l\theta}}{P_{l\theta} + P_\theta + P_{l\phi} + P_\phi} = \left(\frac{\text{XPD}}{1 + \text{XPD}} \right) \frac{K_\theta G_{l\theta}}{1 + K_\theta} \\
\text{iv. } & \frac{K_\phi P_\phi G_{l\phi}}{P_{l\theta} + P_\theta + P_{l\phi} + P_\phi} = \left(\frac{1}{1 + \text{XPD}} \right) \frac{K_\phi G_{l\phi}}{1 + K_\phi} \\
\text{v. } & \frac{2\sqrt{K_\theta P_\theta K_\phi P_\phi G_{l\theta} G_{l\phi}}}{P_{l\theta} + P_\theta + P_{l\phi} + P_\phi} = \frac{2}{1 + \text{XPD}} \sqrt{\frac{\text{XPD} K_\theta G_{l\theta} K_\phi G_{l\phi}}{(1 + K_\theta)(1 + K_\phi)}}
\end{aligned}$$

Finally, by inserting Item i, ii, iii, iv and v into Equation (5.25), the formulation for MEG in Ricean channel with antenna and LoS components phases can be defined as:

$$\begin{aligned}
\text{MEG} = & \frac{1}{1 + \text{XPD}} \oint \left[\underbrace{\frac{\text{XPD } p_\theta G_\theta}{(1 + K_\theta)} + \frac{p_\phi G_\phi}{(1 + K_\phi)}}_{\text{Scattering part}} \right] d\Omega \\
& + \frac{1}{1 + \text{XPD}} \left[\underbrace{\left(\frac{K_\theta}{1 + K_\theta} \right) \text{XPD } G_{l\theta} + \left(\frac{K_\phi}{1 + K_\phi} \right) G_{l\phi}}_{\text{LoS part i}} \right] \\
& + 2 \underbrace{\sqrt{\frac{\text{XPD} K_\theta G_{l\theta} K_\phi G_{l\phi}}{(1 + K_\theta)(1 + K_\phi)}} \cos(\psi_{ch} - \psi_{ant})}_{\text{LoS part ii}} \Big]. \tag{5.26}
\end{aligned}$$

The new MEG formulation comprises of three parts where the first part only considers the antenna response to the scattering part of the incident waves. It is identical to

the MEG formulation in Rayleigh fading channel when the value of K_θ and K_ϕ is zero. As for the other two parts, both are related to the antenna reaction to the LoS component of the incoming waves. Aside from the value of K factors and XPD, the magnitude of the LoS part is strongly dependent on the polarisation mismatch parameter between the LoS component and the corresponding antenna gain, which is represented by $\cos(\psi_{ch} - \psi_{ant})$. This allows for an accurate MEG evaluation of a generally polarised antenna such as circular, elliptical or linear in a Ricean fading channel that contains a LoS component with various polarisation states. When the LoS component and the antenna field are perfectly matched, the polarisation mismatch parameter will have a value of 1 which then provide the maximum magnitude of the LoS part. However, for a total mismatch, the polarisation mismatch parameter will take value of -1 which in this case the contribution of the LoS part will be the very minimum.

5.2.3 MEG analysis of a dual circularly polarised SFPQHA array

Antenna system for case study

The selected antenna system for this analysis is a dual circularly polarised single folded printed quadrifilar helix antenna (SFPQHA) array with a separation distance between the two orthogonally polarised components is 80 mm. In order for the formulation to be computed, the three dimensional (3-D) θ and ϕ components of the antennas gain pattern and the phase difference of θ and ϕ components of the antennas field pattern are required. Due to limited antenna measurement capabilities that are available for this work especially in terms of accurate 3-D angle positioning, simulated result of the these parameters are utilised as the inputs in the MEG formulation. Fig. 5.1 shows the 3-D co and cross-polarised gain pattern of the right and left hand circular polarised SFPQHAs.

Channel parameters

In the proposed MEG formulation, there are five basic channel parameters that are needed, which are the channel cross polarisation discrimination XPD, Ricean K factor

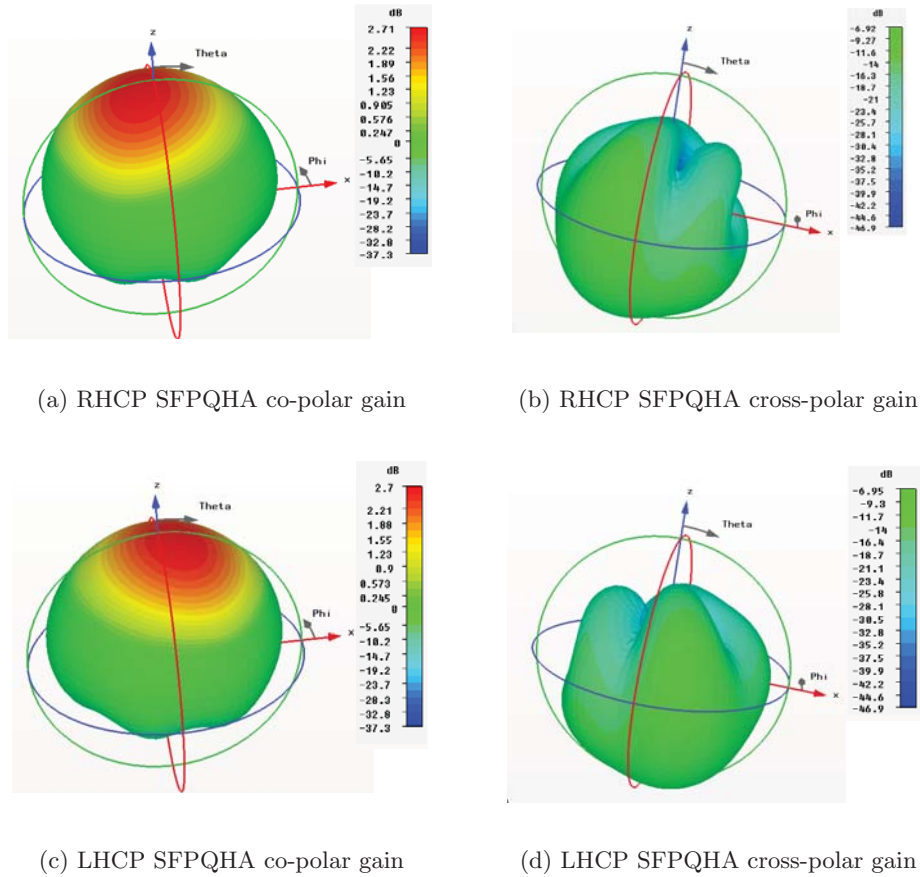


Figure 5.1: 3-D co and cross polarised gain patterns of the SFPQHA array.

in both polarisations $K_{\theta|\phi}$, AoA density function of the incoming incident fields $p_{\theta|\phi}$, AoA of the LoS component of the incident field (θ_l, ϕ_l) and phase difference between θ and ϕ components of the LoS incident field. In order to investigate the impact of the channel parameters on the MEG performance of an antenna, each of the parameters is fixed or varied depending on the requirement of the study. In our case, the following characteristics are used for the channel parameters:

- XPD is varied from -10 dB to 10 dB. These values are taken as representatives of the depolarisation mechanism in a realistic environment. Although higher absolute value of XPD may be possible especially for a linear polarised transmission in a LoS channel, the used range is deemed sufficient to provide a comprehensive view on its impact.

- Ricean K factors of the θ and ϕ components of the incident waves are considered to be equal ($K_\theta = K_\phi$) and its values are $-\infty$ (complete NLoS channel), -20 , -10 , -5 , 0 , 5 , 10 , 20 and ∞ dB (complete LoS channel).
- AoA of the LoS incident field (θ_l, ϕ_l) in terms of co-elevation and azimuth angles is $(60^\circ, 90^\circ)$. This corresponds to a satellite elevation angle of 30° and the direction of the satellite is perpendicular to the antenna azimuthally. The value of 30° is taken as it is the mean of elevation angle for Iridium low earth orbit (LEO) satellites system [126] at the London attitude (51.5° N). Apart from that, it is also the value of the highest elevation angle for Inmarsat geostationary earth orbit (GEO) satellites for the United Kingdom [127].
- AoA density functions of the θ and ϕ components of the scattering waves are considered to be equal ($p_\theta(\theta, \phi) = p_\phi(\theta, \phi)$) and it is normally distributed with its mean of co-elevation angle m_θ of 60° (from zenith) and mean of azimuth angle m_ϕ of 90° . The standard deviation for both co-elevation and azimuth components $\sigma_{\theta|\phi}$ is fixed at 20° . Mathematically, both AoA density functions can be written as:

$$p_{\theta|\phi}(\theta, \phi) = p_{\theta|\phi}(\theta) \cdot p_{\theta|\phi}(\phi) \quad (5.27)$$

where

$$p_{\theta|\phi}(\theta) = C_1 e^{-\frac{[\theta - m_\theta]^2}{2\sigma_\theta^2}} \quad \text{and} \quad p_{\theta|\phi}(\phi) = C_2 e^{-\frac{[\phi - m_\phi]^2}{2\sigma_\phi^2}} \quad (5.28)$$

and C_1 and C_2 are constants determined by Equation (5.16).

- Phase difference between θ and ϕ components of the LoS incident field is varied from -0.5π rad to 0.5π rad which correspond to right hand (RHCP) and left hand (LHCP) circular polarisations respectively.

Ricean K factor $K_{\theta|\phi} = -\infty$ dB or NLoS channel

For $K_{\theta|\phi}$ value of $-\infty$ dB, the channel behaves as a total NLoS channel with its envelope and phase are Rayleigh and uniformly distributed respectively. Going back to the MEG formulation in Equation (5.26), this formulation is reduced to the MEG equation in Rayleigh channel (Equation (2.27)) when both K factors are $-\infty$ dB or zero in linear

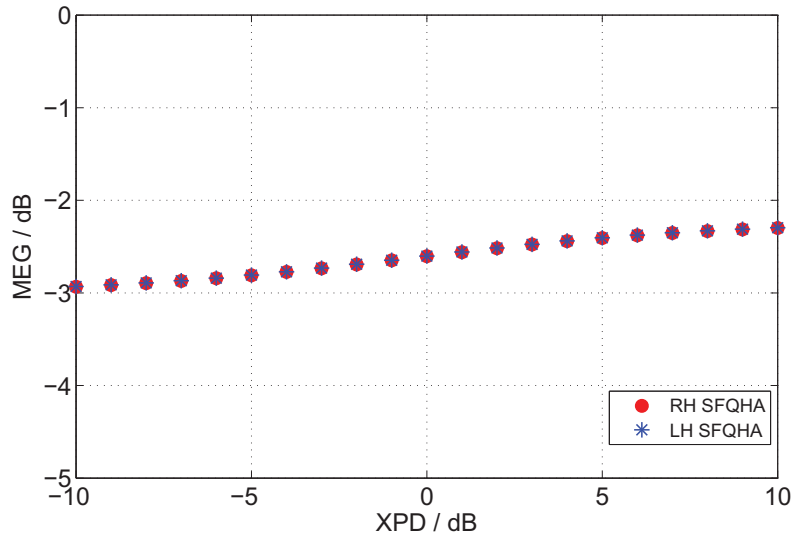


Figure 5.2: MEG of the RHCP and LHCP SFPQHAs at Ricean K factor of $-\infty$ dB with varying XPD.

scale. Fig. 5.2 shows the MEG of RHCP and LHCP SFPQHA with $K_{\theta|\phi} = -\infty$ dB and varying value of XPD. The SFPQHAs have almost identical values of MEG for every XPD although they are orthogonally polarised. This shows that orthogonal circularly polarised antennas exhibit equal received power properties in a NLoS channel regardless of the value of XPD as the radiation field of both antenna consists equal magnitude of θ and ϕ components.

Ricean K factor $K_{\theta|\phi} = -20$ dB, -10 dB and -5 dB

Three values of K factor that correspond to the condition where LoS component power is less than the power of scattering components are utilised in this study, which are -20 , -10 and -5 dB as shown in Fig. 5.3. For a very low K factor, the LoS component phase ψ_{ch} has little influence on the MEG value of both antennas as indicated by Fig. 5.3a for K factor of -20 dB. As the K factor increases gradually to -5 dB, the MEG value of RHCP and LHCP SFPQHAs started to be influenced by the ψ_{ch} variations where the biggest difference of MEG between the two antennas is when the ψ_{ch} are at the values of -0.5π rad and 0.5π rad. Meanwhile the lowest difference is when ψ_{ch} is 0,

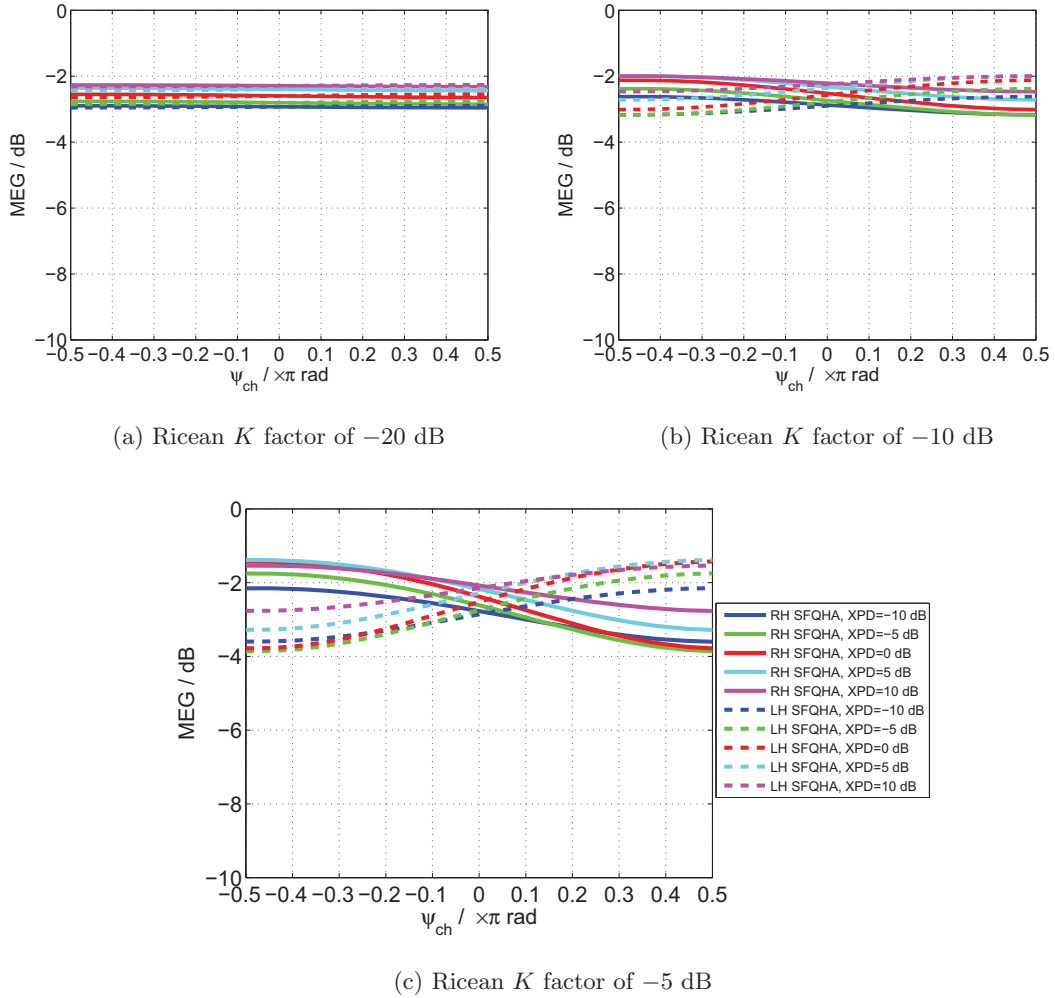


Figure 5.3: MEG of the RHCP and LHCP SFPQHAs at Ricean K factor of -20 , -10 and -5 dB with varying XPD and ψ_{ch} .

which implies that the LoS component is 45° slanted linearly polarised for XPD of 0 dB. As for the XPD, its impact on the MEG value when the K factor is very low is not significant as shown in Fig. 5.3a where for value of XPD ranges from -10 to 10 dB, the difference of MEG between the antennas is only about 1 dB. However, its impact grows as the K factor increases with the biggest difference of MEG is when the XPD equals to 0 dB.

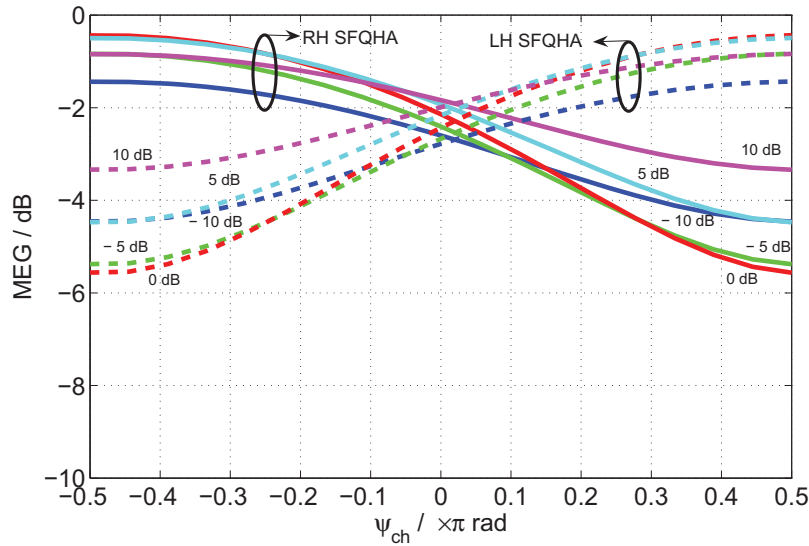


Figure 5.4: MEG of the RHCP and LHCP SFPQHAs at Ricean K factor of 0 dB with varying XPD and ψ_{ch} .

Ricean K factor $K_{\theta|\phi} = 0$ dB

For Ricean K factor of 0 dB, which implies that the LoS component power is equal to the power of the scattering components, it is shown in Fig. 5.4 that a much pronounced separation between the MEG values of RHCP and LHCP SFPQHAs especially when ψ_{ch} are near to -0.5π rad and 0.5π rad. The MEG of both antennas seems to converge at a point of $\psi = 0$ rad, which indicated that average received power of both antenna is nearly equal when the LoS component phase difference is nearly zero. When the LoS component is nearly circular polarised either RHCP or LHCP, the XPD of 0 dB always provide the biggest MEG difference between the two antennas while higher absolute value of XPD reduces this gain difference.

Ricean K factor $K_{\theta|\phi} = 5$ dB, 10 dB and 20 dB

The effect of XPD and ψ_{ch} on the MEG values of the SFPQHA array was also investigated for Ricean K factor of 5, 10 and 20 dB as shown in Fig. 5.5 where the LoS component power is significantly higher than the scattering component power. The convergence of MEG values of both antennas to the point of $\psi_{ch} = 0.02\pi$ rad becomes

stronger as the K factor increases from 5 to 20 dB. Apart from that, the increase of K factor also further widens the MEG difference between the two antennas regardless of the channel XPD, which is clearly shown when comparing the result of K factor of 5 dB in Fig. 5.5a with the K factor of 20 dB result as shown in Fig. 5.5c. By taking the K factor of 20 dB as an example, the biggest MEG difference of about 20 dB between the two orthogonally polarised SFPQHAs is achieved when the XPD is 0 dB and the LoS component is either RHCP or LHCP. As the XPD increases in absolute term, the MEG values between the antennas become closer to each other where in the case of K factor of 20 dB and ψ_{ch} is $\pm\frac{\pi}{2}$ rad, the difference is only about 4.5 dB for XPD of 10 dB.

Rice K factor $K_{\theta|\phi} = \infty$ dB or LoS channel

In a total LoS channel, the value of Ricean K factor will be nearing to ∞ dB since the channel only consisting of LoS component. Therefore, the MEG formulation of Equation (5.26) can be reduced to

$$\text{MEG} = \frac{1}{1 + \text{XPD}} \left[\text{XPD}G_{l\theta} + G_{l\phi} + 2\sqrt{\text{XPD}G_{l\theta}G_{l\phi}} \cos(\psi_{ch} - \psi_{ant}) \right]. \quad (5.29)$$

By utilising this equation, the impact of XPD and ψ_{ch} on the MEG of both antennas can be investigated in a complete LoS channel. Fig. 5.6 shows the MEG value of RHC and LHCP SFPQHAs with XPD value from -10 to 10 dB and varying value of ψ_{ch} . When the LoS component has the same sense of elliptical polarisation with either of the antennas, the XPD has little impact on the MEG value as indicated by the MEG of RHCP SFPQHA when ψ_{ch} has negative value, which indicated that the LoS component has right sense of polarisation. The same can also be said about LHCP SFPQHA when the phase of LoS component is in the range from 0 to 0.5π rad. The biggest MEG difference between the two antennas occurred when the LoS component is completely circularly polarised, which is characterised by XPD of zero dB and ψ_{ch} of $\pm\frac{\pi}{2}$ rad.

Effect of Ricean K factor with XPD fixed at 0 dB

The impact of Ricean K factor on the MEG value is also studied where in this case, the channel XPD is fixed at 0 dB. Fig. 5.7a and 5.7b show the MEG value when the K

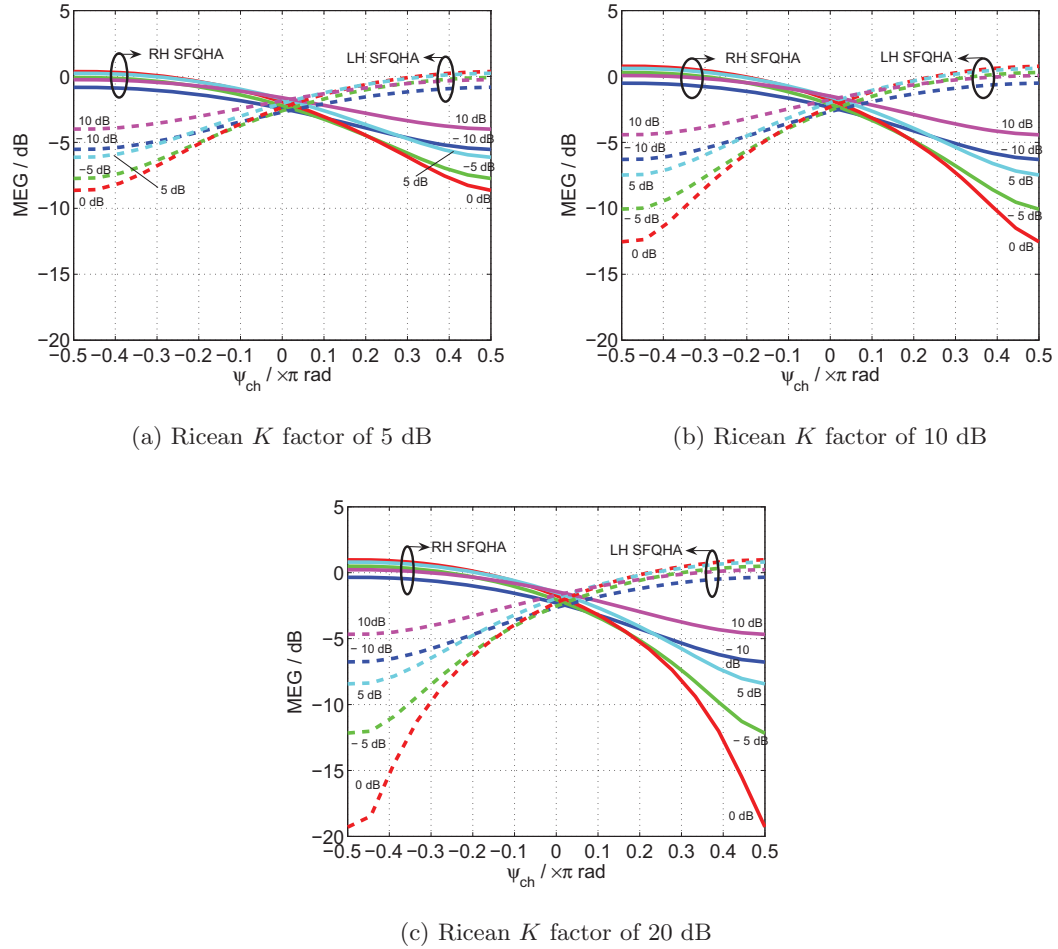


Figure 5.5: MEG of the RHCP and LHCP SFPQHAs at Ricean K factor of 5, 10 and 20 dB with varying XPD and ψ_{ch} .

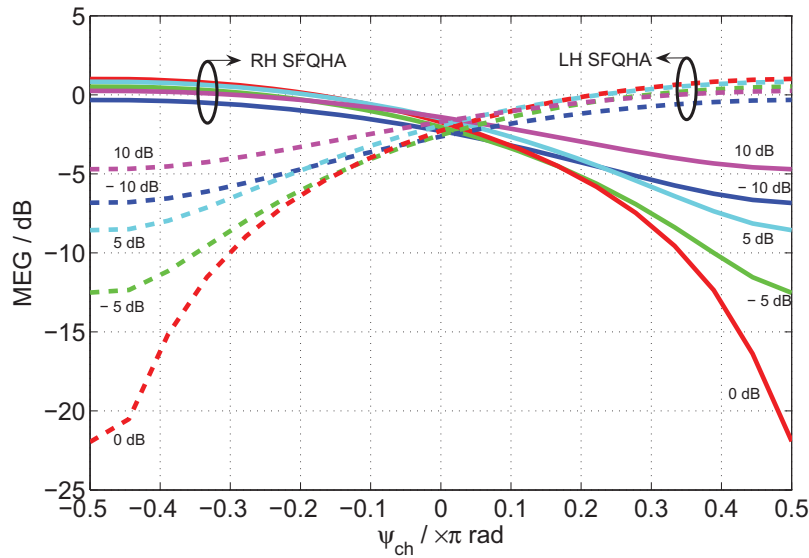


Figure 5.6: MEG of the RHCP and LHCP SFPQHAs at Ricean K factor of ∞ dB with varying XPD and ψ_{ch} .

factor increases from $-\infty$ to ∞ dB with varying ψ_{ch} for RHC and LHCP SFPQHAs respectively. For both antennas, the increase of K factor is beneficial to the antenna's MEG only when the LoS component has the same sense of polarisation as the antenna. However, when the antenna and LoS component have opposite sense of polarisation, an increase of K factor reduces the antenna capability as indicated by the reduction of antenna's MEG. For other values of channel XPD, it is expected that the resultant graphs will be much straighter and the impact of K factor on the MEG value will be less visible. This conclusion is supported by looking at previous result such as in Fig. 5.6 where higher absolute values of XPD provide a much levelled magnitude of MEG as the ψ_{ch} changes, hence a straighter graph of MEG value with varying ψ_{ch} .

5.3 Correlation analysis

5.3.1 Complex correlation in Rayleigh and Ricean channels

Complex correlation between the received voltage of two antennas in Rayleigh channel can be calculated using Equation (2.24), which requires the antennas 3-D complex field

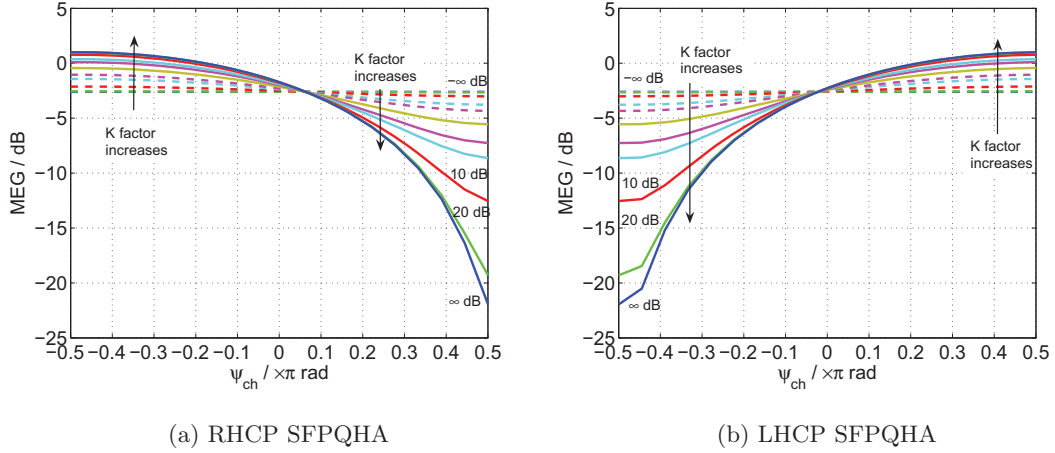


Figure 5.7: MEG of the RHCP and LHCP SFPQHAs with fixed XPD = 0 dB and varying Ricean K factor and ψ_{ch} .

pattern and the channel's XPD and AoA distribution. One important characteristic of complex correlation is that it only evaluates the random component of the channel [128]. Therefore, evaluation of complex correlation in Ricean channel does not depend on the LoS component but only considers the random part of the channel.

5.3.2 Effect of the channel properties

In the formulation of complex correlation, there are two channel characteristics that can be adjusted which are the channel XPD and AoA distribution of the incident waves. In this investigation, the value of channel XPD is varied from -20 dB to 20 dB. As for the AoA distribution of the θ and ϕ components of the incident waves, its co-elevation and azimuth distribution is taken to be normally distributed with equal mean and standard deviation. The mean of the co-elevation and azimuth distribution ($m_{\theta|\phi}$) is given as 0° , 30° , 60° and 90° from zenith while the standard deviation ($\sigma_{\theta|\phi}$) of 1° , 5° , 10° , 20° and 30° .

In order to investigate the impact of the channel on the complex correlation of a dual circularly polarised array, the SFPQHA arrays with separation distance of 20 mm and 80 mm are utilised. Their 3-D complex polarimetric field patterns are extracted from simulation which then become the input for the complex correlation computation.

SFPQHA array with 20 mm separation distance

Fig. 5.8 shows the magnitude of complex correlation of the SFPQHA array with 20 mm separation for various values of channel XPD, mean and standard deviation of the AoA distribution. Variation of channel XPD from -20 dB to 20 dB has a very pronounced impact on the complex correlation where the lowest correlation occurred when the XPD is 0 dB regardless of the AoA distribution properties. This effect is due to the fact that for an XPD of 0 dB, the incident waves has equal average power in θ and ϕ components which indicates that the channel is totally decorrelated in terms of its θ and ϕ components. Such channel decorrelation will certainly provide the lowest value of complex correlation for an orthogonally polarised antennas. However, when the XPD increases or decreases to 20 dB or -20 dB respectively, the correlation also increases depending on the $m_{\theta|\phi}$ and $\sigma_{\theta|\phi}$ of the channel AoA.

In Fig. 5.8a of $m_{\theta|\phi} = 0^\circ$, it is shown that $\sigma_{\theta|\phi}$ has significant impact on the complex correlation where $\sigma_{\theta|\phi} = 1^\circ$ causes the highest correlation as the XPD increases or decreases while lower correlation is experienced with the widening of $\sigma_{\theta|\phi}$ to 30° . However, the impact of $\sigma_{\theta|\phi}$ on the complex correlation is reduced when the mean of the AoA distribution $m_{\theta|\phi}$ increases from 0° (zenith) to 90° as shown by Fig. 5.8d. In this figure of $m_{\theta|\phi} = 90^\circ$, the variation of $\sigma_{\theta|\phi}$ from 1° to 30° only marginally reduces the correlation where the magnitude of the complex correlation for $\sigma_{\theta|\phi} = 30^\circ$ is still higher than 0.6. This effect is due to the reduction of polarisation orthogonality of the antennas at $\theta = 90^\circ$, which corresponds to the $m_{\theta|\phi}$ and also for other co-elevation angle higher than 90° . Therefore, the effect of $\sigma_{\theta|\phi}$ on the complex correlation is also dependent on the mean of the AoA due to changes in polarisation orthogonality of the antenna with regards to the co-elevation angle.

SFPQHA array with 80 mm separation distance

The impact of channel properties on the complex correlation of a SFPQHA array with 80 mm separation distance is also investigated and its results are presented in Fig 5.9. As a whole, it can be stated that the effects of channel XPD and AoA distribution on the antennas are largely similar to the SFPQHA array with 20 mm separation

array. Therefore, it would be interesting to study the impact of separation distance on the complex correlation and this study will be presented in the next subsection. For the channel XPD, the value of 0 dB again causes the antennas to exhibit the lowest complex correlation for all values of $m_{\theta|\phi}$ and $\sigma_{\theta|\phi}$ of the AoA distribution. Meanwhile, the channel AoA distribution which is presented by $m_{\theta|\phi}$ and $\sigma_{\theta|\phi}$ has exactly the same impacts on the complex correlation of these antennas as the one with a much closer separation.

5.3.3 Effect of antenna spacing

Based on previous studies on SFPQHA arrays with 20 mm and 80 mm separation, it is implied that spacing between two antennas is less influential in determining the complex correlation of these arrays. In order to verify this preliminary implication, complex correlation of six SFPQHA arrays with separation distance of 20 mm, 40 mm, 60 mm, 80 mm, 100 mm and 120 mm that correspond to 0.164λ to nearly 1λ at 2.45 GHz frequency was computed for two values of $m_{\theta|\phi}$ and $\sigma_{\theta|\phi}$. Results of this investigation are provided in Fig. 5.10. For $m_{\theta|\phi} = 0^\circ$ of the AoA distribution, although there are some variations of the magnitude of complex correlation with regards to the antenna spacing as shown in Fig 5.10a and 5.10b, its marginal effect can only be considered to be secondary when compared to the impact of channel XPD and $\sigma_{\theta|\phi}$.

Meanwhile, for $m_{\theta|\phi} = 60^\circ$, a more visible impact of the antenna spacing on the complex correlation of the antennas is evident especially for $\sigma_{\theta|\phi} = 30^\circ$. In this case, the magnitude of complex correlation reaches its maximum value at 40 mm or 60 mm spacings and then reduces as the spacing increases to 120 mm. This observation is valid for all values of XPD except for XPD of 0 dB where its complex correlation is hardly changed with respect to the antenna spacing. The difference of spacing impact on the correlation with $\sigma_{\theta|\phi} = 30^\circ$ is due to the changes of $m_{\theta|\phi}$ where for $m_{\theta|\phi} = 0^\circ$, the antennas have significantly higher polarisation purity at the surrounding region of the antenna zenith. However, when $m_{\theta|\phi} = 60^\circ$, the antenna field patterns at the corresponding region has higher cross polarisation which increases the correlation between the two closely spaced antennas. Then, by increasing the antenna spacing to

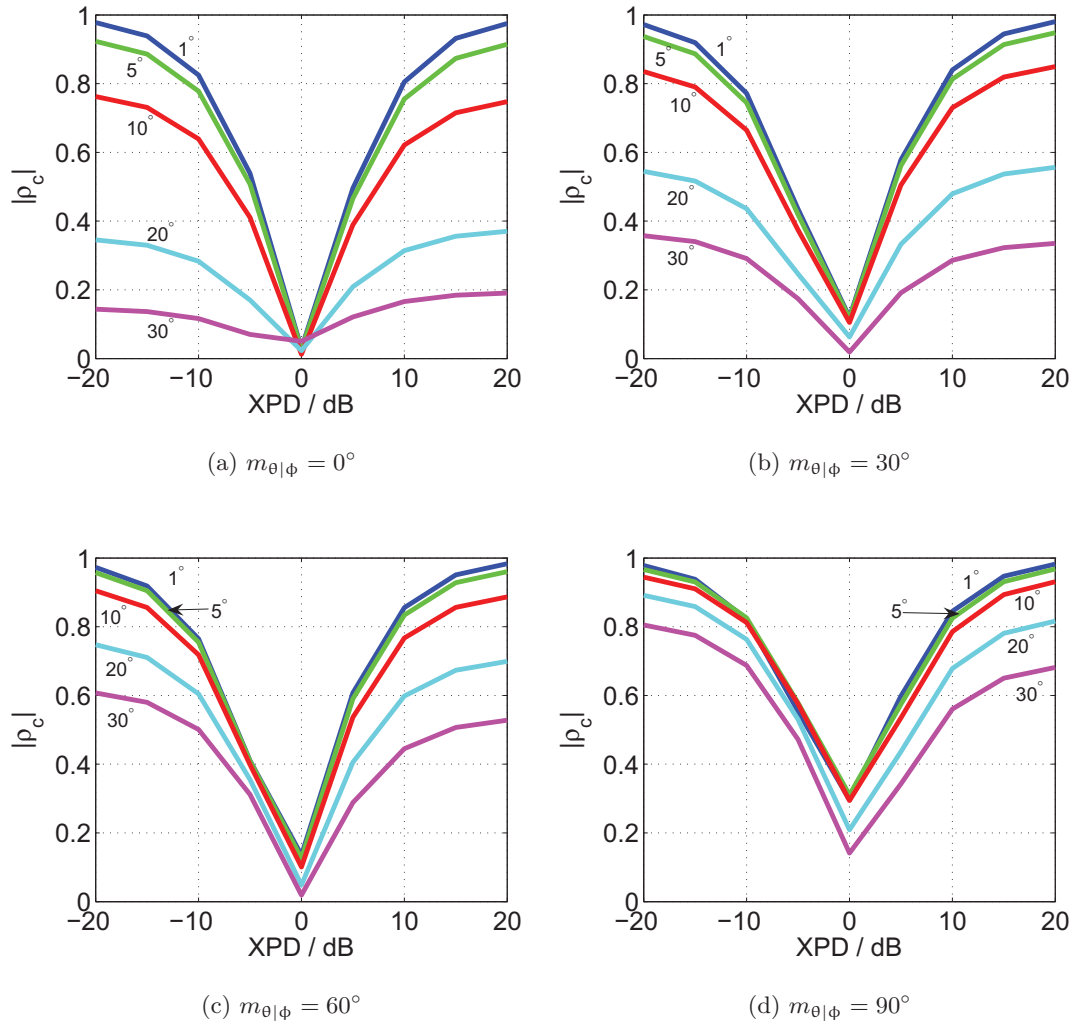


Figure 5.8: Magnitude of complex correlation of SFPQHA array with 20 mm antenna spacing with various values of channel XPD, $m_{\theta|\phi}$ and $\sigma_{\theta|\phi}$ of the AoA distribution.

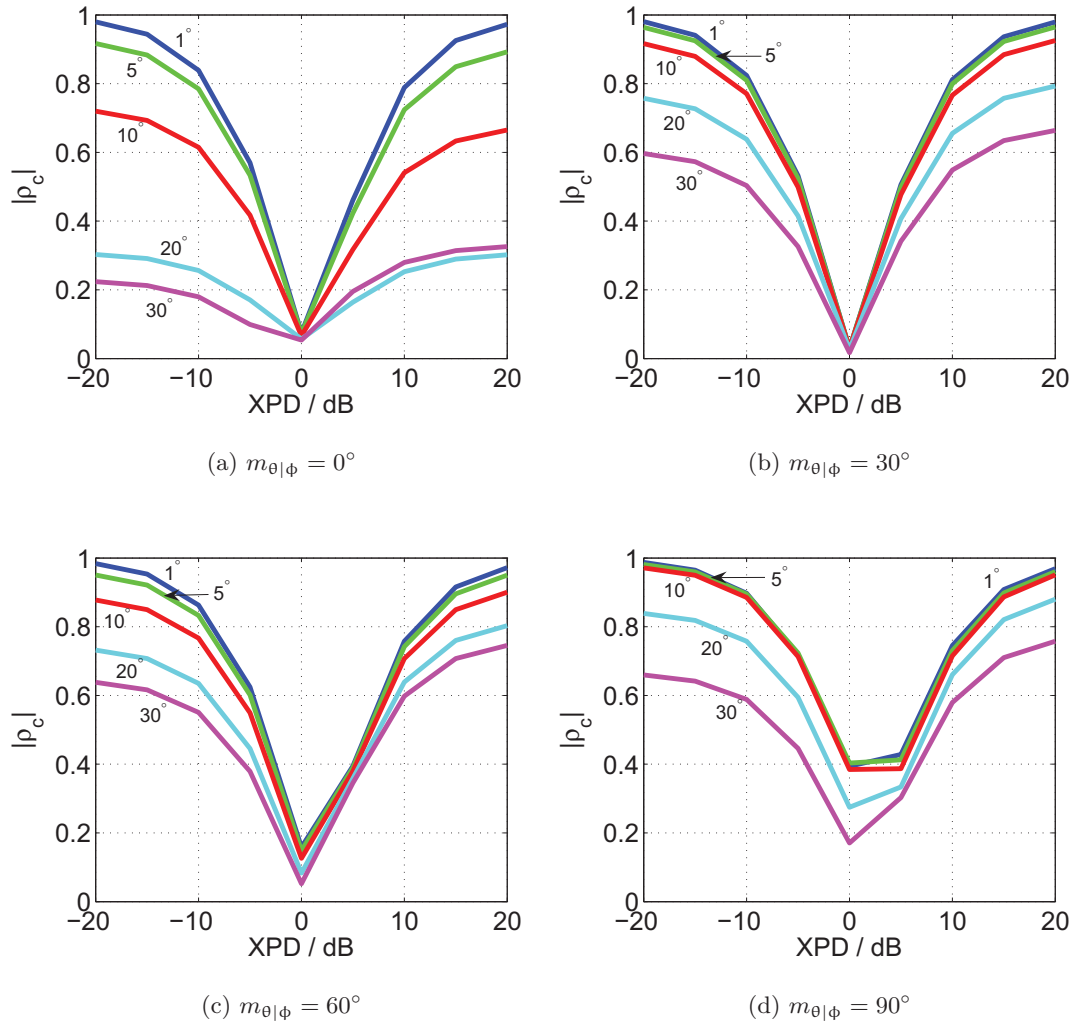


Figure 5.9: Magnitude of complex correlation of SFPQHA array with 80 mm antenna spacing with various values of channel XPD, $m_{\theta|\phi}$ and $\sigma_{\theta|\phi}$ of the AoA distribution.

120 mm, the correlation started to decrease as a result from spatial decorrelation as presented in Fig. 5.10d.

5.3.4 Effect of antenna polarisation

Another important aspect of the antenna characteristic that can be influential to the complex correlation of a dual circularly polarised array is the polarisation purity of the antenna. In order to isolate the impact of antenna polarisation on the correlation from other effects, the complex correlation formulation is revised so that only the polarisation of the antennas will be included in describing the antenna field pattern. In other words, other effects of antenna properties apart from polarisation are suppressed by removing these properties from the antennas field pattern and also collocating these antennas to remove the spatial dependency. Therefore, the antenna is represented as an isotropic antenna where its polarisation is defined to be constant over the whole angular domain.

Complex correlation formulation of an isotropic co-located dual circularly polarised array

For co-located dual polarised antennas, the complex correlation formulation can be written as:

$$\rho_{12} = \frac{R_{12}}{\sqrt{\sigma_1^2 \sigma_2^2}} \quad (5.30)$$

where

$$R_{12} = \oint (XPDA_{\theta 1}(\Omega)A_{\theta 2}^*(\Omega)p_{\theta}(\Omega) + A_{\phi 1}(\Omega)A_{\phi 2}^*(\Omega)p_{\phi}(\Omega)) d\Omega \quad (5.31)$$

and

$$\sigma_n^2 = \oint (XPDA_{\theta n}(\Omega)A_{\theta n}^*(\Omega)p_{\theta}(\Omega) + A_{\phi n}(\Omega)A_{\phi n}^*(\Omega)p_{\phi}(\Omega)) d\Omega. \quad (5.32)$$

In this formulation, the phase difference due to spatial separation is removed in order to evaluate the complex correlation of co-located antennas. Since only isotropic antenna with constant polarisation over the angular domain are considered, a compact way of representing polarisation needs to be included in this formulation. In [129], any polarisation of a plane wave can be described by polarisation ellipse as shown in Fig 5.11

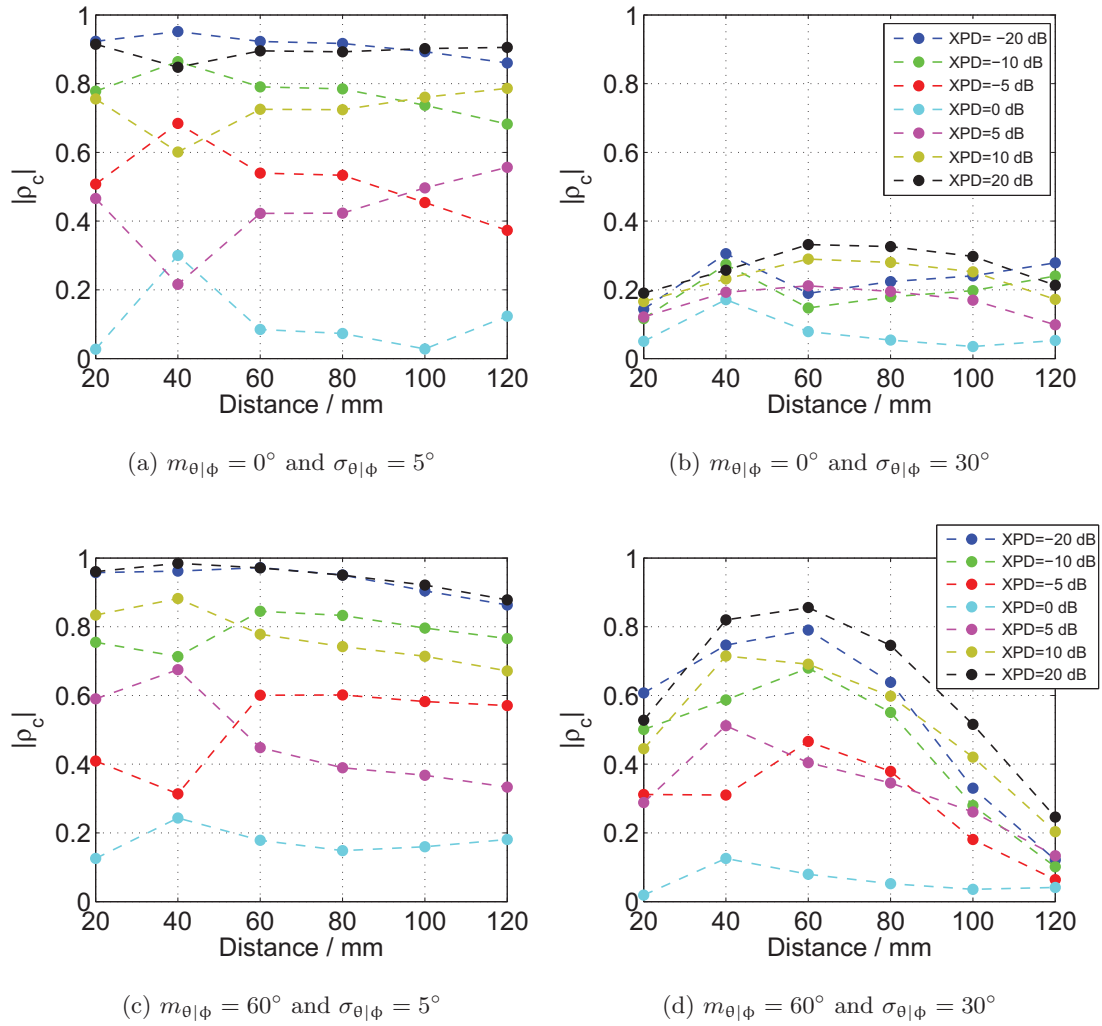


Figure 5.10: Magnitude of complex correlation of SFPQHA array with various antenna spacing in channels characterised by XPD, $m_{\theta|\phi}$ and $\sigma_{\theta|\phi}$ of the AoA distribution.

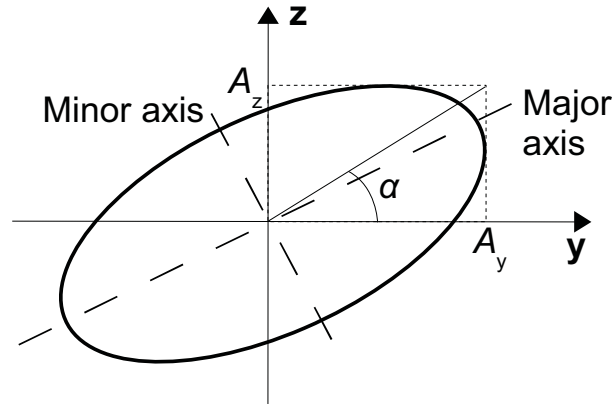


Figure 5.11: The polarisation ellipse showing the amplitudes A_z and A_y and angle α .

where the ellipse tracks the extremities of the resultant electric field. The polarisation ellipse can be described in various ways and one of them is by describing the ellipse in terms of α and ψ where the former is the angle from the y -axis to the diagonal of a box with sides parallel to the y and z axes that just encloses the ellipse and the latter denotes the phase by which A_z leads A_y . Mathematically, α can be written as:

$$\alpha = \arctan \left| \frac{A_z}{A_y} \right|. \quad (5.33)$$

For an isotropic antenna, its normalised radiated field A_i can be written in terms of α and ψ in spherical coordinate system as:

$$\begin{aligned} A_i &= \begin{pmatrix} A_{i,\theta} e^{j\xi_\theta} \\ A_{i,\phi} e^{j\xi_\phi} \end{pmatrix} = \begin{pmatrix} -\sin \alpha \\ \cos \alpha e^{j(\xi_\phi - \xi_\theta)} \end{pmatrix} \\ &= \begin{pmatrix} -\sin \alpha \\ \cos \alpha e^{j\psi} \end{pmatrix} \end{aligned} \quad (5.34)$$

where $\psi = \xi_\phi - \xi_\theta$ and ξ_θ and ξ_ϕ are the phases of the θ and ϕ components of the antenna field. By using the polarisation ellipse description, the isotropic antenna 1 and 2 far field patterns can be compactly approximated as:

$$\begin{pmatrix} A_{\theta 1}(\Omega) & A_{\phi 1}(\Omega) \\ A_{\theta 2}(\Omega) & A_{\phi 2}(\Omega) \end{pmatrix} = \begin{pmatrix} -\sin \alpha_1 & \cos \alpha_1 e^{j\psi_1} \\ -\sin \alpha_2 & \cos \alpha_2 e^{j\psi_2} \end{pmatrix} \quad (5.35)$$

where α_1 and α_2 are the polarisation ellipse angle of antenna 1 and 2 fields pattern and ψ_1 and ψ_2 are the phase difference of the first and second antennas 3-D θ and ϕ field components respectively.

By inserting elements of Equation (5.35) into Equation (5.31), a new formulation of R_{12} can be obtained as:

$$\begin{aligned} R_{12} &= \oint \left[\text{XPD}(-\sin \alpha_1)(-\sin \alpha_2)^* p_\theta + (\cos \alpha_1 e^{j\psi_1})(\cos \alpha_2 e^{j\psi_2})^* p_\phi \right] d\Omega \\ &= \oint \left[\text{XPD} \sin \alpha_1 \sin \alpha_2 p_\theta + \cos \alpha_1 \cos \alpha_2 e^{j(\psi_1 - \psi_2)} p_\phi \right] d\Omega \end{aligned} \quad (5.36)$$

Meanwhile, the σ_1 and σ_2 can also be given as:

$$\sigma_1^2 = \oint [\text{XPD} \sin^2 \alpha_1 p_\theta + \cos^2 \alpha_1 p_\phi] d\Omega \quad (5.37)$$

$$\sigma_2^2 = \oint [\text{XPD} \sin^2 \alpha_2 p_\theta + \cos^2 \alpha_2 p_\phi] d\Omega \quad (5.38)$$

Therefore, ρ_{12} can be calculated for isotropic polarised array using the new R_{12} , σ_1 and σ_2 and it is written as:

$$\rho_{12} = \frac{\oint [\text{XPD} \sin \alpha_1 \sin \alpha_2 p_\theta + \cos \alpha_1 \cos \alpha_2 e^{j(\psi_1 - \psi_2)} p_\phi] d\Omega}{\sqrt{\oint [\text{XPD} \sin^2 \alpha_1 p_\theta + \cos^2 \alpha_1 p_\phi] d\Omega} \cdot \sqrt{\oint [\text{XPD} \sin^2 \alpha_2 p_\theta + \cos^2 \alpha_2 p_\phi] d\Omega}} \quad (5.39)$$

Complex correlation evaluation of an isotropic polarised array

The formulation given in Equation (5.39) provides a simple method of studying the impact of antenna polarisation on the complex correlation of a polarised array in any described channel. For completeness, apart from the antenna polarisation, one channel property that is related to the polarisation response of the antenna which is the channel XPD is also varied from -20 dB to 20 dB. Meanwhile, the AoA distribution characteristics given as $m_{\theta|\phi}$ and $\sigma_{\theta|\phi}$ are considered to be fixed at 90° and 5° since the co-location and uniformity of the antennas causes the antennas to respond in the same way for any mean and standard deviation of the AoA distribution.

In this study, antenna 1 is fixed as a LHCP antenna with the polarisation of the antenna 2 is varied by changing the α_2 and ψ_2 of the polarisation ellipse. Therefore, the value of α_1 and ψ_1 are given as 0.25π rad and 0.5π rad that represents a LHCP antenna. For α_2 , the values from 0 rad to 0.5π rad are used where the former represented horizontal

polarisation and the latter is vertical polarisation. Meanwhile, the value of ψ_2 is taken from $-\pi$ rad to π rad. Listed below are some of the polarisation states that can be defined by the combination of α_2 and ψ_2 :

- $\alpha_2 = 0$ rad is a horizontal polarisation for all values of ψ_2
- $\alpha_2 = 0.25\pi$ rad and $\psi_2 = \pm\pi$ rad is a -45° slanted linear polarisation
- $\alpha_2 = 0.25\pi$ rad and $\psi_2 = -0.5\pi$ rad is a RH circular polarisation
- $\alpha_2 = 0.25\pi$ rad and $\psi_2 = 0$ rad is a 45° slanted linear polarisation
- $\alpha_2 = 0.5\pi$ rad is a vertical polarisation for all values of ψ_2

Fig. 5.12 presents the magnitude of complex correlation of a co-located polarised array where the polarisation of antenna 2 is varied depending on the values of α_2 and ψ_2 in a channel that is defined by its XPD and AoA distribution. In Fig. 5.12a where the channel XPD is -20 dB, it indicates that the power of the incident waves are highly concentrated in the horizontal polarisation. In this channel condition, it is observed that low correlation occurred when $\alpha_2 \simeq 0.5\pi$ rad which corresponds to the antenna 2 to be vertically polarised. Apart from $\alpha_1 \simeq 0.5\pi$ rad, all other combinations of α_2 and ψ_2 exhibit high correlation between the two antennas. As the channel XPD increases from -20 dB to -5 dB, the polarisation of antenna 2 started to shape the pattern of the complex correlation of these two antennas. By taking the result of XPD = -5 dB shown in Fig. 5.12c as an example, a region of low correlation is formed for $\alpha_2 \geq 0.25\pi$ rad and $\psi_2 \leq 0$ rad. Its effect can be attributed to the fact that the polarisation of antenna 2 in this region is badly matched with the incident wave and at the same time it is nearly orthogonal to the polarisation of antenna 1. These figures also reiterate the well known fact that the highest correlation occurred when antenna 2 has the same polarisation as antenna 1, which is defined by $\alpha_2 = 0.25\pi$ rad and $\psi_2 = 0.5\pi$ rad.

When the channel has the same average power in orthogonal polarisations (XPD = 0 dB), the region of low correlation is concentrated at $\alpha_2 = 0.25\pi$ rad and $\psi_2 = -0.5\pi$ rad which referred to the polarisation of antenna 2 to be RHCP. Therefore, perfect orthogonality of polarisation between antennas will only induce the lowest correlation when the channel XPD is 0 dB. Apart from that, the region where $\psi_2 \leq 0$ rad will always obtain low correlation since antenna 2 has the opposite sense of phase difference

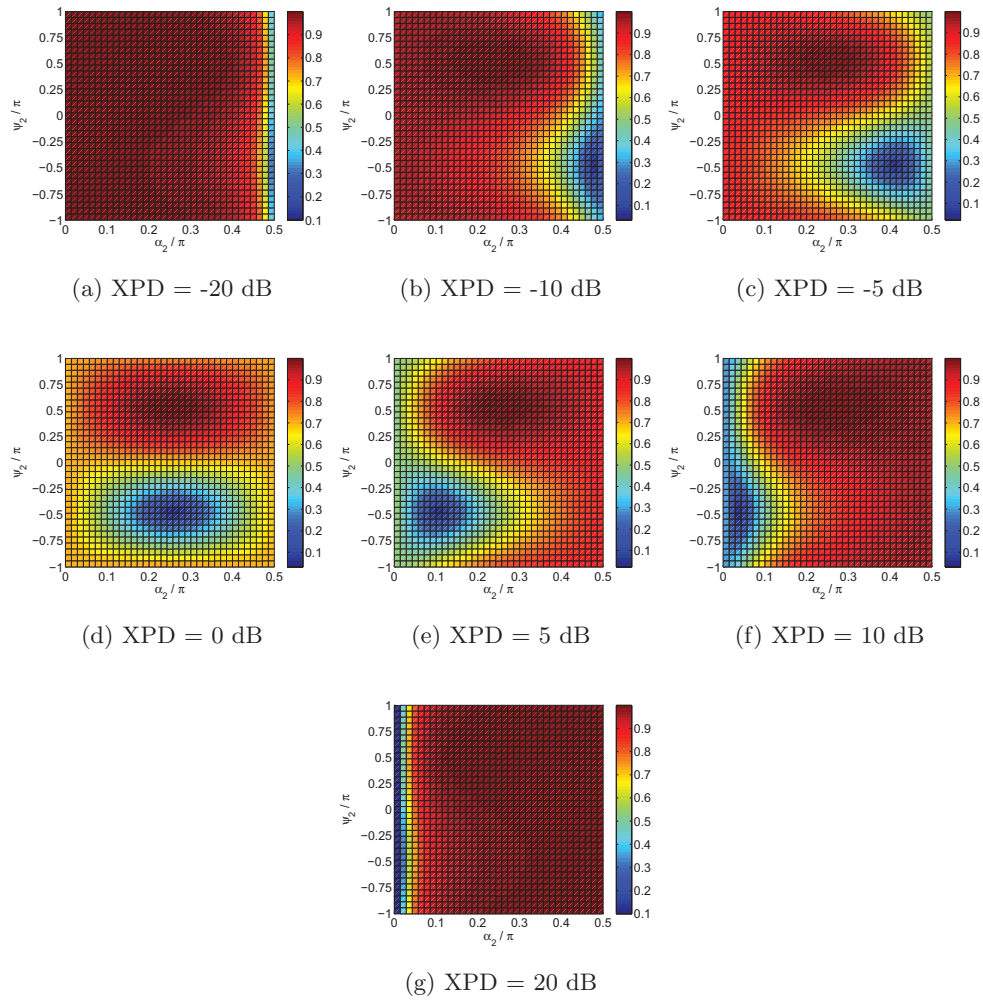


Figure 5.12: Magnitude of complex correlation of polarised array where antenna 1 is LHCP and antenna 2 polarisation is varied based on α_2 and ψ_2 in a channel characterised by various values of XPD and $\sigma_{\theta|\phi}$ of the AoA.

(ψ) when compared to antenna 1. Meanwhile, when we consider a channel with XPD of 5 dB and 10 dB, the complex correlation characteristic of these antennas is the mirror opposite of the results from XPD = -5 dB and XPD = -10 dB. For example, when the channel XPD = -5 dB, the low correlation region occurred when $\alpha_2 \leq 0.25\pi$ rad and $\psi_2 \leq 0$ rad as opposed to $\alpha_2 \geq 0.25\pi$ rad for XPD = 5 dB. As for the final value of XPD that was investigated, which is 20 dB, the complex correlation between the two antennas is at its lowest when $\alpha_2 \simeq 0$ rad regardless of the value of ψ_2 . At this value of XPD, the average channel power is highly concentrated in vertical polarisation while the lowest correlation occurred when antenna 2 is almost horizontally polarised as indicated by its α_2 .

5.4 Summary

For the purpose of analysing the received power of circularly polarised antennas in a Ricean channel, a new formulation of MEG that includes the LoS incident field and the corresponding antenna field phases is proposed in this chapter. This formulation allows for a more detailed evaluation of the MEG of a more generally polarised antenna in a Ricean channel by taking into account the effect of polarisation matching between the LoS incident field with the corresponding antenna field. In the case of evaluating a SFPQHA array, it is shown that the phase difference of the LoS component given as ψ_{ch} influences the branch power ratio of these antennas where its impact increases as the LoS component power increases, which is indicated by the Ricean K factor.

The complex correlation of a dual circularly polarised SFPQHA array was also studied for various channel conditions that are described by its XPD and AoA distribution. For any given AoA distribution, the complex correlation is highly dependent on the channel XPD where in the case of SFPQHA array, the lowest achievable correlation is at XPD= 0 dB. Meanwhile, the impact of $\sigma_{\theta|\phi}$ of the AoA distribution on the SFPQHA array correlation becomes less prominent as the $m_{\theta|\phi}$ moving closer to the azimuth plane ($m_{\theta|\phi} = 90^\circ$). This correlation difference can be attributed to the reduction of polarisation purity of the SFPQHA as the angle of incident becomes closer to the azimuth plane which is a common feature of a quadrifilar helix antenna where its axial

ratio decreases with the increase of co-elevation angle (taken from zenith). As for the effect of antenna spacing on the complex correlation of the SFPQHA array, it only plays a secondary role when compared to the effects of channel properties and antenna polarisation. The final part of this chapter presents a newly derived formulation which allows explicit evaluation of the antenna polarisation effect on the complex correlation of a co-located polarised isotropic antennas.

Chapter 6

Evaluation of receive MIMO antennas in LMS MIMO system via measurement campaigns

6.1 Introduction

A comprehensive evaluation of multiple antennas in a MIMO system requires the capacity of the system which utilises the evaluated antennas to be determined in the intended operating environment. The achieved capacity is then compared with the capacity of the same system but utilises a single antenna system or other multiple antennas system in the same operating environment. As mentioned in Section 2.4.2, effects of antennas on the capacity performance of a MIMO system can be evaluated by using three methods, which are the complete channel simulation with antenna effects, direct measurement and Over-the-Air (OTA) MIMO antenna testing where each method has its own advantages and disadvantages.

In the case of a land mobile satellite (LMS) MIMO system, due to the lack of channel models which integrate the receive antenna properties and facilities for OTA testing, the proposed dual circularly polarised arrays are evaluated in terms of their MIMO capabilities by conducting several measurement campaigns in different environments

where the proposed antennas are utilised as the receive antenna of the system. The satellite can be emulated using a transmitter placed at higher altitude than the receiver as to create a certain angle of elevation between the transmitter and the receiver. In this work, two measurement campaigns have been conducted in two different environments where the first one was in a rural area while the second campaign was carried out in a suburban environment. Apart from that, a preliminary study on the impact of antenna orientation on the system performance was also implemented where the receive antennas were tilted in a certain direction and angle during the measurements.

6.2 Measurement equipments and procedures

In this section, the equipments that were used in these measurements are explained in detail including the utilised channel sounder. The basic principles of the channel sounder are described together with its transmit and receive subsystems. It is then extended to the descriptions of the transmit and receive antennas that were used in the measurement campaigns. Aside from the measurement hardware, the procedures of conducting measurements are also given starting from the steps taken before the measurement up to the analysis of the measured data.

6.2.1 Elektrobit Propsound MIMO wideband channel sounder

The channel sounder used in these measurement campaigns is the Elektrobit Propsound MIMO wideband channel sounder, owned by the University of Surrey and has been utilised before in various measurements including the first measurement that characterised the LMS MIMO channel [29]. It comes with dedicated transmitter and receiver modules as shown in Fig. 6.1 which can be separated to allow outdoor measurements to be conducted. Descriptions of the transmitter and receiver modules will be provided in the subsequent subsections.

The sounder operation is based on direct sequence spread spectrum (DSSS) system where it transmits pseudo-noise (PN) codes over the air and the receiver utilises cross correlator techniques to extract the channel impulse response from the received sig-

nals. As for the MIMO channel matrix measurement which requires transmission and reception over multiple transmit and receive antennas, the sounder uses time division multiplexing (TDM) and electrical switching to change from one transmit/receive antenna to another transmit/receive antenna. In order to obtain the location data during an outdoor measurement, the transmitter and receiver modules of the sounder are equipped with a global positioning system (GPS) receiver.



(a) Transmitter



(b) Receiver

Figure 6.1: Elektrobit Propounder wideband channel sounder.

Transmitter

The sounder transmitter consists of four main modules, which are the controller module, IF module, RF module and antenna array subsystem as indicated in Fig. 6.2. The PN code generator provides the pre-determined maximal-length PN sequences, which are later binary phase-shifted keying (BPSK) modulated. The modulated signal is then up-converted to the selected carrier frequency and amplified for transmission. At the final stage, the antenna selection for the transmission is implemented at the antenna switching unit (ASU). In order to provide a precise timing reference to all modules, the sounder uses a stabilised rubidium clock which needs to be synchronised with the receiver's clock before the measurement commences.

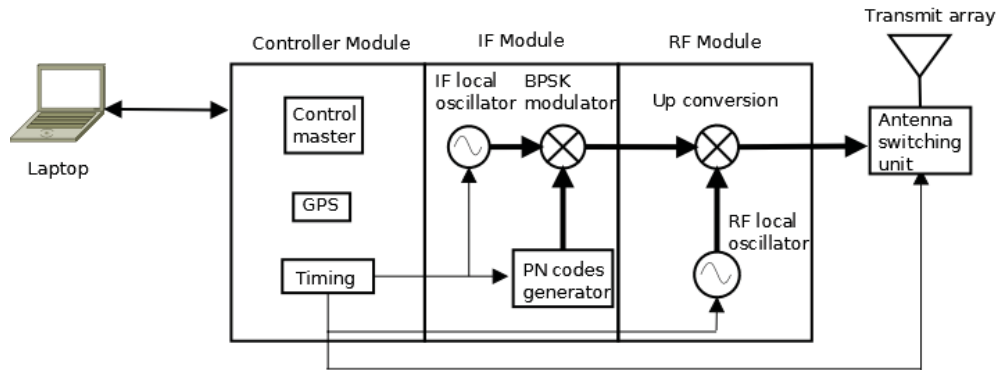


Figure 6.2: Channel sounder's transmitter architecture.

Receiver

At the receiver, the received signal from the selected receive antenna (based on ASU) was first down-converted and demodulated. The resultant baseband I/Q data is then sampled using high speed analog-to-digital converter (ADC) and stored at the RBPU module. Similar to the transmitter, the receiver also utilises a stabilised rubidium clock as the timing and frequency references for its operation. For the determination of the channel impulse response, the stored I/Q data is post-processed where the cross correlator approach is performed digitally. Fig. 6.3 shows the basic diagram of the architecture of the channel sounder's receiver.

Synchronisation and timing

Synchronisation between transmitter and receiver frequency reference is highly critical in the operation of channel sounding in order to ensure the process of capturing the impulse response at the receiver is done in the correct timing sequence. In the Prop-sound channel sounder, a rubidium clock is used at both transmitter and receiver as the precise and stable frequency reference. However, before any measurement is conducted, both rubidium clocks in both transmitter and receiver need to be synchronised. This synchronisation process consists of two phases which are the coarse frequency and fine phase tunings.

Timing configuration in a MIMO channel sounder is mainly concerned with selecting the appropriate chip and code properties for the measurement purposes and synchro-

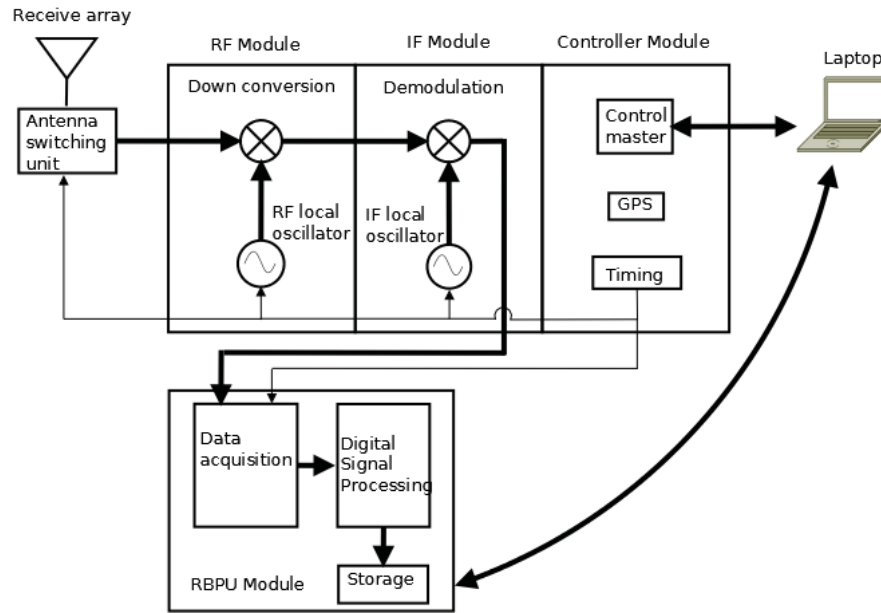


Figure 6.3: Channel sounder's receiver architecture.

nisng the generated code with the transmit and receive antennas switching unit. The transmitted codes consists of an N length of chips, where each chip is a bit of maximal-length PN sequence. The chip rate R_c is related to the null to null bandwidth of the transmitted signal B_{rf} with two samples per chip as:

$$B_{rf} = 2R_c. \quad (6.1)$$

For example, if the sounder is set to probe the channel at a bandwidth of 200 MHz, then the chip rate is 100 MHz which corresponds to a 10 ns for the duration of a single chip. A higher chip per code configuration can provide an increased processing gain but at the same time reduces the MIMO channel matrix sampling rate as each code will have a longer duration. In term of the code length, it must be configured so that it is longer than the expected total delay (absolute delay and excess delay) of the channel to avoid intersymbol interference.

Fig. 6.4 shows the timing configuration of the channel sounder together with the transmit and receive antennas switchings. In the diagram, the duration of a chip is represented by T_c and it is the inverse of the chip rate R_c . For a single code, its length T_{code} can be calculated as the multiplication of T_c with N_c , where N_c is the total number of chips per code. The value provides the capturing time window for the receiver

and it must be higher than the expected total delay of the channel. With regards to the antenna switching, the first transmit antenna is connected for the duration of $T_{code} \times (R_n + 1)$ where R_n is the number of receive antenna used. By doing so, the transmit antenna remains fixed while the receive antennas are connected one by one. The symbol G in the timing diagram denotes the guard band between each sequence of receive antenna switching. For a complete capturing of a single MIMO channel matrix, this process is repeated until the last transmit antenna.

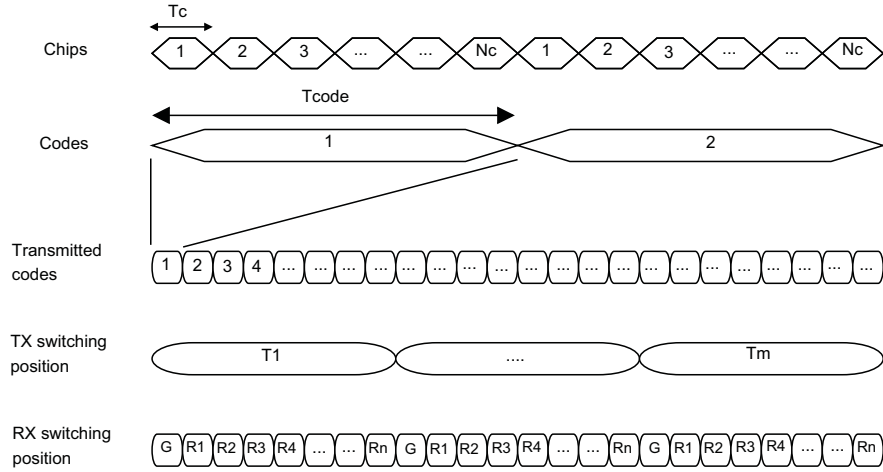


Figure 6.4: Timing diagram of the channel sounder.

Sampling

To ensure that the Doppler effect can be detected by the measurement, the sampling rate of a single MIMO channel matrix must be more than twice the maximum Doppler frequency experienced at the receiver due to its movement. Mathematically, this condition can be written as:

$$f_{samp} > 2f_{dmax} \quad (6.2)$$

where f_{dmax} is the maximum Doppler frequency at the receiver. Apart from that, the MIMO channel matrix must also be sampled within the channel coherence time, which is related to the Doppler spectrum.

Sensitivity and dynamic range

Sensitivity of the sounder's receiver determines the minimum power level that can be detected by the sounder during the measurement. Based on the sounder's manual provided by Elektrobit, the receiver sensitivity S_{rx} can be calculated by:

$$S_{rx} = n_{therm} + 10 \log_{10}(B_{rf}) + n_{sys} \quad (6.3)$$

where n_{therm} is the thermal noise of resistor which is given as -174 dBm/Hz, B_{rf} is the null-to-null bandwidth and n_{sys} denotes the noise figure of system which also is given at 3 dB. For example, a measurement with a bandwidth of 200 MHz will exhibit receiver sensitivity of -88 dBm as shown in calculation below:

$$\begin{aligned} S_{rx} &= n_{therm} + 10 \log_{10}(B_{rf}) + n_{sys} \\ &= -174 + 10 \log_{10}(200\text{M}) + 3 \\ &= -88 \text{ dBm.} \end{aligned}$$

Aside from the sensitivity of the receiver, the impulse response dynamic range (IRDR) is also highly important in the operation of the channel sounder. Its theoretical value $IRDR_{th}$ can be computed based on the following formulation:

$$IRDR_{th} = P_{tx} - A_{max,path} - S_{rx} + G_{process} \quad (6.4)$$

where P_{tx} denotes the transmit power, $A_{max,path}$ is the maximum path loss from the transmitter to the receiver, S_{rx} is as defined earlier and $G_{process}$ is the processing gain. The processing gain of the sounder $G_{process}$ can then be calculated as:

$$G_{process} = 10 \log_{10}(N_c) \quad (6.5)$$

where N_c is defined earlier as the number of chips per code. However, the measurable IRDR may also be limited by a value given by user as long as the theoretical IRDR is higher than the user-defined IRDR.

6.2.2 Transmit antennas

The antennas used at the transmitter of the sounder are highly directional patch antennas with circular polarisation either RHCP or LHCP senses as shown in Fig. 6.5a.

The implementation of highly directional antennas in these measurements is mainly to emulate the transmission from satellite which is always equipped with directional antennas. Elevation patterns of the radiated beam of both RHCP and LHCP transmit patch antennas are presented in Fig.6.6 where the antennas' maximum gain is around 12 to 13 dBic and their 3 dB beamwidth is approximately 30° .



(a) Transmit antennas



(b) Reference antenna

Figure 6.5: Photographs of the transmit antennas and reference antenna used in the measurements.

6.2.3 Receive antennas

There are three types of receive antennas that were used in the measurement campaigns, which are reference antennas, a dual polarised folded meandered printed quadrifilar helix antenna (FMPQHA) vertical array and a dual polarised single folded PQHA (SFPQHA) horizontal array. The reference antennas as pictured in Fig. 6.5b have an omnidirectional pattern in azimuth and its elevation pattern as provided in Fig. 6.7 has a maximum gain at 60° with 70° beamwidth. Meanwhile, the structural properties, radiation and impedance characteristics of the fabricated FMPQHA and SFPQHA arrays that were utilised in these measurements have been presented in Section 4.3.4 and 4.4.3 respectively.

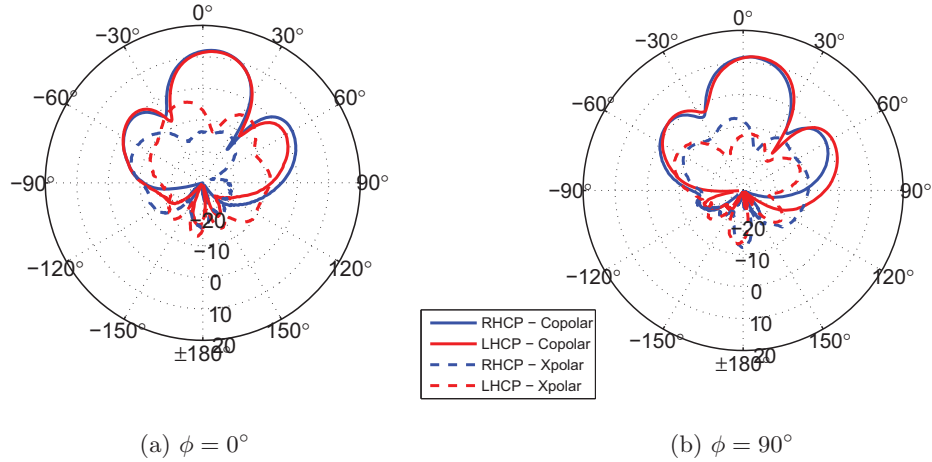


Figure 6.6: RHCP and LHCP transmit antennas elevation patterns (dBic).

6.2.4 Procedures

Environment survey

Before any outdoor measurement can be conducted, a non operational license (formerly known as test and development license) must be applied for from the Office of Communication (Ofcom) well in advance. Details of the measurement such as measurement location, type of transmission, equipments used and plenty more are required for the application. Further information on this matter can be referred to the Ofcom website [130].

Potential locations of the measurement needed to be surveyed earlier to ensure that the measured data can be used to achieve the predetermined objectives of conducting such measurements. Since measurement is usually a time consuming and costly activity, the error of selecting a measurement environment that is not be beneficial to the overall objectives must be avoided. Specific to the LMS measurement, the determination of the elevation angle between the transmitter and the receiver in the measurement route must also be considered as it is highly influential to the overall behaviour of the channel. Without the use of a helicopter or an aeroplane to carry the transmitter, the available elevation angles are much restricted as it depends on the highest point in the environment, which can be on top of a hill or a tall building.

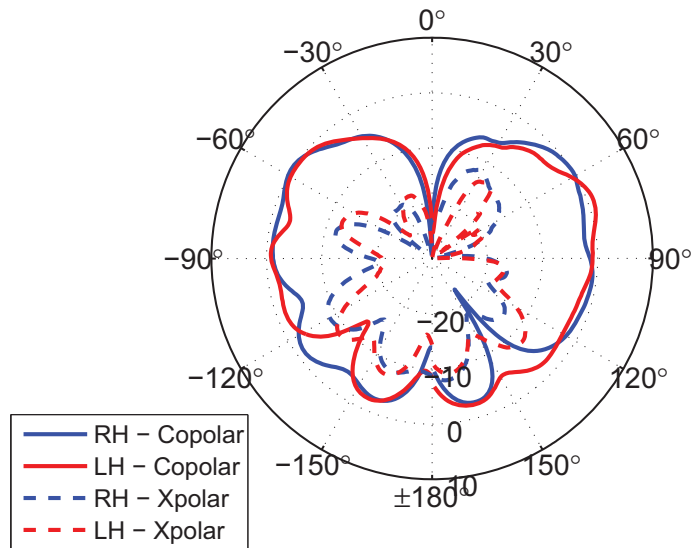


Figure 6.7: Elevation pattern ($\phi = 90^\circ$) of RHCP and LHCP reference antennas.

Since directional antennas are used at the transmitter, the selected measurement route must be within the 3 dB beamwidth so that the cross-polarised gain of the transmit antennas remains at a low level with respect to their co-polarised gain. This is highly important especially in polarised measurements. The measurement route and the position of the transmitter must be finalised and the maximum distance between the transmitter and the receiver is also to be estimated as it will be needed during the sounder configuration.

Measurement operation

An outdoor measurement operation must be planned in great detail in order to reduce the probability of errors or problems occurring during the measurement. Before the start of the measurement, the channel sounder must be configured depending on various parameters that have been determined earlier during the measurement planning process. The selection of these parameters are based on the type of the environment and also the desired outputs from the measurement. Another important part of the channel sounder configuration is the synchronisation of the rubidium clock in both transmitter and receiver. Before or during the configuration process, the transmit and

receive antennas are positioned at their respective places to ensure faster operation as the channel sounder is usually powered by batteries.

To obtain the location of both devices during each measurement run, the GPS device at both the transmitter and receiver is activated at the same time as the start of each run. During the measurement run, it is also desirable for the speed of the receiver to be nearly constant and it must not be faster than the pre-determined maximum speed to ensure adequate sampling of the received signal.

Post-processing analysis

The stored measurement data must be post-processed before it can be utilised for channel characterisation or system performance evaluation. As the objective of the measurement is mainly to evaluate the performance of the receive antennas, only the narrowband data is of interest which needs to be obtained. The captured raw I/Q data is first converted and saved as impulse response (IR) data using a MATLAB implementation of Propsound post-processing tool provided by Elektrobit. The first stage of the process is the removal of any interference signal from the captured IR data especially Wi-Fi signals originated from adjacent houses or offices. The removal of the interference signal will also delete the desired signal in the same sampling time, which needs to be replaced with an interpolated signal. If the interference signal covers multiple sampling times, then it is advisable to avoid using the interfered region as interpolation alone is no longer an accurate correction method.

The narrowband data is extracted by fast fourier transform (FFT)-ing the IR signal in the delay domain for each time sample and selecting the signal of the carrier frequency. Calibration of the narrowband signal to remove the effects of path loss, transmit antenna gain, cable loss at both transmitter and receiver and back-to-back gain of the sounder is then implemented. By doing so, the resultant narrowband signal will only be a composition of the effects of the channel characteristics and the receive antennas. Finally, the narrowband data is ready to be utilised for studying the measured channel conditions and the performance of the receive antennas in terms of its MIMO capability.

6.3 Measurement campaigns

Two outdoor measurement campaigns were conducted in two different environments to investigate the performance of the receive antennas in a LMS MIMO system. In the measurements, different set of receive antennas was used where in the first measurement campaign, an array of circularly polarised reference antennas and the dual circularly polarised FMPQHA vertical array were used at the receiver. Meanwhile, the second measurement campaign was only equipped with the dual circularly polarised SFPQHA horizontal array.

6.3.1 Newlands Corner measurement

Environment

The first measurement campaign was conducted in Newlands Corner near Guildford, where the measurement route is a rural tree-lined road. As the place is relatively hilly, the transmitter was positioned on top of a hill overlooking the measurement route. The average elevation angle between the transmitter and receiver is at 10° . This represented a very low elevation angle propagation from a satellite to a mobile receiver. Fig. 6.8 shows the top view of the measurement route and the transmitter position labelled as (\bullet) during the measurement where the blue line denotes the route taken by the receiver.

Transmitter setup

The sounder's transmitter and its transmit antennas were positioned on top of a hill to obtain a very low elevation angle of about 10° with regards to the receiver. For better clearance of the first Fresnel zone of the antenna beam, the antennas were attached to a contest mast and lifted 10 m up from the ground as shown in Fig. 6.9. Four closely located directional antennas were connected to the sounder's transmitter with two of them are RHCP and the rest are LHCP.

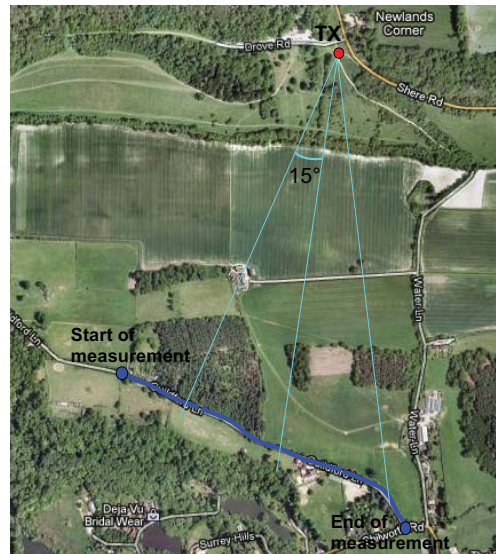
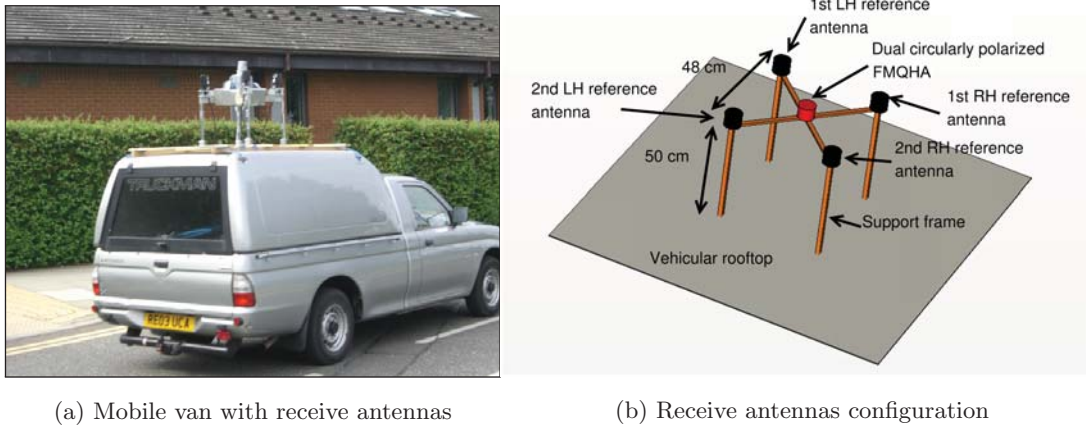


Figure 6.8: Top view of Newlands Corner measurement route.



Figure 6.9: Photograph of the transmit antennas used in Newlands Corner measurement.



(a) Mobile van with receive antennas

(b) Receive antennas configuration

Figure 6.10: Setup of the receive antennas in Newlands Corner measurement.

Receiver setup

A mobile van was used to carry the sounder's receiver and its receive antennas as pictured in Fig. 6.10a, where the antennas were positioned on the van rooftop. Configuration of the receive antennas, which are consisting of two RHCP reference antennas, two LHCP reference antennas and a dual circularly polarised FMPQHA vertical array is shown in Fig. 6.10b where the reference antennas were spatially separated for about four wavelengths and FMPQHA array was positioned in the middle of the setup.

Measurement procedure

Before the start of the measurement, the sounder was configured based on the setup parameters in Table 6.1. The sounder was tuned to the carrier frequency of 2.43 GHz with a null-to-null bandwidth of 50 MHz. The selected bandwidth was chosen as it was deemed sufficient for such rural environment where the required delay resolution can be relaxed. Based on Equation (6.1) which provides the relationship between bandwidth and chip rate, the chip rate was then set as 25 MHz where its corresponding duration of a single chip was 40 ns. Meanwhile, the code length of the transmitted signal was set at 63 chips or 2.54 μ s. As the maximum speed of the receiver is limited to 26.6 m s^{-1} , the maximum Doppler frequency that may be experienced by the receiver was calculated to be 217.4 Hz. Therefore, the sampling frequency of a complete 6×4 MIMO channel

matrix was taken as 708.6 Hz which is several times the maximum Doppler frequency to ensure the Nyquist sampling rule is obeyed.

Table 6.1: Channel sounder parameters configuration in Newlands Corner measurement.

Parameter	Value
Carrier frequency	2.43 GHz
Maximum transmit power	23 dBm
Null-to-null bandwidth	50 MHz
Chip rate	25 MHz
Chip duration	40 ns
Chip sample rate	Two samples per chip
Code length	63 chips / 2.52 μ s
Maximum distance	1500 m
Max. allowable receiver speed	26.6 m s^{-1}
Average receiver speed	13.33 m s^{-1}
Sampling frequency	708.6 Hz
TX antenna no.	4
RX antenna no.	6

After channel sounder has been configured and their clocks were synchronised, the transmitter and receiver were then connected to their respective antenna switching units. Two measurement runs were carried out with different receive antennas configurations where in the first run, the FHQMA array was oriented upright with the main beam was pointed to the zenith. Meanwhile, for the second run, the FMPQHA array was tilted 75° from the zenith in the direction of the transmitter to investigate the impact of antenna orientation on the system performance.

6.3.2 Bishops Court measurement

Environment

To complement the earlier measurement in a rural environment, another measurement was conducted in a suburban area of Guildford town. To obtain a relatively higher

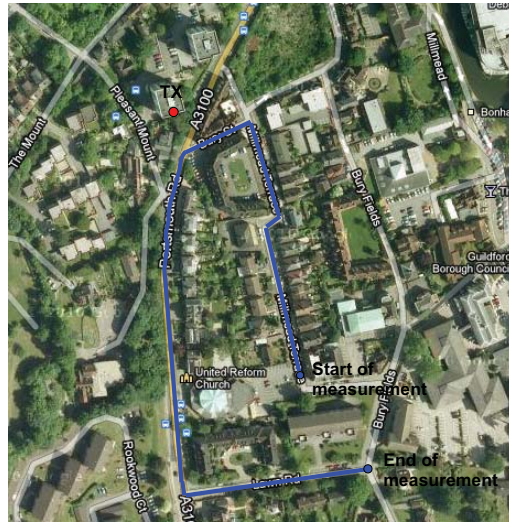


Figure 6.11: Top view of Bishops Court measurement route.

elevation angle in the range of 20° to 30° , the transmitter was placed on the rooftop of a ten storey apartment building. Fig. 6.11 shows the position of the transmitter labelled as (\bullet) and the measurement route of the receiver.

Transmitter setup

As the transmitter was placed on a building rooftop, the transmit antennas were positioned about 2 m above the roof ground and then placed at the edge of the roof. To ensure that the measurement route was within the 3 dB beamwidth of the transmit antenna pattern, the antennas were slightly tilted downward as indicated in Fig. 6.12. Contrary to the first measurement, the transmitter was only equipped with two directional antennas with orthogonal circular polarisations.

Receiver setup

In the second measurement campaign, a different type of receive antennas was utilised which is the dual polarised SFPQHA array with antenna spacing of 80 mm. The antennas were positioned on top of a van rooftop without the structural frame that was used earlier in the first measurement as pictured in Fig. 6.13. The antennas were



Figure 6.12: Photograph of the transmit antennas used in Bishops Court measurement.



Figure 6.13: Photograph of the receive antennas used in Bishops Court measurement.

covered by a thin cardboard box to provide some protection from wind and flying debris.

Measurement procedure

Table 6.2 provides the parameters values used in configuring the channel sounder before the measurement can be conducted. In this measurement, the sounder bandwidth was set at the maximum value of 200 MHz as the environment has higher density of scatterers at the receiver's surrounding. Based on these parameters, the chip rate was given at 100 MHz with the corresponding chip duration of 10 ns which provides an adequate delay resolution for the receiver. As for the code length, it was set at 1023

chips or $10.23 \mu\text{s}$ to ensure a sufficient delay length for the maximum distance-travelled multipath components to be detected. Meanwhile, the sampling frequency of a complete 4×2 MIMO channel matrix is configured at 488.8 Hz based on the calculated maximum Doppler frequency of 116 Hz for a maximum speed of 13.9 m s^{-1} .

Table 6.2: Channel sounder parameters configuration.

Parameter	Value
Carrier frequency	2.45 GHz
Maximum transmit power	23 dBm
Null-to-null bandwidth	200 MHz
Chip rate	100 MHz
Chip duration	10 ns
Chip sample rate	Two samples per chip
Code length	1023 chips / $10.23 \mu\text{s}$
Maximum distance	500 m
Max. allowable receiver speed	13.9 m s^{-1}
Average receiver speed	4.47 m s^{-1}
Sampling frequency	488.8 Hz
TX antenna no.	2
RX antenna no.	4

Two measurement runs were conducted during the Bishops Court campaign where Fig. 6.14 shows a simplified description of the measurement setup with the position of the transmitter and receiver. In order to investigate the effect of receive antenna orientation, two different orientations of the receive antenna were used where in the first run, the SFPQHA array was pointing to the zenith (straight). Meanwhile, in the second run of the measurement, the antenna was tilted 50° from the zenith where the main beam is pointing to the direction of the transmitter at the start of the run.

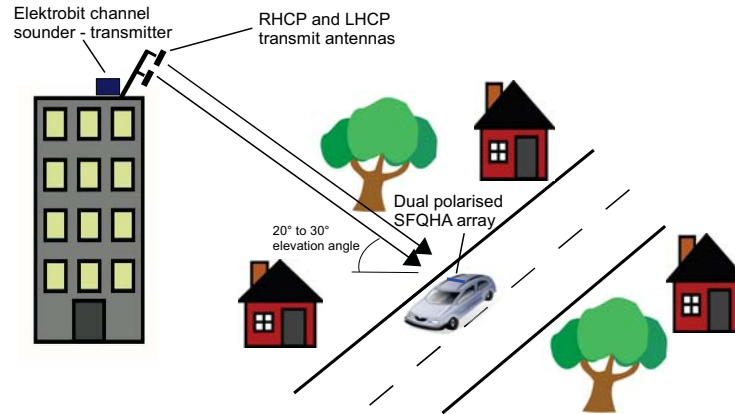


Figure 6.14: Measurement setup for Bishops Court.

6.4 Results from Newlands Corner measurement

6.4.1 Narrowband channel characteristics

In order to characterise the measured narrowband channel, only the received signals of a pair of orthogonally polarised reference antennas were used to create a 2×2 MIMO channel matrix $\mathbf{H}_{2 \times 2}$ as given below:

$$\mathbf{H}_{2 \times 2} = \begin{pmatrix} h_{rr} & h_{rl} \\ h_{lr} & h_{ll} \end{pmatrix} \quad (6.6)$$

where h_{rr} , h_{rl} , h_{lr} and h_{ll} are the channel response from the RHCP antenna to the RHCP antenna, the LHCP antenna to the RHCP antenna, the RHCP antenna to the LHCP antenna and the LHCP antenna to the LHCP antenna respectively. Three main properties of the channel will be presented, which are the small scale fading distribution, Doppler spectrum and channel depolarisation. Since we are only interested in evaluating the receive antennas' performance in a MIMO system, the large scale fading and shadowing effects are excluded in this process as their impacts are identical for any type of antenna and its configuration. Categorisation of the measured area in terms of its small scale properties was then used to separate the performance of the receive antennas in different channel conditions.

Small scale fading distribution

Visual inspection of the measurement map and the unnormalised narrowband signal shows that there are potentially line-of-sight (LoS) and non-line-of-sight (NLoS) areas with different channel characteristics. After averaging out the large scale fading and shadowing to obtain the small scale fading signal, the distribution of the resultant signal in each area was then estimated using a distribution fitting tool available in MATLAB. Table 6.3 presents the distribution of the co-polarised signals which indicates the availability of LoS component in certain parts of the measurement route.

Table 6.3: Small scale distribution of co-polarised signals in LoS and NLoS areas.

Area	Co-polarized signal	Distribution
LoS	RR	Ricean with $K = 8.2$ dB
	LL	Ricean with $K = 8.8$ dB
NLoS	RR	Rayleigh
	LL	Rayleigh

Doppler spectrum

The Doppler spectrum of the received signals by the reference antennas was also provided in Fig. 6.15 in both LoS and NLoS areas. In the LoS area, both co-polarised received signals experienced a Doppler frequency of -10 dB which is much lower than the maximum Doppler frequency based on the provided maximum receiver speed in Table 6.1. This is mainly due to the fact that the actual average speed of the receiver is much slower than the maximum allowable speed and also the movement direction of the receiver is perpendicular to the direction of the transmitted beam. Meanwhile, the characteristic of the Doppler spectrum in the NLoS area infers that the angular spread of the incoming waves is sufficiently large due to the scattering from trees and houses. From the Doppler spectrum, it can be seen that the minimum and maximum Doppler frequency occurred at around ± 90 Hz, which is slightly lower than the theoretical maximum Doppler frequency of 109 Hz that can be experienced by the receiver with an average speed of 13.3 m s^{-1} . This huge increase of Doppler frequency at the NLoS area

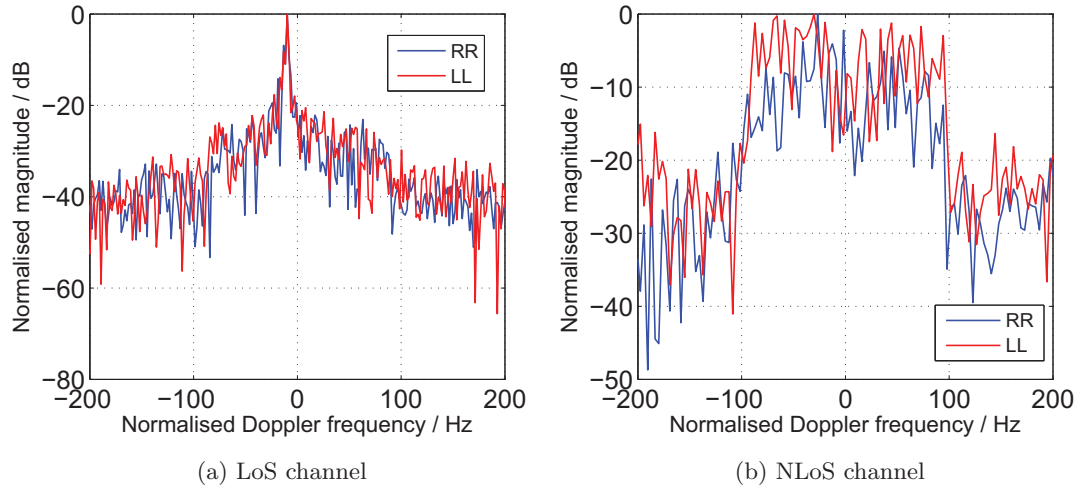


Figure 6.15: Doppler spectrum in LoS and NLoS areas.

when compared to the LoS area is mainly attributed to the change of receiver direction in the NLoS area, which is located nearly at the end of the measurement route. In this region, the receiver movement is almost parallel to the direction of the transmitted beam, hence increases the experienced Doppler frequency of the receiver.

Channel depolarisation

As a circularly polarised system is used, the channel cross polarisation discriminations and co-polarised power ratio that are of interest are defined in Equation (2.13), (2.14) and (2.15) respectively. As expected, the XPD for both circular polarisations is significantly higher in the LoS area than in the NLoS condition. In the NLoS area, the XPDs are near to zero dB which indicates that the transmitted signals are almost completely depolarised by the environment. The results also shows the XPD_I to be slightly higher than XPD_R , which is probably due to the difference in cross-polarised pattern of the receive reference or transmit antennas. Meanwhile, the CPR values in both channel condition are near to zero dB thus shows that the co-polarised signals have the same power level regardless of the availability of the LoS component.

Table 6.4: XPD and CPR of the dual polarised channel in LoS and NLoS areas.

Parameter	LOS area (dB)	NLOS area (dB)
XPD _r	7.58	1.03
XPD _l	9.84	1.10
CPR	-0.82	-0.06

6.4.2 Received power

Performance of the receive antennas in terms of its ability to capture the incoming waves is investigated by comparing the cumulative distribution function (CDF) of the co and cross-polarised signals of each receive antenna. In Fig. 6.16, the received power CDFs of a pair of orthogonally polarised reference antennas are presented for both channel conditions. In the LoS area, although the co-polarised signals have almost similar CDF, the cross-polarised components' CDFs have different gradient where the LHCP reference antenna seems to receive higher cross-polarised signal (RHCP signal) than the opposite case. Since the environment is very much unlikely to discriminate one circular polarisation over the other as shown by the co-polarised signals CDFs, the difference of cross-polarised CDFs can be attributed to the cross-polarised pattern at both reference antennas. As for the NLoS area, all co and cross-polarised received signals by the reference antennas have identical CDFs which shows that the transmitted signals have been equally depolarised by the environment.

Fig. 6.17a and 6.17b present the received power CDFs of the straight and 75° tilted FMPQHA arrays in the LoS and NLoS areas respectively. In the LoS area, the process of tilting the antenna produces a slightly higher co-polarised signals' CDF as shown by the tilted FMPQHA array. This is highly expected as the main beam of the antenna is directly pointed to the main direction of the transmitted signals. However, one negative impact of FMPQHA tilting is the huge increase of the cross-polarised signal power for the RHCP FMPQHA (labelled as dashed blue line). This increase is mainly due to the high cross-polarised gain at the zenith of the RHCP FMPQHA since it was positioned on the lower part of the array. Similar to the reference antennas, the CDF of the co and cross-polarised powers in the NLoS channel for both FMPQHA array orientations

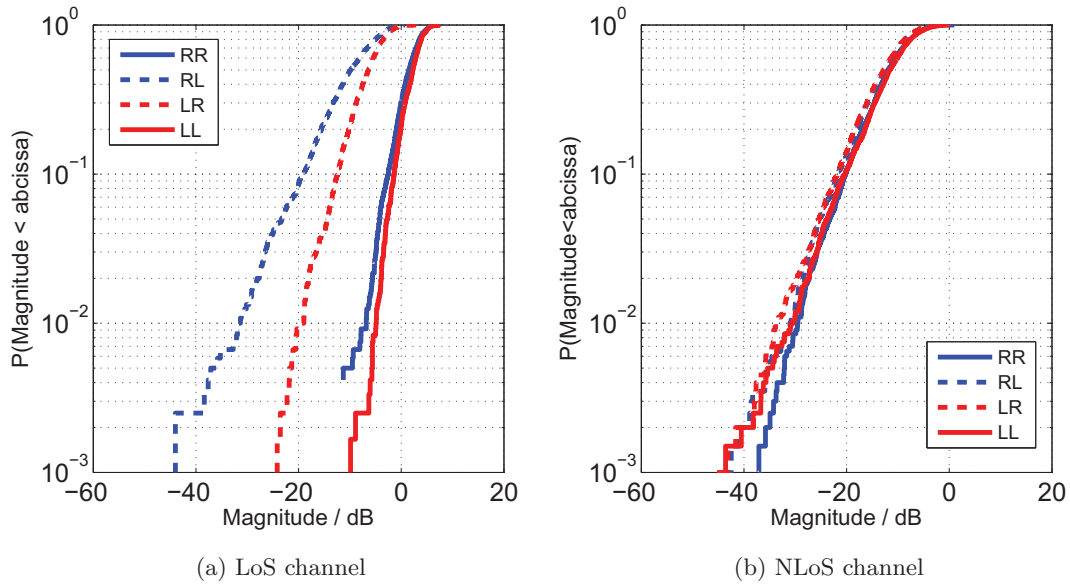


Figure 6.16: Received power CDFs of the reference antenna in LoS and NLoS areas.

is almost equal which indicates that for such depolarising and dispersive channel, the received power is not dependent on the antenna orientation.

6.4.3 Correlation

Instead of only providing the receive correlation coefficient, the full complex channel correlation matrix (using the definition provided by Equation (2.12)) for each antenna configuration and channel condition is calculated and listed in Table 6.5. In the LoS channel, the straight FMPQHA array provides the lowest receive correlation with the magnitude of 0.47 when compared to the other two receive antenna configurations, which are the reference antennas with correlation of 0.50 and 75° tilted FMPQHA array with 0.63.

Meanwhile, the complex receive correlation in the NLoS channel is significantly lower than the one in the LoS channel for all antennas configurations with the magnitude of 0.24, 0.28 and 0.38 for reference antennas, straight FMPQHA and 75° tilted FMPQHA arrays respectively. This result is highly expected as the increase of scattering and the lack of LoS component in the NLoS channel provide a much better signal decorrelation

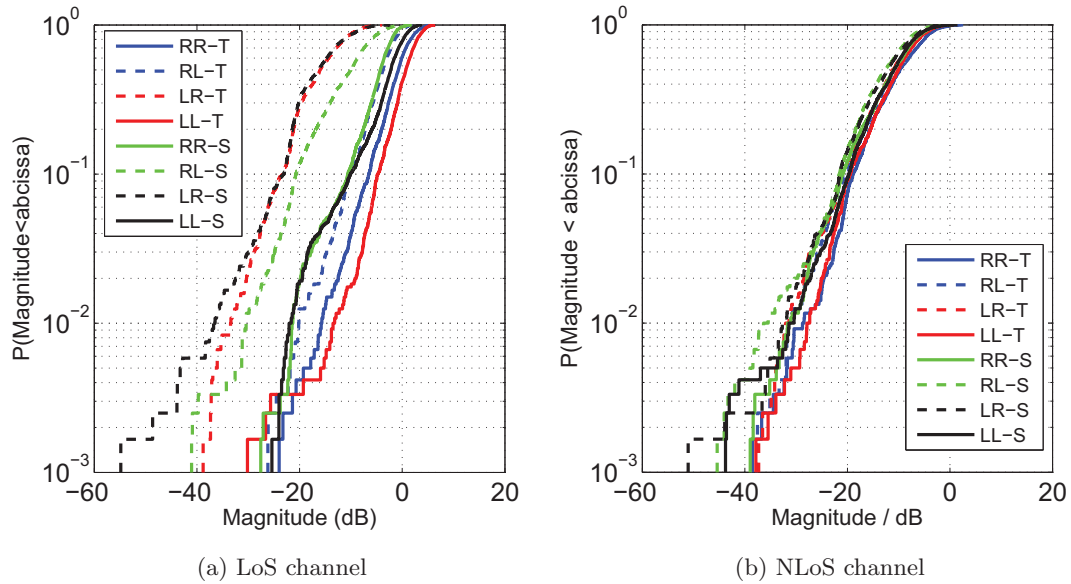


Figure 6.17: Received power CDFs of the FMPQHA array in LoS and NLoS areas.

for all antennas.

6.4.4 Capacity

The use of system capacity in evaluating MIMO antennas has been well established as stated in Section 2.4.1 with its own advantages and disadvantages. In order to utilise the commonly used capacity formulation based on the signal-to-noise ratio (SNR) as defined in Equation (2.4) in evaluating MIMO antennas, proper normalisation of the channel matrix needs to be carried out where it must preserve the antenna radiation pattern and the channel XPD effects. This is to ensure a fair comparison between different antenna configurations used in the measurement. Therefore, the normalization factor N_{norm} is defined as the total average received power from a co-polarized signal, which in our case is the RHCP co-polarized signal from the reference antenna, and it can be calculated as:

$$N_{norm} = \left(\frac{1}{N_r^R N_t^R} \sum_{i=1}^{N_r^R} \sum_{j=1}^{N_t^R} E\{|h_{ij}^{RR}|^2\} \right)^{1/2} \quad (6.7)$$

where $N_{r,t}^R$ denotes the number of RHCP antennas at the receiver and transmitter and h_{ij}^{RR} is the channel element of RHCP signal. The same normalization factor used for

Table 6.5: Complex correlation of receive antennas in LoS and NLoS areas (R - Reference antennas, S - Straight FMPQHA array, T - 75° Tilted FMPQHA array).

Channel	Correlation	Magnitude		
		R	S	T
LoS	ρ_r	0.50	0.47	0.63
	ρ_t	0.64	0.45	0.59
	ρ_{cp}	0.29	0.95	0.88
	ρ_{xp}	0.49	0.16	0.34
NLoS	ρ_r	0.24	0.28	0.38
	ρ_t	0.34	0.28	0.40
	ρ_{cp}	0.46	0.63	0.34
	ρ_{xp}	0.15	0.10	0.15

the reference antenna was then applied to other antenna configurations in order to take into account the loss in gain due to the co-located antennas.

The capacity CDFs for all receive antenna configurations in both LoS and NLoS channels at SNR of 10 dB are presented in Fig. 6.18a and 6.18b respectively. From the figures, it shows that in LoS area, the reference antennas have the highest value of 10% outage MIMO capacity with the value of 3.8 bit/s/Hz while the tilted and straight FMPQHA arrays only obtain 3.4 bit/s/Hz and 2.1 bit/s/Hz for their 10% outage MIMO capacity respectively. As for the NLoS channel, the reference antennas remains as the best performed antennas with 10% outage MIMO capacity of 3.5 bit/s/Hz. Meanwhile, the straight and tilted FMPQHA arrays has almost the same value of capacity in the NLoS area with 2.8 and 2.9 bit/s/Hz respectively. It can be concluded based on this measurement that the reference antenna exhibits the best performance in both LoS and NLoS areas due to the direction of its main beam which is matched with the mean direction of the incoming waves. However, when an axially directional antenna is used such as FMPQHA, then its orientation becomes highly significant to the overall system capacity in a LoS channel.

These results also show that in a NLoS environment, performance of colocated FMPQHA array is nearly equal to the spatially separated reference antennas even though

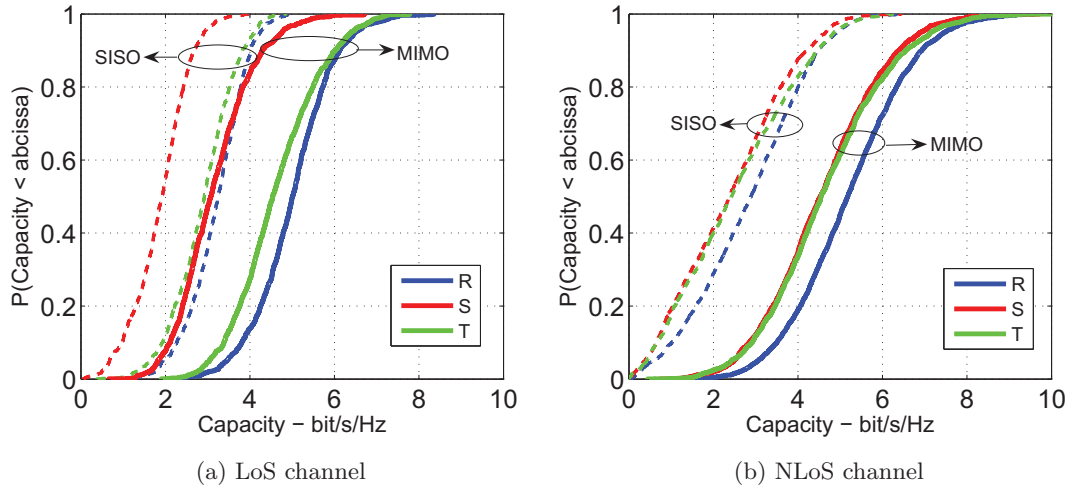


Figure 6.18: Capacity CDFs of all receive antennas configurations in the LoS and NLoS areas (R-reference antennas, S-Straight FMPQHA array, T-75° tilted FMPQHA array).

the lower FMPQHA has higher cross-polarized gain pattern. As for the LoS area, comparable capacity performance between the FMPQHA array and reference antenna can be achieved by proper orientation of the FMPQHA, as shown by the capacity CDF of the 75° tilted FMPQHA array.

6.4.5 Eigenvalue distribution

Another way of investigating the performance of multiple antennas in a MIMO system is by studying the eigenvalues distribution of the measured channel data. Since the MIMO capacity can be calculated from the summation of the channel eigenvalues [5], they provide a more detailed way of studying the transmission quality of the created subchannels. For a 2×2 channel matrix, the magnitude of the two resultant eigenvalues indicates the strength of the subchannel gain that can be exploited by the MIMO system.

Fig. 6.19 presents the CDFs of the measured eigenvalues for each antenna configuration in both LoS and NLoS channels. In the LoS channel as shown in Fig. 6.19a, λ_1 of the reference antennas and 75° tilted FMPQHA array has almost the same CDF behaviour

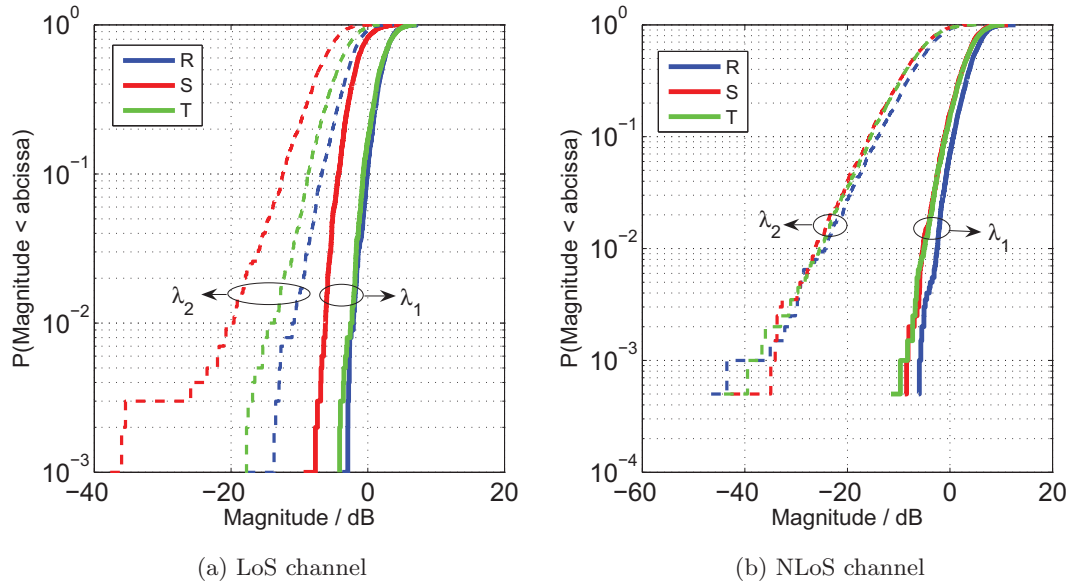


Figure 6.19: Eigenvalues CDFs of all receive antennas configurations in the LoS and NLoS areas (R-reference antennas, S-Straight FMPQHA array, T-75° tilted FMPQHA array).

while for the straight FMPQHA array, its λ_1 has in general lower magnitude hence a weaker CDF. Meanwhile, the differences between the magnitude of the λ_1 and λ_2 CDFs in the LoS channel at 1 % probability are approximately 9 dB, 12 dB and 14 dB respectively, which indicates that polarisation multiplexing can be implemented. As for the NLoS channel, all antennas configurations seem to have similar characteristic of their eigenvalues' CDF as presented by Fig. 6.19b with a slight advantage to the reference antennas. In contrast to the LoS channel, the magnitude difference between the CDF of the λ_1 and λ_2 at 1 % probability is in the region of 20 dB, which is significantly more than in the LoS area.

6.5 Results from Bishops Court measurement

6.5.1 Narrowband channel characteristics

For the characterisation of the narrowband channel from the Bishops Court measurement, the captured data of the straight SFPQHA array was analysed in terms of its small scale fading distribution, Doppler spectrum and channel depolarisation. Results of the analyses are provided in the following subsections. Similar to the Newlands Corner analysis, the channel matrix is defined as in Equation (6.6) and the small scale distribution behaviour will then be used as a separation category in evaluating the performance of receive antennas.

Small scale fading distribution

Distribution of the small scale received signals from both SFPQHA arrays were studied using the same distribution fitting tool in MATLAB as the one used in the previous measurement. Two main parts of the measurement route that may represent both LoS and NLoS areas were identified where their small scale fading distributions were estimated for validation. Table 6.6 lists the distribution of the co-polarised small scale signals received by the straight SFPQHA array in both LoS and NLoS areas.

Table 6.6: Small scale distribution of co-polarised signals in LoS and NLoS areas.

Area	Co-polarized signal	Distribution
LoS	RR	Ricean with $K = 12.2$ dB
	LL	Ricean with $K = 12.9$ dB
NLoS	RR	Rayleigh
	LL	Rayleigh

Doppler spectrum

The received signals of the straight SFPQHA array was investigated in terms of its Doppler characteristic in both LoS and NLoS areas. Significant Doppler shift at the

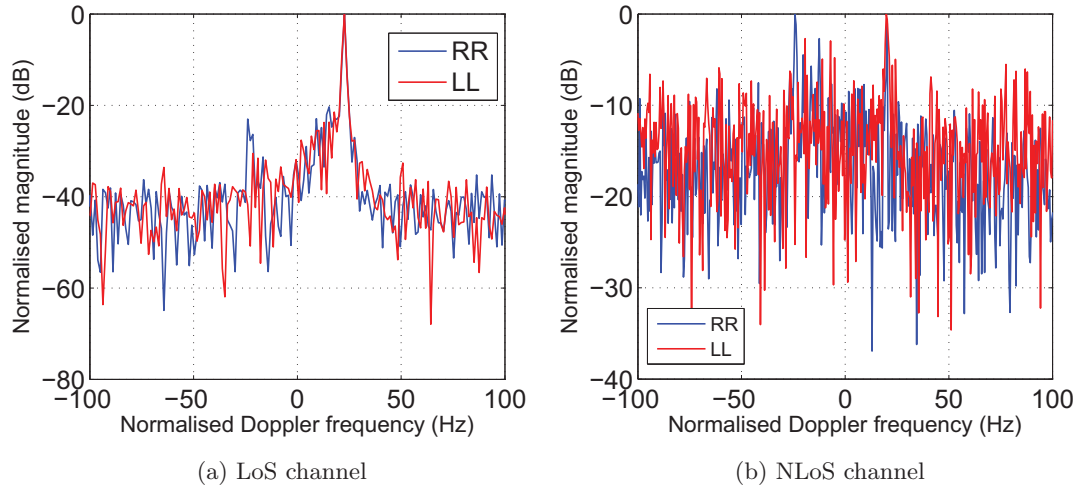


Figure 6.20: Doppler spectrum in LoS and NLoS areas.

value of 23 Hz is evident in the LoS channel as presented in Fig 6.20a. Based on the positive value of the Doppler shift, it shows that the receiver is moving towards the transmitter in the LoS area which implies that the LoS area is at the beginning of the measurement route. As for the NLoS area, the recorded Doppler spectrum for both co-polarised signals has a weak bathtub shape where the RHCP signal spectrum peaks at 20 Hz and -24 Hz while the LHCP signal spectrum peaks at 20 Hz with its corresponding negative frequency component is slightly weaker at -19.3 Hz. From the average speed of 4.47 m s^{-1} of the receiver, the theoretical maximum Doppler frequency is around 35.8 Hz. It can be implied from the bathtub shape of the Doppler spectrum that the incoming waves has a large angular spread in the azimuth angle domain. However, as for its angular spread in the elevation angle domain, it is not as large as in the azimuth domain due to the fact that the Doppler spectrum is not level within the maximum experienced Doppler frequencies.

Channel depolarisation

Channel depolarisation is usually parameterised by the channel XPD and CPR which in both measurements, are defined in accordance to the polarisation of the transmitted signal. For this measurement, the channel XPDs and CPR are calculated and presented

Table 6.7: XPD and CPR of the dual polarized channel in LoS and NLoS environments.

Parameter	LoS area (dB)	NLoS area (dB)
XPD _r	8.5	-0.64
XPD _i	9.5	0.61
CPR	-0.6	-1.1

in Table 6.7 where their values are given for both LoS and NLoS channels. In general, the characteristic of the channel depolarisation is similar to the first measurement where the channel XPD values are much higher in LoS area than in the NLoS area. Meanwhile, the CPR in the NLoS area is slightly higher than the value obtained in the LoS area.

6.5.2 Received power

Evaluation of the SFPQHA array performance in a LMS MIMO system is first conducted by studying the CDF of the received co and cross-polarised powers of the antennas at the receiver. In this measurement, the SFPQHA array were configured into the straight and 50° tilted orientations in the measurement in order to investigate the impact of such orientation to the system performance. Therefore, Fig. 6.21 provides the CDFs of the received co and cross-polarised powers for both SFPQHA arrays in the LoS and NLoS areas. It is clearly shown that in the LoS area, the tilted SFPQHA array has a higher level of both co and cross-polarised powers than the straight configuration. For both antenna configurations, their co-polarised power seems to have identical CDF while each of cross-polarised power CDF has different gradient due to the differences in cross-polarised pattern of each antenna configuration. Received power comparison between the straight and 50° tilted orientations in the NLoS area reveals that the straight orientation has a slight advantage over the tilted antennas. This difference can be attributed to the fact that most of the diffuse waves are coming from higher elevation angles which are better matched with the radiated beam of the straight SFPQHA array. As for the tilted SFPQHA array, since its radiated beam which is pointed to the 50° co-elevation angle, the incoming waves from higher elevation angles due to building

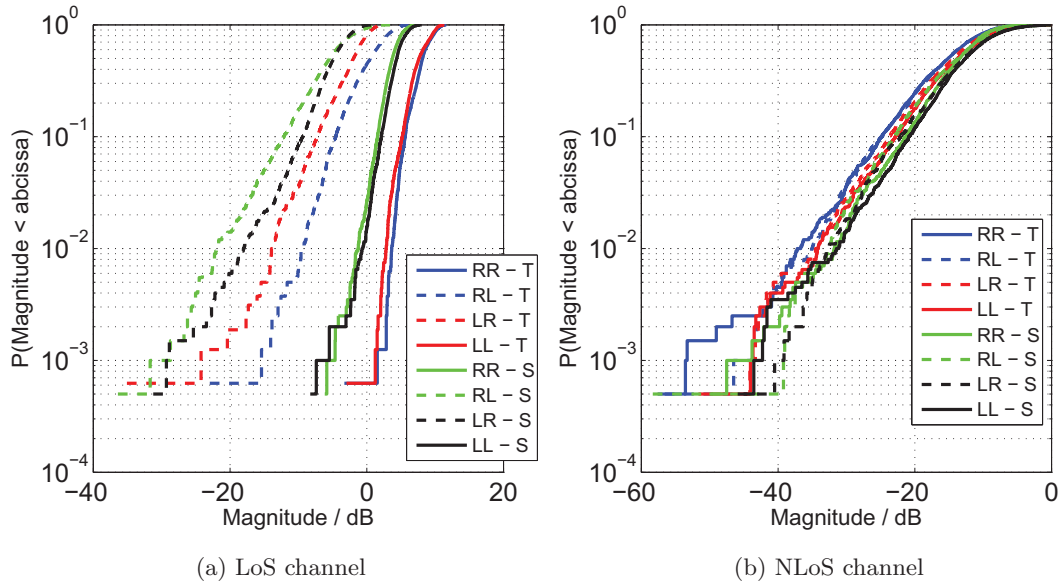


Figure 6.21: Received power CDFs of the SFPQHA array in LoS and NLoS areas.

reflection and roof diffraction are less likely to be received.

6.5.3 Correlation

Similar to the analysis of the first measurement data, the complex channel correlation matrix was computed for each SFPQHA array orientation in both LoS and NLoS channels and its results are presented in Table 6.8. In general, signal correlation for orthogonally polarised antennas is more likely to be influenced by the availability of the LoS component than the orientation of the antenna itself as demonstrated by the investigation of the SFPQHA array's signal correlation. However, due to a very limited case of antenna orientation that was investigated, such conclusion needs to be further scrutinised for its validity.

6.5.4 Capacity

Impact of the utilisation of the SFPQHA array and its orientation on the system capacity were also investigated where the capacity CDF of the measured channel data for both antennas configurations at SNR of 10 dB are compared in both LoS and NLoS

Table 6.8: Complex correlation of receive antennas in LoS and NLoS areas.

Channel	Correlation	Magnitude	
		Straight SFPQHA array	Tilted SFPQHA array
LoS	ρ_r	0.85	0.82
	ρ_t	0.84	0.84
	ρ_{cp}	0.95	0.94
	ρ_{xp}	0.70	0.71
NLoS	ρ_r	0.18	0.12
	ρ_t	0.19	0.19
	ρ_{cp}	0.36	0.04
	ρ_{xp}	0.11	0.07

areas as shown in Fig. 6.22a and Fig. 6.22b respectively. For a fair comparison between the two antenna orientations, the channel normalisation factor is defined similar to Equation (6.7) used in previous analysis where the RHCP co-polarised signal from the straight SFPQHA array is selected as the reference signal. In the LoS channel, it is clear that the 50° tilted SFPQHA array has almost double the 10 % outage capacity than the straight SFPQHA array with the value of 4.6 bit/s/Hz and 2.8 bit/s/Hz respectively. This huge increase in capacity for the tilted SFPQHA array can be attributed to the higher level of received power for the tilted antennas compared to the straight antennas, since the signal correlation of both antennas configurations is nearly the same in the LoS area.

A more interesting case is the comparison of capacity CDFs of the straight and 50° tilted SFPQHA arrays in the NLoS area as presented in Fig. 6.22b. In this area, the straight SFPQHA array provides a slightly better performance in terms of the 10 % outage capacity against the tilted array with the value of 4.2 bit/s/Hz and 3.8 bit/s/Hz respectively. The main result for this performance difference is mainly to do with the higher received power by the straight array in the NLoS area.

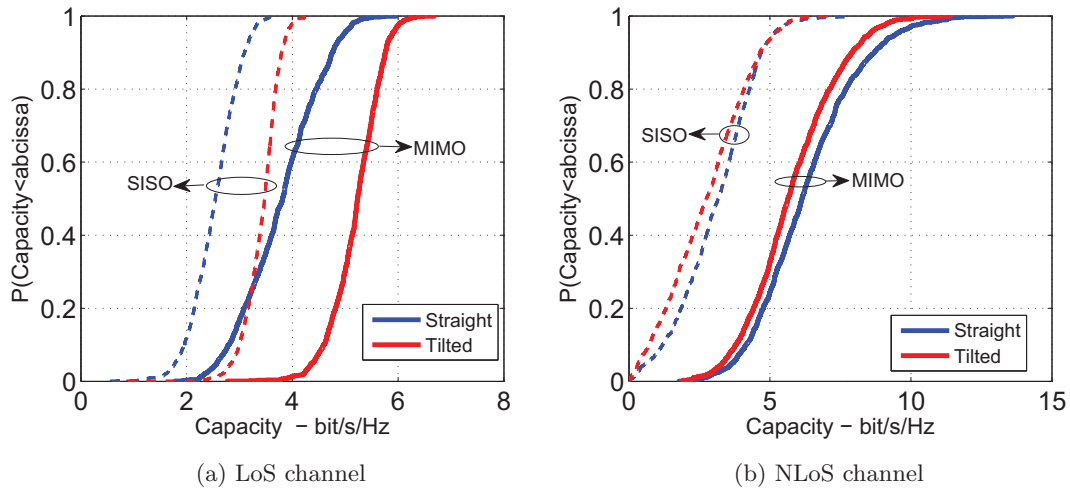


Figure 6.22: Capacity CDFs at SNR of 10 dB of the straight and 50° tilted SFPQHA arrays in the LoS and NLoS areas.

6.5.5 Eigenvalue distribution

The cumulative distribution function (CDF) of the two channel matrix's eigenvalues for each orientation of SFPQHA array is presented in Fig. 6.23. The advantage of tilted orientation in the LoS area is succinctly expressed in the Fig. 6.23a where the λ_1 and λ_2 of the tilted array are about 4 dB and 6 dB higher than the values for the straight array at 1 % probability. Meanwhile, in the NLoS area as shown in Fig. 6.23b, the difference between the straight and tilted arrays is very small which then leads to the slightly higher capacity of the straight SFPQHA array when compared to the titled array.

6.6 Summary

The utilisation of field measurement in evaluating the performance of various multiple antennas in a LMS MIMO system as the receive antenna has been presented in this chapter. Although a measurement campaign has its own disadvantages, the lack of any other credible methods in evaluating the antennas and also the availability of the necessary equipments provides author with the perfect opportunity to directly measure

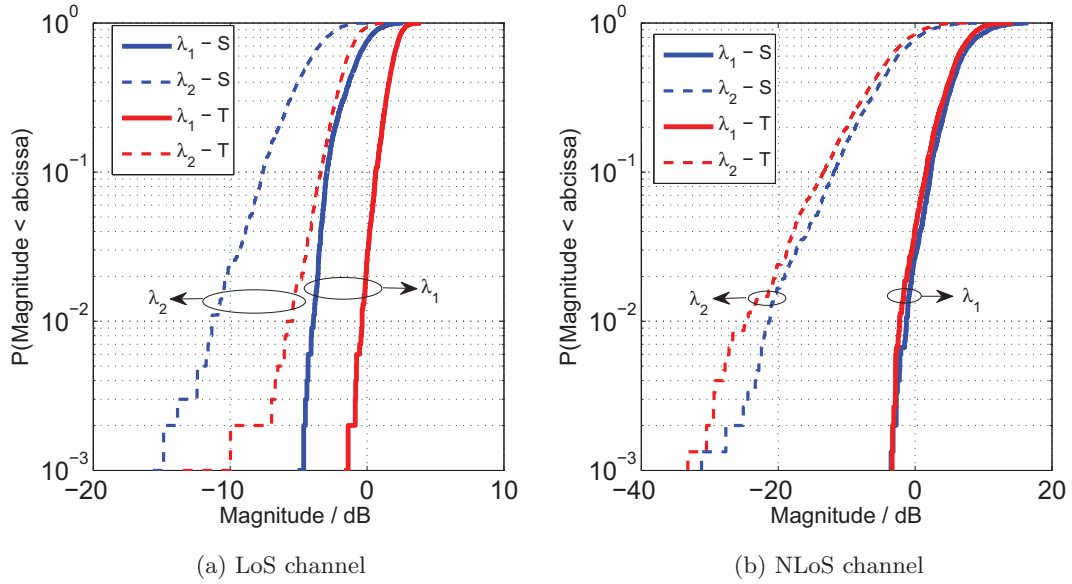


Figure 6.23: Eigenvalues CDFs at SNR of 10 dB of the straight and 50° tilted SFPQHA arrays in the LoS and NLoS areas.

the received signals from these antennas and then evaluate their performance using the measured data. In the first measurement that was conducted in a rural area, it has been shown that the proposed dual polarised FMPQHA array can provide a comparable performance to the reference antennas in a NLoS environment even though the former was co-located while the latter was spatially separated. As for the LoS area, proper orientation of the FMPQHA array is required for it to achieve almost the same capacity performance as the reference antennas.

The second measurement investigated the performance evaluation of another type of dual polarised array, which is the dual polarised SFPQHA horizontal array in a suburban environment. It can be concluded from these measurements that the orientation of the receive antenna is highly influential in determining the system capacity in both LoS and NLoS areas. Further investigations on the impact of receive antennas and its orientation on the performance of a LMS MIMO system are required to complement this rather limited study. This calls for a more robust method of evaluating multiple antennas and its properties as the receive antennas in a LMS MIMO system, which will be the main focus for the next chapter in this thesis.

Chapter 7

LMS MIMO channel simulation for receive antennas evaluation

7.1 Introduction

Although measurement campaigns have been utilised in evaluating the performance of a receive array in the land mobile satellite (LMS) MIMO system, it only provides a limited view on the effect of the array properties on the MIMO performance parameters. A comprehensive study on the antenna effects using a measurement campaign only is highly impractical due its limitations such as the measurement not being easily repeatable for each type of array and its properties as well as costly and very time consuming. Therefore, a more realistic and practical approach in evaluating the performance of the receive array and also studying the antenna properties impacts on the system performance is required and will be the main focus of this chapter.

This chapter introduces a new LMS MIMO channel model which includes the receive antennas properties such as polarimetric radiation pattern, spacing and orientation that can be utilised for evaluating the performance of the receive array. This is achieved with the combination of statistical modelling of the large scale fading and shadowing and the 3-D hemisphere geometric scattering approach for modelling of the small scale fading behaviour. By using this new modelling approach, various properties of the

receive array such as its orientation, spacing and polarisation can be investigated in terms of their impacts on the capacity of the LMS MIMO system. Apart from that, this new channel model will also be used to compare the performance of the designed SFPQHA array with other types of antennas as the receive array in the LMS MIMO system.

7.2 Basic channel description

A MIMO channel can be represented by a double directional channel model, which is characterised by its double directional impulse response [131]. It incorporates all L resolvable propagation paths between transmitter and receiver. Each path is delayed with its excess delay, τ_l and adjusted with its fading complex amplitude, $a_l e^{j\psi_l}$. Then, the Angle-of-Departure, Ω_{Tx} of each path and its corresponding Angle-of-Arrival, Ω_{Rx} are also included in the formulation of the impulse response. Mathematically, the impulse response can be written as:

$$\begin{aligned} h(t, \tau, \Omega_{Tx}, \Omega_{Rx}) &= \sum_{l=1}^L h_l(t, \tau, \Omega_{Tx}, \Omega_{Rx}) \\ &= \sum_{l=1}^L a_l e^{j\psi_l} \delta(\tau - \tau_l) \delta(\Omega_{Tx} - \Omega_{Tx,l}) \delta(\Omega_{Rx} - \Omega_{Rx,l}) \end{aligned} \quad (7.1)$$

where $\delta(\cdot)$ is Dirac delta function. It is important to note that each parameter in this formulation is time variant, which means that its value changes with the absolute time, given as t . For a dual circularly polarised single land mobile satellite (LMS) MIMO channel, the complex amplitude which incorporates the channel depolarisation effect can be defined as:

$$\mathbf{a} = \begin{pmatrix} a_{rr} e^{j\psi_{rr}} & a_{rl} e^{j\psi_{rl}} \\ a_{lr} e^{j\psi_{lr}} & a_{ll} e^{j\psi_{ll}} \end{pmatrix} \quad (7.2)$$

where a_{rr} , a_{rl} , a_{lr} and a_{ll} denote the path attenuation of the co and cross-polarised signals in terms of right hand and left hand circular polarisations. Meanwhile, the phase shifts of the co and cross-polarised signals are represented by ψ_{rr} , ψ_{rl} , ψ_{lr} and ψ_{ll} . Therefore, each element of \mathbf{a} can be substituted into Equation (7.1) for the impulse response calculation of a polarised channel.

The channel description with transmit and receive antenna array which is the MIMO channel matrix, \mathbf{H} where each element H_{ij} with $(i = 1 : N_{\text{rx}})$ and $(j = 1 : N_{\text{tx}})$ can be given as:

$$H_{ij} = \sum_{l=1}^L \mathbf{g}_{\text{Rx},i}(\Omega_{\text{Rx}}) \cdot h(\tau_l, \Omega_{\text{Rx},l}, \Omega_{\text{Tx},l}) \cdot \mathbf{g}_{\text{Tx},j}(\Omega_{\text{Tx}}) \cdot e^{j\psi_{\text{Rx},i}} \cdot e^{j\psi_{\text{Tx},i}} \quad (7.3)$$

where $\mathbf{g}_{\text{Rx},i}(\Omega_{\text{Rx}})$ and $\mathbf{g}_{\text{Tx},j}(\Omega_{\text{Tx}})$ are the polarised complex amplitude pattern of the receive antenna i and transmit antenna j , N_{Rx} and N_{Tx} are the number of receive and transmit antennas respectively and $\psi_{\text{Rx},i}$ and $\psi_{\text{Tx},i}$ are the phase difference between the antenna position and the fixed reference point for each receive and transmit antennas respectively.

In general, LMS channel characteristics can be categorised into three main components namely large scale fading, shadowing and small scale fading. Each of the component describes the channel in a different scale of time variation where the large scale fading (including path loss) refers to a very slow time variation while the small scale fading characterises the channel in a fast time variation. Since the total received signal is the product of these three factors, then it is customary and beneficial to model each component separately.

In this LMS MIMO channel, the large scale fading and shadowing are modelled statistically while the small scale fading is modelled using the 3-D geometric scattering approach. For the next section, the large scale fading and shadowing modelling approaches will be explained. This is followed by a detailed description of the modelling aspect of the small scale fading.

7.3 Large scale fade modelling

7.3.1 Markov state modelling

In a LMS channel, the large scale fading describes large variation of fading from being in line-of-sight (LoS) with the transmitter to total blockage due to trees and buildings. Due to large dynamic range of the received signal and its very slow time variation, this type of fading is better statistically modelled by using a state-oriented approach. The

common approach is to use a first order Markov stochastic process with several states that correspond to different received power levels such as LoS, moderate blocking and deep blocking[27]. This process is governed by two matrices which are:

- state probability matrix (\mathbf{W})
- state transition probability matrix (\mathbf{P})

Each element of \mathbf{W} , W_i represents the total probability of being in state- i while elements of \mathbf{P} , P_{ij} are the probability of change from state- i to state- j .

Another variation of the state-based model is the Semi Markov process where fade (BAD) and nonfade (GOOD) states duration is determined by a lognormal distribution with different mean and standard deviation $(\mu_{dur}, \sigma_{dur})$ for both states [46]. The differences between these two approach are the removal of self loops in the Semi Markov and its state transitions occurred at the end of current state duration instead of regular time intervals. Apart from that, the Markov chain may also give an unrealistic value of the duration of states, as the state duration distribution is exponential [132]. A comprehensive compilation of $(\mu_{dur}, \sigma_{dur})$ for BAD and GOOD states in S and L band with different satellite elevation angles can be obtained from [46]. The lognormal distribution formulation can be given as:

$$f(a) = \frac{8.686}{\sigma_{dB} a \sqrt{2\pi}} \exp \left[- \frac{20 \log_{10}(a) - \mu_{dB}}{2\sigma_{dB}^2} \right] \quad (7.4)$$

For this channel model, the Semi Markov process has been chosen to model the large scale fading due to its realistic state duration and simpler characterisation of the fade (BAD) and nonfade (GOOD) states. It also can be safely assumed that all subchannels will experience that same state due to the colocation of antennas at both transmitter and receiver.

7.3.2 Shadowing

Shadowing effect describes the small changes in the large-scale attenuation as the mobile travels in the shadow of the same obstacle such as group of trees or building. It can be

modelled as an auto and cross-correlated random process with a lognormal distribution for each channel. Temporal correlation is applied to the random process using a method described in [11] where the autocorrelation function is modelled with a simple, first order exponential model given as:

$$\rho_s = e^{\left(\frac{-d_s}{L_{corr}}\right)} \quad (7.5)$$

where it is characterised by the correlation distance, L_{corr} and sampling spacing, d_s . Such a model allows a simple way of computer simulation with the use of single pole IIR filter and scaling with its mean m_{corr} and location variability σ_L . The transfer function of the single pole filter can be written in term of Z-transform as:

$$H(z) = \frac{1}{1 - az^{-1}} \quad (7.6)$$

where a is defined as the feedback filter coefficient and it is equal to the autocorrelation function ρ_s .

Apart from temporal correlation, the shadowing is also cross-correlated between polarisation subchannels. This effect can be introduced to the channel by multiplying the generated shadowing channel matrix with a polarisation correlation matrix [44] as shown below:

$$\text{vec}(\mathbf{H}_{s,corr}) = \mathbf{C}_s^{1/2} \cdot \text{vec}(\mathbf{H}_s) \quad (7.7)$$

where $\text{vec}(\cdot)$ defines the matrix vectorisation, \mathbf{H}_s and $\mathbf{H}_{s,corr}$ denote the uncorrelated and cross-correlated 2×2 shadowing channel matrices respectively and \mathbf{C} is the 4×4 polarisation shadowing correlation matrix. It is expected for the shadowing polarisation subchannels to have high cross correlation due to the colocation of both transmitter and receiver antennas and huge distance between satellite and mobile receiver.

7.4 Small scale fade modelling

The small scale fading characterises the fast variation of the signal power due to the multipath environment. In order to emulate the multipath environment in terms of its angular and Doppler properties, a 3-D geometric scattering model was utilised in this work where the scatterers are distributed uniformly inside a hemisphere. Further details

on the scattering model are explained in the Section 7.4.1. Meanwhile, for the modelling of the propagation paths, two incident wave components are considered, namely the coherent and incoherent components. This allows for the model to simulate a Ricean fading channel which is more commonly experienced by the receiver in the LMS MIMO system. More importantly, this modelling approach allows for the inclusion of the receive antennas properties in the channel simulation where three antenna characteristics are considered, which are the embedded radiation pattern, antenna spacing and array orientation.

7.4.1 3-D geometric scattering model

The basic principle of any geometric scattering model is that the channel characteristics are emulated by tracing the propagation paths from the transmitter to the receiver through randomly placed scatterers based on specific distribution. Based on the placement of the scatterers, channel properties such as envelope statistics, angular delay spectra and Doppler spectrum can be modelled for the intended environment. By having the correct emulation of these channel parameters, then the correlation of received signals at the multiple antennas can be reproduced accurately. For the small scale fading simulation, a 3-D hemisphere model is used where the scatterers are uniformly distributed inside of a hemisphere with radius, R . This model was first introduced in [133] where a 3-D semispheroid model, which is the general case for hemisphere was investigated in terms of its Angle-of-Arrival (AoA) distribution at the mobile and base station. Application of the 3-D hemisphere geometric scattering approach in modelling the small scale fading of the mobile satellite channel in a NLoS channel (urban) has been first studied in [134] where the Time-of-Arrival (ToA) distribution and power delay profile were investigated for various satellite elevation angles. This model is then extended in this work where the satellite azimuth angle is also considered in formulating the Time-of-Arrival distribution.

In this channel model, only single-bounce scattering process is considered and it is assumed that all propagation processes can be approximated by a finite number of reflections at discrete point scatterers. Fig. 7.1 shows the utilised 3-D hemisphere model

for the LMS channel with a single scatterer in sight. The incoming waves from the transmitter can be approximated as an equal gain plane wave originating from (θ_p, ϕ_p) direction due to the huge distance between the satellite and receiver. The scatterer, denoted as SC in the Fig. 7.1 is positioned inside of the hemisphere with distance of r and angular direction of (θ, ϕ) . Without any loss of generality, the receiver is positioned at the origin. The probability density function (PDF) of the uniformly distributed scatterers in the hemisphere (Cartesian coordinate) is given as $p(x, y, z) = \frac{3}{2\pi R^3}$. Using Jacobian transformation [135], the PDF of the scatterers in the spherical coordinate is written as:

$$p(r, \theta, \phi) = \frac{3 r^2 \sin \theta}{2\pi R^3} \quad (7.8)$$

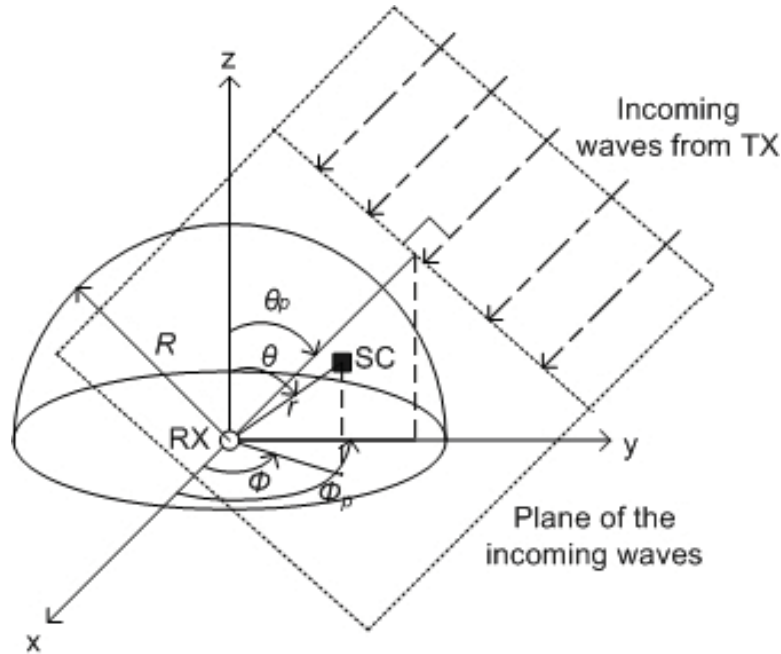


Figure 7.1: 3-D hemisphere scattering model for LMS channel.

AoA distribution at the receiver

The joint probability density function (PDF) of the Angle-of-Arrival (AoA) was given in [133] as:

$$p(\theta, \phi) = \frac{\cos \beta}{2\pi} \quad 0 \leq \phi \leq 2\pi, 0 \leq \beta \leq \pi/2 \quad (7.9)$$

where β is the satellite elevation angle from x-y plane and can be calculated as $\beta = \frac{\pi}{2} - \theta_p$. Based on this joint PDF, the marginal PDF in azimuth is simply $p(\phi) = \frac{1}{2\pi}$ and in elevation is $p(\theta) = \cos \beta$. It is then obvious that the PDF of the AoA is uniform in azimuth and depends only on the satellite elevation angle. Fig. 7.2 shows the marginal PDF of the incident waves in elevation.

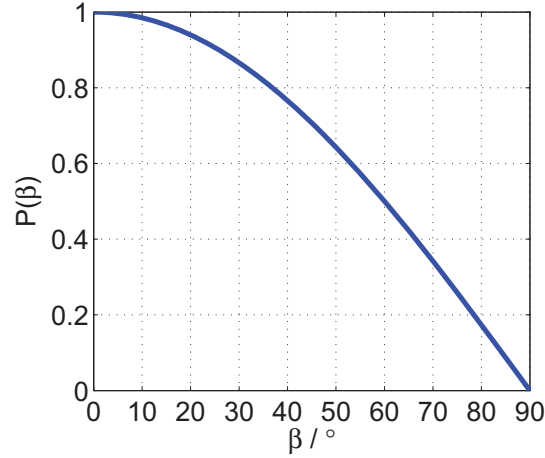


Figure 7.2: PDF of the Angle-of-Arrival of the 3-D hemisphere geometrical scattering model.

ToA of multipath component

In order to evaluate the ToA of each multipath components, the distance from the Tx to the Rx is required. Since we consider the incoming wave from Tx is a plane wave, then a plane with (θ_p, ϕ_p) direction can be defined to represent the transmitted wave as in Fig 7.1. Therefore, the distance between the Tx and Rx, d_{tot} can be written as:

$$d_{tot} = d_{Tx,pl} + d_{pl,sc} + d_{sc,Rx} \quad (7.10)$$

where $d_{Tx,pl}$, $d_{pl,sc}$ and $d_{sc,Rx}$ are the distances from Tx to plane, plane to scatterer and scatterer to Rx respectively. It can be approximated that $d_{Tx,pl}$ is constant for all multipath components due to its huge magnitude compared to the other two parameters. Subsequently, the ToA is formulated based on normalised distance from plane to Rx without considering $d_{Tx,pl}$. The first step in calculating d_{tot} is the determination

of $d_{pl,sc}$, where the scatterer position is given in spherical coordinate as (r, θ, ϕ) . By having the plane placed at the edge of the hemisphere, the equation of the plane is given in Cartesian coordinates as (Appendix B):

$$R - \sin \theta_p \cos \phi_p x - \sin \theta_p \sin \phi_p y - \cos \theta_p z = 0 \quad (7.11)$$

where R is the radius of the hemisphere and (θ_p, ϕ_p) are the AoA of the plane. Based on this equation, the distance between the plane and scatterer $d_{pl,sc}$ in spherical coordinate system can be calculated by using:

$$d_{pl,SC} = |R - r \sin \theta_p \cos \phi_p \sin \theta \cos \phi - r \sin \theta_p \sin \phi_p \sin \theta \sin \phi - r \cos \theta_p \cos \theta| \quad (7.12)$$

The normalised ToA of the scatterer, τ from the plane can then be calculated by:

$$\begin{aligned} \tau &= \frac{d_{pl,sc} + d_{sc,rx}}{c} \\ &= \frac{d_{pl,sc} + r}{c} \end{aligned} \quad (7.13)$$

where c is the speed of light. It can be further simplified as:

$$\tau = \frac{R - r(A - 1)}{c} \quad (7.14)$$

where $A = \sin \theta_p \cos \phi_p \sin \theta \cos \phi + \sin \theta_p \sin \phi_p \sin \theta \sin \phi + \cos \theta_p \cos \theta$. Apart from that, the maximum and minimum time of arrival for this hemisphere model can also be determined geometrically where $\tau_{max} = \frac{(2 + \sin \theta_p)R}{c}$ and $\tau_{min} = \frac{R}{c}$ respectively.

ToA distribution

The ToA/AoA joint distribution can be derived by using Jacobian transformation where its joint distribution is defined as:

$$p(\tau, \theta, \phi) = p(r, \theta, \phi) \cdot |J(\tau, \theta, \phi)| \quad (7.15)$$

where $p(r, \theta, \phi)$ is the PDF of the scatterers in spherical coordinate and $|J(\tau, \theta, \phi)|$ is the determinant of the Jacobian matrix. According to [135], the determinant of the Jacobian matrix is defined as:

$$|J(\tau, \theta, \phi)| = \left| \frac{\partial(r, \theta, \phi)}{\partial(\tau, \theta, \phi)} \right|. \quad (7.16)$$

By using this definition, the Jacobian matrix for this distribution transformation can be obtained as below:

$$\begin{aligned}
|J(\tau, \theta, \phi)| &= \left| \frac{\partial(r, \theta, \phi)}{\partial(\tau, \theta, \phi)} \right| \\
&= \begin{vmatrix} \frac{\partial r}{\partial \tau} & \frac{\partial \theta}{\partial \tau} & \frac{\partial \phi}{\partial \tau} \\ \frac{\partial r}{\partial \theta} & \frac{\partial \theta}{\partial \theta} & \frac{\partial \phi}{\partial \theta} \\ \frac{\partial r}{\partial \phi} & \frac{\partial \theta}{\partial \phi} & \frac{\partial \phi}{\partial \phi} \end{vmatrix} \\
&= \left| \frac{\partial r}{\partial \tau} \right| \\
&= \left| \frac{\partial \tau}{\partial r} \right|^{-1} \\
&= \frac{c}{1-A}
\end{aligned} \tag{7.17}$$

Inserting Equation (7.8) and Equation (7.17) into Equation (7.15), the ToA/AoA joint distribution is given as:

$$p(\tau, \theta, \phi) = \left(\frac{3r^2 \sin \theta}{2\pi R^3} \right) \frac{c}{1-A} \tag{7.18}$$

To introduce τ into Equation (7.18), r in this equation is substituted with using Equation (7.14) and the resultant equation for the ToA/AoA joint distribution can be written as:

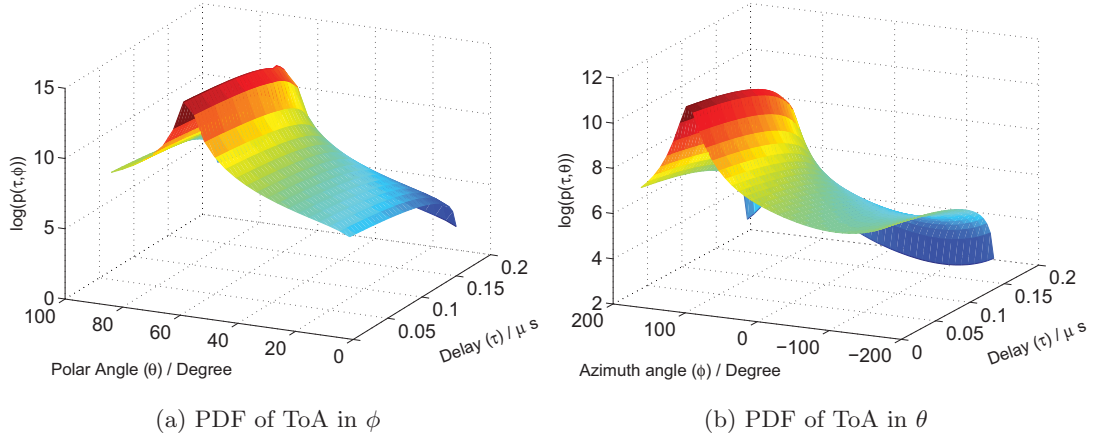
$$p(\tau, \theta, \phi) = \frac{3c(\tau c - R)^2 \sin \theta}{2\pi R^3(1-A)^3} \tag{7.19}$$

A joint PDF of ToA in ϕ and θ can be defined by integrating over θ and ϕ angles where these PDFs are given as:

$$\begin{aligned}
p(\tau, \phi) &= \int_{\theta_{min}}^{\theta_{max}} p(\tau, \theta, \phi) d\theta \\
&= \int_0^{\pi/2} \frac{3c(\tau c - R)^2 \sin \theta}{2\pi R^3(1-A)^3} d\theta
\end{aligned} \tag{7.20}$$

$$\begin{aligned}
p(\tau, \theta) &= \int_{\phi_{min}}^{\phi_{max}} p(\tau, \theta, \phi) d\phi \\
&= \int_{-\pi}^{\pi} \frac{3c(\tau c - R)^2 \sin \theta}{2\pi R^3(1-A)^3} d\phi
\end{aligned} \tag{7.21}$$

As an example of the solution of these joint ToA/AoA PDFs, Fig. 7.3a and Fig. 7.3b show the PDF of ToA in ϕ and θ angles when the direction of the transmitted waves from the satellite is given as $(\theta_p, \phi_p) = (60^\circ, 110^\circ)$.

Figure 7.3: PDF of the ToA in ϕ and θ angles.

7.4.2 Coherent component

The coherent component in this model represent the line-of-sight (LoS) propagation path between the transmitter and receiver without any scatterer interaction. In order to model a realistic LoS propagation path with its polarisation characteristic, the channel cross polarisation discrimination XPD and co-polarised power ratio CPR in a nonfade or LoS channel need to be included where their values may be obtained from measurement campaigns or full ray tracing simulations. As for its magnitude with respect to the incoherent component, the Ricean K factor of the LoS channel is used since it provides the value of ratio between the two channel components. Therefore, the amplitude matrix of the coherent component can be written as:

$$\mathbf{a}_{los} = \begin{pmatrix} 1 & \sqrt{\mu_{los} \cdot \chi_{l,los}} \\ \sqrt{\chi_{r,los}} & \sqrt{\mu_{los}} \end{pmatrix} \sqrt{\frac{K}{K+1}} P_{co} e^{j\psi_d} \quad (7.22)$$

where χ_{los} and μ_{los} are the inverse of cross polarisation discrimination XPD and cross polar ratio CPR in the LoS channel, K is the Ricean K factor, P_{co} denotes the co-polarised received power and ψ_d is defined as the phase shift due to distance travelled.

7.4.3 Incoherent component

Each propagation path that travelled to the receiver after interacting with scatterer is defined as the incoherent component where the interaction processes may include reflection, diffraction and diffuse scattering. For simplicity, instead of modelling each scattering process individually, the Ricean K factor is used to describe the total power of scattering components where the power to each scatterer is calculated by averaging the total power with the number of scatterer. The main advantages of using this approach are its modelling simplicity and adaptivity depending on the provided input data. However, its disadvantage is the model requires priori data such as K factor and XPD which need to be obtained from measurement or full ray tracing simulation. The amplitude matrix of each scatterer can be defined as:

$$\mathbf{a}_{nlos} = \begin{pmatrix} 1 & \sqrt{\mu_{nlos} \cdot \chi_{l,nlos}} \\ \sqrt{\chi_{r,nlos}} & \sqrt{\mu_{nlos}} \end{pmatrix} \sqrt{\frac{\frac{1}{K+1} P_{co}}{N_{sc}}} e^{j\psi_s} \quad (7.23)$$

where definition of μ_{nlos} , $\chi_{l,nlos}$ and $\chi_{r,nlos}$ are the same as in coherent component but only in different channel condition and N_{sc} is the number of scatterers generated in the simulation. The phase shift due to the scattering, ψ_s is modelled as a 2×2 matrix with uniformly distributed and independent elements, $\psi_s \sim U(0, 2\pi]$ for each polarisation component of each scatterer.

7.4.4 Inclusion of receive antenna properties

Embedded radiation pattern

In order to consider the receive antennas' radiation pattern in the channel model, it requires the 3-D co and cross-polarised embedded gain patterns of the antennas, which may be obtained using electromagnetic simulation or polarimetric gain measurement. An embedded gain pattern of a single antenna in an array is a gain pattern that is measured/simulated not in isolation but with its neighbouring antennas that have been terminated properly. The use of embedded gain pattern is very important especially for a closely spaced antennas since the effect of mutual coupling is included in determining the embedded gain pattern of an antenna. Apart from that, if the patterns are taken

from simulations, it is also recommended to use the value of realised gain instead of gain or directivity so that the overall antenna efficiency will also be accounted.

For its utilisation in this model, the obtained co and cross-polarised gain patterns of a single antenna are organised as shown in the following equations:

$$\mathbf{G}_{cp,n} = \begin{bmatrix} G_{cp,n}(\theta_1, \phi_1) & G_{cp,n}(\theta_1, \phi_2) & \cdots & G_{cp,n}(\theta_1, \phi_{360}) \\ G_{cp,n}(\theta_2, \phi_1) & G_{cp,n}(\theta_2, \phi_2) & \cdots & G_{cp,n}(\theta_2, \phi_{360}) \\ \vdots & \vdots & \ddots & \vdots \\ G_{cp,n}(\theta_{180}, \phi_1) & G_{cp,n}(\theta_{180}, \phi_2) & \cdots & G_{cp,n}(\theta_{180}, \phi_{360}) \end{bmatrix} \quad (7.24)$$

$$\mathbf{G}_{xp,n} = \begin{bmatrix} G_{xp,n}(\theta_1, \phi_1) & G_{xp,n}(\theta_1, \phi_2) & \cdots & G_{xp,n}(\theta_1, \phi_{360}) \\ G_{xp,n}(\theta_2, \phi_1) & G_{xp,n}(\theta_2, \phi_2) & \cdots & G_{xp,n}(\theta_2, \phi_{360}) \\ \vdots & \vdots & \ddots & \vdots \\ G_{xp,n}(\theta_{180}, \phi_1) & G_{xp,n}(\theta_{180}, \phi_2) & \cdots & G_{xp,n}(\theta_{180}, \phi_{360}) \end{bmatrix} \quad (7.25)$$

where $\mathbf{G}_{cp,n}$ and $\mathbf{G}_{xp,n}$ are the co and cross-polarised gain matrix for antenna n . Although the simulated AoA and AoD of the channel may take the value of a real number where $0^\circ < \theta \leq 180^\circ$ and $0^\circ < \phi \leq 360^\circ$, the value of θ and ϕ need to be rounded to the nearest integer in order for it to be matched with the corresponding antenna gain.

Spacing

It is well known that antenna spacing in an array influences the radiation pattern and efficiency of an antenna due to the effect of mutual coupling. However, the effect of mutual coupling has been included in this model with the use of embedded gain pattern which leaves the antenna spacing only to affect the phase difference between these antennas. The phase difference between the receive antennas and the reference point at the receive array (e.g. centre of the array) $e^{j\phi_{rx}}$ can be defined as:

$$e^{j\phi_{rx}} = \begin{bmatrix} e^{j\frac{2\pi}{\lambda}x_1} & e^{j\frac{2\pi}{\lambda}x_2} \end{bmatrix} \quad (7.26)$$

where x_1 and x_2 are the path length differences between the receive antennas and the reference point from the transmitter. This path length difference can be then calculated as $x = d \sin \theta \sin \phi$ with d is the spacing between antenna and the reference point.

Orientation

Inclusion of receive antenna orientation in the channel model requires the simulated or measured 3-D co and cross polarised gain patterns of the antennas. Orientation of the receive antennas is defined by two parameters, which are azimuth pointing angle, ϕ_{ant} and inclination angle, θ_{ant} . The angle ϕ_{ant} indicates the angle between antenna azimuth pointing vector and receiver movement vector, v_m while θ_{ant} denotes the inclination angle of the receive antennas from the zenith as shown in Fig. 7.4. It also should be noted that ϕ_{ant} is calculated counterclockwise when looking towards the antenna from above.

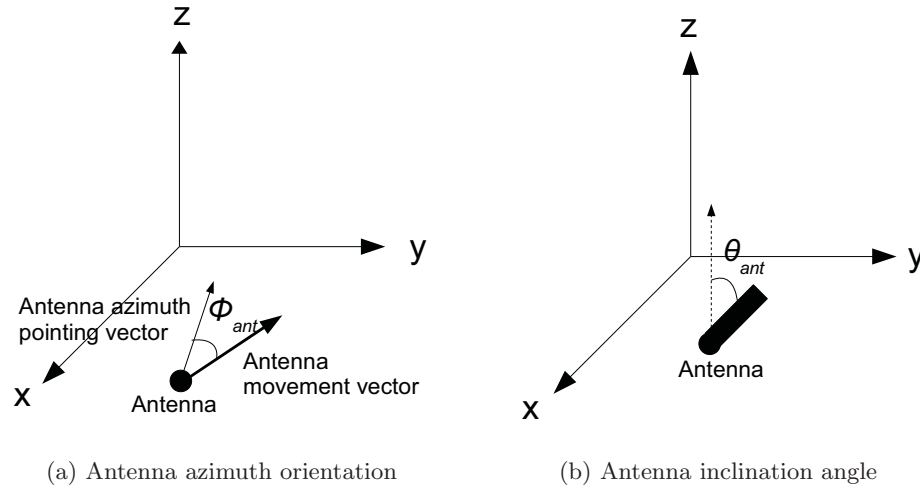


Figure 7.4: Antenna azimuth pointing and inclination angles definition.

For different antenna orientation, the incoming waves arrive in different azimuth and elevation angles when looking from antenna's local axes. The difference of the local AoA polar angles changes the antenna response to the channel since a realistic antenna pattern is not omnidirectional and its gain varies in angular domain. The basic idea in order to include the antenna orientation is to recalculate the AoA of each incoming wave with respect to the new transformed antenna local axes based on its orientation as shown in Fig. 7.5. Based on the new local AoA, the correct receive antenna gain can be applied to the corresponding incident waves.

The transformation of local axes with respect to the antenna orientation can be calculated by simple 3-D rotation transformation. The 3-D coordinate system rotation of x ,

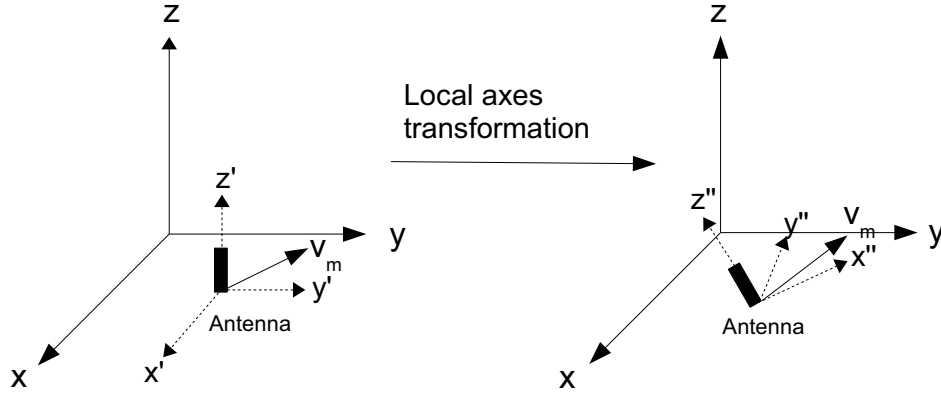


Figure 7.5: Transformation of antenna local axes based on its orientation.

y and z axes in the counterclockwise direction looking towards the local origin can be defined by rotation matrices, \mathbf{R} :

$$\begin{bmatrix} x'' \\ y'' \\ z'' \end{bmatrix} = \mathbf{R} \begin{bmatrix} x' \\ y' \\ z' \end{bmatrix} \quad (7.27)$$

where \mathbf{R} is a combination of $\mathbf{R}_x(v)$, $\mathbf{R}_y(\gamma)$ and $\mathbf{R}_z(\zeta)$ as defined below:

$$\mathbf{R}_x(v) = \begin{bmatrix} 1 & 0 & 0 \\ 0 & \cos v & \sin v \\ 0 & -\sin v & \cos v \end{bmatrix}, \quad \mathbf{R}_y(\gamma) = \begin{bmatrix} \cos \gamma & 0 & -\sin \gamma \\ 0 & 1 & 0 \\ \sin \gamma & 0 & \cos \gamma \end{bmatrix},$$

$$\mathbf{R}_z(\zeta) = \begin{bmatrix} \cos \zeta & \sin \zeta & 0 \\ -\sin \zeta & \cos \zeta & 0 \\ 0 & 0 & 1 \end{bmatrix} \quad (7.28)$$

The v , γ and ζ angles refer to the counterclockwise angle between axis x'' and x' , y'' and y' and z'' and z' when looking to the origin. The new local AoA of the incoming waves, which constitute the coherent and incoherent components that corresponds to the antenna pattern can then be calculated based on the transformed local coordinate system. Finally, the corresponding antenna gain can be matched with the new local AoA of the incident waves.

7.5 Narrowband simulation and results comparison with measurement

7.5.1 Measurement used in result comparison

Before the simulation of the proposed channel model can be conducted, the model must be validated by comparing its results with results from a measurement campaign. For an accurate comparison, the simulation parameters in terms of channel properties must follow closely the corresponding actual environment of the measurement campaign. In this work, the Bishops Court measurement campaign is used where the measurement conditions and results are as described in Section 6.3.2. The reason for selecting the Bishops Court measurement campaign is because the chosen 3-D geometric scattering model with the scatterers uniformly distributed in a hemisphere is more suitable for simulating a channel in suburban and urban environments.

7.5.2 Simulation procedure and parameters

The newly developed LMS MIMO channel model can be simulated by separately modelling each component of the channel, which are the Markov state, shadowing and small scale fading. The complete channel impulse response can then be obtained by multiplying these components. Fig. 7.6 presents the flowchart detailing the process of modelling the new LMS MIMO channel where each components is modelled separately with their own parameters.

The Markov state and shadowing simulation parameters used in this work were taken from published satellite measurement works that have approximately the same environment as the Bishops Court measurement campaign. Table 7.1 shows the markov state, shadowing, scatterers and transmit antennas parameters that were used in the simulation. There are three basic parameters of the scatterer distribution which can be adjusted depending on the environment, namely number of scatterers, regenerative distance, L_{sc} and maximum distance between scatterers to the receiver. It is important to note that unlike conventional fading simulators where the main objective is to emulate

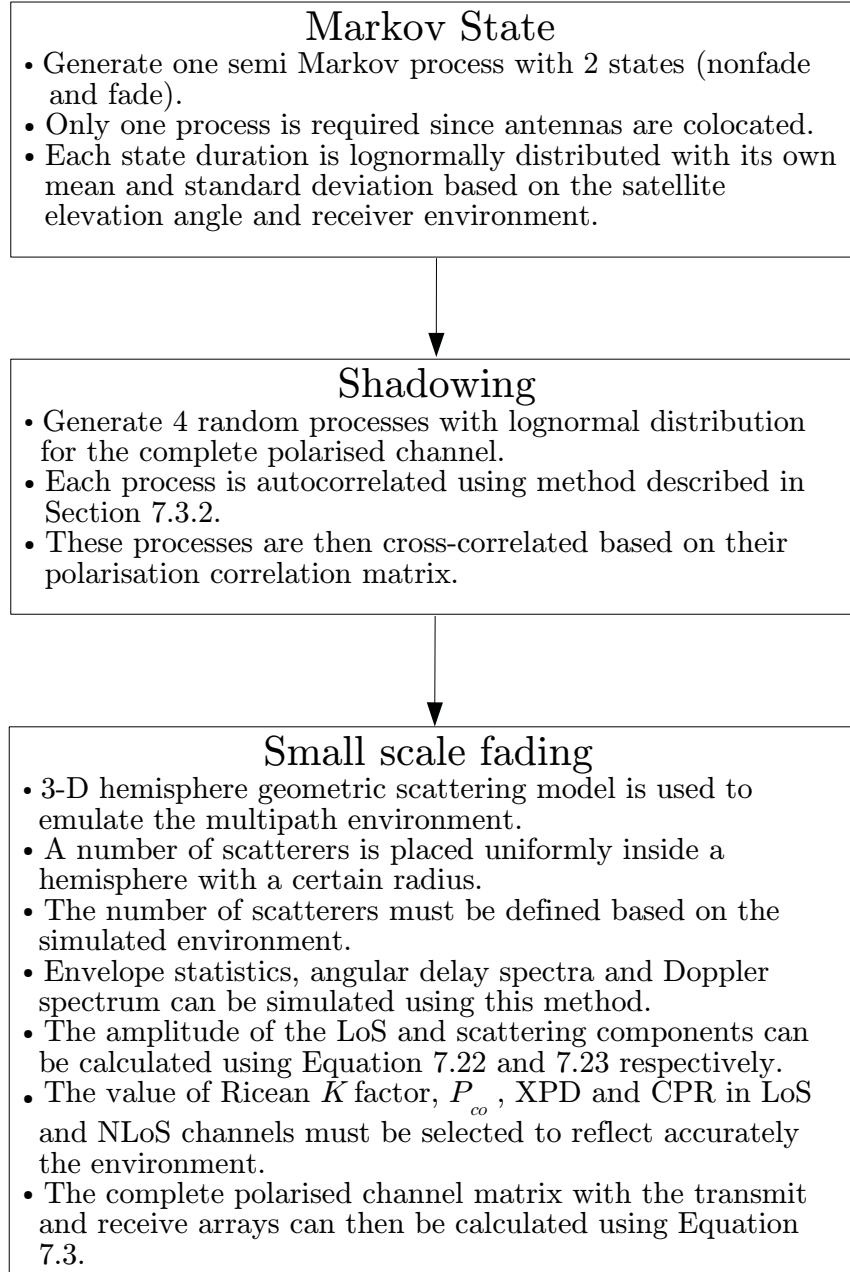


Figure 7.6: Flowchart of the new LMS MIMO channel model.

as closely as possible the theoretical amplitude statistic (e.g. Rayleigh or Nakagami) which corresponds to infinite number of scatterers for the best-case scenario, the number of scatterers in geometric scattering channel represents the resolvable independent paths between the transmitter and receiver. Therefore, its quantity is very much limited and the value of 20 can be considered to be realistic for outdoor environment [131]. Meanwhile, the regenerative distance defines the distance of which the scatterers are regenerated randomly to account for the mobile movement and the scatterers lifetime. The scatterers lifetime can be linked to the cluster visibility region, where [136] has stated that the visibility regions are in the range from 10λ to 100λ . In our case, the scatterers lifetime value is taken to be 5 m or nearly 41λ . The maximum distance describes the utmost allowable distance between receiver and scatterers.

As mentioned in previous subsection, the estimated Ricean K factor, channel XPDs and CPR from the measurement were used in the simulation in order to model the small scale fading of the channel. However, the usage is not straightforward as it seems since the measured K factor and XPD include the effect of antenna polarised gain pattern. Ideally, the small scale parameters need to be measured using omnidirectional perfectly polarised antenna so that its values depends only on the channel, not the receiving antennas. In the channel simulation, the simulated 3-D co and cross-polarised gain patterns of the horizontal array of dual circularly polarised SFPQHAs were used for the MIMO channel matrix computation.

7.5.3 Results comparison

Results from the Bishops Court measurement and the channel simulation are compared for the two SFPQHA array orientations in two channel conditions, which are the GOOD state (LoS channel) and the BAD state (NLoS channel). Firstly, the received signal characteristics in terms of envelope distribution, received power, channel XPD and signal correlation are compared between the measurement and simulation data. Then, the results from the capacity and eigenvalues evaluation using both measured and simulation signals are provided for comparison.

Table 7.1: Simulation parameters

Item	Parameter	Values		Source	
		GOOD	BAD		
Markov state	Semi-markov, suburban 20°	μ_{dur}	28.4108	28.5458	[46]
		σ_{dur}	11.6658	8.1245	
Shadowing	Correlation distance, L_{corr} (m)	10		[29]	
	Location variability, σ_L (dB)	3			
	Polarisation correlation matrix	$\begin{bmatrix} 1 & 0.86 & 0.85 & 0.9 \\ 0.86 & 1 & 0.91 & 0.87 \\ 0.85 & 0.91 & 1 & 0.88 \\ 0.9 & 0.87 & 0.88 & 1 \end{bmatrix}$			
Scatterer	Number of scatterers	20		[131]	
	Regenerative distance (m)	5		[136]	
	Maximum distance (m)	50			
Transmit antennas	Angle of elevation	30°		[126]	
	Normalised cross-polarised gain (dB)	-20			

Envelope statistics

The envelope distribution of the small scale co-polarised signals in the LoS and NLoS channels are compared in Table 7.2. There is a small variation about 1 dB between the measured and simulated K factors in the LoS channel while in the NLoS area, all subchannels amplitudes are Rayleigh distributed. This discrepancy is mainly due to the difficulty in estimating the accurate Ricean K factor from the measurement since the gain of the receive antennas is not omnidirectional.

Received power and channel XPD

Fig. 7.7 and Fig. 7.8 show the cumulative distribution functions (CDF) of the normalised received power by the straight and 50° tilted SFPQHA arrays in LoS and NLoS channels respectively. It can be seen that the simulated results are in good agreement with the measured received power. In the LoS channel, it is clear that the co-polarised signals have significantly higher received power than the cross-polarised

Table 7.2: Comparison of envelope distribution of the co-polarised subchannels.

Channel	SFPQHA orientation	Subchannel	Distribution	
			Measured	Simulated
LoS	Straight	RR	Ricean $K = 12.2$ dB	Ricean $K = 11.7$ dB
		LL	Ricean $K = 12.9$ dB	Ricean $K = 11.8$ dB
	50° tilted	RR	Ricean $K = 14.8$ dB	Ricean $K = 15.9$ dB
		LL	Ricean $K = 14.5$ dB	Ricean $K = 15.8$ dB
NLoS	Straight	RR	Rayleigh	Rayleigh
		LL	Rayleigh	Rayleigh
	50° tilted	RR	Rayleigh	Rayleigh
		LL	Rayleigh	Rayleigh

signals for both antenna configurations. As expected that in the NLoS, all subchannels will exhibit nearly the same received power characteristics. The XPDs of the channel as defined in Equation (2.13) and (2.14) give the average value of the depolarisation experienced by the receive antennas due to the effect of channel and antenna where its measured and simulated values are listed in Table 7.3.

Table 7.3: Comparison of the measured and simulated cross polarisation discriminations.

Channel	SFPQHA orientation	XPD _r (dB)		XPD _l (dB)	
		Measured	Simulated	Measured	Simulated
LoS	Straight	8.5	8.9	9.5	9.2
	50° tilted	10.1	9.8	9.2	9.5
NLoS	Straight	-0.64	-0.15	0.61	0.31
	50° tilted	-0.49	-0.1	0.76	0.15

Correlation

Table 7.4 lists the receive, co-polar subchannels and cross-polar subchannels correlation coefficients (ρ_r , ρ_{cp} and ρ_{xp} respectively as defined in Equation (2.12)) of the straight

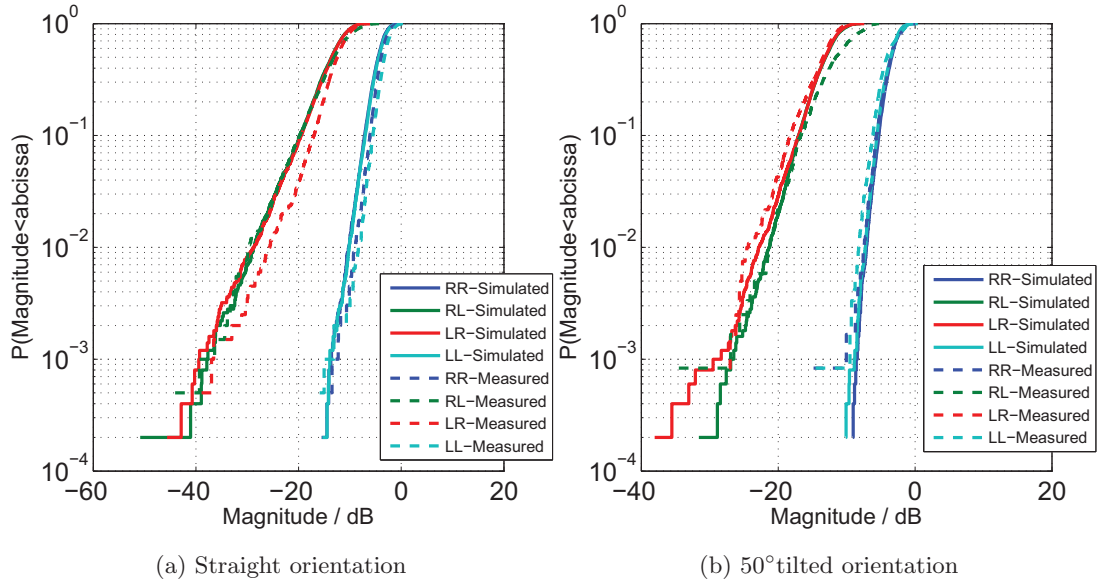


Figure 7.7: Received power CDFs of the straight and 50° tilted SFPQHA arrays in the LoS channel.

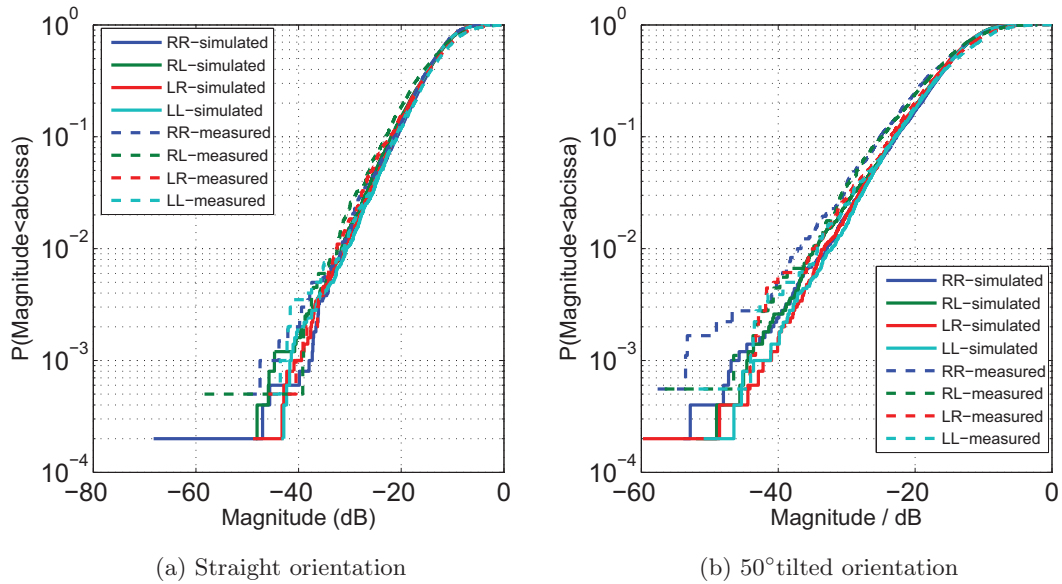


Figure 7.8: Received power CDFs of the straight and 50° tilted SFPQHA arrays in the NLoS channel.

and 50° tilted SFPQHA arrays in a LoS channel. In this channel condition, all correlation coefficients have a very high value due to the existence of a LoS component. This result also shows that there is a close proximity between the simulated and measured correlation values which indicates that the simulation is able to replicate the correlation behaviour of the received signals in a LoS channel.

Meanwhile, the comparison between correlation coefficients of the measured and simulated received signals of the SFPQHA arrays with two orientations in a NLoS channel is provided in Table 7.5. For the straight orientation, although both measured and simulated results indicate a low value for all correlations, it seems that the simulation has slightly underestimated the correlation coefficients where their values are considerably lower than the measured data. However, the channel simulation with the tilted SFPQHA array managed to provide much closer values of correlations to the measurement data in the NLoS channel.

Table 7.4: Comparison of measured and simulated receive, co-polar subchannels and cross-polar subchannels correlations in the LoS channel.

Orientation	Correlation	Magnitude	
		Measured	Simulated
Straight	ρ_r	0.89	0.80
	ρ_{cp}	0.95	0.94
	ρ_{xp}	0.70	0.84
50% tilted	ρ_r	0.84	0.91
	ρ_{cp}	0.97	0.98
	ρ_{xp}	0.80	0.94

Capacity and eigenvalues

Fig. 7.9a shows the CDFs of the MIMO capacity for the straight and 50° tilted SFPQHA arrays in simulated and measured LoS channels. Good agreement between the simulation and measurement results are evident especially at lower outage capacity. At 10% outage capacity, the simulation gave a slight increase of capacity of about 0.2 bit/s/Hz for straight SFPQHA when compared to the measured channel. Eigenvalue

Table 7.5: Comparison of measured and simulated receive, co-polar subchannels and cross-polar subchannels correlations in the NLoS channel.

Orientation	Correlation	Magnitude	
		Measured	Simulated
Straight	ρ_r	0.21	0.08
	ρ_{cp}	0.36	0.16
	ρ_{xp}	0.11	0.07
50% tilted	ρ_r	0.05	0.12
	ρ_{cp}	0.07	0.08
	ρ_{xp}	0.03	0.03

distribution comparison between the straight and 50° tilted SFPQHA in the LoS channel is shown in Fig. 7.10a. It is important to note that simulation has overestimated the magnitude of λ_1 while underestimated the magnitude of λ_2 in both cases of antenna configurations.

The capacity CDFs of the arrays in the simulated and measured NLoS channels are given in Fig. 7.9b. Based on the CDFs, it is evident that the straight SFPQHA provides a slightly better capacity compared to the tilted SFPQHA in both simulated and measured NLoS channels with a difference of 0.4 bit/s/Hz at 10% outage probability. In order to provide a complete evaluation of the MIMO performance, the eigenvalue distribution in simulated and measured NLoS channels are presented in Fig. 7.10b where the simulated CDFs agree well with the measured CDFs. This agreement between measured and simulated eigenvalues in both LoS and NLoS channels implies the resultant AoA distribution from the scatterers placement manages to replicate the characteristics of the measurement environment thus provides a good Ricean channel model for further analysis.

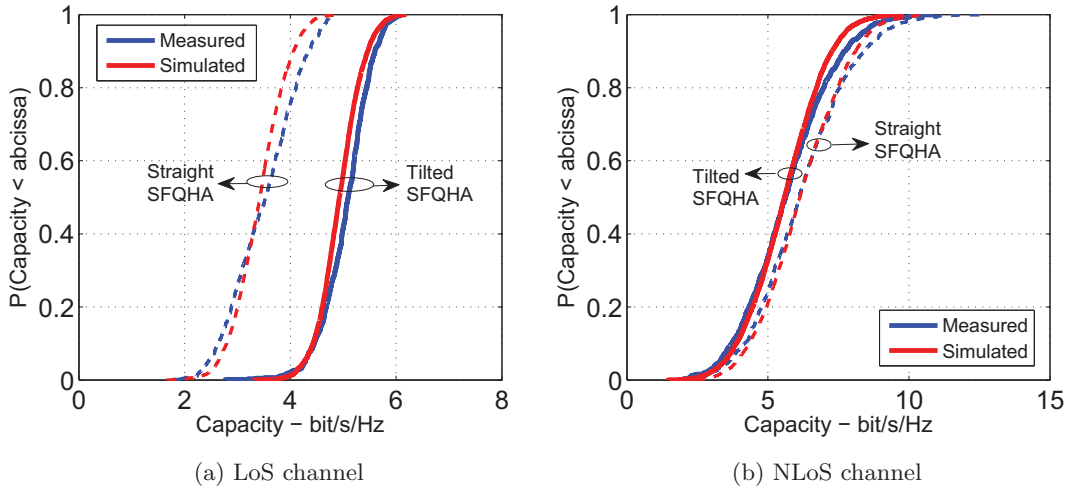


Figure 7.9: Capacity CDFs at SNR of 10 dB of the straight and 50° tilted SFPQHA arrays in measured and simulated channels.

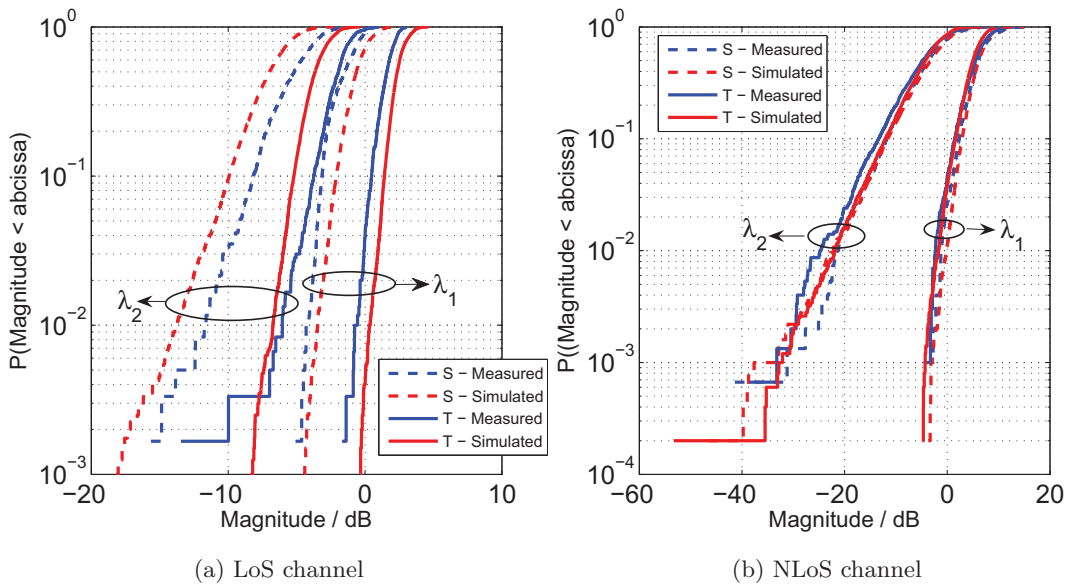


Figure 7.10: Eigenvalues CDFs at SNR of 10 dB of the straight and 50° tilted SFPQHA arrays in measured and simulated channels.

7.6 Effects of receive antenna orientation

7.6.1 Antennas parameters and orientations

Antennas parameters

A dual circularly polarised SFPQHA array with antenna spacing of 80 mm as presented in Fig. 4.18 was used as the receive antenna in this study to investigate the impact of antenna orientation on the capacity of a LMS MIMO system. This study utilises the newly developed channel model where it has been designed to include the receive antenna orientation in its simulation. Therefore, 3-D co and cross-polarised simulated gain patterns of the SFPQHA array were taken as the representation of the antennas in the channel simulation.

Orientation configuration

The receive antenna orientation with respect to the direction of the transmitter (i.e. satellite) must first be defined in order to provide an unambiguous representation of the antenna orientation in the channel simulation. This is conducted by utilising the two parameters of antenna orientation that were introduced earlier, which are ϕ_{ant} and θ_{ant} where the former denotes the azimuth counterclockwise angle from the direction of movement to the forward direction of the antenna while the latter provides the value of the inclination angle from the zenith to the antenna boresight axis. Fig. 7.11 shows the description of both parameters with respect to the antenna and transmitter direction. For the purpose of this study, ϕ_{ant} is varied with the values of 0° , 45° , 90° , 135° and 180° in the transmitter's side while θ_{ant} is taken to be 0° , 30° , 60° and 90° from the zenith.

In determining the value of ϕ_{ant} for the simulation, the following method can be used where the direction of movement and forward direction of the antenna are assigned with its respective unit vector given as \mathbf{v}_m and \mathbf{v}_{ant} . Then, ϕ_{ant} is calculated using

$$\phi_{ant} = \text{atan2}(\mathbf{v}_m \times \mathbf{v}_{ant}, \mathbf{v}_m \cdot \mathbf{v}_{ant}) \quad (7.29)$$

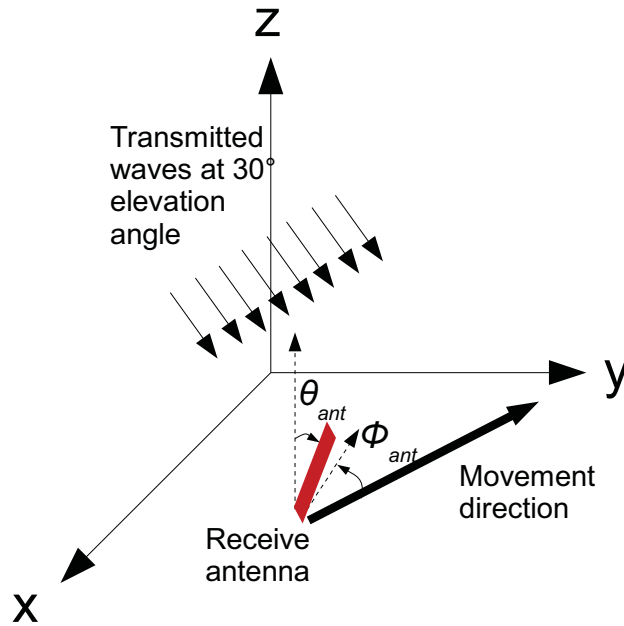


Figure 7.11: Orientation configuration of the receive array.

where atan2 is a variation of arctangent function in order to include angles from -180° to 180° [137]. The cross and dot products of the two vectors provide the value of the sine and cosine of the counterclockwise angle from \mathbf{v}_m to \mathbf{v}_{ant} .

7.6.2 Simulation parameters and procedure

In evaluating the receive antenna orientation, the newly proposed channel model was utilised since it has been developed to include the properties of the receive antennas. As the channel has been validated by using Bishops Court measurement results, which was conducted in a suburban area, this evaluation will only consider the antenna performance in the same environment as the validated channel simulation. In this study, the simulation parameters in terms of the channel characteristics and scatterers properties are provided in Table 7.6. However, the implemented large scale fading and shadowing conditions are not listed in this table as their parameters are similar to the one provided in Table 7.1. For simulating the small scale fading in the GOOD state (LoS channel), the Ricean K factor was selected to be 12.5 dB for both right hand and left hand circular polarisations while in the BAD state (NLoS channel), the small scale fade

envelope was considered to be Rayleigh distributed. As for the channel depolarisation in both states, the XPD_r and XPD_l in the GOOD state are considered to be equal and given a value of 14 dB. In the BAD state, both XPDs are chosen to be 0 dB since the channel is assumed to be highly depolarising as indicated by earlier measurement campaigns.

The scatterer properties that were utilised in this simulation are also similar to the parameters used in earlier validated channel simulation to replicate the Bishops Court measurement. The number of scatterers is kept at 20 with a regenerative distance of 5 m where the scatterers' position is randomly generated. Meanwhile, the maximum allowable distance between the receiver and the scatterers was fixed at 50 m. For the transmitter configuration, its elevation angle is fixed at 30° from the horizontal plane. In term of the azimuth angle of the transmitter, it was directed at 90° from the movement direction of the receiver as shown in Fig. 7.11.

Table 7.6: Simulation parameters

Item	Parameter	Values
Small scale fading	Ricean K factor (dB)	12.5
	XPD_{LoS} (dB)	14
	XPD_{NLoS} (dB)	0
Scatterer	Number of scatterers	20
	Regenerative distance (m)	5
	Maximum distance (m)	50
Simulation	Carrier frequency (GHz)	2.45
	Receiver speed ($m s^{-1}$)	5
	Sampling rate per λ	16
Transmit antennas	Elevation angle	30°
	Azimuth angle	90°
	Normalised cross-polarised gain (dB)	-20

7.6.3 Results

Instead of displaying the entire capacity CDF graphs for all variations of azimuth and inclination angle orientations, only the value of 10% outage capacity at SNR of 10 dB for each orientation is provided in order to compare the antenna performance in various positions. A 10% outage capacity implies that there are 10% probability that the capacity will be lower than the indicated value. This is written mathematically as:

$$P(C \leq C_{out}) = p_{out} \quad (7.30)$$

where C_{out} denotes the outage capacity and p_{out} is the outage probability of the capacity C to be lower than C_{out} . Due to the different small scale fading statistics between the GOOD and BAD states of large scale fading, the capacity results from these simulations are categorised into two parts which are the LoS channel (GOOD state) and the NLoS channel (BAD state).

LoS channel

The 10% outage capacity of a LMS MIMO system in a LoS channel that utilises a dual polarised SFPQHA array as the receive antenna in various orientations is presented in Fig. 7.12. When the array is oriented with $\phi_{ant} = 90^\circ$ in azimuth which is in the direction of the transmitter, the capacity is shown to be higher for all θ_{ant} except for straightly oriented array ($\theta_{ant} = 0^\circ$) when compared to other azimuth orientation as indicated by Fig. 7.12a. It is also apparent in this figure that for ϕ_{ant} in the range of 45° to 135° , the difference in outage capacity is very small for an array that is oriented 30° and more in inclination. Meanwhile, for ϕ_{ant} of 0° and 180° , a straightly oriented array offers a better outage capacity than other inclination angles.

Fig. 7.12b meanwhile provides the 10% outage capacity results when the inclination angle (θ_{ant}) of the array is varied from 0° to 90° which represents an increase in array tilting. Two cases of outage capacity magnitude variations can be obtained when the inclination angle is increased from 0° to 90° where the first one is for arrays that are pointed azimuthally to the direction of movement and its opposite ($\phi_{ant} = 0^\circ, 180^\circ$) while the second case is for $45^\circ, 90^\circ$ and 135° azimuthally oriented arrays. For the first

pattern, the increase of array tilting causes the outage capacity to decrease by about 2 bit/s/Hz where the minimum value is at $\theta_{ant} = 90^\circ$. However, the opposite effect occurs for the second case where by increasing the array tilting, the outage capacity increases with the highest increase is registered for array that is 90° azimuthally oriented.

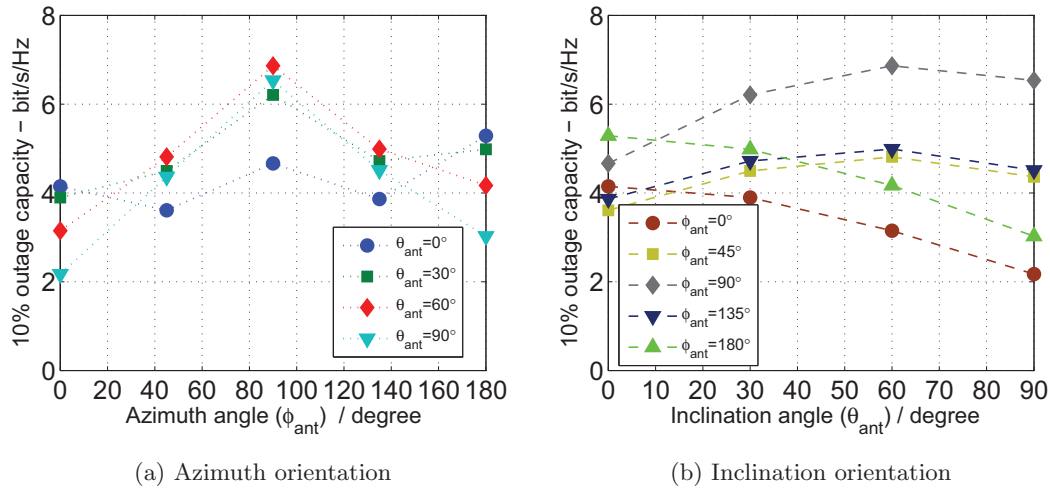


Figure 7.12: 10% outage capacity at SNR of 10 dB for various azimuth and inclination orientation of the SFPQHA array in the LoS channel with its direct component at 30° in elevation.

NLoS channel

The effect of receive array orientation on the performance of a LMS MIMO system was also investigated in a NLoS channel as presented in Fig. 7.13. In Fig. 7.13a, it is implied that variation in azimuth orientation (ϕ_{ant}) of the array with a fixed value of θ_{ant} has no visible impact to the outage capacity as its value remains almost constant over the range from 0° to 180° . Meanwhile, the results in Fig. 7.13b indicates that by tilting the array to 90° , the outage capacity reduces by almost 1 dB and this capacity reduction effect is valid regardless of the azimuth orientation of the array. Therefore, in a NLoS channel, it is more beneficial for the antenna boresight to point at the zenith in order to obtain a better capacity performance.

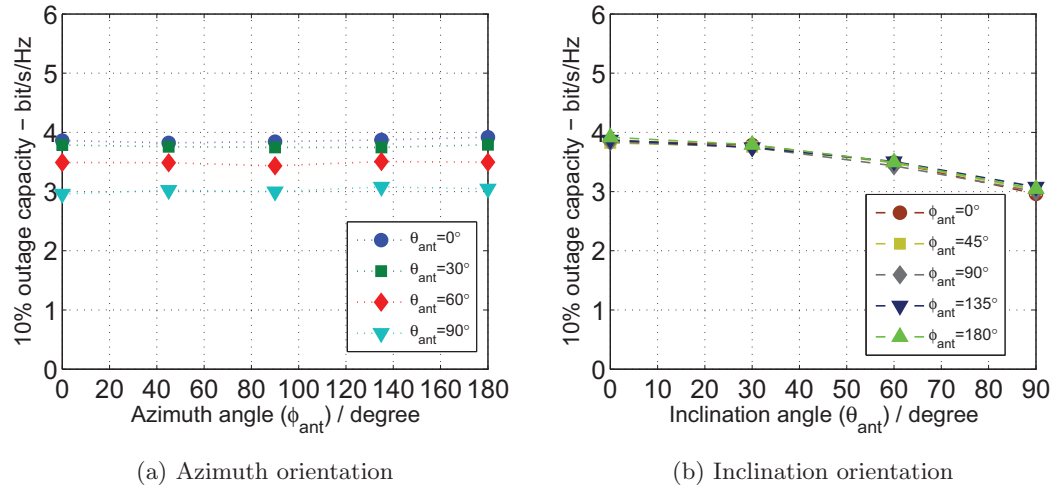


Figure 7.13: 10% outage capacity at SNR of 10 dB for various azimuth and inclination orientation of the SFPQHA array in the NLoS channel.

7.7 Effects of receive antenna spacing

7.7.1 Antennas parameters

The receive antenna array used in evaluating the impact of antenna spacing on the MIMO performance parameters of a LMS MIMO system are the SFPQHA arrays with variation of spacings with the value of 20 mm, 40 mm, 60 mm, 80 mm, 100 mm and 120 mm. The simulated co and cross-polarised embedded realised gain patterns of these arrays are utilised in the channel simulation to generate the required narrowband received signals which then will be used in calculating the performance parameters. As for its orientation, the array is configured in an upright position ($\theta_{ant} = 0^\circ$) and at the same time, the array front is pointed to the direction of the transmitter ($\phi_{ant} = 90^\circ$).

7.7.2 Simulation parameters and procedure

The simulation parameters in terms of propagation channel, scatterers and transmit antenna characteristics have been taken in this study to be identical to the previous study on the impact of antenna orientation as presented in Table 7.6. Furthermore,

the used large scale fading and shadowing behaviours of the channel were also exactly the same as in Table 7.1.

7.7.3 Results

The results of this investigation are provided in terms of the capacity and eigenvalues of the LMS MIMO system that utilises these SFPQHA arrays as its receive antennas. Fig. 7.14 shows the capacity CDFs of the SFPQHA array with its antenna spacing variation from 20 mm to 120 mm in both LoS and NLoS channels where the spacing variation is more likely to influence the system performance when array is in a LoS channel as indicated in Fig. 7.14a. There is however one anomaly in the case of LoS channel where the SFPQHA array with antenna spacing of 40 mm has the lowest capacity where its 10% outage capacity is 3.6 bit/s/Hz. As for other spacing values, their 10% outage capacities are quite close with one another in the range of 4.0 bit/s/Hz to 4.3 bit/s/Hz. The same behaviour is also apparent in the case of eigenvalues distribution where it is clear that the magnitude of λ_1 and λ_2 of the SFPQHA array with 40 mm separation is visibly lower than the rest of the array spacings as presented in Fig. 7.15a.

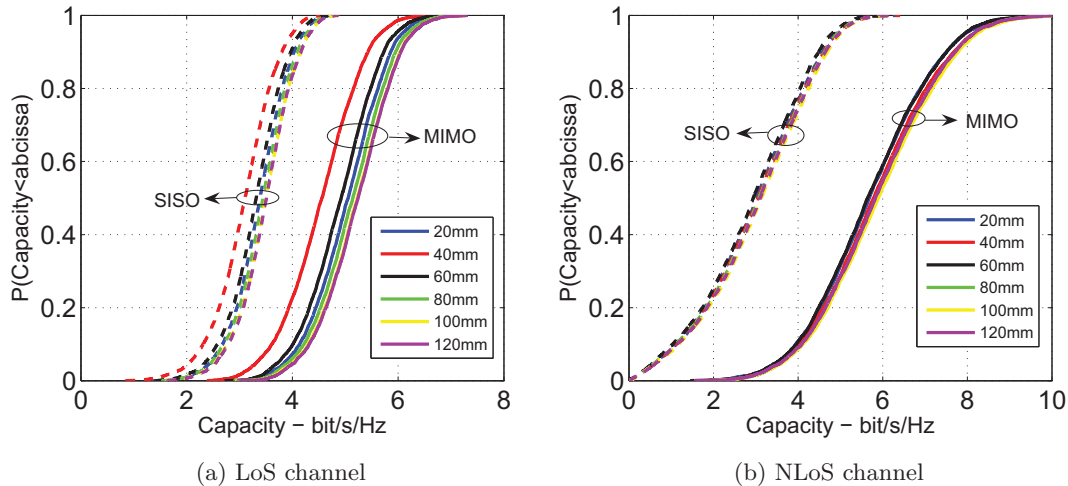


Figure 7.14: Capacity CDFs at SNR of 10 dB of the SFPQHA array with varying antenna spacing in both LoS and NLoS channels.

In the NLoS channel, the capacity of the SFPQHA array is not affected at all by the variation of its antenna spacing where its 10% outage capacity remains around 4 bit/s/Hz when the spacing is varied from 20 mm to 120 mm as shown in Fig. 7.15a. This behaviour implies that for a dual circularly polarised array in a NLoS channel, its spacing has no impact to its performance provided that the radiation pattern and efficiency of the antennas is not significantly altered. This result is supported by Fig. 7.15b, which shows the eigenvalues CDFs of the SFPQHA array with variation of antenna spacing in the NLoS channel. These capacity and eigenvalue results in both LoS and NLoS channels are in good agreement with the fact that these antennas are not affected by its close spacing, which is indicated by the mutual coupling coefficient as presented in Fig. 4.21.

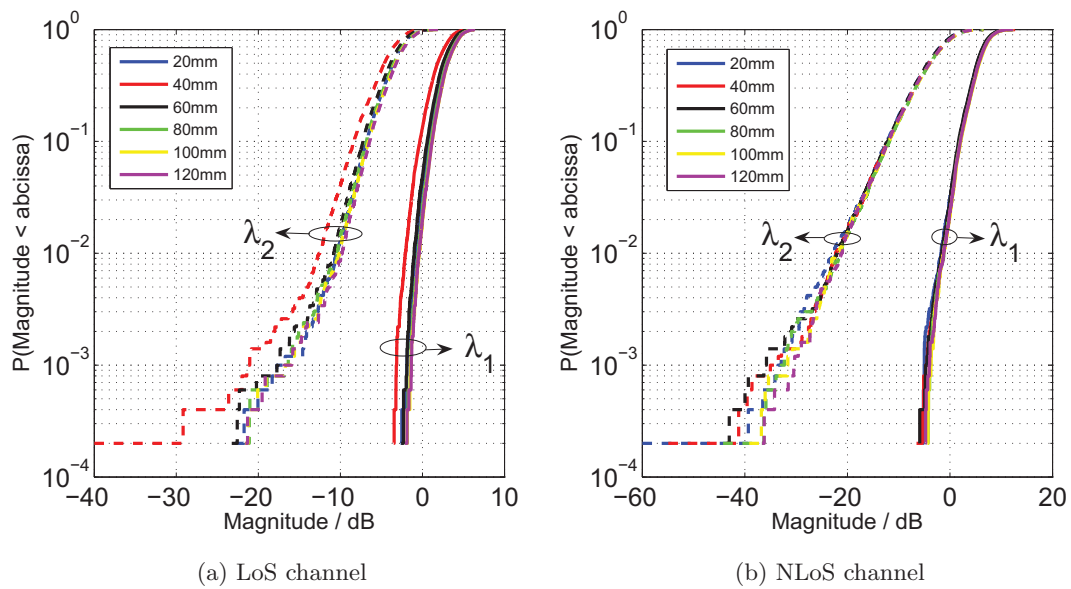


Figure 7.15: Eigenvalues CDFs at SNR of 10 dB of the SFPQHA array with varying antenna spacing in both LoS and NLoS channels.

7.8 Effects of receive antenna polarisation

7.8.1 Antennas parameters

For a definitive study on the impact of receive antenna polarisation, other antenna characteristics such as orientation, spacing between elements and pattern directionality must be suppressed so that only the polarisation of the antenna will be included in the evaluation. Therefore, the evaluated antennas are considered to be isotropic and its polarisation is defined to be constant over the whole angular domain. Apart from that, the removal of spatial dependency from the array properties is achieved by collocating these antennas to a single position. It should be noted that at its ideal condition, both transmit antennas are perfectly orthogonally polarised. The same behaviour is also applied to the receive antennas. Therefore, for this investigation, the polarisation purity of both orthogonally polarised antennas set at the transmitter and receiver is reduced where both antennas in the same set (transmitter or receiver) have similar cross-polarised gain (in different polarisations).

In this study, the antenna polarisation is characterised by its cross polarisation ratio (XPR) which defines the gain difference between the co-polarised and cross-polarised patterns and its value is taken to be constant for the whole angular domain. For a more comprehensive view on the impact of antenna polarisation, both transmit and receive antennas polarisations are varied with the values of 0 dB, 5 dB, 10 dB, 20 dB, 30 dB and ∞ dB where 0 dB represent equal co and cross-polarised gains while ∞ dB indicates that the antenna is purely co-polarised and its cross polarised gain is zero. This means that at ‘TXP’ condition, both transmit antennas are perfectly orthogonally polarised while at ‘TX10’ case, the transmit antennas have an XPR of 10 dB for each polarisation. It is also important to note that the total radiated power of both transmit and receive antennas patterns remains the same for all values of XPR.

7.8.2 Simulation parameters and procedure

Similar to previous simulations, this simulation utilises the proposed channel model with the same large scale fading and shadowing characteristics as the one that has been

validated by the measurement. As for the small scale fading properties, the Ricean K factor of the GOOD state is taken to be 15 dB and its XPD in the same state is considered to be infinity in dB, which means that the channel is not depolarising at all. The main reason for selecting the value of ∞ dB for the channel XPD is so that the depolarisation effect is only contributed by the polarisation impurity at both transmit and receive antennas. Table 7.7 lists the small scale fading, scatterers and simulation parameters and their selected value for the executed channel simulation in evaluating the impact of the antenna polarisation.

Table 7.7: Simulation parameters

Item	Parameter	Values
Small scale fading	Ricean K factor (dB)	15
	XPD _{LoS} (dB)	∞
	XPD _{NLoS} (dB)	0
Scatterer	Number of scatterers	20
	Regenerative distance (m)	5
	Maximum distance (m)	50
Simulation	Carrier frequency (GHz)	2.45
	Receiver speed (m s^{-1})	5
	Sampling rate per λ	16
Transmit antennas	Elevation angle	30°
	Azimuth angle	90°

7.8.3 Results

The simulation results are presented in terms of the correlation coefficient and outage capacity for various values of transmit and receive antennas's XPR in both LoS and NLoS channels. The LoS channel represents the GOOD state of the large scale fading categorisation where there is a direct LoS component while the NLoS channel implies the BAD state that indicates that the incoming waves are only consisting of incoherent components from the surrounding scatterers.

LoS channel

Fig. 7.16 presents the receive, co-polar subchannels and cross-polar subchannels correlations (ρ_r , ρ_{cp} and ρ_{xp} respectively) of the isotropic array with varying values of transmit and receive antennas' XPR in a LoS channel. The XPR of both transmit and receive antennas is varied from 0 dB to ∞ dB where in the case of transmit antenna, this variation is labelled in the figure legend by the number after the 'TX' with the exception of character 'P' which indicates that the transmit antennas are purely co-polarised or has an XPR of ∞ dB. When the transmit antennas have equal co and cross-polarised gains which are labelled as 'TX0', the receive antennas' XPR has no visible impact to the receive correlation as indicated in Fig 7.16a. However, as the transmit antennas' XPR increases which implies an increase of the polarisation purity for the transmit antennas, the receive correlation started to be affected by the receive antennas' XPR especially after the transmit antennas' XPR becomes more than 20 dB.

As for the co-polar subchannels correlation ρ_{cp} , neither the transmit antennas's XPR nor the receive antennas' XPR has any effect on the correlation value which is very close to one. This indicates that in a LoS channel, ρ_{cp} is largely independent of the polarisation purity of the utilised antennas at both sides of the transmitter and receiver. Meanwhile, the behaviour of the cross-polar subchannels correlation with respect to the polarisation characteristic of both transmit and receive arrays is largely similar to the receive correlation where for the correlation value to be low, the antennas at both sides need to be highly orthogonal in polarisation.

The next result which is presented in Fig. 7.17 shows the 10% outage capacity at SNR of 10 dB of a LMS MIMO system for each combination of polarisation purity of the transmit and receive antennas in a LoS channel. It is expected that the system will have the highest value of 10% MIMO outage capacity when the transmit antennas are perfectly orthogonally polarised ('TXP') and the receive array also exhibits a very high polarisation orthogonality between its antennas. When the polarisation orthogonality of the transmit antennas remain at a high level (≥ 20 dB), the outage capacity begin to decrease significantly as the receive antennas' XPR has the value lower than 20 dB. The results also show that the outage capacity for a SISO link where its utilised transmit

antennas are purely orthogonally polarised and the receive antennas' XPR are varied accordingly. It can be seen that for receive antennas' XPR larger than 20 dB, the SISO link provides a similar or better performance in terms of outage capacity when compared to MIMO links with 'TX0' and 'TX5' conditions.

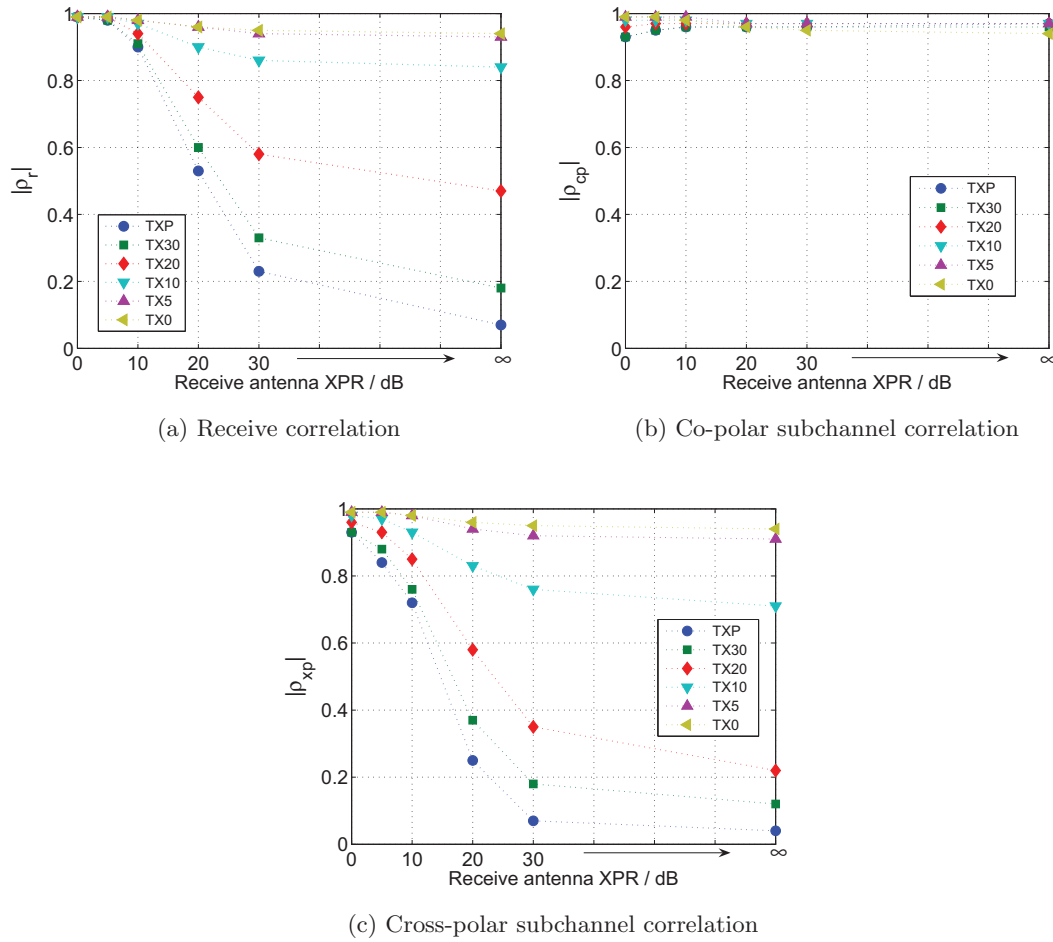


Figure 7.16: Correlation coefficients for various values of transmit and receive antennas' XPR in the LoS channel.

NLoS channel

The results of the correlation analysis for a NLoS channel are also provided in Fig. 7.18 in terms of the receive, co-polar subchannels and cross-polar subchannels correlation coefficients. For the receive correlation, it is clear that the transmit antennas' XPR has

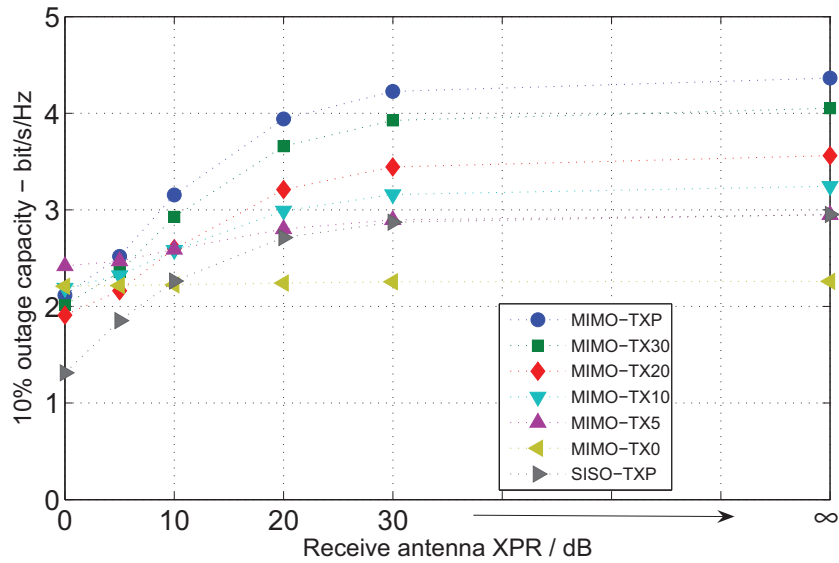


Figure 7.17: 10% outage capacity at SNR of 10 dB for various values of transmit and receive antennas' XPR in the LoS channel.

no impact on the correlation where its value only decreases as the receive antennas' XPR reduces. In this type of environment, a reasonably low receive correlation can be achieved even when the receive antennas have only an XPR of 10 dB. For the case of the co-polar subchannels correlation, a low correlation can be obtained for all values of receive antennas' XPR as long as the transmit antennas have an XPR higher than 10 dB. This implies in this channel condition, the co-polar subchannels correlation can be reduced by having highly orthogonal polarised antennas at either the transmitter or receiver. Meanwhile, the cross-polar subchannels correlation has almost identical characteristics as its co-polar counterpart in a NLoS channel as shown in Fig. 7.18c.

In Fig. 7.19, the 10% outage capacity at SNR of 10 dB is presented for various combinations of the transmit and receiver antennas' XPRs. In general, an increase in the polarisation purity of the transmit and receive antennas will always provide a better outage capacity for the system. However, the outage capacity improvement begins to level off after the value of XPR becomes greater than 20 dB in both cases of antennas sides. Therefore, in this channel condition, a perfectly orthogonal polarised antennas at both transmitter and receiver may only provide a marginal outage capacity improvement when compared to the case of antennas with XPR of 20 dB. It is also interesting

to note that for all cases of XPR value, the MIMO outage capacity is always higher than the outage capacity of a SISO link of purely polarised antennas.

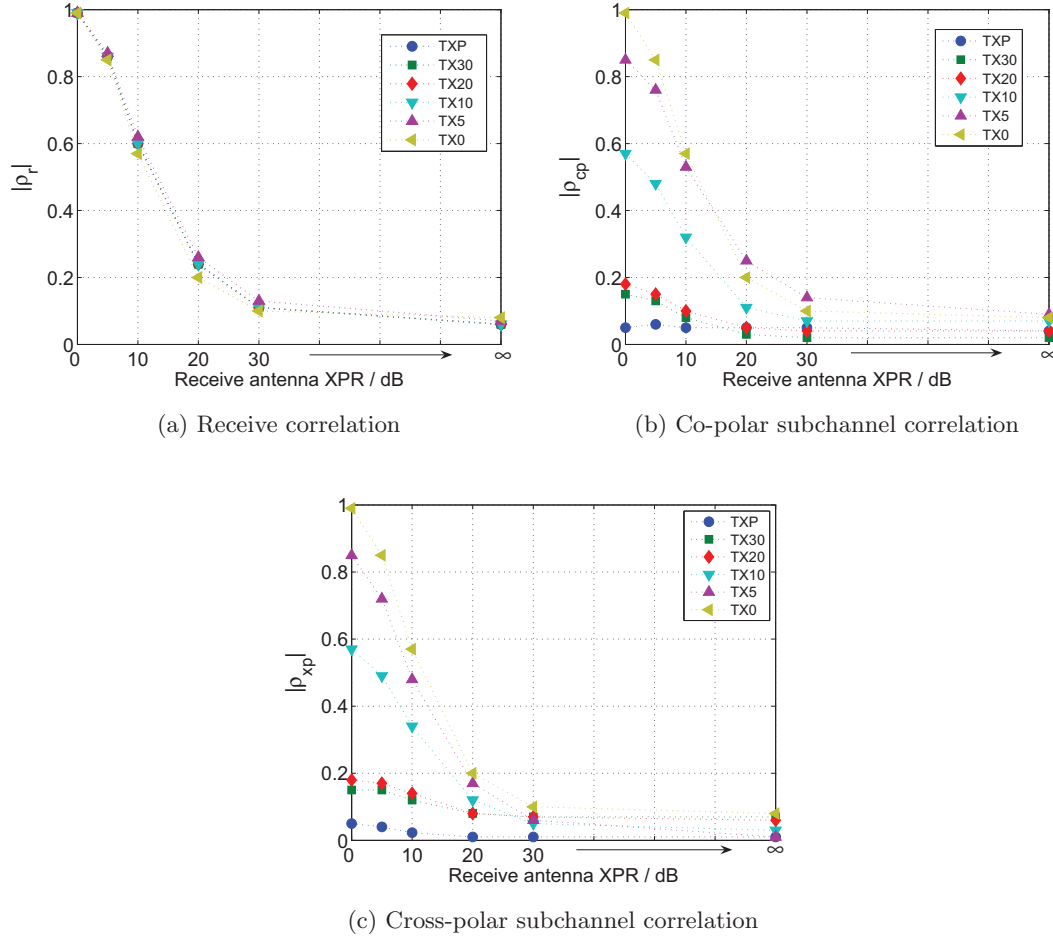


Figure 7.18: Correlation coefficients for various values of transmit and receive antennas' XPR in the NLoS channel.

7.9 Performance comparison of several receive antennas

7.9.1 Objectives

The main objective of this investigation is to compare the performance of the designed SFPQHA array with several receive antennas in a LMS MIMO system using the newly proposed channel model in both LoS and NLoS channels. Three main parameters

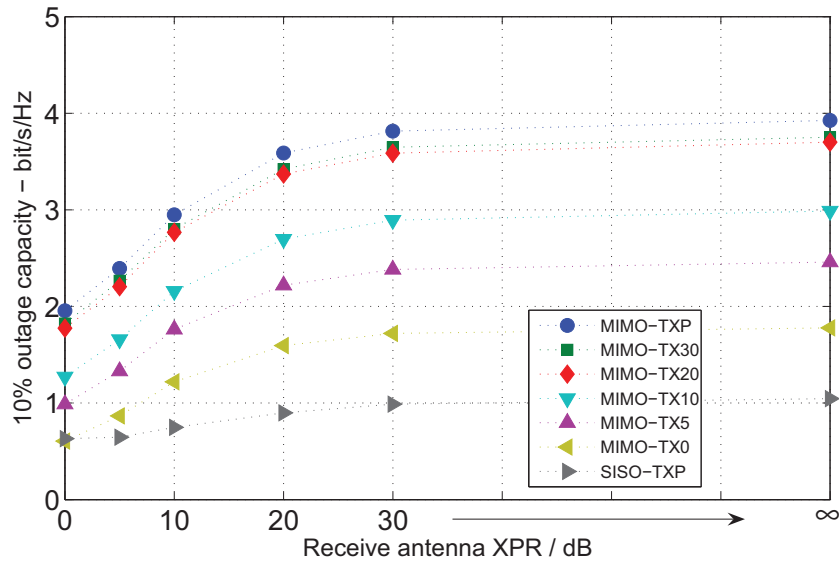


Figure 7.19: 10% outage capacity at SNR of 10 dB for various values of transmit and receive antennas' XPR in the NLoS channel.

will be evaluated in this work where the correlation of the received signals was first investigated and followed by capacity and eigenvalues computation for each antenna.

7.9.2 Receive antennas

Antennas

Four types of receive antennas were selected for this simulation which are the dual circularly polarised SFPQHA array with 80 mm separation, dual circularly polarised patch with diagonal slot array with 80 mm spacing, co-located 45° slanted cross dipoles and dipole array with 80 mm spacing. The reason for choosing these four arrays is mainly to provide as much as possible realistic variations of the antennas properties in terms of radiation pattern, polarisation and element spacing where each array has its own distinctive characteristics. For the patch array, the cross-polarised gain is higher when compared to the cross polarised gain of the SFPQHA array where at the boresight, a difference of 10 dBic between the co and cross-polarised gains is evident for each patch. This is due to the fact that the considered patch with diagonal slot design has not been optimised for a very low XPD in order to provide a realistic value

of patch's XPD when it is fitted into a small handheld device which does not allow for a large ground plane. Meanwhile, the last two arrays which consist of arrangement variation of dipoles with linear polarisation were included in this simulation to analyse the performance difference between linearly and circularly polarised arrays. The 3-D simulated co and cross-polarised gain patterns of the SFPQHA and patch array are presented in Fig. 5.1 and Fig. 7.20 respectively while Fig. 7.21 shows the 3-D absolute gain patterns of the dipole array and cross dipoles.

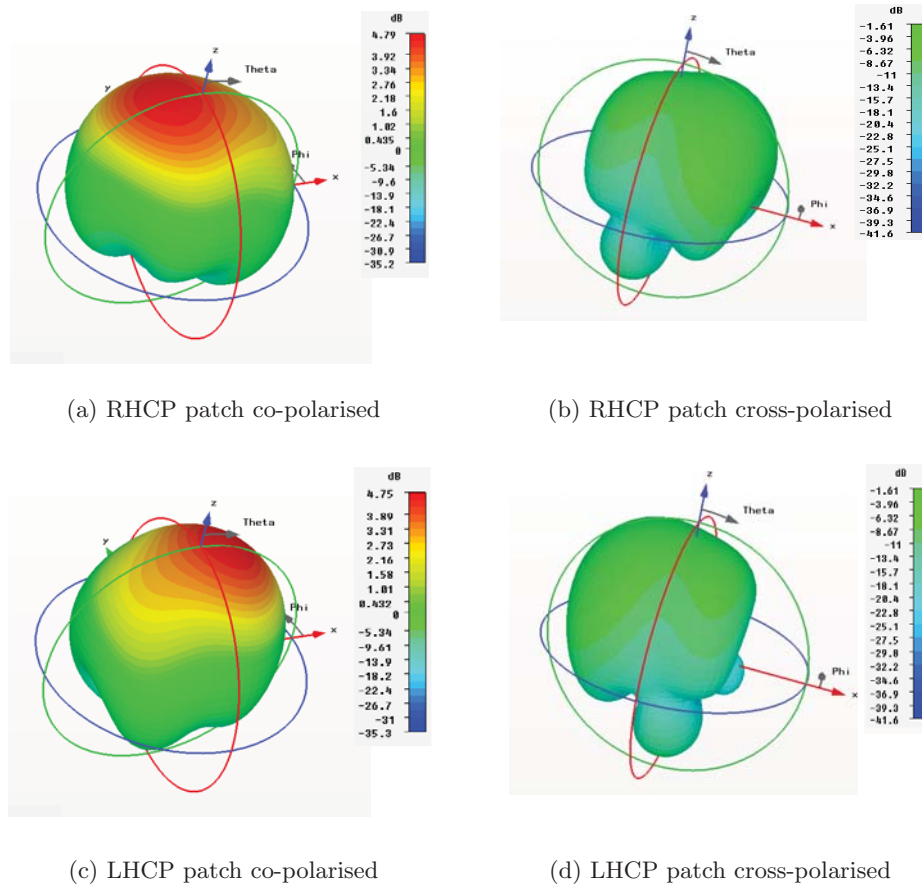


Figure 7.20: 3-D co and cross polarised gain patterns of the patch array.

Orientations

Aside from the antenna type and radiation pattern, the impact of antenna orientation on the system performance was also investigated where each array is oriented in four different directions. Each orientation is characterised by its azimuth and inclination

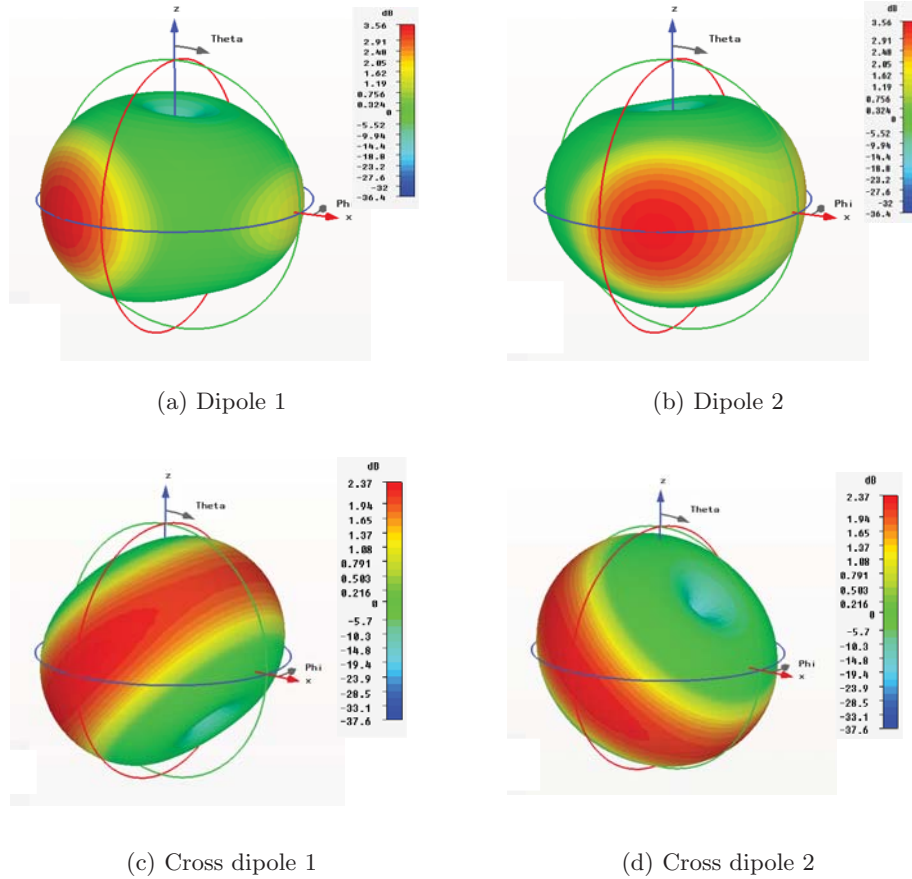


Figure 7.21: 3-D absolute gain patterns of the dipole array and cross dipoles.

angles as follows:

- First orientation - $(\phi_{ant} = 0^\circ, \theta_{ant} = 0^\circ)$.
- Second orientation - $(\phi_{ant} = 0^\circ, \theta_{ant} = 60^\circ)$.
- Third orientation - $(\phi_{ant} = 90^\circ, \theta_{ant} = 0^\circ)$.
- Fourth orientation - $(\phi_{ant} = 90^\circ, \theta_{ant} = 60^\circ)$.

7.9.3 Simulation parameters and procedure

In this study, the simulation utilises the same large scale fading and shadowing parameters as used in the first simulation that has been validated by the measurement campaign which is listed in Table 7.1. As for the small scale fading parameters, the Ricean K factor for the GOOD state is taken to be 12.5 dB while the small scale fading

distribution in the BAD state is considered to be Rayleigh. In terms of the channel cross polarisation discrimination (XPD), its value in the GOOD state XPD_{LoS} and XPD_{NLoS} are given by 14 dB and 0 dB respectively.

Table 7.8: Simulation parameters

Item	Parameter	Values
Small scale fading	Ricean K factor (dB)	12.5
	XPD_{LoS} (dB)	14
	XPD_{NLoS} (dB)	0
Scatterer	Number of scatterers	20
	Regenerative distance (m)	5
	Maximum distance (m)	50
Simulation	Carrier frequency (GHz)	2.45
	Receiver speed (m s^{-1})	5
	Sampling rate per λ	16
Transmit antennas	Elevation angle	30°
	Azimuth angle	90°
	Normalised cross-polarised gain (dB)	-20

7.9.4 Correlation results

The simulated receive, co-polar and cross-polar subchannels correlation coefficients for each antenna system are listed in Table 7.9 and Table 7.10 for both LoS and NLoS channels respectively. In the LoS channel, with the exception of the dipole array with $(\phi_{ant} = 90^\circ, \theta_{ant} = 60^\circ)$ orientation, all values of correlation coefficient for all antennas and orientations are significantly high and close to one. For the receive correlation ρ_r , its high value even for the SFPQHA array which has a high simulated XPR ($\sim 30\text{dB}$) can be explained by taking into account the effects of the channel depolarisation parameter XPD as well as the transmit antennas cross-polarised gain on the signal correlation. Since the transmit antennas has an XPR of 20 dB, the receive correlation is estimated to be around 0.6 for a dual polarised array that exhibit an XPR of 30 dB in a LoS channel with no depolarisation (refer to ‘TX20’ condition in Fig. 7.16a). However, when

the channel XPD has a value lower than the transmit antennas' XPR as in this case, then the channel XPD will be the new limiting factor and this will push the receive correlation to a higher value than 0.6.

As for the co-polar subchannels correlation, its value is expected to be close to one since both co-polarised received signals will exhibit a similar fading behaviour in a LoS channel. Meanwhile, for the anomalous case of the dipole array with orientation of ($\phi_{ant} = 90^\circ, \theta_{ant} = 60^\circ$) that provides a low value for all correlation coefficients, this result can be attributed to the fact that in this orientation, the corresponding antenna gain to the LoS component is very low which then leads to a low correlation value.

Table 7.9: Receive, co-polar subchannels and cross-polar subchannels correlations for arrays with various orientations in the LoS channel.

Antenna	Correlation	Orientation			
		1 st	2 nd	3 rd	4 th
SFPQHA array	ρ_r	0.88	0.87	0.83	0.92
	ρ_{cp}	0.94	0.93	0.94	0.98
	ρ_{xp}	0.82	0.82	0.74	0.87
Patch array	ρ_r	0.88	0.91	0.84	0.96
	ρ_{cp}	0.92	0.92	0.94	0.98
	ρ_{xp}	0.83	0.81	0.83	0.92
Cross dipoles	ρ_r	0.99	0.99	0.86	0.99
	ρ_{cp}	0.97	0.97	0.79	0.95
	ρ_{xp}	0.97	0.97	0.79	0.95
Dipole array	ρ_r	0.93	0.96	0.93	0.16
	ρ_{cp}	0.94	0.95	0.94	0.13
	ρ_{xp}	0.93	0.95	0.94	0.09

Table 7.10 provides the simulated value of all correlation coefficients for each antenna system and orientation in the NLoS channel. In general, all correlation coefficients that were calculated for all arrays and orientations have a low magnitude except for the case of the receive correlation of the 45° slanted cross dipoles for all type of orientations. This may be due to the geometric arrangement of the array where both dipoles have

identical vertically-polarised vector fields and opposing horizontally polarised vector fields. Therefore, its correlation is much higher as any vertical component of the incoming waves will be received equally by both slanted dipoles. Apart from that, as the cross dipoles is colocated, there is no spatial decorrelation effect that may reduce its receive correlation.

Table 7.10: Receive, co-polar subchannels and cross-polar subchannels correlations for arrays with various orientations in the NLoS channel.

Antenna	Correlation	Orientation			
		1 st	2 nd	3 rd	4 th
SFPQHA array	ρ_r	0.17	0.11	0.09	0.05
	ρ_{cp}	0.06	0.04	0.12	0.15
	ρ_{xp}	0.07	0.05	0.08	0.03
Patch array	ρ_r	0.11	0.28	0.19	0.18
	ρ_{cp}	0.07	0.06	0.08	0.07
	ρ_{xp}	0.04	0.09	0.07	0.04
Cross dipoles	ρ_r	0.84	0.85	0.85	0.86
	ρ_{cp}	0.11	0.13	0.20	0.24
	ρ_{xp}	0.12	0.15	0.23	0.22
Dipole array	ρ_r	0.19	0.22	0.23	0.17
	ρ_{cp}	0.10	0.11	0.07	0.03
	ρ_{xp}	0.10	0.13	0.09	0.15

7.9.5 Capacity and eigenvalues results

Performance evaluation of these receive arrays in terms of capacity and eigenvalues were then conducted where its results are compartmentalised by the array orientation. For a fair comparison between the receive arrays in each orientation, the simulated channel is normalised by the total received power of a single co-polarised signal which in this case is the RHCP signal of the SFPQHA array. In each orientation category, the capacity and eigenvalues results are given for both LoS and NLoS channels.

First Orientation - ($\phi_{ant} = 0^\circ, \theta_{ant} = 0^\circ$)

For the first orientation where the arrays are pointed to 0° in azimuth and 0° inclined, Fig. 7.22 and Fig. 7.23 present the capacity and eigenvalues CDFs of all evaluated receive arrays in both LoS and NLoS channels. In the first channel condition, it is indicated that the SFPQHA array and cross dipoles offer the best performance with a difference of almost 1 bit/s/Hz at 10% outage capacity when compared to the other two array of patch antennas and dipoles. The antennas performance in a LoS channel was then further examined by comparing the CDFs of the eigenvalues for each array as shown in Fig. 7.23a. The magnitude of λ_1 for the cross dipoles is significantly larger than the other arrays which leads to a higher capacity even though its λ_2 has the lowest magnitude among the others. As for the SFPQHA array, although its λ_1 is slightly weaker than the cross dipoles, it has the best performing λ_2 which then help to bring its capacity to the same level as the cross dipoles. The dipoles and dual polarised patch arrays meanwhile have a lower capacity than the SFPQHA array due to their weaker λ_2 even though they have almost the same magnitude of the λ_1 .

In the NLoS channel, the patch array is the best performing array amongst other arrays, which is a complete opposite of its LoS channel performance. Its 10% outage capacity at 4.1 bit/s/Hz is only 0.5 bit/s/Hz, 0.8 bit/s/Hz and 1.1 bit/s/Hz higher than the SFPQHA array, cross dipoles and dipole array respectively as presented in Fig. 7.22b. The drastic improvement of the patch array performance in the NLoS channel can be attributed to the fact that in such channel, the antenna's polarisation purity is no longer an important parameter that affects its receiving ability since the incoming waves are largely depolarised. As the patch array has the highest co and cross-polarised gain patterns in the upper hemisphere, therefore it is able to register a higher power level of received signal when compared to other arrays. The results of the capacity performance of these arrays are supported by the CDFs of the eigenvalues as presented in Fig. 7.23b.

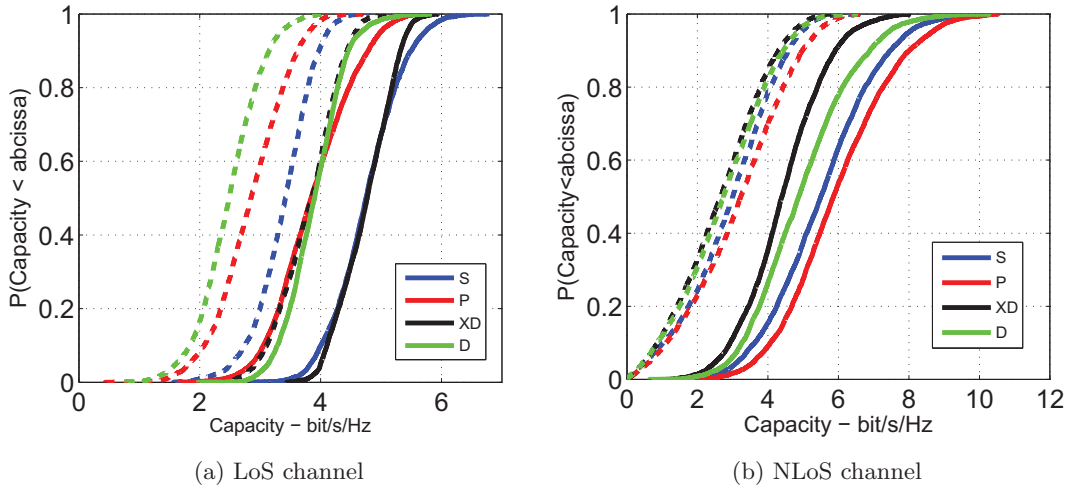


Figure 7.22: Capacity CDFs at SNR of 10 dB of the SFPQHA array (S), patch array (P), cross dipoles (XD) and dipole array (D) with $(\phi_{ant} = 0^\circ, \theta_{ant} = 0^\circ)$ orientation in both LoS and NLoS channels.

Second Orientation - $(\phi_{ant} = 0^\circ, \theta_{ant} = 60^\circ)$

The second orientation implies that the arrays are directed to 0° in azimuth and inclined to 60° . The results of the simulation in terms of the capacity of a LMS MIMO system when utilising these arrays as the receive antenna are provided in Fig. 7.24. In the LoS channel, again the cross dipoles has the highest 10% outage capacity at 4.7 bit/s/Hz amongst other evaluated arrays while the patch array registers the lowest value at 3 bit/s/Hz. The reason for the cross dipoles to display an excellent capacity performance in a LoS channel is that the Angle-of-Arrival of the LoS component coincides with the maximum gain of one of the tilted cross dipoles. This reasoning can be further validated by the eigenvalues CDFs presented in Fig. 7.25a where the λ_1 of the cross dipoles has the biggest magnitude while its λ_2 has the lowest value among other arrays.

When the arrays are evaluated in a NLoS channel, it is indicated that the patch and dipole arrays have a 10% outage capacity of 3.9 bit/s/Hz while the other two arrays have a slightly lower capacity around 3.5 bit/s/Hz as shown in Fig. 7.24b. A closer examination on their eigenvalues CDFs as presented in Fig. 7.25b reveals that the λ_1 of all arrays has almost the same magnitude while for the λ_2 , the cross dipoles has the

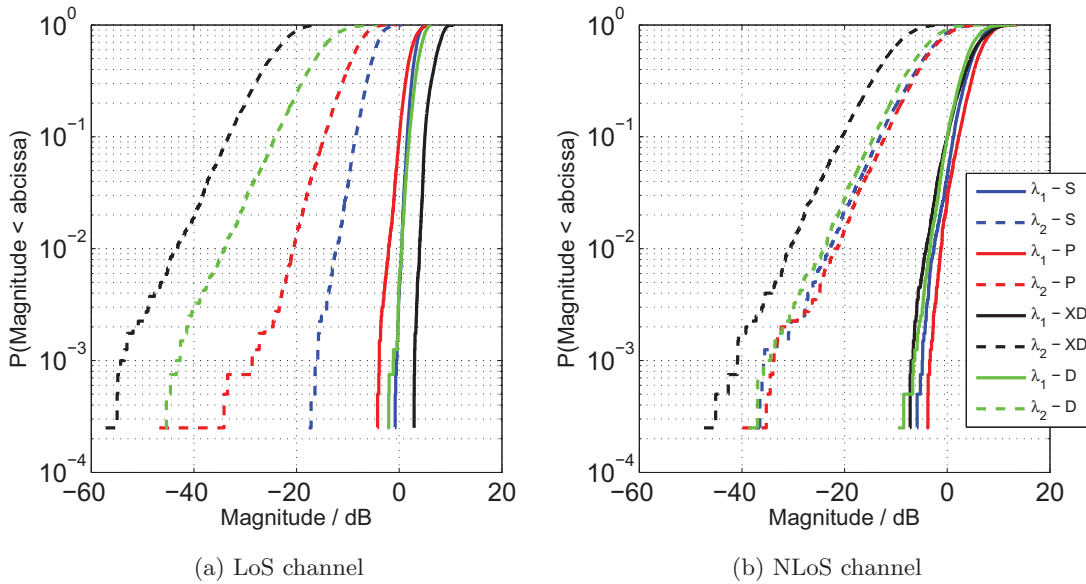


Figure 7.23: Eigenvalues CDFs at SNR of 10 dB of the SFPQHA array (S), patch array (P), cross dipoles (XD) and dipole array (D) with $(\phi_{ant} = 0^\circ, \theta_{ant} = 0^\circ)$ orientation in both LoS and NLoS channels.

lowest magnitude when compared to the other arrays.

Third Orientation - $(\phi_{ant} = 90^\circ, \theta_{ant} = 0^\circ)$

For this orientation, the arrays are pointed azimuthally to the direction of the transmitter (90° from the movement direction) while at the same time remain in upright position. The capacity CDFs of the evaluated arrays in a LoS channel are displayed in Fig. 7.26a where the SFPQHA array obtains the highest 10% outage capacity at 4.2 bit/s/Hz. Meanwhile, the other three arrays have about the same 10% outage capacity with the value of 3.5 bit/s/Hz. The capacity difference between the SFPQHA array and the three arrays may be due to the fact that in this orientation, the SFPQHA array provides the best combination of the magnitude of λ_1 and λ_2 where its λ_2 is hugely stronger than other arrays' λ_2 as indicated in Fig. 7.27a. Therefore, even though the SFPQHA array's λ_1 has about the same magnitude behaviour as the others, its significantly better λ_2 contributes to increase the array's MIMO capacity. This shows that in an upright position (0° from the zenith), the SFPQHA array is highly

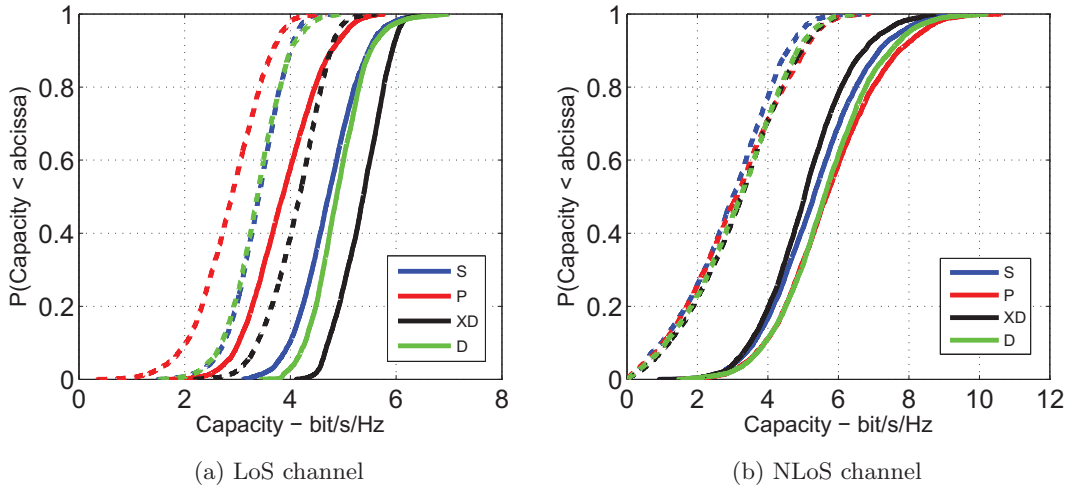


Figure 7.24: Capacity CDFs at SNR of 10 dB of the SFPQHA array (S), patch array (P), cross dipoles (XD) and dipole array (D) with $(\phi_{ant} = 0^\circ, \theta_{ant} = 60^\circ)$ orientation in both LoS and NLoS channels.

suitable to be utilised as a receive array in a circular polarisation multiplexing system since its eigenvalues magnitude is relatively stronger in order to create two artificial subchannels.

Meanwhile, in a NLoS channel, the capacity CDFs of both SFPQHA and patch arrays have almost the same characteristic where their 10% outage capacity are at 3.8 bit/s/Hz while for the other two dipole arrays, their outage capacity value are slightly lower in comparison. In detail, the 10% outage capacity of the dipole array and cross dipoles are at 3.4 and 2.8 bit/s/Hz respectively. By studying the eigenvalues distribution of each array in Fig. 7.27b, it is clear that the SFPQHA and patch arrays' λ_1 and λ_2 are slightly stronger than the rest of the arrays which contribute to a higher capacity. However, for the cross dipoles, both of its eigenvalues have a lower magnitude especially the λ_2 that causes the array to obtain the worst capacity performance amongst the evaluated arrays.

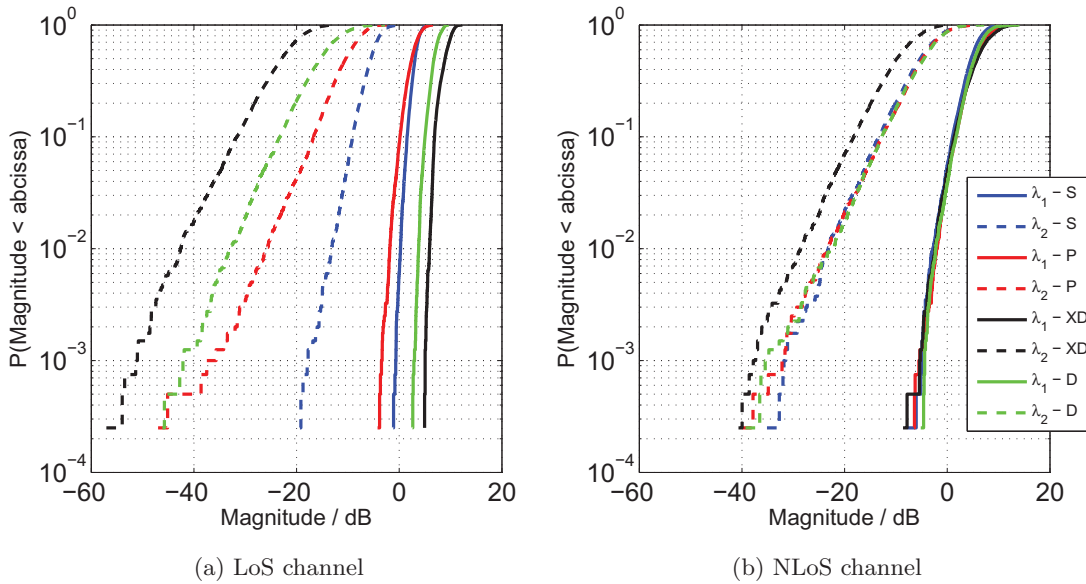


Figure 7.25: Eigenvalues CDFs at SNR of 10 dB of the SFPQHA array (S), patch array (P), cross dipoles (XD) and dipole array (D) with $(\phi_{ant} = 0^\circ, \theta_{ant} = 60^\circ)$ orientation in both LoS and NLoS channels.

Orientation 4 - $(\phi_{ant} = 90^\circ, \theta_{ant} = 60^\circ)$

The final array orientation is when the arrays are oriented azimuthally towards the transmitter (90° in azimuth) and they are also 60° tilted from the zenith. Therefore, it can be said that for an axially radiated antenna, this orientation provides a perfect match between the antenna's main beam with the LoS component of the incoming waves. In Fig. 7.28a, the capacity CDFs of all evaluated arrays in a LoS channel are presented where it indicates clearly that the SFPQHA and patch arrays are the best performing array with a 10% outage capacity of 4.3 and 4.0 bit/s/Hz respectively while the dipole array has the lowest capacity when compared to other antennas and orientations. The enormous decrease of capacity that was experienced by the dipole array is due to the very low corresponding antenna gain in the direction of the LoS component.

As for the NLoS channel, Fig. 7.28b and Fig. 7.29b show the capacity and eigenvalues CDFs of the SFPQHA array, patch array, cross dipoles and dipole array respectively.

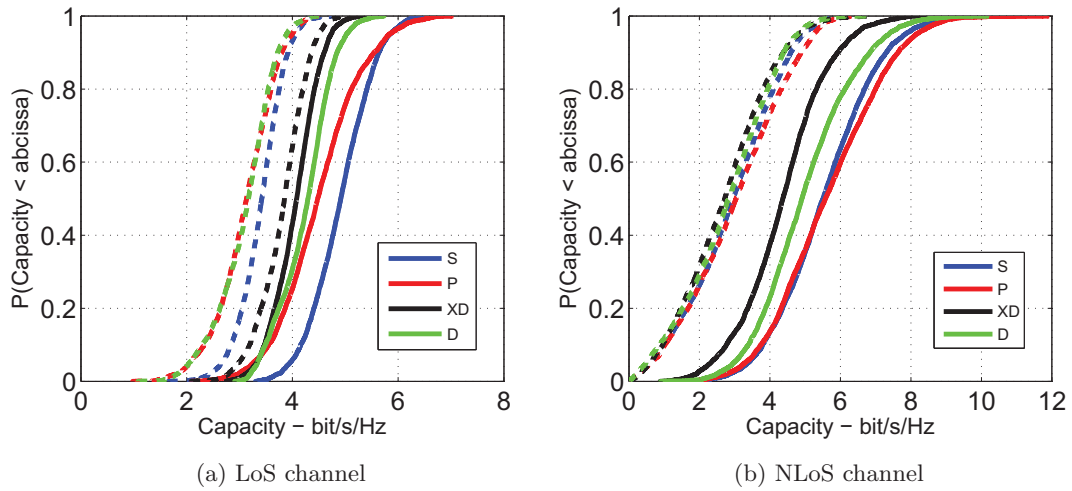


Figure 7.26: Capacity CDFs at SNR of 10 dB of the SFPQHA array (S), patch array (P), cross dipoles (XD) and dipole array (D) with $(\phi_{ant} = 90^\circ, \theta_{ant} = 0^\circ)$ orientation in both LoS and NLoS channels.

In general, these figures indicate a similar behaviour of the capacity and eigenvalues distributions in this orientation with the earlier orientation of $(\phi_{ant} = 90^\circ, \theta_{ant} = 0^\circ)$ where the patch and SFPQHA arrays has the highest outage capacity. As for the cross dipoles and dipole array, their 10% outage capacities are slightly lower at 3.0 and 3.5 bit/s/Hz respectively.

7.10 Summary

A new approach in modelling the land mobile satellite (LMS) MIMO channel has been proposed in this chapter where its main purpose is to include the receive antennas properties in the channel simulation. To achieve this objective, the proposed model combines the statistical method in modelling the large scale fading and shadowing and the geometric scattering method for the small scale fading modelling. The new channel model was then validated using results from Bishops Court measurement where its narrowband characteristics and MIMO figures of merit are compared.

Using the developed channel model, the effects of three array properties which are the

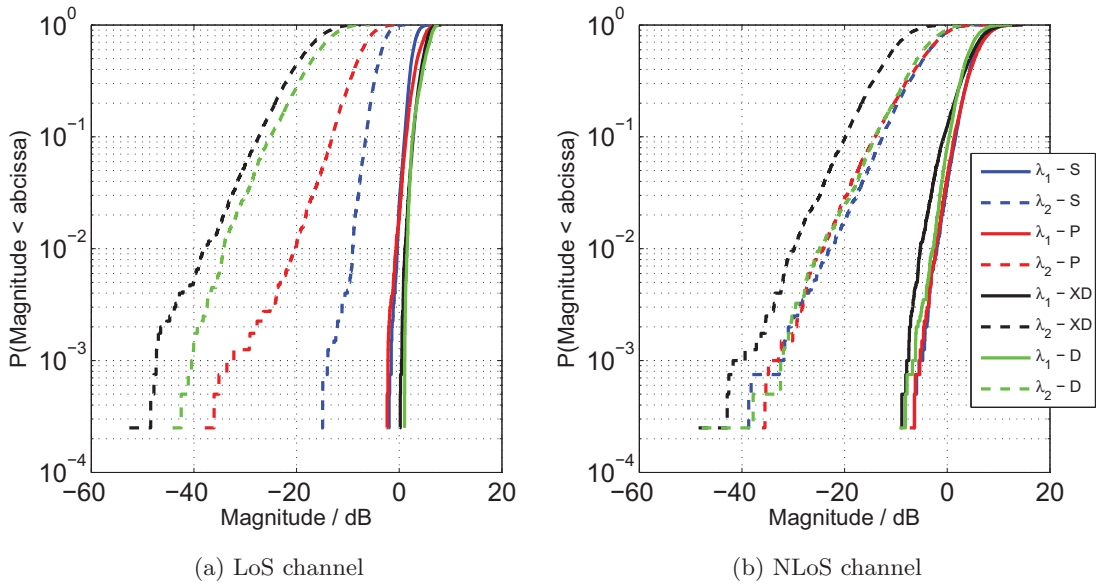


Figure 7.27: Eigenvalues CDFs at SNR of 10 dB of the SFPQHA array (S), patch array (P), cross dipoles (XD) and dipole array (D) with $(\phi_{ant} = 90^\circ, \theta_{ant} = 0^\circ)$ orientation in both LoS and NLoS channels.

orientation, spacing and polarisation on the performance parameters of the LMS MIMO system were investigated in both LoS and NLoS channels. A summary of these effects of each array properties are presented as below

- Orientation: In the LoS channel, the complex behaviour of the capacity very much depends on the azimuth orientation of the antenna and its inclination angle. For the best capacity performance, the antenna's main beam needs to be directed as closely as possible to the transmitter's direction. However, the capacity performance in the NLoS channel is only slightly influenced by the antenna's inclination angle but not its azimuth orientation. It also would be interesting to investigate whether by having two or three arrays where each array pointing to different azimuth angles but with the same inclination angle to cover the whole angular domain can be a viable option for vehicular applications when considering the complexities of such system to be constructed.
- Spacing: In general, the receive antenna spacing has little impact on the capacity

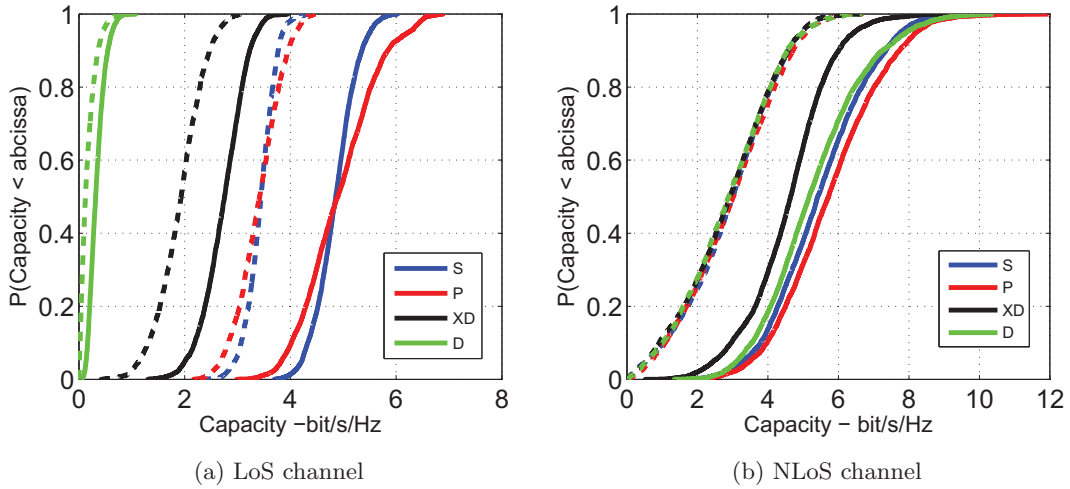


Figure 7.28: Capacity CDFs at SNR of 10 dB of the SFPQHA array (S), patch array (P), cross dipoles (XD) and dipole array (D) with $(\phi_{ant} = 90^\circ, \theta_{ant} = 60^\circ)$ orientation in both LoS and NLoS channels.

of the LMS MIMO system in both LoS and NLoS channels. This is mainly due to the fact that the SFPQHAs with orthogonal circular polarisation are able to maintain its radiation pattern and polarisation purity even at a very close spacing.

- **Polarisation:** Both the transmit and receive arrays' polarisation purities are fundamental in determining the MIMO performance of the LMS MIMO system where its capacity is hugely affected by both properties in the LoS and NLoS channels. The best capacity performance in both channel conditions can be achieved by having the array at both sides of transmitter and receiver to be perfectly dual polarised. However, a more practical option is for the transmit antennas to be designed with XPR around 30 dB while the receive antenna can be configured for a slightly lower value of XPR at 20 dB.

For the final analysis, performance comparison between the dual polarised SFPQHA array, dual polarised patch array, 45° slanted cross dipoles and dipoles array were conducted in both LoS and NLoS channels. Their performances are categorised into four orientations where its purpose is to demonstrate the effect of orientation on each array performance. In the LoS channel and with the exception of the second orientation

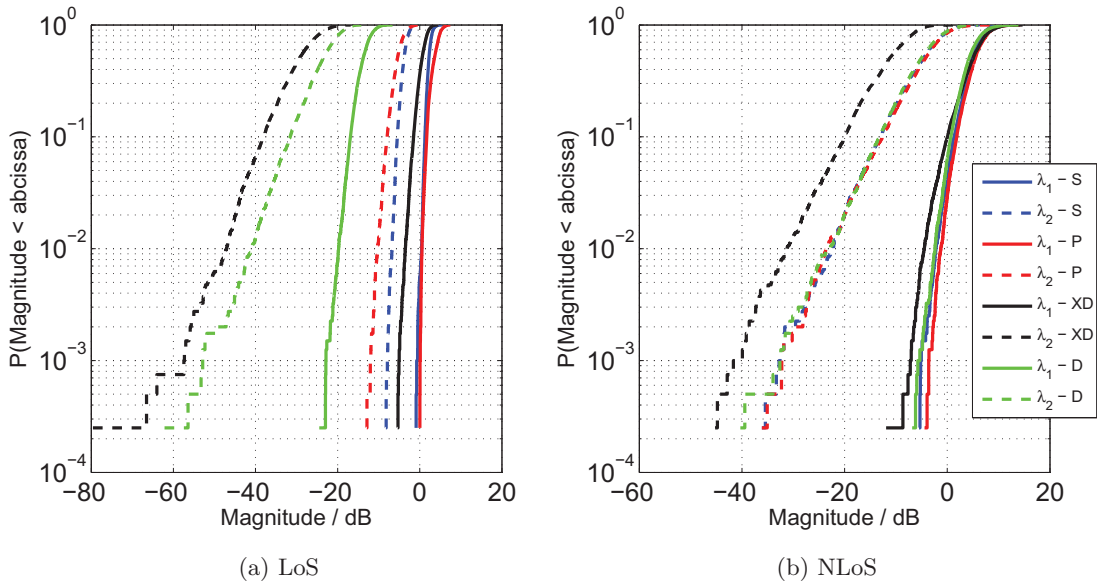


Figure 7.29: Eigenvalues CDFs at SNR of 10 dB of the SFPQHA array (S), patch array (P), cross dipoles (XD) and dipole array (D) with $(\phi_{ant} = 90^\circ, \theta_{ant} = 60^\circ)$ orientation in both LoS and NLoS channels.

$(\phi_{ant} = 0^\circ, \theta_{ant} = 60^\circ)$, the best performance in terms of outage capacity can be obtained by using the SFPQHA array as the receive antenna. As for the NLoS channel and again with the exception of the second orientation, the patch and SFPQHA arrays offer better outage capacity than the other two arrays. Even for the second orientation, the capacity CDF between these four arrays in the NLoS channel is very close where the value of 10% outage capacity of all arrays is within 3.5 to 4 bit/s/Hz.

The eigenvalue distribution of the received signal from all these arrays also can reveals the suitability of the antenna to be used in the LMS MIMO system that utilises polarisation multiplexing where the closer the magnitude between the antenna eigenvalues, the more suited such antenna for this system. From this investigation, the SFPQHA array is shown to be the best antenna for supporting polarisation multiplexing among these studied antennas where its eigenvalues has the closest range of magnitude for all orientations in the LoS channel. In conclusion, the designed SFPQHA array has an excellent performance when compared to other antennas in most of the orientation category in both channel conditions.

Chapter 8

Conclusions and Further Work

8.1 Conclusions

As stated in the first chapter of this thesis, the aim of this research work is to develop a novel antenna system by utilising printed quadrifilar helix antenna (PQHA) for the land mobile satellite (LMS) MIMO receiver terminal and also to evaluate its performance in terms of its MIMO capabilities. Therefore, it is only fitting that the question on whether the aim is been achieved is answered in this conclusion. This thesis has proposed the use of dual circularly polarised array of miniaturised PQHAs such as folded meandered PQHA (FMPQHA) and single folded PQHA (SFPQHA) arrays as the receive antenna of the system. Since the antennas need to be evaluated in terms of its MIMO capabilities, which are highly dependent on the propagation channel, the evaluation method must incorporate the channel characteristics for an accurate assessment of the antenna performance. Three main figures of merit which are the branch power ratio, correlation and capacity/eigenvalues have been selected as the performance parameters in evaluating these arrays. For each figure of merit, different types of evaluation method were used where each method needs to be adapted so that it includes the characteristics of the LMS MIMO channel. Based on the results of these evaluations, it can be concluded that the proposed array provides an optimal performance in order for it to be utilised as th receive antenna of the LMS MIMO system. The following paragraphs will summarise the main ideas of each chapter in this thesis and

thus provide a comprehensive conclusion of this research.

A detailed review on three main areas of research, which are the LMS MIMO system, quadrifilar helix antenna and its advancements and performance evaluation of MIMO antennas has been presented in chapter 2 of this thesis. The review reveals that there has not been a single study that explicitly investigated the design and implementation of the receive array of this system as well as its impacts to the overall system performance. In this work, the quadrifilar helix antenna is considered to be a promising candidate for the basic antenna element of the receive array of the LMS MIMO receiver due to its good circularly polarised beam and wide beamwidth to cater for various satellite elevation angles. However, there are several other issues regarding the PQHA's properties especially its size before it can be used as the receive antenna. Finally, the chapter provides a summary of various figures of merit and its evaluation methods in determining the performance of MIMO antennas that can be used in this work. It has been found that most of the evaluation methods are designed specifically for terrestrial communication and therefore requires further adaptation and modifications for them to be used in evaluating MIMO antennas in the LMS MIMO system.

Chapters 3 and 4 of this thesis described the design, simulation, fabrication and measurement of the proposed miniaturised PQHAs and also its variation of dual circularly polarised arrays. Miniaturisation of the PQHA has been achieved by using two new methods which are element folding and combination of element folding and meandering. Axial length reduction of more than 50% can be obtained using both methods without significant degradation in radiation and impedance properties of the antenna. The miniaturised PQHAs which are the SFPQHA and FMPQHA were used as the basic element in designing a dual circularly polarised array. Meanwhile, in chapter 4, three configurations of a dual circularly polarised array that utilise PQHA and its compact variants (SFPQHA and FMPQHA) have been presented. Evaluation of these arrays was first conducted using electromagnetic simulation and then later selected arrays were fabricated and its radiation pattern and impedance characteristics were measured. The selected array were then utilised as the receive array for the LMS MIMO system.

In order to precisely evaluate the branch power ratio of the proposed dual circularly

polarised array in the LMS MIMO channel, chapter 5 introduced a new formulation of mean effective gain (MEG) in a Ricean fading channel that includes not only the magnitude but also the phase of the LoS component of the incident waves and the corresponding antenna field pattern. This allows for a more accurate evaluation of the MEG of a more generally polarised antenna in a Ricean channel. This is due to the fact that by including the phases of both components, the polarisation mismatch between the LoS component and the antenna field are taken into account when calculating the MEG of the antenna. By using the developed formulation, the SFPQHA array was evaluated in terms of its branch power ratio in Ricean channels with K factor varying from $-\infty$ dB to ∞ dB with the polarisation of LoS component is varied from right hand (RH) to left hand (LH) circular polarisations. It has been shown that the impact of the LoS component phase on the array's branch power ratio increases with the increase of the LoS component power which is given by the Ricean K factor. The chapter also investigated the correlation between the SFPQHAs of the dual circularly polarised array for various channel conditions that are described by its cross polarisation discrimination (XPD) and Angle-of-Arrival (AoA) distribution. The study showed the lowest correlation between the SFPQHAs in the array occurred when the channel XPD is close to zero dB. The chapter concluded with the derivation of a new formulation of complex correlation that only includes the antenna polarisation as the antenna parameter for calculation.

Due to the lack of any other mean in determining the capacity of the LMS MIMO system that utilises the proposed FMPQHA and SFPQHA arrays, measurement campaigns have been conducted where the proposed arrays are used as the receive antennas. Chapter 6 provides a detailed description of the measurements and also its results that include narrowband channel characteristics and MIMO figures of merit of the receive array. For each environment, the antennas were evaluated in two channel conditions, which are the LoS and NLoS channels. The results clearly showed a significant increase of capacity when the system uses the proposed arrays when compared to a single antenna system in both channel conditions. Apart from that, the measurements also indicated the importance of receive array orientation in influencing the capacity of the LMS MIMO system.

Chapter 7 focuses on the development of a new approach in LMS MIMO channel modelling which combines the receive array characteristics with the propagation channel simulation. This is achieved with the use of statistical method in the large scale fading and shadowing modelling and the 3-D hemisphere geometric scattering model for the small scale fading which allows for the receive antennas properties to be included in the simulation. A comprehensive evaluation of the receive array performance can then be implemented using this new channel modelling approach. Firstly, the array properties such as orientation, spacing and polarisation were studied in terms of their impact on the MIMO performance of the system. Then, the performance of the proposed dual circularly polarised SFPQHA array was compared with other arrays in both LoS and NLoS channels at four different orientations.

8.2 Further Work

Incorporating two orthogonally polarised QHAs on one cylindrical structure

Currently, an array needs to be constructed in order to obtain the capability of dual circular polarisation where its basic element is a QHA or its variant. Although the current designed arrays have a relatively compact size due to the miniaturisation of the QHA and the use of high permittivity material for the feeding network, it would be more advantageous if the ability to radiate both polarisation can be obtained by only a single cylindrical structure. The typical way of helical winding is not sufficient to achieve this goal and therefore requires a novel method in combining two opposite directed helical elements on a single structure. Since a QHA consists of four helical element, combination of two opposing directed QHAs will introduce eight helical elements on a cylindrical structure which make it impossible for the elements to be wound without any connection. Apart from that, since each element will be very close to one another, the effect of mutual coupling between these elements can be very strong thus further complicating the helical elements arrangement.

Designing a novel and compact feeding network

As the design of a QHA requires its element to be fed in phase quadrature and equal amplitude, the feeding network of a QHA can be quite complicated and bulky. This is even more so when the dual circularly polarised array is considered where eight feed lines need to be designed and arranged. In this work, the use of circuit board substrate with relative permittivity of 10 and SMD size resistors have managed to reduce substantially the area size of the feeding network. However, the size of the designed feeding network can still be regarded as slightly bulky for it to be fitted into a small handheld device. Therefore, a novel approach in designing the feeding network is urgently required to further reduce its size. One conventional solution is the use of multilayer circuit for the feeding network. As for the feed network of dual polarised QHAs that are co-located, another issue that needs to be considered is the reduction of mutual coupling effect between the feed lines especially when they are in a very close spacing. Ultimately, a more radical way of feeding the antenna that can remove the need for a complicated circuitry is very much of interest since it will drastically increase the applicability of the QHA.

Extension of the measurement campaign

In the current measurement campaigns that have been conducted, the maximum achievable satellite elevation angle is around 30° which only provides a rather limited view of the land mobile satellite system configuration where its maximum elevation angle may be up to 80° . Therefore, a more comprehensive coverage of the satellite elevation angle especially the higher angles in future measurement campaigns is very much needed as it will provide valuable information on the overall characteristics of the LMS MIMO channel. It also would be beneficial if these measurements can be extended to other types of environment such as urban and motorway areas.

Performance evaluation of MIMO antennas using various simulation or analytical methods requires an accurate representation or model of the propagation channel's Angle-of-Arrival (AoA) and Angle-of-Departure (AoD). For the terrestrial channel in various environments, numerous measurements have been conducted to characterise the AoA

and AoD of the channel, which are used as the basis for the AoA and AoD models development. However, the same cannot be said about LMS channel where to the best of author's knowledge, there have not been a single measurement that investigates the angular characteristics of the channel and also introduces a workable and validated AoA and AoD models. Hence, the research on the angular properties of LMS MIMO channel especially at the receiver is crucial to be undertaken and leads to a more accurate performance evaluation of the antennas.

Improvement of the proposed channel model

There are several improvements that can be made to the developed channel model especially in terms of its small scale fading modelling. Currently, the scatterers in the geometric scattering model is considered to be uniformly distributed inside of a hemisphere which leads to its AoA to be distributed as described by Equation (7.9). However, if there is a new AoA distribution that is regarded to be more accurate for this model, then the scatterer distribution needs to be reconfigured so that the new AoA distribution can be realised. At the moment, the model does not have the flexibility in configuring its AoA characteristics due to the fixed scatterer distribution. Therefore, a new method of distributing the scatterers that allows for AoA reconfiguration is considered to be a major extension of the development of this model. This also allows for the model to be used in other environments that exhibit different channel AoA properties. This strengthen the need for AoA measurements in circular polarisation which may be possible to be conducted using sphere of helices coupled with signal processing technique to provide an estimation the angular characteristics of the channel.

Appendix A

Derivation of turns of straight segment N_{ss} of the FMPQHA

The pitch angle φ_p of a conventional QHA can be defined as [138]:

$$\varphi_p = \arctan\left(\frac{S_{conv}}{2\pi r}\right) \quad (\text{A.1})$$

where S_{conv} denotes the spacing between turns (centre to centre) and r is the antenna radius. The spacing between turns S is related to the axial length L_{ax} and turn N of the QHA by the following equation [138]:

$$S_{conv} = \frac{L_{ax}}{N}. \quad (\text{A.2})$$

For the design of the FMQHA, it has been stated that its pitch angle is identical to the pitch angle of the conventional QHA. Since the radius of both antennas is the same, it is implied that the spacing between turns for the conventional QHA is equal to the FMQHA provided that both antennas have the same pitch angle. Meanwhile the axial length of the FMQHA $L_{ax,fm}$ is given as:

$$L_{ax,fm} = N_{ss} \sqrt{\frac{1}{(N_{ss})^2} (a^2 - (2\pi r)^2)} \quad (\text{A.3})$$

where N_{ss} denotes the turn of the straight segment of the FMQHA and a is the length of the straight segment of the FMQHA. This equation is reformulated by including

$S_{fm} = \frac{L_{ax, fm}}{N_{ss}}$ which is the spacing between turns for FMQHA as:

$$S_{fm} = \sqrt{\frac{1}{(N_{ss})^2} (a^2 - (2\pi r)^2)}. \quad (\text{A.4})$$

Since S_{fm} is equal to the S_{conv} , Equation A.4 can be inserted into Equation A.1 to obtain:

$$\tan \varphi_p = \frac{\sqrt{\frac{1}{(N_{ss})^2} (a^2 - (2\pi r)^2)}}{2\pi r} \quad (\text{A.5})$$

After a simple rearrangement, the turn of straight segment N_{ss} can be written as:

$$N_{ss} = \frac{a}{2\pi r \sqrt{\tan^2 \varphi_p + 1}} \quad (\text{A.6})$$

Appendix B

Equation of the transmitted wave plane

In determining the distance between the scatterer and the transmitted wave plane, the plane must first be defined mathematically by providing its equation. It is assumed that the plane touches the hemisphere surface at a single point (x_0, y_0, z_0) as shown in Fig. B.1. The equation of the plane can be derived by considering that the normal vector of the plane \mathbf{P}_n and tangent vector of the plane \mathbf{P}_t is orthogonal or in terms of dot product operation:

$$\mathbf{P}_t \cdot \mathbf{P}_n = 0 \quad (\text{B.1})$$

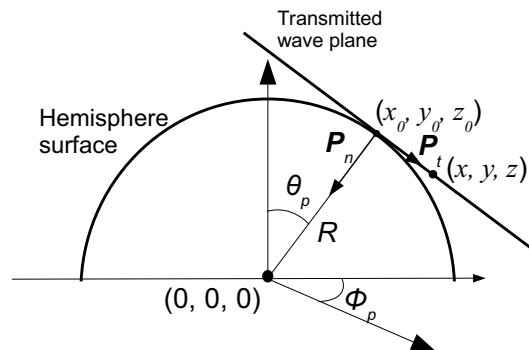


Figure B.1: 2-D view of the transmitted wave and hemisphere planes.

where $\mathbf{P}_t = [(x - x_0)\mathbf{e}_x, (y - y_0)\mathbf{e}_y, (z - z_0)\mathbf{e}_z]$ and $\mathbf{P}_n = [x_0\mathbf{e}_x, y_0\mathbf{e}_y, z_0\mathbf{e}_z]$. The point (x_0, y_0, z_0) can also be written in spherical coordinates system as:

$$(R \sin \theta_p \cos \phi_p, R \sin \theta_p \sin \phi_p, R \cos \theta_p). \quad (\text{B.2})$$

Then, Equation B.1 can be extended as:

$$\mathbf{P}_t \cdot \mathbf{P}_n = 0 \quad (\text{B.3})$$

$$[(x - x_0)\mathbf{e}_x, (y - y_0)\mathbf{e}_y, (z - z_0)\mathbf{e}_z] \cdot [x_0\mathbf{e}_x, y_0\mathbf{e}_y, z_0\mathbf{e}_z] = 0$$

$$(x - x_0)(x_0) + (y - y_0)(y_0) + (z - z_0)(z_0) = 0$$

$$R \sin \theta_p \cos \phi_p x - R^2 \sin^2 \theta_p \cos^2 \phi_p + R \sin \theta_p \sin \phi_p y - R^2 \sin^2 \theta_p \sin^2 \phi_p +$$

$$R \cos \theta_p z - R^2 \cos^2 \theta_p = 0$$

$$R \sin \theta_p \cos \phi_p x + R \sin \theta_p \sin \phi_p y + R \cos \theta_p z - R^2 = 0$$

$$R - \sin \theta_p \cos \phi_p x - \sin \theta_p \sin \phi_p y - \cos \theta_p z = 0.$$

The final equation is then used as the plane equation of the transmitted wave as presented in Equation 7.11.

Bibliography

- [1] P.-S. Kildal and K. Rosengren, “Correlation and capacity of MIMO systems and mutual coupling, radiation efficiency, and diversity gain of their antennas: simulations and measurements in a reverberation chamber,” *Communications Magazine, IEEE*, vol. 42, no. 12, pp. 104–112, 2004.
- [2] D. G. Brennan, “Linear diversity combining techniques,” *Proceedings of the IRE*, vol. 47, no. 6, pp. 1075–1102, 1959.
- [3] J. Winters, “On the capacity of radio communication systems with diversity in a rayleigh fading environment,” *Selected Areas in Communications, IEEE Journal on*, vol. 5, no. 5, pp. 871 – 878, Jun. 1987.
- [4] G. J. Foschini, “Layered space-time architecture for wireless communication in a fading environment when using multiple antennas,” *Bell Labs Technical Journal*, pp. 41 – 59, 1996.
- [5] I. E. Telatar, “Capacity of multi-antenna gaussian channels,” *European Transactions on Telecommunications*, vol. 10, no. 6, pp. 585–595, 1999. [Online]. Available: <http://dx.doi.org/10.1002/ett.4460100604>
- [6] M. Andrews, P. Mitra, and R. Decarvalho, “Tripling the capacity of wireless communications using electromagnetic polarization,” *Nature*, vol. 409, no. 6818, pp. 316–318, 2001.
- [7] W. Lee and Y. Yeh, “Polarization diversity system for mobile radio,” *Communications, IEEE Transactions on*, vol. 20, no. 5, pp. 912–923, 1972.

-
- [8] S. Kozono, T. Tsuruhara, and M. Sakamoto, "Base station polarization diversity reception for mobile radio," *Vehicular Technology, IEEE Transactions on*, vol. 33, no. 4, pp. 301–306, 1984.
- [9] R. G. Vaughan, "Polarization diversity in mobile communications," *Vehicular Technology, IEEE Transactions on*, vol. 39, no. 3, pp. 177–186, 1990.
- [10] G. J. Foschini and M. J. Gans, "On limits of wireless communications in a fading environment when using multiple antennas," *Wireless Personal Communications*, vol. 6, pp. 311–335, 1998.
- [11] S. R. Saunders and A. Aragon-Zavala, *Antennas and propagation for wireless communication systems*, 2nd ed. John Wiley & Sons, Ltd., 2007.
- [12] D.-S. Shiu, G. Foschini, M. Gans, and J. Kahn, "Fading correlation and its effect on the capacity of multielement antenna systems," *Communications, IEEE Transactions on*, vol. 48, no. 3, pp. 502–513, Mar. 2000.
- [13] M. Ozdemir, E. Arvas, and H. Arslan, "Dynamics of spatial correlation and implications on MIMO systems," *Communications Magazine, IEEE*, vol. 42, no. 6, pp. S14 – S19, Jun. 2004.
- [14] J.-A. Tsai, R. Buehrer, and B. Woerner, "The impact of AOA energy distribution on the spatial fading correlation of linear antenna array," in *Vehicular Technology Conference, 2002. VTC Spring 2002. IEEE 55th*, vol. 2, 2002, pp. 933 – 937.
- [15] C. Oestges and A. J. Paulraj, "Beneficial impact of channel correlations on MIMO capacity," *Electronics Letters*, vol. 40, no. 10, pp. 606–608, 2004.
- [16] H. Ozcelik and C. Oestges, "Some remarkable properties of diagonally correlated MIMO channels," *Vehicular Technology, IEEE Transactions on*, vol. 54, no. 6, pp. 2143–2145, 2005.
- [17] P. Driessen and G. Foschini, "On the capacity formula for multiple input-multiple output wireless channels: a geometric interpretation," *Communications, IEEE Transactions on*, vol. 47, no. 2, pp. 173–176, Feb. 1999.

-
- [18] D. McNamara, M. Beach, P. Fletcher, and P. Karlsson, "Capacity variation of indoor multiple-input multiple-output channels," *Electronics Letters*, vol. 36, no. 24, pp. 2037–2038, Nov. 2000.
- [19] T. Svantesson and J. Wallace, "On signal strength and multipath richness in multi-input multi-output systems," in *Communications, 2003. ICC '03. IEEE International Conference on*, vol. 4, May 2003, pp. 2683–2687.
- [20] M. Shafi, M. Zhang, A. L. Moustakas, P. J. Smith, A. F. Molisch, F. Tufveson, and S. H. Simon, "Polarized MIMO channels in 3-D: models, measurements and mutual information," *Selected Areas in Communications, IEEE Journal on*, vol. 24, no. 3, pp. 514–527, 2006.
- [21] L. Jiang, L. Thiele, A. Brylka, S. Jaeckel, and V. Jungnickel, "Polarization characteristics of multiple-input multiple-output channels," in *Proc. IEEE 19th Int. Symp. Personal, Indoor and Mobile Radio Communications PIMRC 2008*, 2008, pp. 1–5.
- [22] H. Asplund, J.-E. Berg, F. Harrysson, J. Medbo, and M. Riback, "Propagation characteristics of polarized radio waves in cellular communications," in *Proc. VTC-2007 Fall Vehicular Technology Conf. 2007 IEEE 66th*, 2007, pp. 839–843.
- [23] P. King and S. Stavrou, "Capacity improvement for a land mobile single satellite MIMO system," *Antennas and Wireless Propagation Letters, IEEE*, vol. 5, no. 1, pp. 98–100, Dec. 2006.
- [24] P.-D. Arapoglou, P. Burzigotti, A. B. Alamanac, and R. De Gaudenzi, "Capacity potential of mobile satellite broadcasting systems employing dual polarization per beam," in *Proc. 5th Advanced satellite multimedia systems conference (ASMA) and the 11th signal processing for space communications workshop (SPSC)*, 2010, pp. 213–220.
- [25] F. Perez-Fontan, M. Vazquez-Castro, S. Buonomo, J. Poiaries-Baptista, and B. Arbesser-Rastburg, "S-band LMS propagation channel behaviour for different environments, degrees of shadowing and elevation angles," *Broadcasting, IEEE Transactions on*, vol. 44, no. 1, pp. 40–76, Mar. 1998.

-
- [26] P. Chini, G. Giambene, and S. Kota, "A survey on mobile satellite systems," *International Journal of Satellite Communications and Networking*, vol. 28, no. 1, pp. 29–57, 2010. [Online]. Available: <http://dx.doi.org/10.1002/sat.941>
- [27] F. P. Fontan, M. Vazquez-Castro, C. E. Cabado, J. P. Garcia, and E. Kubista, "Statistical modeling of the LMS channel," *Vehicular Technology, IEEE Transactions on*, vol. 50, no. 6, pp. 1549–1567, 2001.
- [28] P. Horvath and I. Frigyes, "Application of the 3D polarization concept in satellite MIMO systems," in *Global Telecommunications Conference, 2006. GLOBECOM '06. IEEE*, Dec. 2006, pp. 1–5.
- [29] P. King and S. Stavrou, "Low elevation wideband land mobile satellite MIMO channel characteristics," *Wireless Communications, IEEE Transactions on*, vol. 6, no. 7, pp. 2712–2720, Jul. 2007.
- [30] T. Heyn, E. Eberlein, D. Arndt, B. Matuz, F. L. Blasco, R. Prieto-Cerdeira, and J. Rivera-Castro, "Mobile satellite channel with angle diversity: The MiLADY project," in *Antennas and Propagation (EuCAP), 2010 Proceedings of the Fourth European Conference on*, Apr. 2010, pp. 1–5.
- [31] D. Arndt, A. Ihlow, A. Heuberger, T. Heyn, E. Eberlein, and R. Prieto-Cerdeira, "Mobile satellite broadcasting with angle diversity - performance evaluation based on measurements," in *Broadband Multimedia Systems and Broadcasting (BMSB), 2010 IEEE International Symposium on*, Mar. 2010, pp. 1–8.
- [32] "MIMOSA project webpage," <http://telecom.esa.int/telecom/www/object/index.cfm?fobjectid=31061>, accessed: 12/05/2011.
- [33] E. Eberlein, F. Burkhardt, C. Wagner, D. Heuberger, D. Arndt, and R. Prieto-Cerdeira, "Statistical evaluation of the MIMO gain for LMS channels," in *Antennas and Propagation (EuCAP), 2011 Proceedings of the Fourth European Conference on*, Apr. 2011, pp. 2848–2852.
- [34] C. Tzaras, B. Evans, and S. Saunders, "Physical-statistical analysis of land

-
- mobile-satellite channel,” *Electronics Letters*, vol. 34, no. 13, pp. 1355 –1357, Jun. 1998.
- [35] C. Oestges, “A stochastic geometrical vector model of macro- and megacellular communication channels,” *Vehicular Technology, IEEE Transactions on*, vol. 51, no. 6, pp. 1352 – 1360, Nov. 2002.
- [36] C. Oestges and D. Vanhoenacker-Janvier, “Physical-statistical prediction of performance for land mobile satellite communication systems,” *Microwaves, Antennas and Propagation, IEE Proceedings -*, vol. 146, no. 5, pp. 362 –368, Oct. 1999.
- [37] P. King, B. Evans, and S. Stavrou, “Physical-statistical model for the land mobile satellite channel applied to satellite/HAP-MIMO,” in *11th European Wireless Conference*, Apr. 2005, pp. 1–5.
- [38] P. Horváth, G. K. Karagiannidis, P. R. King, S. Stavrou, and I. Frigyes, “Investigations in satellite MIMO channel modeling: Accent on polarization,” *EURASIP J. Wireless Comm. and Networking*, vol. 2007, 2007.
- [39] M. Cheffena, F. Perez-Fontan, F. Lacoste, E. Cobel, and H.-J. Mametsa, “Land mobile satellite dual polarised MIMO channel along roadside trees: Modelling and performance evaluation,” in *Antennas and Propagation (EuCAP), 2011 Proceedings of the Fourth European Conference on*, Apr. 2011, pp. 3709 –3714.
- [40] S. Torrico, H. Bertoni, and R. Lang, “Modeling tree effects on path loss in a residential environment,” *Antennas and Propagation, IEEE Transactions on*, vol. 46, no. 6, pp. 872 –880, Jun. 1998.
- [41] M. Sellathurai, P. Guinand, and J. Lodge, “Space-time coding in mobile satellite communications using dual-polarized channels,” *Vehicular Technology, IEEE Transactions on*, vol. 55, no. 1, pp. 188 – 199, Jan. 2006.
- [42] K. Liolis, J. Gomez-Vilardebo, E. Casini, and A. Perez-Neira, “Statistical modeling of dual-polarized MIMO land mobile satellite channels,” *Communications, IEEE Transactions on*, vol. 58, no. 11, pp. 3077 –3083, Nov. 2010.

-
- [43] T. Brown and A. Kyrgiazos, "On the small scale modelling aspects of dual circular polarised land mobile satellite MIMO channels in lone of sight and in vehicles," in *Antennas and Propagation (EuCAP), 2011 Proceedings of the Fourth European Conference on*, Apr. 2011, pp. 3718–3721.
- [44] P. R. King, "Modelling and measurement of the land mobile satellite MIMO radia propagation channel," Ph.D. dissertation, University of Surrey, UK, 2007.
- [45] C. Loo, "A statistical model for a land mobile satellite link," *Vehicular Technology, IEEE Transactions on*, vol. 34, no. 3, pp. 122–127, Aug. 1985.
- [46] R. Prieto-Cerdeira, F. Perez-Fontan, P. Burzigotti, A. Bolea-Alamaac, and I. Sanchez-Lago, "Versatile two-state land mobile satellite channel model with first application to DVB-SH analysis," *International Journal of Satellite Communications and Networking*, vol. 28, no. 5-6, pp. 291–315, 2010. [Online]. Available: <http://dx.doi.org/10.1002/sat.964>
- [47] A. Agius, S. Saunders, and B. Evans, "The design of specifications for satellite PCN handheld antennas," vol. 1, May 1997, pp. 36–40 vol.1.
- [48] X. Bao and M. J. Ammann, "Dual-frequency dual-sense circularly-polarized slot antenna fed by microstrip line," *Antennas and Propagation, IEEE Transactions on*, vol. 56, no. 3, pp. 645–649, 2008.
- [49] M.-H. Ho, M.-T. Wu, C.-I. G. Hsu, and J.-Y. Sze, "An RHCP/LHCP switchable slotline-fed slot-ring antenna," *Microwave and Optical Technology Letters*, vol. 46, no. 1, pp. 30–33, 2005. [Online]. Available: <http://dx.doi.org/10.1002/mop.20892>
- [50] J. Howell, "Microstrip antennas," *Antennas and Propagation, IEEE Transactions on*, vol. 23, no. 1, pp. 90–93, 1975.
- [51] P. Sharma and K. Gupta, "Analysis and optimized design of single feed circularly polarized microstrip antennas," *Antennas and Propagation, IEEE Transactions on*, vol. 31, no. 6, pp. 949–955, 1983.
- [52] L. Shen, "The elliptical microstrip antenna with circular polarization," *Antennas and Propagation, IEEE Transactions on*, vol. 29, no. 1, pp. 90–94, 1981.

-
- [53] F. Yang and Y. Rahmat-Samii, "A reconfigurable patch antenna using switchable slots for circular polarization diversity," *Microwave and Wireless Components Letters, IEEE*, vol. 12, no. 3, pp. 96–98, 2002.
- [54] W.-S. Yoon, J.-W. Baik, H.-S. Lee, S. Pyo, S.-M. Han, and Y.-S. Kim, "A reconfigurable circularly polarized microstrip antenna with a slotted ground plane," *Antennas and Wireless Propagation Letters, IEEE*, vol. 9, pp. 1161–1164, 2010.
- [55] E. Aloni and R. Kastner, "Analysis of a dual circularly polarized microstrip antenna fed by crossed slots," *Antennas and Propagation, IEEE Transactions on*, vol. 42, no. 8, pp. 1053–1058, 1994.
- [56] A. Petosa and S. Thirakoune, "Circularly polarized array of bent monopoles for l-band mobile satellite communications," in *Proc. 5th European Conf. Antennas and Propagation (EUCAP)*, 2011, pp. 244–248.
- [57] W.-I. Son, W.-G. Lim, M.-Q. Lee, S.-B. Min, and J.-W. Yu, "Design of compact quadruple inverted-F antenna with circular polarization for GPS receiver," *Antennas and Propagation, IEEE Transactions on*, vol. 58, no. 5, pp. 1503–1510, 2010.
- [58] X. Yang, Y. Z. Yin, W. Hu, and S. L. Zuo, "Low-profile, small circularly polarized inverted-L antenna with double-folded arms," *Antennas and Wireless Propagation Letters, IEEE*, vol. 9, pp. 767–770, 2010.
- [59] H. A. Wheeler, "A helical antenna for circular polarization," *Proceedings of the IRE*, vol. 35, no. 12, pp. 1484–1488, 1947.
- [60] J. D. Kraus, "The helical antenna," *Proceedings of the IRE*, vol. 37, no. 3, pp. 263–272, 1949.
- [61] C. Kilgus, "Resonant quadrafilar helix," *Antennas and Propagation, IEEE Transactions on*, vol. 17, no. 3, pp. 349 – 351, May 1969.
- [62] —, "Spacecraft and ground station applications of the resonant quadrifilar helix," in *Antennas and Propagation Society International Symposium, 1974*, vol. 12, Jun. 1974, pp. 75 – 77.

-
- [63] A. Agius, S. Saunders, and B. Evans, "Antenna design for the ICO handheld terminal," in *Antennas and Propagation, Tenth International Conference on (Conf. Publ. No. 436)*, vol. 1, Apr. 1997, pp. 385–389 vol.1.
- [64] S. Leach, A. Agius, S. Stavrou, and S. Saunders, "Diversity performance of the intelligent quadrifilar helix antenna in mobile satellite systems," *Microwaves, Antennas and Propagation, IEE Proceedings -*, vol. 147, no. 4, pp. 305–310, Aug. 2000.
- [65] T. Brown, K. Chew, and S. Saunders, "Analysis of the diversity potential of an intelligent quadrifilar helix antenna," in *Antennas and Propagation, 2003. (ICAP 2003). Twelfth International Conference on (Conf. Publ. No. 491)*, vol. 1, Mar. 2003, pp. 194–198 vol.1.
- [66] D. Chew, L. Morfis, D. Mavrikis, and S. Stavrou, "Quadrifilar helix antenna for MIMO system," *Antennas and Wireless Propagation Letters, IEEE*, vol. 3, pp. 197–199, 2004.
- [67] T. Brown and S. Saunders, "The intelligent quadrifilar helix: A compact MIMO antenna for IEEE 802.11n," in *Antennas and Propagation, 2007. EuCAP 2007. The Second European Conference on*, Nov. 2007, pp. 1–4.
- [68] C. Kilgus, "Resonant quadrifilar helix design," *Microwave Journal*, pp. 49–53, 1970.
- [69] M. Amin and R. Cahill, "Effect of helix turn angle on the performance of a half wavelength quadrifilar antenna," *Microwave and Wireless Components Letters, IEEE*, vol. 16, no. 6, pp. 384–386, Jun. 2006.
- [70] K. Keen, "Bandwidth dependence of resonant quadrifilar helix antennas," *Electronics Letters*, vol. 46, no. 8, pp. 550–552, Apr. 2010.
- [71] J. Louvigne and A. Sharaiha, "Broadband tapered printed quadrifilar helical antenna," *Electronics Letters*, vol. 37, no. 15, pp. 932–933, Jul. 2001.
- [72] Y. W. Chow, E. K. N. Yung, and H. T. Hui, "Quadrifilar helix antenna with

-
- parasitic helical strips,” *Microwave and Optical Technology Letters*, vol. 30, no. 2, pp. 128 – 130, Jul. 2001.
- [73] Y. Letestu and A. Sharaiha, “Broadband folded printed quadrifilar helical antenna,” *Antennas and Propagation, IEEE Transactions on*, vol. 54, no. 5, pp. 1600 –1604, May 2006.
- [74] R. Sainati, J. Groppelli, R. Olesen, and A. Stanland, “A band-switched resonant quadrifilar helix,” *Antennas and Propagation, IEEE Transactions on*, vol. 30, no. 5, pp. 1010 – 1013, Sep. 1982.
- [75] D. Lamensdorf and M. Smolinski, “Dual-band quadrifilar helix antenna,” in *Antennas and Propagation Society International Symposium, 2002. IEEE*, vol. 3, 2002, pp. 488 – 491.
- [76] A. Sharaiha and C. Terret, “Overlapping quadrifilar resonant helix antenna,” *Electronics Letters*, vol. 26, no. 14, pp. 1090 –1092, May 1990.
- [77] S. Liu and Q.-X. Chu, “A novel dielectrically-loaded antenna for GPS/CNSS dual-band applications,” in *Microwave and Millimeter Wave Technology, 2008. ICMMT 2008. International Conference on*, vol. 4, Apr. 2008, pp. 1664 –1666.
- [78] Y. Letestu and A. Sharaiha, “Multiband printed quadrifilar helical antenna,” *Electronics Letters*, vol. 46, no. 13, pp. 885 –886, Jun. 2010.
- [79] J. Rabemanantsoa and A. Sharaiha, “Size reduced dual-band printed quadrifilar helix antenna,” in *Antennas and Propagation (EuCAP), 2010 Proceedings of the Fourth European Conference on*, Apr. 2010, pp. 1 –4.
- [80] S. R. Saunders and D. K. C. Chew, “Multifilar helix antenna,” U.S. Patent 7 142 170, Nov. 28, 2006.
- [81] M. Amin, R. Cahill, and V. Fusco, “Mechanically tunable multiband compact quadrifilar helix antenna with dual mode operation,” *Antennas and Propagation, IEEE Transactions on*, vol. 56, no. 6, pp. 1528 –1532, Jun. 2008.
- [82] J. Rashed and C.-T. Tai, “A new class of resonant antennas,” *Antennas and Propagation, IEEE Transactions on*, vol. 39, no. 9, pp. 1428–1430, 1991.

-
- [83] D. Chew and S. Saunders, "Meander line technique for size reduction of quadrifilar helix antenna," *Antennas and Wireless Propagation Letters, IEEE*, vol. 1, pp. 109 – 111, 2002.
- [84] Y. Letestu, A. Sharaiha, and P. Besnier, "A size reduced configurations of printed quadrifilar helix antenna," in *Antenna Technology: Small Antennas and Novel Metamaterials, 2005. IWAT 2005. IEEE International Workshop on*, Mar. 2005, pp. 326 – 328.
- [85] A. Takacs, N. Fonseca, H. Aubert, and X. Dollat, "Miniaturization of quadrifilar helix antenna for VHF band applications," in *Antennas Propagation Conference, 2009. LAPC 2009. Loughborough*, Nov. 2009, pp. 597 –600.
- [86] B. Bhandari, S. Gao, and T. Brown, "Meandered variable pitch angle printed quadrifilar helix antenna," in *Antennas Propagation Conference, 2009. LAPC 2009. Loughborough*, Nov. 2009, pp. 325 –328.
- [87] B. Desplanches, A. Sharaiha, and C. Terret, "Parametrical study of printed quadrifilar helical antennas with central dielectric rods," *Microwave and Optical Technology Letters*, vol. 20, no. 4, pp. 249 – 255, Feb. 1999.
- [88] O. Leisten, J. Vardaxoglou, P. McEvoy, R. Seager, and A. Wingfield, "Miniaturised dielectrically-loaded quadrifilar antenna for global positioning system (GPS)," *Electronics Letters*, vol. 37, no. 22, pp. 1321 –1322, Oct. 2001.
- [89] Y.-S. Wang and S.-J. Chung, "A miniature quadrifilar helix antenna for global positioning satellite reception," *Antennas and Propagation, IEEE Transactions on*, vol. 57, no. 12, pp. 3746 –3751, Dec. 2009.
- [90] D. Filipovic, M. Tassoudji, and E. Ozaki, "A coupled-segment quadrifilar helical antenna," in *Wireless Applications Digest, 1997., IEEE MTT-S Symposium on Technologies for*, Feb. 1997, pp. 43 –46.
- [91] M. Amin and R. Cahill, "Compact quadrifilar helix antenna," *Electronics Letters*, vol. 41, no. 12, pp. 672 – 674, Jun. 2005.

-
- [92] K. Sulonen, P. Suvikunnas, L. Vuokko, J. Kivinen, and P. Vainikainen, "Comparison of MIMO antenna configurations in picocell and microcell environments," *Selected Areas in Communications, IEEE Journal on*, vol. 21, no. 5, pp. 703 – 712, Jun. 2003.
- [93] J. Boerman and J. Bernhard, "Performance study of pattern reconfigurable antennas in MIMO communication systems," *Antennas and Propagation, IEEE Transactions on*, vol. 56, no. 1, pp. 231 –236, Jan. 2008.
- [94] J.-H. Choi and S.-O. Park, "Exact evaluation of channel capacity difference of MIMO handset antenna arrays," *Antennas and Wireless Propagation Letters, IEEE*, vol. 9, pp. 219–222, 2010.
- [95] T. Taga, "Analysis of correlation characteristics of antenna diversity in land mobile radio environments," *Electronics and Communications in Japan (Part I: Communications)*, vol. 74, no. 8, pp. 101–116, 1991.
- [96] R. H. Clarke, "A statistical theory of mobile radio reception," *Bell Labs Technical Journal*, vol. 47, pp. 957–1000, July-August 1968.
- [97] T. Brown, S. Saunders, and B. Evans, "Analysis of mobile terminal diversity antennas," *Microwaves, Antennas and Propagation, IEE Proceedings -*, vol. 152, no. 1, pp. 1 – 6, Feb. 2005.
- [98] K. Ogawa, S. Amari, H. Iwai, and A. Yamamoto, "Effects of received power imbalance on the channel capacity of a handset MIMO," in *Personal, Indoor and Mobile Radio Communications, 2007. PIMRC 2007. IEEE 18th International Symposium on*, Sep. 2007, pp. 1 –5.
- [99] T. Taga, "Analysis for mean effective gain of mobile antennas in land mobile radio environments," *Vehicular Technology, IEEE Transactions on*, vol. 39, no. 2, pp. 117 –131, May 1990.
- [100] "IEEE standard definitions of terms for antennas." 1993, IEEE Std 145-1993.
- [101] C. A. Balanis, *Antenna Theory - Analysis and Design*, 3rd ed. John Wiley & Sons, 2005.

-
- [102] R. Tian, B. K. Lau, and Z. Ying, "Multiplexing efficiency of MIMO antennas," *Antennas and Wireless Propagation Letters, IEEE*, vol. 10, pp. 183–186, 2011.
- [103] P. Suvikunnas, J. Villanen, K. Sulonen, C. Icheln, J. Ollikainen, and P. Vainikainen, "Evaluation of the performance of multiantenna terminals using a new approach," *Instrumentation and Measurement, IEEE Transactions on*, vol. 55, no. 5, pp. 1804–1813, 2006.
- [104] R. Tian, V. Plicanic, B. K. Lau, and Z. Ying, "A compact six-port dielectric resonator antenna array: MIMO channel measurements and performance analysis," *Antennas and Propagation, IEEE Transactions on*, vol. 58, no. 4, pp. 1369–1379, 2010.
- [105] F. Harrysson, J. Medbo, A. Molisch, A. Johansson, and F. Tufvesson, "Efficient experimental evaluation of a MIMO handset with user influence," *Wireless Communications, IEEE Transactions on*, vol. 9, no. 2, pp. 853–863, 2010.
- [106] Cellular Telecommunications & Internet Association (CTIA), "CTIA test plan for mobile station over the air performance, Revision 2.2," CTIA, Washington DC, Tech. Rep., Nov. 2006.
- [107] C. L. Holloway, D. A. Hill, J. M. Ladbury, P. F. Wilson, G. Koepke, and J. Coder, "On the use of reverberation chambers to simulate a rician radio environment for the testing of wireless devices," *Antennas and Propagation, IEEE Transactions on*, vol. 54, no. 11, pp. 3167–3177, 2006.
- [108] T. Sakata, A. Yamamoto, T. Hayashi, K. Ogawa, K. Olesen, J. Nielsen, and G. F. Pedersen, "Experimental investigation of a dual-band handset MIMO antenna using a spatial fading emulator," in *Proc. IEEE Antennas and Propagation Society Int. Symp. (APSURSI)*, 2010, pp. 1–4.
- [109] O. Darvishi, B. Abolhassani, and H. Rad, "On the efficiency of directional antennas in MIMO communication systems," in *Sarnoff Symposium, 2009. SARNOFF '09. IEEE*, Mar. 2009, pp. 1–5.

-
- [110] C. Waldschmidt, T. Fugen, and W. Wiesbeck, "Spiral and dipole antennas for indoor MIMO-systems," *Antennas and Wireless Propagation Letters, IEEE*, vol. 1, pp. 176 – 178, 2002.
- [111] R. U. Nabar, H. Bolcskei, V. Erceg, D. Gesbert, and A. J. Paulraj, "Performance of multiantenna signaling techniques in the presence of polarization diversity," *Signal processing, IEEE Transactions on*, vol. 50, no. 10, pp. 2553–2562, 2002.
- [112] T. Svantesson, M. A. Jensen, and J. W. Wallace, "Analysis of electromagnetic field polarizations in multiantenna systems," *Wireless Communications, IEEE Transactions on*, vol. 3, no. 2, pp. 641–646, 2004.
- [113] T. Svantesson and A. Ranheim, "Mutual coupling effects on the capacity of multielement antenna systems," in *Acoustics, Speech, and Signal Processing, 2001. Proceedings. (ICASSP '01). 2001 IEEE International Conference on*, vol. 4, 2001, pp. 2485 –2488.
- [114] R. Janaswamy, "Effect of element mutual coupling on the capacity of fixed length linear arrays," *Antennas and Wireless Propagation Letters, IEEE*, vol. 1, pp. 157 – 160, 2002.
- [115] V. Jungnickel, V. Pohl, and C. von Helmolt, "Capacity of MIMO systems with closely spaced antennas," *Communications Letters, IEEE*, vol. 7, no. 8, pp. 361 – 363, Aug. 2003.
- [116] D. Browne, M. Manteghi, M. Fitz, and Y. Rahmat-Samii, "Experiments with compact antenna arrays for MIMO radio communications," *Antennas and Propagation, IEEE Transactions on*, vol. 54, no. 11, pp. 3239 –3250, Nov. 2006.
- [117] B. Clerckx, C. Craeye, D. Vanhoenacker-Janvier, and C. Oestges, "Impact of antenna coupling on 2×2 MIMO communications," *Vehicular Technology, IEEE Transactions on*, vol. 56, no. 3, pp. 1009 –1018, May 2007.
- [118] X. Li and Z.-P. Nie, "Effect of array orientation on performance of MIMO wireless channels," *Antennas and Wireless Propagation Letters, IEEE*, vol. 3, pp. 368 – 371, 2004.

-
- [119] A. Forenza and J. Heath, R.W., “Impact of antenna geometry on MIMO communication in indoor clustered channels,” in *Antennas and Propagation Society International Symposium, 2004. IEEE*, vol. 2, Jun. 2004, pp. 1700 – 1703 Vol.2.
- [120] A. A. Abouda, H. M. El-Sallabi, and S. G. Haggman, “Effect of antenna array geometry and ULA azimuthal orientation on MIMO channel properties in urban city street grid,” *Progress In Electromagnetics Research*, vol. 64, pp. 257 – 278, 2006.
- [121] A. Petros and S. Licul, “Folded quadrifilar helix antenna,” in *IEEE Antennas and Propagation Society International Symposium*, vol. 4, 2001, pp. 569 –572.
- [122] S. Licul and A. A. Chatzipetros, “Folded helix antenna design,” U.S. Patent 6 229 499, May 8, 2001.
- [123] A.-A. Agius, “Antennas for handheld satellite personal communicators,” Ph.D. dissertation, University of Surrey, June 1999.
- [124] A. Alayon Glazunov, “Theoretical analysis of mean effective gain of mobile terminal antennas in ricean channels,” in *Proc. VTC 2002-Fall Vehicular Technology Conf. 2002 IEEE 56th*, vol. 3, 2002, pp. 1796–1800.
- [125] A. Alayon Glazunov, A. F. Molisch, and F. Tufvesson, “Mean effective gain of antennas in a wireless channel,” *IET Microwaves, Antennas & Propagation*, vol. 3, no. 2, pp. 214–227, 2009.
- [126] C. Oestges, “Propagation modelling of low earth-orbit satellite personal communication systems,” Ph.D. dissertation, Université catholique de Louvain, 2000.
- [127] E. Gambaruto, M. Richharia, and E. Trachtman, “Results of inmarsat bgan-x land vehicular propagation tests,” in *Proc. Second European Conf. Antennas and Propagation EuCAP 2007*, pp. 1–8.
- [128] E. Mondre, “Complex and envelope covariance for rician fading communication channels,” *IEEE Transactions on Communication Technology*, vol. 19, no. 1, pp. 80–84, 1971.

-
- [129] W. L. Stutzman, *Polarization in electromagnetic systems*. Artech House, 1992.
- [130] “OFCOM non-operational license,” <http://licensing.ofcom.org.uk/radiocommunication-licences/non-operational-tech-licence/>, accessed: 04/11/2011.
- [131] A. Molisch, “A generic model for MIMO wireless propagation channels in macro- and microcells,” *Signal Processing, IEEE Transactions on*, vol. 52, no. 1, pp. 61 – 71, 2004.
- [132] L. E. Braten and T. Tjelta, “Semi-markov multistate modeling of the land mobile propagation channel for geostationary satellites,” *IEEE Transactions on Antennas and Propagation*, vol. 50, no. 12, pp. 1795–1802.
- [133] R. Janaswamy, “Angle of arrival statistics for a 3-d spheroid model,” *IEEE Transactions on Vehicular Technology*, vol. 51, no. 5, pp. 1242–1247, 2002.
- [134] S. Lu, T. Liu, and M. Zheng, “A wideband space time statistical model for characterization of satellite communication channel in dense multipath environment,” in *Proc. IEEE 71st Vehicular Technology Conf. (VTC 2010-Spring)*, 2010, pp. 1–5.
- [135] E. Weissten. “Jacobian.” From MathWorld—A Wolfram Web Resource. [Online]. Available: <http://mathworld.wolfram.com/Jacobian.html>
- [136] M. Zhu, F. Tufvesson, and G. Eriksson, “MIMO channels in suburban environments at 300 MHz - analysis and modeling,” Lund University, Tech. Rep., 2012.
- [137] E. W. Weisstein. “Inverse Tangent.” From MathWorld—A Wolfram Web Resource. [Online]. Available: <http://mathworld.wolfram.com/InverseTangent.html>
- [138] J. D. Kraus and R. J. Marhefka, *Antennas for all applications*, 3rd ed. McGraw-Hill, 2002.